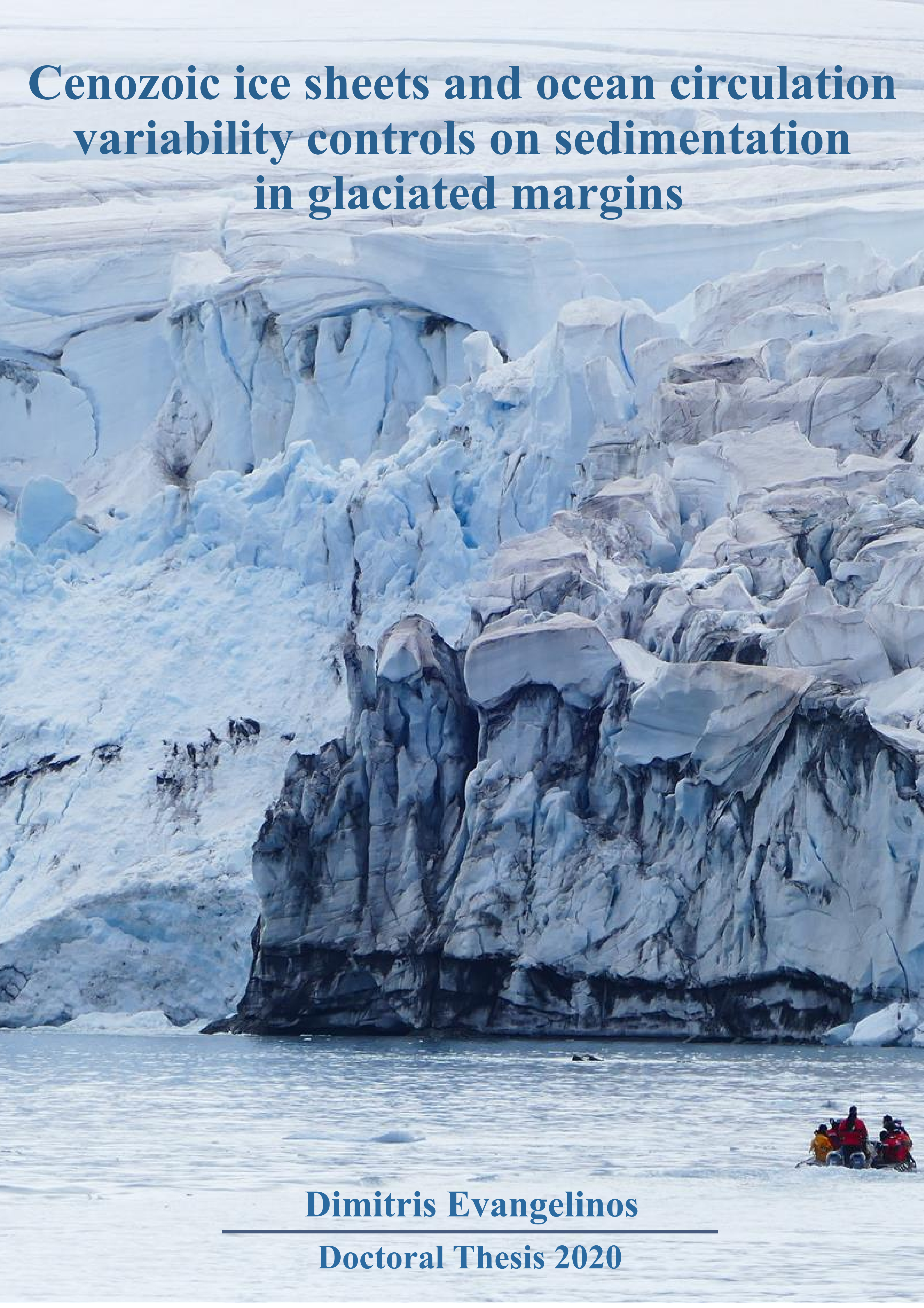

Cenozoic ice sheets and ocean circulation variability controls on sedimentation in glaciated margins

Dimitris Evangelinos

Doctoral Thesis 2020

IACT
INSTITUTO ANDALUZ DE CIENCIAS DE LA TIERRA
CSIC
CONSEJO SUPERIOR DE INVESTIGACIONES CIENTÍFICAS
UNIVERSIDAD
DE GRANADA

Cenozoic ice sheets and ocean variability controls on sedimentation in glaciated margins

Dimitris Evangelinos
Supervisor Dr. Carlota Escutia Dotti

Ph.D. Thesis
2020

Departamento de Geociencias Marinas
Instituto Andaluz de Ciencias de la Tierra (CSIC-UGR)

Programa Doctorado
Ciencias de la Tierra

Editor: Universidad de Granada. Tesis Doctorales
Autor: Evangelinos, Dimitris
ISBN: 78-84-1306-635-6
URI: http://hdl.handle.net/10481/63903

The front cover photograph shows a group of scientists (*Meghan, Johan and Dimitris*) in a zodiac approaching the Johnson Glacier in the Livingston Island, Antarctica, during the Spanish Antarctic Expedition "*Drake 2018*".

This PhD Thesis has been carried out in the Department of Marine Geosciences, at the Instituto Andaluz de Ciencias de la Tierra. Financial support was provided by the Onassis Foundation Scholarship ID: F ZL 016-1/2015-2016. Funding for research was provided by the Spanish Ministry of Science and Innovation (grants CTM2014-60451-C2-1-P and CTM2017-89711-C2-1-P).

ITHAKA

As you set out for Ithaka
hope the voyage is a long one,
full of adventure, full of discovery.
Laistrygonians and Cyclops,
angry Poseidon—don’t be afraid of them:
you’ll never find things like that on your way
as long as you keep your thoughts raised high,
as long as a rare excitement
stirs your spirit and your body.
Laistrygonians and Cyclops,
wild Poseidon—you won’t encounter them
unless you bring them along inside your soul,
unless your soul sets them up in front of you.

Hope the voyage is a long one.
May there be many a summer morning when,
with what pleasure, what joy,
you come into harbors seen for the first time;
may you stop at Phoenician trading stations
to buy fine things,
mother of pearl and coral, amber and ebony,
sensual perfume of every kind—
as many sensual perfumes as you can;
and may you visit many Egyptian cities
to gather stores of knowledge from their scholars.

Keep Ithaka always in your mind.
Arriving there is what you are destined for.
But do not hurry the journey at all.
Better if it lasts for years,
so you are old by the time you reach the island,
wealthy with all you have gained on the way,
not expecting Ithaka to make you rich.

Ithaka gave you the marvelous journey.
Without her you would not have set out.
She has nothing left to give you now.

And if you find her poor, Ithaka won’t have fooled you.
Wise as you will have become, so full of experience,
you will have understood by then what these Ithakas mean.

C. P. Cavafy, 1911.
Translated by Edmund Keeley and Philip Sherrard.

Acknowledgements

A PhD is a voyage, like an expedition to Antarctica. It all starts a sunny and peaceful day in a lively harbour. The sea close to the coast is calm. You embark on this trip with high hopes and expectations. Along the voyage, quickly things change. You come across high seas and storms. You feel dizzy, start losing your orientation. All these until you see the first iceberg. At that moment you feel the excitement and understand why you decided to sail in the first place. As you approach closer to the Antarctic continent, you see the ice covering the sea surface as far as you can see. You remain speechless for hours thinking about the first explorers who tried crossing the sea ice in search of the unknown. Their explorations might have stopped here, but they continued dreaming about what lays beyond the ice. And then, you see the end; the great Antarctic continent emerging from the horizon. The continent of peace and science. You have made it. You are there.

Like an Antarctic expedition, the PhD is not a lonely journey. Many people contribute directly and indirectly. In my journey, I was lucky enough to have so many great people who helped me to finish my voyage and eventually find my Antarctica. Please allow me to express my gratitude to them and forgive me if I have forgotten someone.

First and foremost, I owe my sincerest gratitude to my director, mentor and great teacher Carlota Escutia. Carlota offered me the most unique opportunity, a dream. But she also taught me how to pursue this dream with her continuous encouragement, unwavering support, guidance and patience. During my PhD I was so privileged to participate in four Antarctic expeditions. Each and every one of them extremely unique. But it would not have been possible if Carlota had not given me these opportunities. She has been, she is and (I know) she will always be there to encourage, give advice and provide support. Carlota, I cannot express enough my gratitude and appreciation to you.

I am very much grateful to Hans Nelson. Through his eyes I saw that science is not a job, science is fun. Science is a dream. Hans taught me how to make the big step from having a bunch of results to forming hypotheses and how to outline my ideas. Thank you Hans, for all these hours working together always being calm and enthusiastic. Your work and passion have always inspired me.

I would like to express my gratitude to Tina Van de Flierdt for giving me the opportunity to explore the world of geochemistry. I feel incredibly grateful that I was a part of your really MAGIC laboratory even though it was for a short time. I have learnt so many things during my visits at the Imperial College London. I still remember these long nights and early mornings we spent together in the mass spectrometry lab. Thank you Tina, for sharing your passion for science and allowing me to grow as a research scientist. I am very grateful to Katharina Kreissig for providing priceless training, finding some time for me in her busy schedule in the lab and preparing all the necessary material for my tiny samples. Thank you Katharina, for your guidance, effort and for being always so positive and patient. I would also like to thank Claire Huck, Liam Holder, Patric Pereira and Bari Coles for their valuable help.

I am very thankful to my tutor, Francisca Martínez Ruiz for always being so helpful and supportive.

At this point, I would like to thank to the Onassis Foundation for the financial support, which allowed me to pursue this research and especially to Katerina Magkel for her technical support and professionalism.

This PhD would not have been possible without the help and contribution of a large number of great collaborators. I am grateful to Luis Valero, Jose-Abel Flores, Francisco Jimenez-Espejo, Francisco Rodriguez-Tovar, Peter Bijl, Frida Hoem, Manu Ducassou, Marie-Claire Perello, Katrina Kerr and David Harwood for their assistance over these years. I wish also to thank the "*Spanish Armada*" and especially Paco Lobo and Marga Garcia for their extensive help with the core descriptions and core sampling in the IODP Gulf Core repository in College Station (Texas).

I should not forget to sincerely thank my two great teachers, Thomas Hasiotis and Marc de Batist for helping me to take my first steps in science.

I am especially thankful to Leanne Armand and Phil O´Brien for giving me the opportunity to participle in my first Antarctic Expedition (*IN2017_V01*) in the Sabrina Coast (East Antarctica). I will never forget these two months. Everything I saw, how I felt and the things I have learnt. I would also like to thank the whole scientific team of the Research Vessel *Investigator* and especially my good friends, Kelly, Rushi Meghan and Liam for all the beautiful moments we shared during the expedition.

I sincerely express my gratitude to a great and inspiring Chief, Fernando Bohoyo, who always considered me as part of the Spanish team during the two Spanish Antarctic expeditions: *DRAKE 2018* and *POWELL 2020* in the Drake Passage. Two breath taking expeditions. I am also grateful to all the members of the scientific and UTM teams, the captains and the Spanish military crew members for the unforgettable days we spent in the Research Vessel *Hespéride*s and the Spanish Antarctic Stations *Juan Carlos I* in Livingston Island and *Gabriel de Castilla* in Deception Island.

A special thank you to Jung-Hyun Kim for giving me the opportunity to see with my own eyes the spectacular scenery of the Ross Sea. Breaking the sea ice with the Research Vessel *Araon* was something I will never forget. "Gamsahamnida" to my Korean friends Sujin, Sumin, Dahae, Jijy and Nahyeon for introducing me to the Korean culture, food and taught me some Korean.

I am thankful to the personnel of the Instituto Andaluz de Ciencias de la Tiera and especially to Karolina Carmona Pérez, Juani Ocaña and Ana Echaguibel Rad for dealing with all the paperwork during these years, having always a big smile in their face. I would also like to thank Elisa Cabrera Holanda, Amparo Salido Ruiz and Jesús Román Alpiste for their help and technical support.

A great thank you to my friends and colleagues from IACT (former and current), Leonardo, Enric, Laura, Manu, Nicole, Claudia, Ruben, Alberto, Erwin, Alvaro, Javi, Bob, Alejandro, Sara, Fatima, Muhammad, Ahmed…..for all the interesting and funny talks during the lunch breaks.

Muchísimas Gracias to my friends from the Antarctic group, Ari, Cecilia and Julia for all the special moments we have shared over the past years in so many different places around the world. I owe special thanks to my good friend and colleague Johan for his continuous guidance and support.

I sincerely express my gratitude to my Greek friends in Granada, Electra, Christina and especially to Marievi and Manolis for always being there in good and bad times and mostly for the numerous long discussions and beautiful memories.

Of course, I could not forget my dearest friends Maria and Argiro with whom we started together a journey in the uncharted waters of science back in 2006, in Lesvos Island and we still keep traveling from different harbours. Maria, I will never forget those long hours in skype, while we were writing our PhD theses.

A very special thank you to my fellow traveller Adrian. We have shared so many unique experiences throughout these years. We have seen so many new places and tasted so many different cuisines. I will miss our long talks in the buses, airplanes, research vessels. I never felt I was alone throughout this journey. Thank you for all the great times.

Words are not enough to express my gratitude to my parents, Fanouris and Artemis and siblings Minoas and Eva for their support to my every decision, for believing in me. *One for all and all for one*. I owe you everything I have accomplished until now. Thank you for everything.

Last, but by no means least, I would like to express my very profound gratitude to my partner in life and best friend Silena for providing me with unfailing support and continuous encouragement throughout these years, in good and bad days. Thank you for all the beautiful and happy moments we have shared all these years and for teaching me to keep a balance without losing sight of the big picture. This accomplishment would not have been possible without you.

to my family

Contents

Abbreviation Index

AABW	Antarctic Bottom Water
ACC	Antarctic Circumpolar Current
AIS	Antarctic Ice Sheet
AIS	Antarctic Ice Sheet
ALBW	Adélie Land Bottom Water
AMS	Amundsen Sea
AS	Amery ice shelf
asl	Above sea level
BS	Bellingshausen Sea
CCD	calcium carbonate compensation depth
CDW	Circumpolar Deep Water
CIROS	Cenozoic Investigation in the Western Ross Sea
CO2	Carbon Dioxide
CRP	Cape Roberts Project
DSDP	Deep Sea Drilling Project
EAIS	East Antarctic Ice Sheet
EECO	Early Eocene Climatic Optimum
EOT	Eocene Oligocene Transition
GIA	Glacial Isostatic Adjustment
IODP	Integrated Ocean Drilling Program
IPCC	Intergovernmental Panel on Climate Change
IRD	Iceberg Rafted Debris
L/UCDW	Lower/Upper Circumpolar Deep Water
Ma/myr	million years ago / million years (duration)
mbsf	meters below sea floor
mbsl	meters below sea level
Mi-1	Miocene isotope event 1
MIS	Marine Isotope Stage
MMCO	middle Miocene climatic optimum
MMCT	Middle Miocene climate transitions
MS	Magnetic Susceptibility
MSCL	Multi-Sensor Core Logger
NADW	North Atlantic Deep Water
Nd	Neodymium
ODV	Ocean Data View
Oi-1	Oligocene isotope event 1
OMT	Oligocene Miocene Transition
p-LC:	proto-Leeuwin Current.
PF	Polar Front
ppm	parts per million

ppmv	parts per million by volume
REE	Rare Earth Element
RSDW	Ross Sea Deep Water
SACCF	Southern Antarctic Circumpolar Current Front
SAF	sub-Antarctic Front
SB	Southern Boundary
SLE	Sea level equivalent
SO	Southern Ocean
SPDW	South Pacific Deep Water
SST	Sea Surface Temperature
Sv	Sverdrup
SWW	Southern Westerly Winds
TIC	Totten ice shelf
TWTT	Two-way travel time
WAIS	West Antarctic Ice Sheet
WL	Wilkes Land
WL	Wilkes Land
WSB	Wilkes Subglacial Basin
XRD	X-ray Diffraction
XRF	X-ray Fluorescence
δ^{18}O	ratio of stable isotopes oxygen-18 (^{18}O) and oxygen-16 (^{16}O)
ºC	Degree Celcius

ABSTRACT

The Antarctic Circumpolar Current (ACC) connects all major ocean basins, links the deep and shallow layers of the oceans and has a strong influence on global ocean circulation, biogeochemical cycles, the stability of the Antarctic ice sheet and thereby Earth´s climate system. However, the timing of the onset of the ACC and the establishment of a vigorous, deep circumpolar flow, similar to present-day remain controversial. Moreover, the links between the ACC and the Antarctic ice sheet in past warmer than today climates are poorly known. This knowledge is essential for improving our understanding on ACC-Antarctic ice sheet interactions in the ongoing climate warming that can inform coupled ocean-ice sheet global climate models used to forecast future changes.

In this context, this PhD thesis aims to advance our understanding on the evolution of the ACC since its initiation (proto-ACC) to the time when the modern deep ACC is established over the last 34 million years (Ma). In addition, we aim to relate proto-ACC dynamics offshore the eastern Wilkes Land margin to Antarctic ice sheet behaviour during the warm late Oligocene and the earliest Miocene (24-23 Ma), including the second major Antarctic glaciation (23.03 Ma). To achieve these objectives, we conducted sedimentological, geochemical, and isotopic analyses on sedimentary sequences recovered by the Deep Sea Drilling Project Leg 28 (Sites 269 and 274) and Leg 29 (Site 278) across both sides of the Tasmanian Gateway. In addition, we conducted a study in the glaciated margins of Lake Baikal (Russia). There the tectonic and sea level histories are well known allowing us to test, using bathymetric and seismic reflection data, the climate vs. sea-level changes and tectonic controls on deep-water deposition in glaciated margins.

This PhD Thesis shows that between 34-30 Ma, deep waters from the South Atlantic and Indian Ocean did not flow into the Southwest Pacific via the Tasmanian Gateway. Instead, the Southwest Pacific deep water circulation was characterised by the presence of two deep water masses, one occupying depths between ~2500-4000 m (Equatorial-like Deep Water) and another one, a bottom water mass, occupying depths >= 4000m South Pacific Deep Water). These results indicate the absence of a Circumpolar Deep Water (CDW) connection, like the one found today within the ACC, across the Tasmanian Gateway before 30 Ma. The first evidence of proto-CDW in the Southwest Pacific was previously reported at 30 Ma. Our study however shows the absence of a homogenous deep-reaching proto-CDW in the eastern and western side of the Tasmanian Gateway between 30 Ma and 19 Ma, which indicates a proto-ACC shallower and weaker than the present-day ACC. Between 19 and 4 Ma, we find evidence of a long-term intensification of bottom current flow speeds, coinciding with increasing influence of North Atlantic Deep Water (NADW) in the deep Southwest Pacific. We suggest that the modern deep-reaching ACC flow established at 4 Ma as indicated by a prominent shift to (i) intensified ACC frontal system resulting in enhanced biogenic productivity, (ii) stronger bottom current flow speeds, and (iii) establishment of a homogenous CDW along the polar front in the Southern Ocean

Moreover, our results show that the proto-ACC frontal system offshore the Wilkes Land margin was weaker compared to that of the present-day during the late Oligocene-earliest Miocene (24-23 Ma), allowing warm subtropical waters to reach close to this Antarctic margin. In addition, proto-CDW was circulating closer to the Wilkes Land margin especially during interglacial times (e.g., 23.23 Ma), likely due to reduced Antarctic Bottom Water (AABW) export and ice sheets where retreated in the continent.

Lastly, our results from Lake Baikal highlight that climate is the main control on the development of turbidite system in this glaciated margin. We provide evidence that show that despite the nearly constant lake levels, the late Pleistocene to Holocene changes in lake Baikal turbidite system evolution are the same as marine turbidite systems with ~120 m of sea-level lowering. These results are relevant, when interpreting deep-water deposits in the glaciated margins of Antarctica, which are governed by a complex interplay between ice sheet dynamics, sea level changes and tectonic control.

RESUMEN

La Corriente Circumpolar Antártica (CCA) conecta todas cuencas oceánicas, las aguas superficiales y profundas de los océanos e influye en la circulación oceánica global, los ciclos biogeoquímicos, la estabilidad del casquete de hielo Antártico, y por ende en el sistema climático terrestre. El origen y la evolución de la CCA hasta la alcanzar la configuración actual de una corriente circumpolar, fuerte y profunda, sigue creando controversia. También, es poco el conocimiento sobre la relación entre la evolución de la CCA y la del casquete de hielos Antártico en épocas cálidas del pasado. Sin embargo, en el contexto actual de calentamiento global, este conocimiento es importante para poder informar los modelos acoplados del sistema climático océano-criósfera, utilizados en las predicciones de cambios futuros.

En este contexto, esta tesis doctoral tiene como objetivos el avanzar nuestro conocimiento sobre la evolución de la CCA desde su inicio (proto-CCA) hasta el establecimiento de la CCA actual, abarcando los últimos 34 millones de años (Ma). Además, pretende relacionar la dinámica de la proto-CCA con la del casquete de hielos en el margen continental de la Tierra de Wilkes durante el Oligoceno cálido y el Mioceno inferior (24-23 Ma), periodo que incluye la segunda mayor glaciación continental en la Antártida (23.03 Ma). Para lograr estos objetivos, hemos realizado análisis sedimentológicos, geoquímicos e isotópicos en sedimentos recuperados por el Deep Sea Drilling Project (DSDP) Leg 28 (Sites 269 y 274) y Leg 29 (Site 278) a cada lado del Paso de Tasmania. Además, se ha realizado un estudio en el Lago Baikal (Rusia). La historia tectónica y de los cambios del nivel del Lago Baikal son bien conocidas permitiéndonos testar, usando datos batimétricos y de sísmica de reflexión, el control climático vs. nivel del mar y tectónica en la formación de depósitos profundos en márgenes continentales influenciados por la actividad glaciar.

Los resultados de esta tesis revelan que entre 34-30 Ma, no había flujo de aguas profundas del Atlántico Sur y del Océano Indico a través del Paso de Tasmania. La circulación profunda en el Pacifico Sur estaba caracterizada por la presencia de dos masas de agua, una ocupando profundidades entre ~2500-4000 m (tipo Agua Profunda del Pacifico Ecuatorial), y otra ocupando profundidades >= 4000m (Aguas Profundas del Pacífico Sur). Estos resultados indican la ausencia de la Corriente Profunda circumpolar (CDW), componente principal de la CCA, atravesando el Paso de Tasmania antes de 30 Ma. La primera evidencia de una proto-CDW en el Pacifico suroccidental había sido informada a los 30 Ma. Sin embargo, nuestro estudio muestra la ausencia de una proto-CDW homogénea en la parte occidental del Paso de Tasmania entre 30 y 19 Ma, lo que indica la existencia de una CCA más somera y débil que la actual. Entre 19 y 4 Ma, los sedimentos registran un aumento en la velocidad del flujo de corriente la profunda, coincidiendo con un incremento de la influencia de las Aguas Profundas del Atlántico Norte (NADW) en el Pacífico suroccidental. Nuestros datos sugieren que la formación de una CCA similar a la actual tuvo lugar a los 4 Ma indicado por un marcado cambio en: (i) la intensificación del sistema frontal y como resultado en la productividad biogénica, (ii) intensificación en la velocidad de flujo de la corriente, y (iii) el establecimiento de una CDW de composición homogénea.

Además, nuestros resultados indican que la existencia de una proto-CDW más débil que la actual durante el Oligoceno superior-Mioceno inferior (24-23 Ma) permitía la llegada de aguas cálidas subtropicales cerca de la Antártida. Nuestros datos muestran que la proto-CDW circulaba más próxima al margen de la Tierra de Wilkes durante periodos interglaciares (e.g., 23.23) probablemente debido a

la reducción en la producción de Aguas Profundas Antárcticas (AABW) y cuando los casquetes estaban retirados en el continente.

Por último, nuestros resultados en el Lago Baikal muestran el clima como el factor que controla el desarrollo de sistemas turbidíticos en el margen del lago influido por procesos glaciares. Pese a que los niveles del lago permanecen casi constantes durante el Pleistoceno superior y el Holoceno, la evolución de los sistemas turbidíticos es similar a la observada en sistemas turbidíticos marinos con ~120 m de descenso del nivel del mar. Estos resultados son importantes a la hora de interpretar depósitos profundos en los márgenes glaciares de la Antártida, en los que gobierna una compleja interacción entre factores de control que incluyen la dinámica glaciar, los cambios del nivel del mar y la actividad tectónica.

Context
& Motivation

Human activities have been the dominant cause for the observed warming since the mid-20th century linked, among other, to the increasing amount of greenhouse gases (i.e., carbon dioxide-CO_2) in the atmosphere, (IPCC, 2013, 2019). One of the major natural consequences of the anthropogenic-induced global warming is the instability/melting of ice sheets and their contribution in sea level rise. This will undoubtedly cause unprecedented impacts in the natural, social and economic system (IPCC 2013, 2019). The response of Antarctica´s ice sheets and the Southern Ocean to climate change remains however a key uncertainty in predicting sea level rise during and beyond this century (IPCC 2013; Rintoul et al., 2018; Escutia et al., 2019; Meredith et al., 2019). Two large ice sheets cover the Antarctic continent, the East Antarctic Ice sheet and the West Antarctic Ice Sheet (**Fig. 1A**). Melting of the Antarctic ice sheet can contribute ~58 m of sea level, with ~53.3 m attributed to the East Antarctic Ice sheet and ~4.3m from the West Antarctic Ice sheet (**Fig. 1A**) (Fretwell et al. 2013; Morlinghem et al., 2019).

It has been recently recognised that in addition to the direct impact of rising surface temperatures on surface melting of the ice sheets, ocean warming can also lead to rapid dynamical changes in the ice sheets and consequently sea level fluctuations (Meredith et al., 2019). This is particularly important for Antarctica as large portions of the Antarctic ice sheet rests on bedrock that is below sea level (marine-based) (**Fig. 1B**) (Fretwell et al. 2013; Morlinghem et al., 2019), making them vulnerable to ocean-induced warming (e.g., Rignot et al., 2002, 2013, 2019). However, little is known at this time about ocean-ice sheet interactions and sparse geological records along continental-to-offshore transects around Antarctica prevent our knowledge about the ocean-ice sheet linkages during past warm times (Escutia et al., 2019).

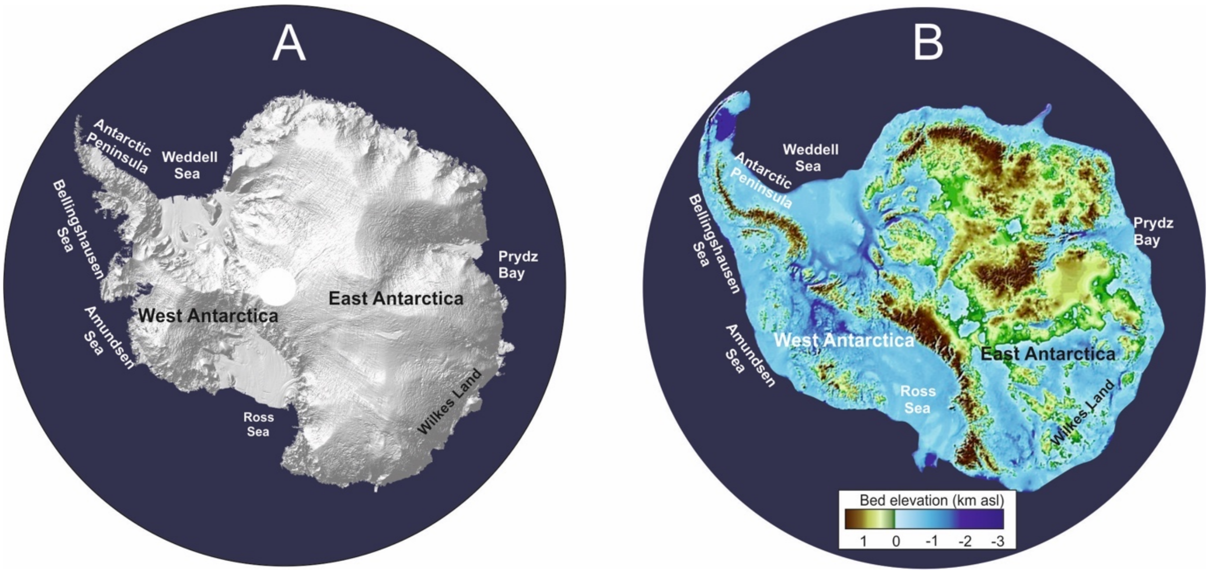

Figure 1: The Antarctic continent. 1A: Digital elevation map of Antarctica modified from Slater et al. (2018). Antarctica´s ice sheet mean thickness excluding the ice shelves is ~2.1 km. 1B: Bed elevation grid with ice sheet removed considering isostatic rebound, modified from Morlinghem et al. (2019). Note most of the West Antarctic ice sheet and large sectors of East Antarctic ice sheet are grounded well below sea level.

The Antarctic Circumpolar Current (ACC), the world´s largest ocean current encircling Antarctica strongly influences the Earth Climate system (Rintoul, 2018) (**Fig. 2A**). The interbasin connection of the ACC is a fundamental feature of the global overturning circulation, which carries heat, carbon and nutrients around the globe. It modulates the exchange of heat, moisture and carbon dioxide (CO_2) between the ocean and the atmosphere and controls local and global marine primary productivity (Sarmiento et al., 2004; Marshall and Speer, 2012; Rintoul, 2018). In addition, the ACC is a key player in controlling the stability of the Antarctica´s ice sheet because its frontal systems serve to thermally isolate the Antarctic continent from receiving warm subtropical ocean surface heat (**Fig. 2A**) (Martinson et al., 2012). However, in regions where the ACC reaches closer to the Antarctic margin, the relative warm deep water of the ACC, namely Circumpolar Deep Water (CDW), upwells to the surface and intrudes into the Antarctic continental shelves leading to excessive ocean heat flux (**Fig. 2B**) (Rintoul et al., 2018; Rignot et al., 2019). Over the last 40 years poleward migration (towards Antarctica) and strengthening of the ACC has been linked to enhanced presence of CDW intruding the Antarctic continental shelf (Aoki et al., 2005; Russell et al., 2006; Spence et al., 2017; Rintoul, 2018; Rignot et al., 2019). Intrusions of CDW on the Antarctic continental shelf have been linked to rapid thinning of ice shelves from below (basal melting) (Pritchard et al., 2012; Rignot et al., 2019; Holland et al., 2020; Smith et al., 2020). Ice shelf thinning reduces back stress and enhances the discharge of grounded ice into the ocean, leading to marine ice sheet instability and consequently sea level rise (Rignot et al., 2002; Reese et al., 2017; Rignot et al., 2019). CDW intrusions have been attributed to ice mass loss in various continental shelves in West and East Antarctica (Rignot et al., 2019). Most of the ocean-driven ice mass loss is centred in the Bellingshausen (Wouters et al., 2015; Zhang et al., 2016), in the Amundsen Sea (Jacobs et al., 2011, 2013; Joughin et al., 2014; Jenkins et al., 2016, Khazendar et al., 2016; Jenkins et al., 2018) and in the Antarctic Peninsula (Martinson and McKee, 2012; Spence et al., 2017; Etourneau et al., 2019). Increased mass loss has been also observed in the East Antarctic Ice Sheet, in particular in the Wilkes Land region, which has been suggested to be linked to ocean-induced warming (Shen et al., 2018; Rignot et al., 2019). CDW has been also identified intruding the continental shelf in the East Antarctic sectors of the Totten and Amery ice shelf (Herraiz-Borreguero et al., 2015; Li et al., 2016; Rintoul et al., 2016; Greene et al., 2017; Silvano et al., 2017).

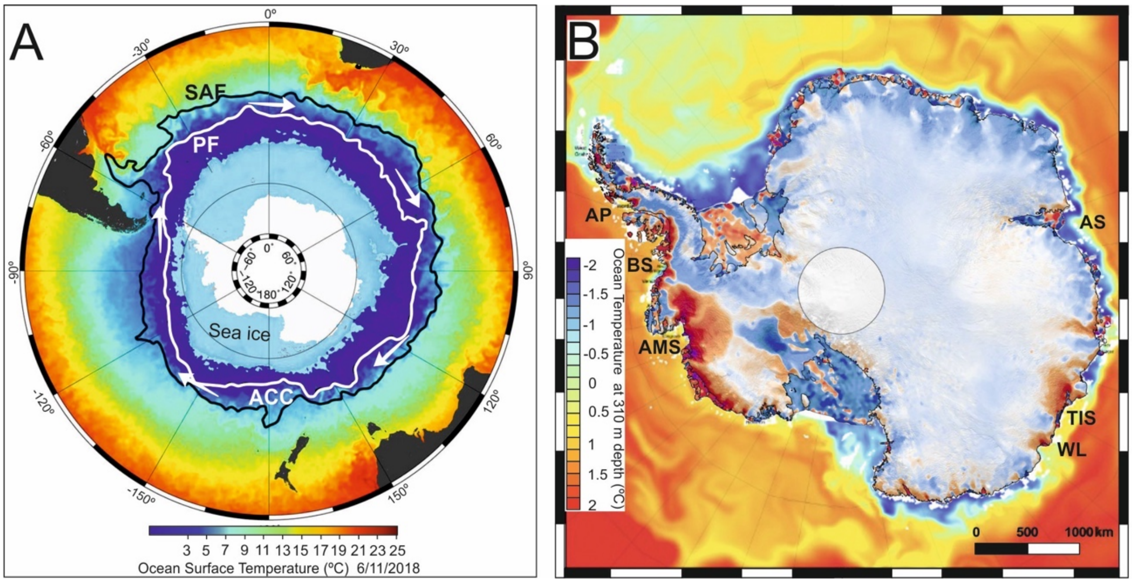

Figure 2: The Antarctic Circumpolar Current (ACC). A: Map of Southern Ocean surface temperatures for 06/11/2018 (modified from the European Copernicus Marine Services). Note the effect of the ACC on the surface temperatures. The black line indicates the long term position of the SubAntarctic Front (SAF) and the white line indicates the long term position of the Polar Front (PF). B: Ocean temperature at 310m (modified from Rignot et al., 2019) and map of ice loss from Antarctica (2003-2019) modified from Smith et al. (2020). Note that the regions with higher ice mass loss correspond with regions where warmer ocean water intrude closer to the continent. AMS: Amundsen Sea, BS: Bellingshausen Sea, WL: Wilkes Land, TIC: Totten ice shelf and AS: Amery ice shelf.

Ongoing rapid climate warming is expected to result in further intensification and poleward shift of the westerlies (Meijers, 2014). This would likely cause strengthening of the ACC and increased upwelling of CDW on Antarctica´s continental shelves, leading to enhanced basal melting and destabilisation of the Antarctic ice sheets. Forecasting of these processes as climate continues to warm is however hampered by our limited understanding of ocean-ice sheet interactions. Indeed, despite the importance of ACC and CDW for the Antarctic ice sheet stability and the Earth Climate system, its onset and consequent evolution, as well as their linkages with the Antarctic ice sheet dynamics in the past remains controversial. This knowledge is key for assessing their response to ongoing climate change, and their influence in the stability of the Antarctic ice sheet and related global sea level (Palter et al., 2018; Rintoul et al., 2018; Escutia et al., 2019; Meredith et al., 2019).

Marine sediment cores preserve the record of past climatic, oceanographic and environmental conditions. Therefore, marine core records around Antarctica are key to investigate past Southern Ocean configurations and interactions with the cryosphere. In this PhD Thesis, aim to provide new insights into the evolution of the Antarctic Circumpolar Current (ACC) and when possible, provide insights into its link to Antarctic ice sheet dynamics. For this, we study sediment core sections recovered by the Deep Sea Drilling Project (DSDP) Leg 28 at Sites 269A and 274 (Hayes et al.,1975) and by DSDP Leg 29 at Site 278 from (Kennett et al., 1975). These sites were strategically selected to cover: (i) a longitudinal transect along the ACC path across the Tasmanian Gateway, and (ii) a latitudinal transect across the ACC fronts. We focus on the Oligocene-late Pleistocene interval (~last 34 Ma), because previous studies suggest that the ACC likely initiated within the middle to late Oligocene interval (Pfuhl and

McCave, 2005; Lyle et al., 2007; Scher et al., 2015), but did not attained its present-day characteristics likely before the late Miocene (~10 Ma) (Bijl et al., 2018b; Sangiorgi et al., 2018). This interval also includes the late Oligocene (26-23.5 Ma) characterized by warmer climates, and a climate threshold during the Oligocene Miocene Transition (OMT; 23.24 and 22.95 Ma), leading to the second Antarctic major glaciation (23.03 Ma) (Zachos et al., 2001). Moreover, the decrease in CO_2 concentrations below 600 ppmv (600-400 ppmv) during the late Oligocene and the OMT remained below these values for most of the Neogene (last 23 Ma) and within the range forecasted by the IPCC (2013) within this century under the “business as usual” scenario.

Aims
& Hypotheses

The overarching aim of this PhD Thesis is to advance our understanding of the evolution of the Antarctic Circumpolar Current (ACC) and to understand ACC configurations during past warm climates and major climate transitions of the Cenozoic. More specifically, we aim to provide new insights into existing controversies regarding the timing of the onset and evolution of the ACC and the establishment of a vigorous deep-reaching ACC, similar to today. In addition, we aim to determine Southern Ocean configurations during past warm periods of the late Oligocene and prior to the second major glaciation in Antarctica during the Oligocene-Miocene transition that can be linked to Antarctic ice sheet dynamics/evolution. Moreover, we investigate the climate control on deep-water deposition on glaciated margins to reinforce the interpretation of our sedimentary records. To achieve our overall aims, four specific objectives were defined in order to tackle our hypotheses, which are briefly presented below.

*Objective 1: Reconstruct the evolution of Circumpolar Deep Water (CDW) flow across both sides of the Tasmanian Gateway from the early Oligocene to the early Miocene (**see Chapter 3**).*

Sedimentary records from the northern part of the Tasmanian Gateway, suggest the initiation of an eastward deep water flow from the South Indian into the South Pacific in the middle Oligocene (30 Ma) (Scher et al., 2015). This has been hypothesized to indicate the onset of the ACC linked to the migration of the gateway within the westerlies (Scher et al., 2015). During the Oligocene, Deep Sea Drilling Project (DSDP) Site 269, was located within the proto-Polar Front in the western side of the Tasmanian Gateway, while DSDP Sites 274 and 278 were located close to proto-Polar Front in the eastern side of the gateway (Hayes et al., 1975; Kennett et al., 1975; Kennett, 1977; Nelson and Cooke, 2001; Scher et al., 2015). This longitudinal transect along the proto-Polar Front can provide insights into the deep water connection between the eastern and the western side of the Tasmanian Gateway and the evolution of the proto-ACC, prior and after the hypothesized onset of the ACC.

*Objective 2: Determine the timing of the establishment of the modern-like, strong, deep-reaching Antarctic Circumpolar Current (**see Chapter 4**).*

Age estimates for the establishment of the ACC provide a wide range of ages varying between 41 Ma to < 10 Ma, and any time in between (e.g., Pfhul and McCave, 2005; Scher and Martin, 2006; Lyle et al., 2007; Scher et al., 2015; Bijl et al., 2018b; Sangiorgi et al., 2018). As DSDP Site 278 remained close to the proto-Polar front throughout the last ~30 million years (Kennett et al., 1975; Kennett, 1977; Nelson and Cooke, 2001; Scher et al., 2015), it likely preserves a unique record of the ACC evolution towards the establishment of its modern-like characteristics (i.e., vigorous, circumpolar deep flow).

*Objective 3: Determine the proto-Antarctic Circumpolar Current dynamics offshore the eastern Wilkes Land margin and its link with the Antarctic ice sheet during the late Oligocene-early Miocene (**see Chapter 5**).*

Based on previous studies, DSDP Site 269, located offshore the eastern Wilkes Land margin, was within the proto-Polar front and thus proto-ACC pathway between the late Oligocene and early Miocene

(Hayes et al., 1975; Nelson and Cooke, 2001; Scher et al. ,2015; Salabarnada et al., 2018). It has therefore the potential of containing a record of oceanic configurations leading to the second major Antarctic glaciation (Oligocene-Miocene transition). In addition, results from Site 269 can be correlated with those obtained from the Integrated Ocean Drilling Project (IODP) Site U1356, which is located 250 km landwards (Escutia et al., 2011), to link ocean configurations with ice sheet dynamics in the Wilkes Land margin prior and during this major climatic transition.

*Objective 4: Decipher climate influence versus other factors controlling deep-water deposition in glaciated margins (**see Chapter 6**).*

Relative changes in lake levels of hundreds of meters in the Quaternary has been documented in Lake Baikal (Hutchinson et al., 1992; Mats, 1993; Back and Strecker, 1998; Colman et al., 1998). However, these lake level changes have been attributed to the well-constrained tectonic activity, while the morphology and hydrology of lake Baikal make its water level insensitive to climate changes (Colman et al., 1998). However, like in most marine turbidite systems (e.g., Nelson and Nilsen, 1984), sediment cores from Lake Baikal show higher sedimentation rates and higher average net sand percentage during the late Pleistocene glacial times compared to the Holocene interglacial climate (Carter and Colman, 1994; Nelson et al., 1995; Back and Strecker, 1998; Nelson et al., 2009). Most prevailing conceptual models attribute turbidite system growth to sea-level lowering during glacial times (e.g., Vail et al., 1977). Lake Baikal turbidite system growth offer an opportunity to differentiate between climate vs other controlling factors in the growth of turbidite systems.

Thesis Structure

This thesis consists of ten separate chapters:

Chapter 1 **General Introduction.** In this chapter we present a brief overview of the Antarctic ice sheet evolution during the Cenozoic era; a review on the present knowledge regarding the evolution of the Antarctic Circumpolar Current (ACC) based on tectonic and paleoceanongraphic evidence; a paleoceanographic history of the Tasmanian Gateway; and a short summary of the main deep-water processes and their deposits in glaciated margins.

Chapter 2 **Materials and Methods.** This chapter consists of a brief description of the material and methodologies used to address the research objectives of this PhD Thesis. Detailed information regarding the methodologies used are presented in each result chapter.

Chapters 3, 4, 5 and 6 **Results.** Chapters 3, 4, 5 address objectives 1, 2 and 3 of this thesis, respectively, regarding ACC evolution and its link to the evolution of the Antarctic Ice Sheet. Chapter 6 focuses on the role of climate in the development of deep-water deposits in glaciated margins using the turbidite systems in Lake Baikal as a case study. Chapter 6 aims to tackle objective 4. Chapters 3, 4, 5 and 6 are or will be published as separate papers in scientific journals. As a consequence, some repetition of statements may occur.

Chapter 3 aims to advance our understanding in the deep ocean circulation patterns across the Tasmanian Gateway during the Oligocene and early Miocene (34-19 Ma). This information is key because this interval includes the: 1) deepening of the Tasmanian Gateway, which occurred between the 33.5 and 30.2 Ma, 2) onset of the first continental-wide glaciation in Antarctica at ~33.6 Ma; and 3) inferred onset of the ACC at 30 Ma. We present new neodymium isotope records generated from fossil fish teeth and bones picked from deep sea sediments recovered from two Deep Sea Drilling Project (DSDP) sites. Neodymium isotope data from DSDP Leg 28 Site 274, provides the first neodymium record proximal to the Ross Sea during the Oligocene. Our results reveal that the Nd isotope composition shifts in response to major steps in Antarctic ice sheet expansion and due to an increased influence of upwelling proto-Circumpolar Deep Water (proto-CDW) at the site. Moreover, the neodymium isotope record from DSDP Leg 29 Site 278 was used to determine the evolution of proto-CDW in the Southwest Pacific. Comparing our neodymium isotope records from Site 278 with available Nd data from the Southern Ocean and central Pacific, we show the absence of a homogenous proto-CDW flow across the Tasmanian Gateway, which contrasts with the modern CDW. Our findings therefore point to the presence of a weaker ACC flow across the Tasmanian Gateway at least until the early Miocene (19 Ma).

Chapter 4 extends the study on Site 278 from the early Miocene to the Pleistocene (19 Ma-500 Ka) in order to determine the time when the ACC flow across the Tasmanian Gateway becomes similar to the one today, characterised by a vigorous deep-reaching circumpolar flow. We present coupled records of neodymium isotopes, sortable silt and biogenic silica data, which indicate an almost concurrent pronounced shift in all three data sets around 4 Ma. We interpret this shift to represent the timing of the establishment of the modern-like, strong, deep-reaching ACC.

Chapter 5 presents the first late Oligocene to early Miocene (~24-23 Ma) paleoceanographic record from the Antarctic eastern Wilkes Land margin, located at the western side of the Tasmanian Gateway. This time interval includes a marked climatic transition that culminated in the second major Antarctic glaciation (known as the Mi-1 event at 23.03 Ma). We provide new sedimentological, palynological, geochemical and isotopic results from deep sea sediments recovered at Site 269 drilled by the DSDP Leg 28. Our multi-proxy data set reveals that sea surface temperature was warmer than today and sea ice was absent or reduced in this sector of Antarctica. The proto-ACC frontal system was weaker than today and frontal migrations were controlled by climate (glacial-interglacial cycles). In addition, proto-CDW was circulating closer to the eastern Wilkes Land margin, likely due to the reduced presence of Antarctic bottom waters. Altogether, our results indicate a fundamentally different oceanographic configuration and a weaker proto-ACC compared to that of the present-day during the late Oligocene (24-23 Ma). The results from this chapter have been accepted for their publication in Global and Planetary Change. Impact Factor 2018-2019: 4.1

Chapter 6 focuses on deciphering the controlling factors in deep-water deposition in glaciated margins. For this, we study the glacially derived turbidite systems of Lake Baikal (Russia) where lake water levels have been insignificant in response to climate change since the late Quaternary, and tectonic control is well constrained. We find that Lake Baikal turbidite systems show maximum growth during the late Pleistocene glacial melt period and reduced when the warmer Holocene climate developed, glaciers disappeared, and forests grew. These changes are similar to other deep sea marine turbidite systems with ~120 m of sea level lowering during the Pleistocene. Our study highlights the importance of climatic control on sediment supply to the deep water turbidite systems that is unrelated to lowered sea level and tectonic effects. In the context of this thesis, these findings are relevant to our interpretation of deep-water deposits in the Antarctic margin, where many of the controlling factors in sedimentation related to regional and global sea level changes (i.e., growth and decay of continental ice sheets, Glacial Isostatic Adjustment, gravitational attraction of the ice sheet on the ocean) are not well constrained. The results of this paper have been published in Geology (Evangelinos et al., 2016. Geology: 45 (2): 179-182, https://doi.org/10.1130/G38163.1). Impact Factor in 2016: 4.7

Chapter 7 **Synopsis and General Discussion** integrates the key findings from each result chapter (3-6) and discusses them in comparison with findings from other workers/regions.

Chapter 8 **Summary and Conclusions** summarizes the major conclusions of this thesis in relation to the initial thesis objectives.

Chapter 9 **Unsettled issues and future research directions** discusses the limitations of our data, the remaining open questions arising from this thesis, and future perspectives.

Chapter 10: **Appendices** includes supplementary material and datasets to Chapters 3, 4, 5 and 6 and a list of co-authored papers related to the topic of this thesis.

Chapter 1

General Introduction

1.1 A brief history on the Antarctic ice sheet evolution in the Cenozoic era

Throughout the Cenozoic era (the past 65 million years), Earth´s climate has undergone a complex evolution with continuous changes from extreme cooling with massive continental ice-sheets and polar ice caps larger than today's, to periods with extreme warmth with ice-free poles. Our current understanding of the evolution of the Antarctic ice sheet during the Cenozoic comes largely from global records of marine oxygen isotopic composition ($\delta^{18}O$) of calcareous shell of benthic foraminifera (**Fig. 1.1**), evidence from rock outcrops on land, limited ice-proximal sedimentary records, seismic data from continental margins, and ice-distal/deep-sea sedimentary records. Below we provide an overview of the Antarctic ice sheet evolution since 54 Ma. Locations mentioned in this overview are shown in **Fig 1.2**.

1.1.1 The pre-ice sheet "Greenhouse world" - ephemeral ice sheets on highlands

The early Cenozoic begins with an increasing trend in the $\delta^{18}O$ values from the early Paleocene, indicating a warming trend, which culminated in the Early Eocene Climatic Optimum (EECO; 54-49 Ma) (**Fig. 1.1**) (Zachos et al 2001, 2008; Mudelsee et al, 2014). The EECO represents the most prolonged warm time interval during the Cenozoic with inferred global annual mean temperatures about 13 ± 2.6°C warmer than pre-industrial times (Lunt et al., 2012; Pross et al., 2012; Caballero and Huber, 2013) and bottom water temperatures ~10°C higher than modern values (Lear et al., 2000; Zachos et al., 2001). This was followed by a ~10 °C long-term cooling trend until the end of the Eocene (~34 Ma; minimum ~5 °C), punctuated by short cold and warm events. Atmospheric carbon dioxide reconstructions show a similar trend, with levels higher than one thousand parts per million by volume (>1000 ppm) during most of the Eocene (**Fig. 1.1a**) (Beerling and Royer, 2011).

Sediments recovered from the eastern Wilkes Land margin show high diverse, near tropical forests existed in the early Eocene (53.9-51.9 Ma) that were replaced by cool temperate forests during the middle Eocene in response to cooling (49.3- 46 Ma) (Pross et al., 2012; Contreras et al. 2013). A similar change to cool temperate forests during the middle to middle to early late Eocene has been reported from cores across the continental margin in the Prydz Bay region (Cooper and O´Brien, 2004) and fossil wood, leaves and pollen found in McMourdo Sound erratics in the Ross Sea (Francis, 2000; Harwood and Levy 2000; Pole et al., 2000). Sea level records and model simulations have suggested that ephemeral ice sheets may have existed on highlands during the cold periods of the early Cenozoic (DeConto and Pollard, 2003; Kominz et al., 2008; Miller et al., 2005a, b, 2008b; Cramer et al., 2011). Geological records from King George Island (Birkenmajer et al, 2005), the Antarctic Peninsula (Anderson et al, 2011) and the McMourdo Sound area in Ross Sea (Harwood and Levy 2000) support the presence of mountain glaciers between the middle Eocene and late Eocene (45-34 Ma). A change in the provenance of sediments delivered to the Kerguelen Plateau has been linked to cooling and ice growth in East Antarctica during the early late Eocene (~37.3 Ma; Scher et al., 2014). Moreover, a widespread Ice Rafted Debris (IRD) deposition in the south eastern margin of the South Orkney microcontinent between ~36.5 and 33.6 Ma, sourced from southern Weddell Sea region, has been taken to indicate widespread glacier calving along the coast of the southern Weddell Sea since ~36.5 Ma (Carter et al., 2017).

1.1.2 The first major continental-scale Antarctic glaciation initiation of the "Icehouse world"

The first continental-scale glaciation in Antarctica occurred during the Eocene-Oligocene Transition (EOT; ~33.6-33.9 Ma), indicated by an abrupt stepwise excursion of ~+1.5 ‰ in the deep-sea benthic δ^{18}O records within ~300kyr, reflecting a combination of global cooling and ice growth (Zachos et al., 2001; Coxall et al., 2005; Miller et al., 2005a, 2008a; Zachos et al., 2008; Cramer et al., 2011; Scher et al., 2011; Mudelsee et al., 2014). The first step is characterised by 2-3°C deep-water cooling and no significant ice volume changes (Lear et al., 2004, 2008; Bohaty et al., 2012; Mudelsee et al., 2014). In contrast, during the second step (culminating in what is known as the Oi-1 event), a major expansion of ice volume up to 125% of the modern Antarctic ice volume has been inferred causing a sea level fall of ~55-90 m (Kominz and Pekar, 2001; Pekar et al., 2002; Lear et al, 2004, Miller et al., 2005a; Katz et al., 2008; Kominz et al., 2008; Lear et al, 2008; Miller et al., 2008a, b).

Sedimentological evidence from cores on Prydz Bay, Maud Rise and Kerguelen Plateau suggest that mountain glaciers reached sea level during the middle to late Eocene (Barron et al., 1991; Breza and Wise, 1992; Ehrmann and Mackensen, 1992; Strand et al., 2003). Circum-Antarctic sediments document a major shift in the clay composition indicating a change from chemical weathering pointing to warmer and humid climates to physical weathering under cooler, drier climate across the Eocene Oligocene Transition (EOT; 33.8 -33.5 Ma) (Ehrmann and Mackensen 1992; Diester-Haass et al., 1996; Robert and Kennett, 1997; Ehrmann, 1998; Ehrmann et al., 2005, 2011; Escutia et al., 2011; Passchier et al., 2013).

Direct evidence of ice-sheet expansion beyond the coastline is provided by sediment cores recovered from around the Antarctic continental margin. Ice sheets were grounded at the Antarctic shelf in the early Oligocene in the Weddell Sea (Barker and Kennett., 1998), in Prydz Bay (Barron et al., 1989;1991; O'Brien et al., 2001; Cooper and O' Brien, 2004; Passchier et al., 2016), in the eastern Wilkes Land margin (Escutia et al., 2011, 2014), and in the Ross Sea (Barrett, 1989, 2007). Moreover, the sudden appearance of IRD in the Kerguelen Plateau (Zachos et al., 1992; Scher et al., 2011) and glacial sediments in the Seymour Island (Ivany et al., 2006) also support ice-sheet expansion beyond coastline during the early Oligocene.

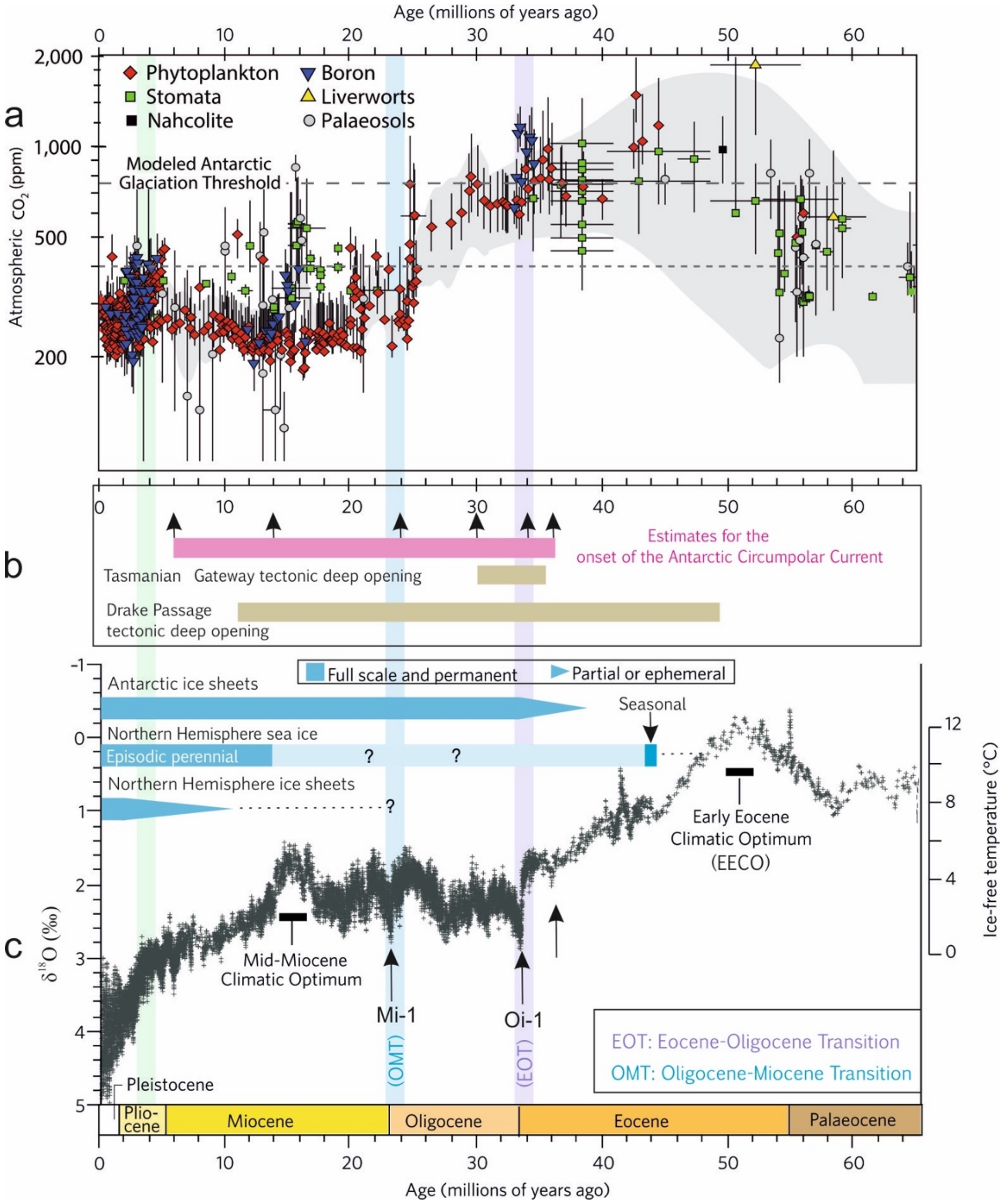

Figure 1.1: Global climate evolution during the Cenozoic era (past 65 Million years). a: Compilation of atmospheric CO_2 over the last 65 Million years (Foster et al., 2012; Badger et al., 2013; Foster and Rohling, 2013; Zhang et al., 2016). b: Estimates for the tectonic deep opening of the last Southern Ocean gateways (Drake Passage, Tasmanian Gateway) and for the onset of the Antarctic Circumpolar Current from Stickley et al. (2004); Barker et al. (2007); Dalziel, (2014). c: Stacked deep-sea benthic foraminiferal oxygen isotope curve ($\delta^{18}O$ records) modified from Zachos et al., 2008. Ice-free temperatures refer to the early Cenozoic (until 35 Million years ago); Oi-1: Oligocene isotope Event 1, Mi-1: Miocene isotope Event 1. Also shown are interpreted inferences regarding the evolution of global ice sheets by these authors.

1.1.3 The Oligocene and the second major Antarctic glaciation-establishment of marine-based ice sheets

During the Oligocene (33.5-23.03 Ma) and the OMT (23.24-22.95 Ma) atmospheric CO_2 concentrations decreased from ~1000 to below 600 ppm (**Fig. 1.1**) (Foster et al., 2012; Badger et al., 2013; Zhang et al., 2016). $\delta^{18}O$ records suggest that ice sheets where highly dynamic and Antarctic ice volumes changed considerably (e.g., Pälike et al., 2006; Holbourn et al., 2007; Liebrand et al., 2011; Beddow et al., 2016). These inferences are supported by drill cores from the Ross Sea and Prydz Bay continental shelves, Weddell Sea slope and Wilkes Land rise (Hayes et al., 1975; Barker et al., 1988; Barron et al., 1989; O'Brien et al., 2001; Escutia et al., 2011; Galleoti et al., 2016; Levy et al., 2019). For example, evidence from the Wilkes Land suggest that the ice sheet reached the coast line and sea ice was present during the early Oligocene (Escutia et al., 2011; Houben et al., 2013; Escutia et al., 2014). In contrast, during the middle Oligocene to late Oligocene (until ~25 Ma), ice sheet retreated, with glaciers or ice caps occupying the lowlands of the terrestrial margin, while warm oligotrophic waters and restricted seasonal sea ice prevailed (Salzmann et al., 2016; Strother et al., 2017; Bijl et al., 2018b; Hartman et al., 2018; Salabarnada et al., 2018). During the Oligocene-Miocene transition (OMT), an ephemeral (~300kyr lasting from 23.24 and 22.95 Ma) isotopic excursion similar in magnitude to the Oi-1 marks the second major glaciation during the Cenozoic, culminating at 23.03 Ma (known as the Mi-1 event) (**Fig. 1.1**) (Miller et al., 1991; Zachos et al., 2001). This major transition corresponds with a drop in CO_2 levels below 600 ppm that remained below these values for most of the Neogene (**Fig. 1.1**) (Zhang et al., 2013). $\delta^{18}O$ records suggest that Antarctic ice sheet was up to 25% larger than the present-day East Antarctic ice sheet, resulting in sea level changes between ~30-90m (Pekar and DeConto, 2006; Liebrand et al., 2011; Beddow et al., 2016; Liebrand et al., 2017). Sedimentological and seismic data from the Ross sea continental shelf indicate a major expansion of marine ice sheets in the Ross Sea shelf in the late Oligocene (24.5 and 24 Ma) (e.g., Levy et al., 2019). These data include for example, the deposition of ice proximal glacimarine sediments (Barrett, 1975, 2007; Kulhanek et al., 2019), major erosional disconformities in ice proximal records recovered from Cape Roberts Project (CRP) and CIROS (Naish et al., 2001, 2008; Wilson and Luyendyk, 2009), and glacial features observed from seismic data (Anderson and Bartek, 1992; Sorlien et al., 2007). In the Antarctic Peninsula, the presence of glacial sediments on south eastern King George Island suggests the local expansion of marine-based ice sheet onto the continental shelf in the early Miocene (Troedson and Riding, 2002). Similarly, in the Prydz Bay region, the presence of glacial sediments in the Prince Charles Mountains, combined with evidence from Prydz Bay indicate a major advance of the Lambert Glacier onto the continental shelf during the late Oligocene to early Miocene (Hambrey and McKelvey, 2000). In the eastern Wilkes Land margin the presence of large glaciogenic debris flow deposits accumulated along the base of the slope and continental rise have been linked to the expansion of the ice sheet into de continental shelf (Escutia et al., 2007, 2011, 2014; Salabarnada, 2020).

1.1.4 Establishment of persistent, cold-based ice sheets

After the Mi-1 event (23.03 Ma), a general warming trend characterises the first half of the Miocene, which culminates in the middle Miocene climatic optimum (MMCO; 17-14 Ma), with average surface temperatures 3-4°C higher than today. A persistent cooling began at around 14 Ma (Middle Miocene climate transition; MMCT) indicated by an increase $\delta^{18}O$ records (**Fig. 1.1**) (Shackleton and Kennett, 1975; Zachos et al., 2001; Miller et al, 2008b; Shevenelle et al., 2008; Cramer et al., 2011; Mudelsee et al., 2014). Large changes in ice volume have been inferred from oxygen isotope data through this period (Holbourn et al., 2015).

Sediment core records around Antarctica indicate that the marine-based ice sheets were highly sensitive to climate changes (Warny et al., 2009; Fielding et al., 2011; Passchier et al., 2011; Levy et al., 2016; McKay et al., 2018; Sangiorgi et al., 2018; Jovane et al., 2019). For example, ice sheets were periodically extended to the Ross Sea shelf at 20.1-19.6 Ma and 19-3-18.7 Ma, whereas ice sheet and sea ice minima are recorded at 16.5-16.3 Ma and 15.7-15.6 Ma (Passchier et al., 2011). Sediment cores from the Wilkes Land margin document also an inland retreat of ice sheet, temperate vegetation and warm oligotrophic waters during the MMCO (17-14.8 Ma) (Sangiorgi et al., 2018). After the MMCO, expansion of a marine-ice sheet takes place in the Wilkes Land, however it remains sensitive to melting driven by warm water incursions (Sangiorgi et al., 2018). Direct evidence from sediment cores around Antarctica show the development of more persistent cold-based ice sheets and intensified polar conditions from 14 Ma to the present, with ice sheet retreats during warm time intervals (Cooper and O'Brien, 2004; Lewis et al., 2007; Escutia et al., 2011; Passchier et al., 2011; Bart and De Santis, 2012; Barrett, 2013; Escutia et al., 2014; Wilson et al., 2018). One example is the Pliocene period (5-3 Ma), which is a key interval (Burke et al., 2018) as it was characterised by global temperatures similar to those predicted for this century (IPCC, 2013; 2019) and atmospheric CO_2 levels similar to today (400 ppmv; Pagani et al., 2010). Evidence from offshore the eastern Wilkes Land margin and the Ross Ice shelf indicate that during the warm intervals of the Pliocene the marine-based ice sheets retreated several times inland (Escutia et al., 2009; Naish et al., 2009; McKay et al., 2012; Barrett, 2013; Cook et al., 2013; Orejola et al., 2014; Patterson et al., 2014; Reinardy et al., 2015). These retreats of the East Antarctic Ice Sheet and West Antarctic Ice Sheet have been also reported from modelling implying a ~ +5 to +20 m of sea level rise in the mid-Pliocene (Pollard et al., 2015; DeConto and Pollard, 2016). Enhanced calving of icebergs and ice sheet retreat has been documented in the Wilkes Land margin between 4.3 and 3.5 Ma, while Southern Ocean cooling and development of perennial sea ice took place between 3.5 and 2.5 Ma (Patterson et al., 2014). Sedimentological records offshore Prydz Bay and west of the Antarctic Peninsula provide evidence of the onset of a cooling trend around 3.7-3.6 Ma, although reduced or no sea ice and reduced ice volume and extent remained until 3.6-3.5 Ma (Escutia et al., 2009). The West Antarctic Ice Sheet became more persistent after 3.3 Ma, accompanied with a major sea ice expansion in the Southern Ocean (McKay et al., 2012). Moreover, the presence of mega debris flow deposits and changes in the margin development at around 3 Ma in different sectors of the Antarctica including the Antarctica Peninsula, Prydz Bay, Wilkes Land, Weddell Sea and the Eastern and Western Ross Sea has been interpreted to indicate the shift from a polythermal to the present polar cold dry-based conditions (Rebesco and Camerlenghi, 2008).

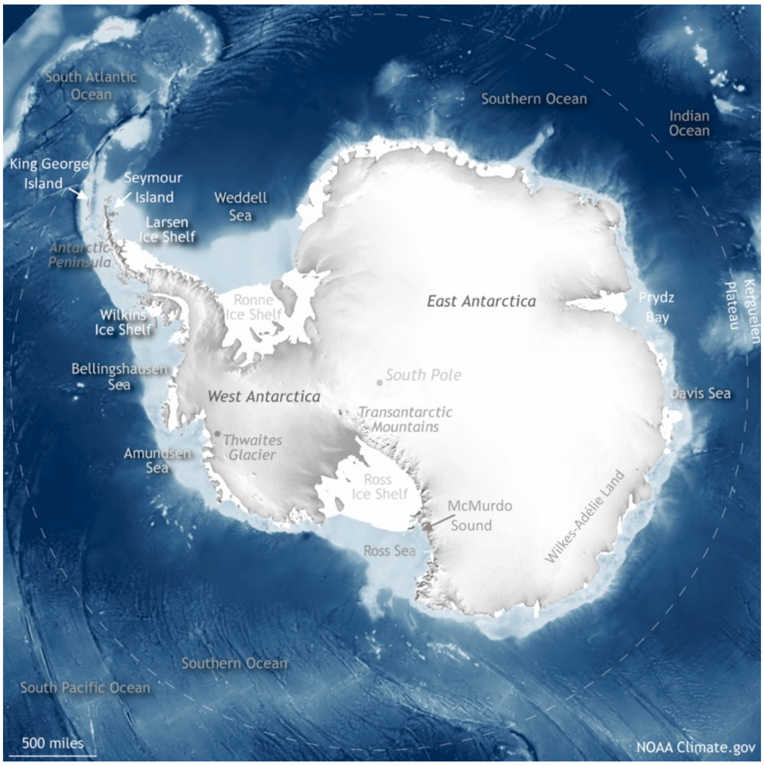

Figure 1.2: Map of Antarctica and Southern Ocean with locations mentioned in the text (adapted from NOAA Climate.gov).

1.2 The onset and evolution of the Antarctic Circumpolar Current based on tectonic and paleoceanographic evidence

Today, the Antarctic Circumpolar Current (ACC) is the planet´s largest ocean current transporting about 137 – 147 ± 10 x 10^6 m^3 s^{-1} from west to east along a roughly 20,000 km long path around Antarctica (**Fig. 1.3A**) (Rintoul and Sokolov, 2001; Cunningham et al., 2003; Legeais et al., 2005). The modern ACC consists of three major circumpolar oceanographic fronts that from north to south are: the sub-Antarctic Front (SAF), the Polar front (PF) and the Southern ACC Front (SACCF), which extend from the sea surface to the seafloor (deep-reaching) (Orsi et al., 1995; Rintoul et al., 2001; Olberns et al., 2004; Sokolov and Rintoul, 2007). The ACC is driven by the westerly winds (westerlies) and buoyancy forcing (Rintoul et al., 2001; Olberns et al., 2004; Rintoul, 2018). The strong westerly winds cause the surface isopycnals of the ACC to slope upwards towards the south (Olberns et al., 2004; Rintoul, 2018). The steeply sloping isopycnals serve to isolate thermally the Antarctic continent from warm surface subtropical waters, but also drive relative warm Circumpolar Deep Waters (CDW) to upwell to the south of it (**Fig. 1.3B**) (Martinson, 2012). Recent observations, show that in regions where CDW reaches the continental shelves, such as the Amundsen and Bellingshausen seas, this ocean heat flux influences the thickness of ice shelves and their buttressing capacity through basal melting, resulting in rapid thinning and ice mass loss (e.g., Pritchard et al., 2012; Rintoul, 2018; Rignot et al., 2019). Therefore, the ACC plays an important role in controlling the stability of the Antarctica´s ice sheet. Moreover, due to the absence of land barriers (i.e. continents) at ~60°S, the ACC connects all the main ocean basins and permits the existence of the global overturning circulation, that strongly influences the exchange of heat, moisture and carbon dioxide (CO_2) with the atmosphere (Marshall and Speer, 2012; Talley, 2013), and the regional and global primary productivity (Sarmiento et al., 2004).

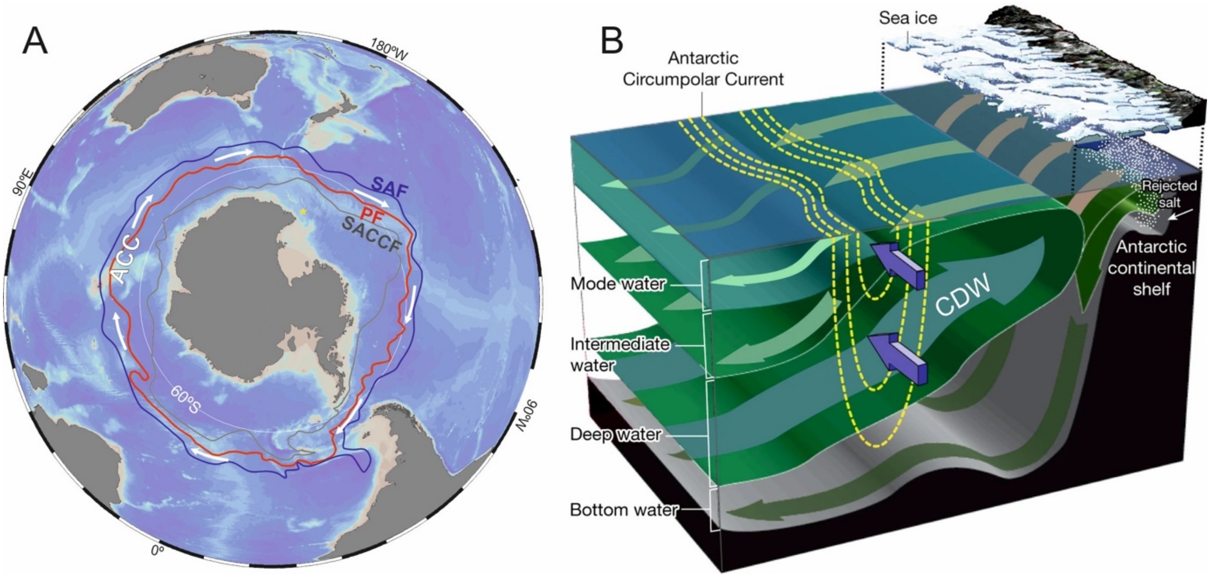

Figure 1.3: The Antarctic Circumpolar Current (ACC) system. A: The ACC frontal system, SAF: Subantarctic front (blue line), PF: Polar front (red line), SACCF: Southern Antarctic Circumpolar Current front (grey line) adapted from Orsi et al. (1995). B: Schematic illustration of the Southern Ocean overturning circulation modified from Rintoul, 2018.

The response of the ACC to future climate changes remains a major uncertainty to be addressed. To determine the onset and evolution of the ACC in the past can provide valuable insights in our understanding on the ACC dynamics and its interactions with the Antarctic ice sheet. For the existence of a strong deep-reaching ACC similar to the present-day, two major features have to be present: i) the westerly winds blowing over the Southern Ocean, and (ii) a continuous circumpolar deep water path with no continental barriers. Although lower temperature gradients before the onset of the first major Antarctic glaciation (Bijl et al., 2009, 2013) would have controlled the strength and position of the westerly winds, models show that these winds were features of the Southern Hemisphere for much of the Cenozoic (Huber et al., 2003, 2004). The two final continental barriers to Southern Ocean circumpolar flow after the breakup of Gondwanaland extended from: (i) south of Tasmania (Tasman Rise) and Antarctica, which after continental separation became the Tasmanian Gateway; and (ii) South America and Antarctica, which after continental separation became the Drake Passage. Both the Tasmanian Gateway and the Drake Passage must be open and deep to enable the continuous circumpolar deep water flow that characterizes the ACC.

Studies on the onset of the ACC come largely from tectonic reconstructions of these two Southern Ocean gateways and from paleoenvironmental and paleoceanographic evidences from sedimentary records around Antarctica. Tectonic studies focus on reconstructing the timing of the development of a deep seaway gap associated with sea-floor spreading that permits a continuous circum-Antarctic pathway. The timing of the development of a deep seaway gap in the Tasmanian Gateway is relatively well constrained between 32 and 30.2 Ma (Stickley et al., 2004). In contrast, reconstructions for the opening and deepening of the Drake Passage include a wide range of proposed estimates between 49 and 10 Ma (Livermore et al., 2005; Barker et al., 2007; Dalziel, 2014). The controversial views largely result from uncertainties in the reconstruction of the paleo-elevation of key regions of the Scotia Arc and Shackleton Fracture Zone (e.g. microcontinental blocks) and the lack of age control (Barker et al., 2007). A tectonic model based on the tectonic evolution of several basins in the Scotia Sea suggest the development of a shallow gap during the late Eocene (50 Ma), followed by the creation of a deep pathway at 34-30 Ma (Livermore et al., 2004; 2007). In the south Scotia Ridge, the opening of the Powell Basin has been suggested to permit the initiation of the ACC at 31± 2 Ma (Lawver and Gahagan, 1998, 2003). In contrast, evidence from seismic profiles in the eastern part of the Shackleton Fracture Zone infer that the ACC should have developed sometime between 22 and 17 Ma. This is based on the presence of a topographic barrier in the North Scotia Sea, which would have precluded ACC flow before 23 Ma, and a shallower Scotia sea floor at the early stages of the opening may have delayed the establishment of the ACC to the Mid-Miocene (Barker and Burrell, 1977; Barker et al., 2001). More recently, it has been proposed that a deep ACC could have formed only after the opening of the narrow conduits in the North Scotia Ridge in the late Miocene (11-10 Ma; Dalziel et al., 2013; Carter et al., 2014).

The history of paleoenvironmental and paleoceanographic changes related to the development of the ACC are provided by direct evidence from geological records. For example, paleoenvironmental indicators that have been used to decipher the development of the inter-ocean connections and circumpolar flow include sedimentation patterns, sediment composition and grain-size, micropaleontological assemblages, and tracers for productivity and ocean circulation patterns. However, these data provide also a wide range of age estimates for the onset of the ACC spanning from ~41 Ma to 6 Ma (Wei and Wise, 1992; Scher and Martin 2004; Bijl et al., 2018b). For example, chemical water mass reconstructions based on neodymium isotopes from the Maud Rise and Agulhas Ridge detect that shallow influx of Pacific seawater into the Atlantic sectors started at 41 Ma, suggesting a shallow seawater connection via the Drake Passage (Scher and Martin 2004, 2006). Increased productivity at several circumpolar locations has been attributed to the onset of the ACC around the Eocene-Oligocene transition (Diester-Hass and Zahn, 2001). More recently, the onset of the ACC at 30 Ma has been argued based on chemical water mass reconstructions around the Tasmanian Gateway, linked to the migration of the Tasmanian Gateway within the westerly wind band (Scher et al., 2015). In contrast, sedimentological evidence from the South Tasman Rise and the South Pacific Ocean report strengthening of bottom current flow speeds within the ACC around the late Oligocene-early Miocene (25-23 Ma), suggesting the onset of the ACC during this time interval (Pfuhl and McCave, 2003, 2005; Lyle et al., 2007). However, recent sedimentological, geochemical, and paleotemperature reconstructions suggest a weaker ACC frontal system at least until the late Miocene (~11 Ma) (Bijl et al., 2018b; Hartman et al., 2018; Salabarnada et al., 2018; Sangiorgi et al., 2018). The youngest age estimate is given by a study of nannofossils from the Kerguelen Plateau, which suggest the development of the modern polar front and thus the onset of the ACC between the late Miocene and early Pliocene (~6 Ma) (Wei and Wise, 1992). In the following section, we provide a brief overview focused on the oceanographic history of Tasmanian Gateway based on reconstructions from sediment records, which is the main focus of this PhD Thesis.

1.3 Palaeoceanographic history of the Tasmanian Gateway

Before 50 Ma, both the Tasmanian Gateway and the Drake Passage were closed and the Southern Ocean circulation was characterised by two large disconnected clockwise gyres (**Fig. 1.4**). One in the South Atlantic-Indian Ocean, which penetrated into the Australian-Antarctic Basin forming the Proto-Leeuwin-Current, and one in the Pacific Ocean (proto-Ross Gyre) (Huber et al., 2004; Sijp et al., 2014). The development of a shallow opening in the Tasmanian Gateway at 50-49 Ma allowed the development of the shallow westward-flowing proto-Antarctic Countercurrent (from the Pacific Ocean into the Indian Ocean) (Bijl et al., 2013; Sijp et al., 2016). The connection of the two gyres has been thought to cause cooling along the Antarctic margin in the western side of the Gateway (Bijl et al., 2013). The initiation of a rapid tectonic deepening of the Tasmanian Gateway between 35.5 – 33.5 Ma (Stickley et al., 2004) caused a throughflow of the eastward flowing proto-Leeuwin Current into the southwest Pacific and the Pacific Ross Sea Gyre (Huber et al., 2004; Stickley et al., 2004). A recent study argues for an invigoration of surface and bottom water circulation around the margins of all Southern Ocean basins, in the easterly winds band, including a westward-flowing Antarctic Countercurrent at 35.7 Ma (Houben et al., 2019). This has been linked to enhanced polar easterly winds due to the late Eocene cooling (Scher et al., 2014), which likely led to increased vertical mixing and primary productivity around the Southern Ocean (Houben et al., 2019). This major change in the circum-Antarctic circulation preceded the Oi-1 by ~2 million years and has been suggested to precondition the first Antarctic continental glaciation (Houben et al., 2019). Between 33.5 – 30.2 Ma, the Tasmanian Gateway reached bathyal depths allowing further inflow of the proto-Leeuwin waters into the southwest Pacific and proto-Ross Sea Gyre (Huber et al. 2004; Stickley et al., 2004). The tectonic northward migration of the Tasmanian Gateway into the westerly winds band has been previously linked to the onset of the ACC at 30 Ma (Scher et al., 2015). However, there is an increasing number of studies suggesting that the ACC did not reach its present-day vigour before the late Oligocene (25-23 Ma; Pfuhl and McCave, 2005; Lyle et al., 2007) or even until the middle Miocene (~11 Ma; Bijl et al. 2018b; Sangiorgi et al., 2018). Further investigation of deep-water deposits across the Tasmanian Gateway are therefore needed in order to obtain the timing of the establishment of the modern deep ACC.

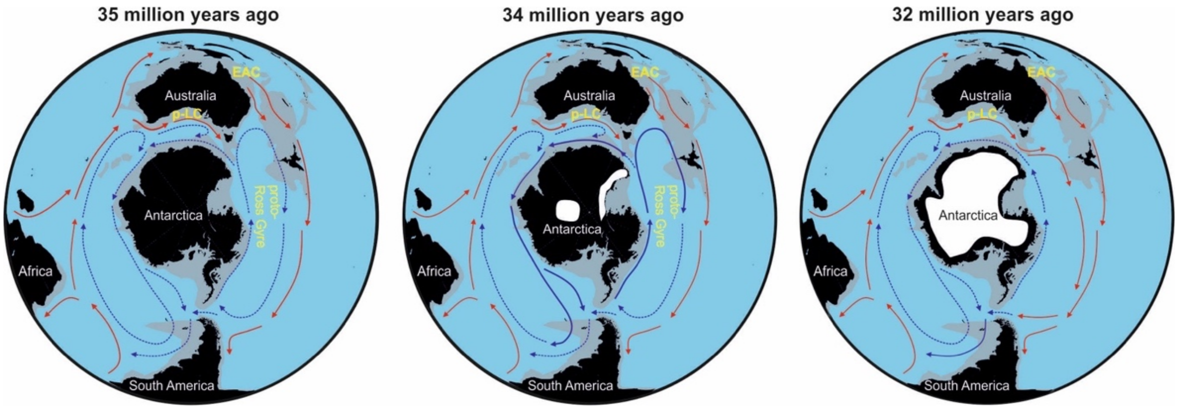
35 million years ago
34 million years ago
32 million years ago

Figure 1.4: Oceanographic changes between the early late Eocene (36 Ma), latest Eocene (34 Ma) and early Oligocene (32 Ma) modified by Houben et al. (2019). Note that at 34 Ma, westward circum-Antarctic circulation intensified (thicker blue lines). White areas on Antarctica indicate the presence of ice sheets. EAC: East Antarctic Current; p-LC: proto-Leeuwin Current.

1.4 Deep-water processes and their deposits in glaciated margins

The main processes that govern the sedimentation in deep water environments in glaciated margins (i.e., deep ocean and lake basins) are gravity driven downslope processes (i.e., debris flows and turbidity currents), bottom currents, hemipelagic/pelagic settling and ice-rafting (**Figs. 1.5 and 1.6**). Each process forms distinct deposits but it is common in the natural system the interplay among processes. In these cases, deciphering among the processes that caused a deposit might be challenging, as they often overlap as part of a continuum (Rebesco et al., 2014; Stow and Smillie, 2020).

Gravity-driven downslope processes are the most important processes in transferring large amounts of terrigenous sediments accumulated in the continental shelf and slope to the abyssal plain environments (tens to hundred kilometres offshore) (**Fig. 1.6**) (e.g., Mulder and Alexander, 2001; Nelson et al., 2011; Paull et al., 2018; Shanmugam, 2018). The initiation of these downslope movements/flows can be triggered by earthquakes, tectonic oversteepening, depositional oversteepening, depositional loading, hydrostatic loading, glacial loading/unloading, eustatic changes in sea level, tsunamis, volcanic eruptions, submarine volcanic activity, and storms, among other (Shanmugam, 2018). Deposits that result from downslope processes driven by gravity are broadly classified into two main types; (i) mass transport and (ii) turbidites.

Mass transport deposits refer to the downslope movement of sediment under the influence of gravity, including slides (movement by plastic deformation), slumps (movement by brittle deformation) and debris flows (plastic or laminar flow) (**Fig. 1.5**) (Nelson et al., 2011; Shanmugam, 2018). A submarine slide is a coherent mass of sediment that moves in a planar surface, characterised by no internal deformation. Slides are common in fjords, because of the steep nature of the glacial valleys and high sedimentation supply coming from the glacier into the fjord. In addition, slides are often generated due to the steep gradients of submarine canyon walls (Green et al., 2006; Shanmugam, 2018). A slump is a coherent mass of sediment, characterized by sliding along a concave-upward surface, causing internal deformation (e.g., Shanmugam, 2018; Stow and Smillie, 2020). Debris flow is a rapid downslope movement of sediments mixed with water driven by gravity. Debris flows may be mud-rich (muddy debrite), sand-rich (sandy debrite) or mixed, and are capable of transporting high concentrations of rock fragments of different shapes and sizes, forming structureless deposits (e.g., Nelson et al., 2011; Shanmugam, 2018; Stow and Smillie, 2020).

Turbidity current is a turbulent suspension of sediment in water, driven by downslope density flow. In contrast to mass transport deposits, they are usually confined to submarine canyons and channels, which act as the main conduit for the transport of these sediments, and to their associated channel-levee complexes and submarine fans (e.g., Nelson et al., 2011; Paull et al., 2018; Stow and Smillie, 2020). In a longitudinal profile, turbidity currents include a head (coarse-grained material deposited), a body and tail (fine-grained material deposited) and a neck (turbulent mixing) (**Fig. 1.5**). Turbidity currents occur as relative short-lived surge events or relative long-lived steady flows that travel for several thousands of kilometres in the deep sea. Sediments deposited by turbidity currents are called turbidites (**Fig. 1.5**). Turbidite facies are well recognised from sediment cores recovered from deep ocean and lake environments, as well as outcrops exposed on land. Bouma (1962) described the vertical succession of an idealised turbidite sequence characterised by a particular fining-upwards grading within the sediments. In addition, they present a suite of characteristic sedimentary structures starting at the base with an erosional contact and followed up-section by parallel laminated to cross-bedded and rippled cross-bedded, and finally laminated siltstone and mudstone (**Fig. 1.5**) (e.g., Bouma, 1962; Mulder and Alexander, 2001; Nelson et al., 2011; Rebesco et al., 2014; Shanmugam, 2018; Stow and Smillie, 2020).

Mass transport deposits and turbidites in glaciated margins can provide important information about past climate changes, ice sheet advances and retreats, and ocean-ice interactions (**Fig. 1.6**) (Rebesco and Camerlenghi, 2008; Nelson et al., 2011; Rebesco et al., 2014; Shanmugam, 2018; Stow and Smillie, 2020). Tectonic activity (i.e., ice load-induced earthquakes) and climate changes (i.e., sea level fluctuations) exert significant control in the volume and grain-size of sediment supply, accommodation space, and consequently in the amount of eroded sediments that reach the shelf break and are transported in the deep sea via downslope processes. A complex interplay between ice sheet dynamics, sea level changes, tectonic processes and interactions with relative warm waters onto the continental shelf favouring ice melting can trigger the development of mass transport deposits and turbidites (**Fig. 1.6**).

Bottom currents rework deep-sea sediments through erosion, transport and deposition of sediment delivered by different processes (**Fig. 1.6**) (Rebesco and Camerlenghi, 2008; Rebesco et al. 2014; Shanmugam, 2018; Stow et al., 2019; Stow and Smillie, 2020). There are several types of currents that influence the deep sea, including wind-driven bottom currents, thermohaline bottom currents, deep-water tidal bottom currents, internal waves and tides, among others (**Fig. 1.5**) (Rebesco et al. 2014; Stow and Smillie, 2020). Bottom currents are considered as a continuous processes over long periods of time (over million years), with relatively low accumulation rates except in areas where high flow velocities cause temporary hiatuses or erosion (Rebesco and Camerlenghi, 2008). Bottom current deposits are called contourites. Contourite composition varies largely depending on the source material including siliciclastic, bioclastic (calcareous, siliceous), volcaniclastic and chemogenic (manganiferous contourites) (Rebesco and Camerlenghi, 2008; Rebesco et al., 2014). Although there is not yet commonly accepted contourite sequence to use as a diagnostic criterion for contourites, some workers have proposed several sedimentary features that can be used to identify contourites, such as extensive bioturbation and bi-gradational or/and coarsening upward grain-size trend (**Fig. 1.5**) (Rebesco and Camerlenghi, 2008). A wide range of contourite facies are now recognised depending on the grain size, ranging from fine muds to silts, sand and gravel lag deposits (**Fig. 1.5**) (Rebesco et al., 2014; Stow and Smillie, 2020). Contourites can provide important insights into changes in the ocean circulation patterns, current velocities, oceanographic history and basin interconnectivity.

Hemipelagic and pelagic settling is a process of vertical settling of biogenic material (phytoplankton and zooplankton) and a varying amount of terrigenous material through the water column to the seafloor (**Figs. 1.5 and 1.6**). Hemipelagic deposition comprises a mixture of biogenic and terrigenous particles (Stow et al., 1998; Stow and Smillie, 2020). The latter can be transported by wind, turbidites and bottom currents. Pelagic deposits contain biogenic material and little or no terrigenous sediments and result from a continuous process (over million years) with variable rates depending of the nature of the area (e.g., low in oligotrophic and high in productive areas) (Stow and Smillie, 2020). Sediment deposited through (hemi)pelagic settling called (hemi)pelagites are typically fine-grained muds and sandy muds (**Fig. 1.5**). Deep sea (hemi)pelagites is the one of the principal marine sediment types forming the "background" facies of many deep-water deposits (Rebesco et al., 2014; Stow and Smillie, 2020). Based on the biogenic material composition, three main types of pelagic sediment deposits are distinguished: 1) siliceous, calcareous, or mixed. Siliceous sediments contain biogenic organisms that their skeleton is made of silica (predominantly diatoms and radiolarian); 2) calcareous sediments are dominated by marine organisms that their skeleton is formed from calcium carbonate (calcareous nannoplankton, foraminifera). Depending on the abundance of biogenic grains in sediments a different name is applied to (hemi)pelagic deposits (**Table 1.1**; Expedition 318 Scientists, 2011). The depth at which production of calcium carbonate equal dissolution is called the calcium carbonate compensation depth (CCD). Below this depth, carbonate organisms dissolve and only terrigenous sediments and/or siliceous organism can accumulate. Pelagic and hemipelagic deposits can provide information about changes in primary productivity related to ocean circulation changes, sea ice occurrence, ocean fronts characteristics (position, migrations and strength) (Rebesco and Camerlenghi, 2008; Rebesco et al., 2014; Stow and Smillie, 2020).

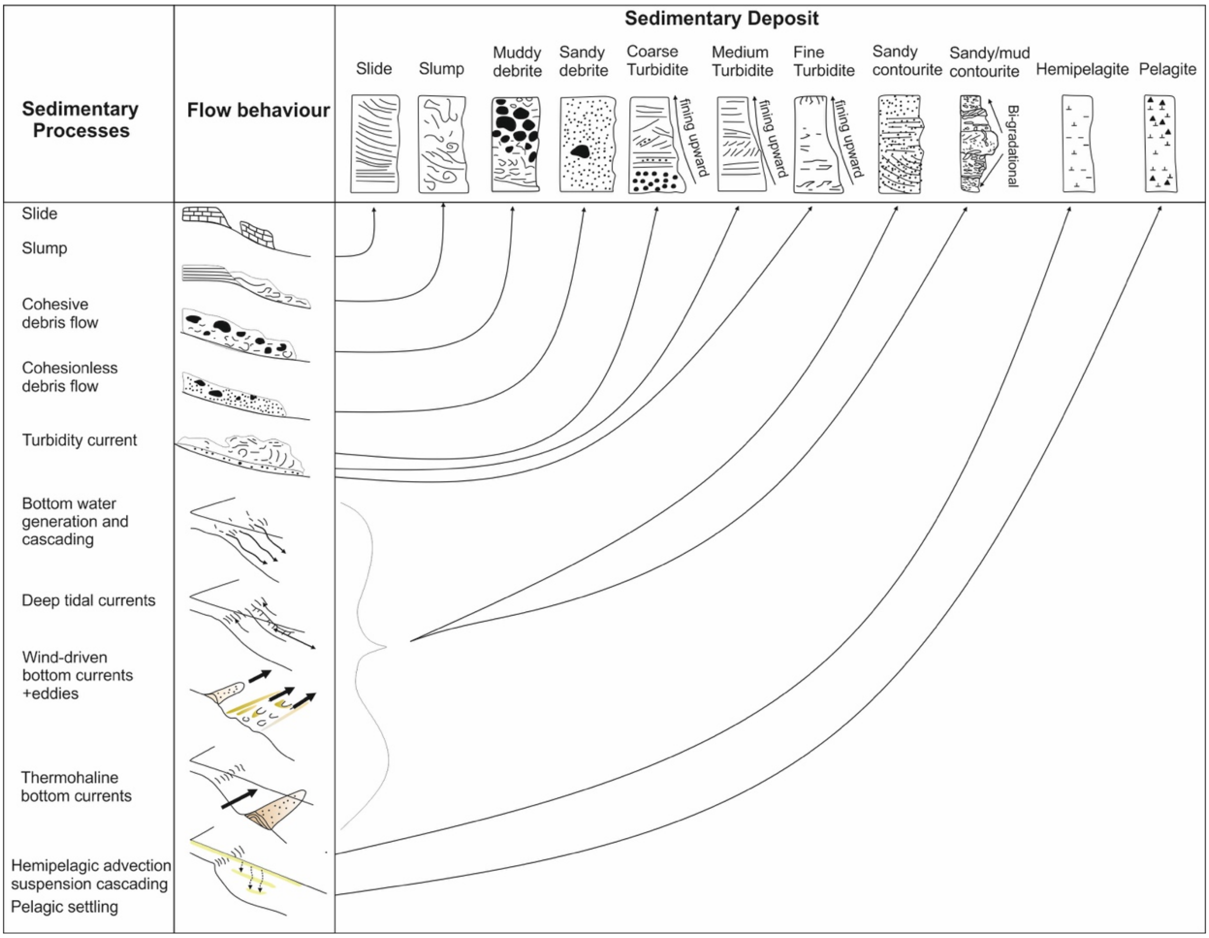

Figure 1.5: Sedimentary processes and deposits in deep-water systems (modified from Stow and Smillie, 2020).

Table 1.1: Classification of sediment with biogenic grains.

Biogenic component abundance	Name	Example
> 50%	-ooze	diatom ooze
25-50%	-rich	diatoms-rich
10-25 %	-bearing	diatom-bearing

Ice rafting is a common process in deep sea environments in marine or lake glaciated margins (Kuijpers et al., 2014). Icebergs form when ice breaks off or calves from glaciers or ice shelves (**Fig. 1.6**). Icebergs drift offshore with ocean currents and winds. Through ice melting terrigenous material [called ice-rafted debris (IRD)] including grains of all sizes, transported within the ice matrix is released into the water column and thus deposited in the marine or lake sediments (**Fig. 1.6).** Ice sheet dynamics, ocean circulation changes, sea level fluctuations, variations in solar parameters and ice-load-induced earthquakes have been proposed being responsible for iceberg surging (Kuijpers et al., 2014; Passchier, 2018). Ocean circulation changes including ocean heat transport, which cause basal melting of floating outlet glaciers and ice shelves, can lead to ice sheet destabilisation and iceberg surging. Additionally, surface air temperature warming influence iceberg calving activity (Passchier, 2018). Used with other indicators in the sediments, the occurrence of iceberg-derived IRD in sedimentary records thus not only provides a tool to reconstruct former ice sheet dynamics, glacier calving activity, and iceberg drift, but can also provide information on ocean current patterns.

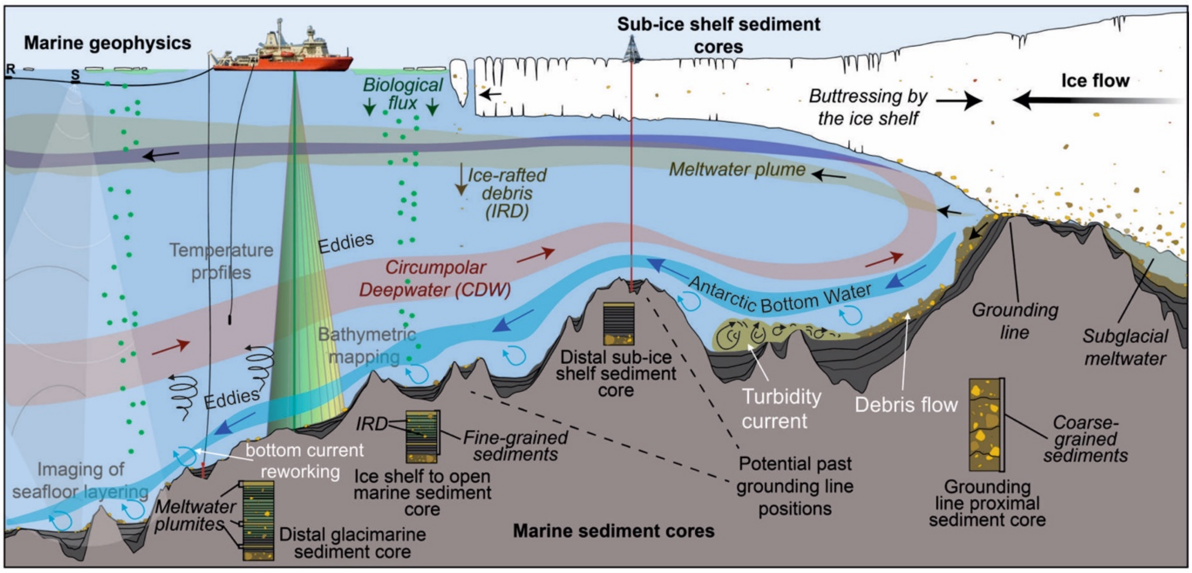

Figure 1.6: Schematic summarising the main sedimentary processes resulting deposits in Antarctic glaciated margins. Also shown are common infrastructures and equipment used in marine geology. Modified from original graphic designed by Rebecca Minzoni (International Thwaites Glacier Collaboration-THOR) https://thwaitesglacieroffshoreresearch.org/research.

Chapter **2**

Materials & Methods

This section presents a brief description of the materials and methodologies used to address the research objectives this PhD Thesis. A multi-proxy approach was conducted to study sedimentary archives across both sides of the Tasmanian Gateway (**Fig. 2.1**), associated with objectives 1, 2, and 3 (see in Aims & Hypotheses). For our study in Lake Baikal (related to objective 4), we used bathymetric and seismic reflection data (**Fig. 2.2**). For further reading in detailed aspects related to the methodologies applied, the method section of each chapter includes all necessary information.

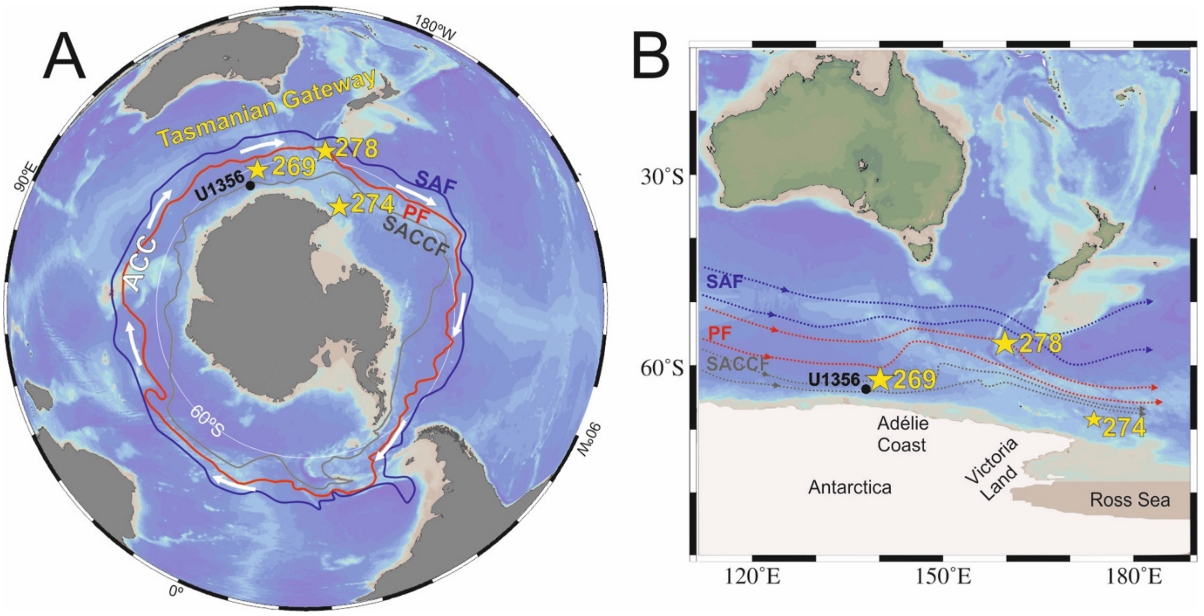

Figure 2.1: Overview map of modern Southern Ocean configuration (Ocean Data View, (Schlitzer, 2016; version 4.79; http://odv.awi.de). A: Antarctic Circumpolar Current (ACC) frontal system, study sites (DSDP Sites 269, 274 and 278) (yellow stars). IODP Site U1356 (black dot; Escutia et al., 2011) is used for comparisons along the latitudinal transect in the western side of the Tasmanian Gateway. SAF: Subantarctic front (blue line), PF: Polar front (red line), SACCF: Southern Antarctic Circumpolar Current front (grey line) adapted from Orsi et al. (1995). B: Map of Tasmanian Gateway. The main transport of the ACC takes place around the PF and SAF.

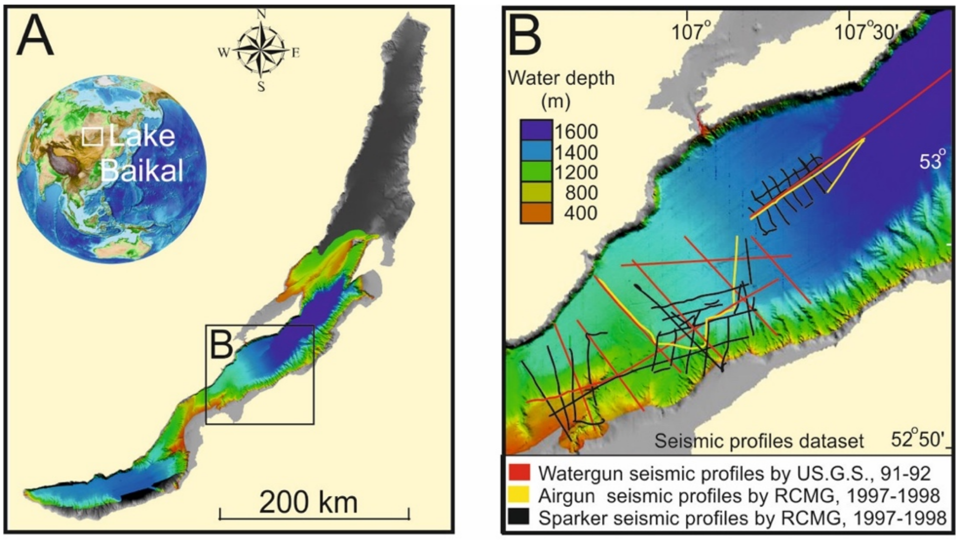

Figure 2.2: Lake Baikal (Russia). A: Location map of Lake Baikal and swath bathymetry B: Seismic profile dataset.

2.1 Tasmanian Gateway

To provide new insights into the evolution of the Antarctic Circumpolar Current (ACC) and its interactions with the Antarctic ice sheet during past warm climates and major climate transitions of the Cenozoic, we studied sediment core sections recovered by the Deep Sea Drilling Project (DSDP) Leg 28 at Sites 269 and 274 (Hayes et al.,1975), and DSDP Leg 29 at Site 278 (Kennett et al., 1975) (**Fig. 2.2; Table 2.1**). These sites were strategically selected to cover (i) a longitudinal transect along the path of the ACC across both sides of the Tasmanian Gateway (i.e., from west to east: Sites 269, 274 and 278), and (ii) two latitudinal transects across the ACC fronts at each side of the gateway (i.e., western side: Sites 269-U1356, and eastern side Sites: 278 and 274). Sediments from Site U1356 are not the focus of this thesis but we compare our results to those from this site (Escutia et al., 2011, 2014; Salabarnada et al., 2018) to investigate the latitudinal transect across the ACC in the western side of the gateway (**Fig. 2.2**).

DSDP Site 269 (Leg 28) is located at 4282 m water depth on the south-eastern edge of the south Indian Abyssal Plain (61º 40.57´S 140º 04.21´E) (Hayes et al.,1975). 958 meters of sediments were discontinuously cored in two holes at Site 269, Hole 269* and Hole 269A, which recovered 11 and 13 cores, respectively, initially dated to span between the early Oligocene to Quaternary (Hayes et al.,1975). Our study focuses on the lower part (cores 7 to 13) of the Hole 269A (655.5 to 956 meters below sea floor (mbsf)), which has 60.9 % recovery (**Table 2.1**). This interval consists of alternations between laminated and bioturbated mudstones, siltstones/sandstones, and carbonate cemented siltstones/sandstones (bioturbated and laminated) (Hayes et al.,1975).

DSDP Site 274 (Leg 28) is located at 3305 m water depth 250 km north-northeast of Cape dare (68º 59.81´S 173º 25.64´E) (Hayes et al.,1975). 408.5 meters of terrigenous sediment rich in siliceous microfossils were cored continuously, spanning from Late Eocene to Quaternary based on the initial age model (Hayes et al.,1975). Our study focuses on the lower part (180.5-415 mbsf; cores 19 to 43) of Site 274, which has 67.2 % recovery (**Table 2.1**). Shipboard description divided the sediments within this interval in two main lithological units: Unit 4, composed of diatom-detrital silty clay and minor silty clay diatom ooze (between 180.5-328 mbsf); and Unit 5, consisting of silty claystone and locally chert-bearing (328-415 mbsf) (Hayes et al., 1975).

DSDP Site 278 (Leg 29) is located at 3675 m water depth on a pelagic contourite drift, on the Southern Emerald Basin (56º 33.42´S, 160º 04.29´E) (Kennett et al., 1975). Approximately 285 m of sediments were continuously cored in two holes (Hole 278* 35 cores; and Hole 278A 2 cores), with sediments initially dated between middle Oligocene to late Pleistocene (Kenneth et al., 1975). Our study focuses on core sections recovered between 101-428 mbsf (cores 2R to 34R) at Hole 278*, which has 86.1 % recovery (**Table 2.1**). Shipboard description divided the sediments within this interval in five main lithological units: Unit 2 (172-101-172 mbsf) consists of nannofossil-rich spicule-bearing diatom ooze. Unit 3 (172-236 mbsf) is composed of siliceous nannofossil ooze. Unit 4 (236-264 mbsf) consists of alternating nannofossil-rich siliceous ooze and diatom-rich nannofossil ooze. Unit 5 (264-386 mbsf) is composed of detrital and nannofossil-bearing radiolarian-diatom ooze, alternating with siliceous oozes. Unit 6 (386-428 mbsf) consists of siliceous nannofossil chalk (Kennett et al., 1975).

Table 2.1: Drill sites information.

Leg	Site	Hole	Latitude	Longitude	Water Depth (m)	Study core sections	Length recovered (m)	Recovery (%)
28	269	A	61º 40.57'S	140º 04.21'E	4282	7-13	40.3	60.9
28	274	*	68º 59.81'S	173º 25.64'E	3305	18-43	279.1	67.2
29	278	*	56º 33.42'S	160º 04.29'E	3675	2-34	267.4	86.1

During both DSDP Leg 28 and Leg 29 sediment cores were collected using rotary core drilling. Site 269A was drilled discontinuously (spotted coring), which was a common drilling practice during the 70´s. Sites 274 and 278 were one of the first deep sea drilling sites where continuous rotary coring was applied. Despite the continuous drilling, technical issues during the drilling processes resulted in generally moderate core recovery at these sites. However, considering that these sites were the first attempts to continuous deep-sea drilling, the core recovery is considered exceptionally good. It is worth mentioning that rotary coring introduces disturbance in the recovered core, but this disturbance did not prevent to establish an age-depth model and to recognize a succession of different lithostratigraphic units (Hayes et al., 1975; Kennett et al., 1975).

Sediment core sections from these legacy DSDP Sites (269A, 274 and 278) are stored at the International Ocean Discovery Program (IODP) facilities of the Gulf Coast Repository at Texas A&M University, College Station (USA). During our first visit at the IODP Gulf Coast Repository in March 2016, we re-described in detail the sediment core sections selected to implement the objectives of this PhD Thesis. In addition, high-resolution photos were taken, using a Nikon 60 mm camera lens mounted on a custom-built line scanner at the IODP facilities at the Gulf Coast Repository. In total 979 sediment samples were collected from the three DSDP sites for further sedimentological, geochemical, isotopic biostratigraphic and paleomagnetic analyses in the framework of this PhD Thesis (**Table 2.2**). In September-October 2016, we re-visited the IODP facilities of the Gulf Coast Repository to scan the core sections from Site 269 Hole A (Cores 7-13) for collecting continuous magnetic susceptibility data. Magnetic susceptibility measurements were taken every 2 cm using a Bartington MS2 mounted in a Geotek Multi-Sensor Core Logger (MSCL). Additionally, core sections were also scanned for collecting non-destructive X-Ray fluorescence data (major and minor chemical elements), using an Avaatech X-ray fluorescence (XRF). Due to the presence of cracks in many core sections, spot measurements were taken rather than scan the section continuously.

Within the frame of this PhD Thesis, a series of analyses were conducted in collaboration with different international research institutions (**Table 2.3**). Our analyses on the sedimentary archives divided into two main lines of analyses: (i) the revision of the age model for each study site, and (ii) analytical work related to the main objectives of the PhD Thesis including sedimentological, geochemical, and isotopic analyses for reconstruction of the sedimentary processes, paleoceanographic conditions and ocean circulation patters. The main methodologies are presented briefly in Table 2.3. Detailed description of the methodologies applied are included separately in each chapter of the results.

The initial age models of our study sites were based on biostatigraphic constraints (Hayes et al., 1975; Kennett et al., 1975). We updated the age model for each site using new paleomagnetic data, integrated with revised biostratigraphy. Paleomagnetic analysis was conducted at the Paleomagntism Laboratory of the Institute of Earth Sciences Jaume Almera in Barcelona (ICTJA-CSIC) by Dr. Luis Valero. Biostratigraphic analysis for calcareous nannofossils was conducted at the University of Salamanca (Spain) by Dr. José Abel Flores. Analysis for diatom biostratigraphy was conducted at the University of Nebraska (USA) by Dr. David Harwood. Analysis for dinoflagellates biostratigraphy was conducted at the Laboratory of Palaeobotany and Palynology at the Institute of Environmental Biology, in Utrecht (The Netherlands) by Dr. Peter Bijl and Frida Hoem. The PhD candidate integrated the data by all these collaborators and coordinated the elaboration of the revised age models presented in this thesis.

The new age model for Site 269 is based on new our paleomagnetic data combined with new time constraints provided by dinoflagellate and calcareous nannofossils biostratigraphy (for details see ***chapter 5***). For Site 274, new paleomagnetic data, combined with revised diatom biostratigraphy and new dinoflagellate biostratigraphic age constraints were used to update the age model (for details see ***chapter 3***). New age constraints for the lower part of Site 278 (Cores 34-26) were provided by paleomagnetic data combined with calcareous nannofossil and diatom biostratigraphy (for details see ***chapter 3***). For the upper part (Cores 25-2), age constraints were derived from calcareous nannofossil and diatom biostratigraphy (for details see ***chapter 4***).

Table 2.2: Total number of sediment samples collected.

Site	Hole	Study core sections	Number of samples for sedimentological, geochemical and isotopic analyses	Number of samples for Paleomagnetic analysis
269	A	Cores: 7-13	170	45
274	*	Cores: 18-43	382	117
278	*	Cores: 2-34	218	47

2.2 Lake Baikal

The research methodology applied for our study on Lake Baikal in order to outline canyon, channel and lobe changes related to the increased growth rate of the Selenga Fan during Pleistocene glacial climates relied on the compilation and analysis of existing data sets, which include: (i) bathymetric and seismic collected by Renard Center of Marine Geology (RCMG) between 1995 and 2010; and (ii) seismic data collected by U.S Geological Survey (USGS) between 1991 to 1992 (**Fig. 2.2; Tables 2.3 and 2.4**). High-resolution swath bathymetry, high- and intermediate-resolution seismic data were compiled, quality controlled and uploaded into a seismic interpretation workstation - Kingdom Suite™ software for their analysis and interpretation.

Table 2.3: Acquisition characteristics of the seismic data used for our study on Lake Baikal.

Acquisition characteristics	Airgun Impuls-1	Airgun Ship	Watergun
Property	RCMG	RCMG	USGS
Year(s) of acquisition	1999	1999	1991-1992
Gun volume (l)	3	3	0.245
Source energy	120 bar	120 bar	200 bar
Sampling interval (ms)	0.5	0.5	0.5
Number of recording channels	1	1	1
Frequency range (Hz)	45-330	80-450	100-650
Dominant frequency in water (Hz)	± 120	± 225	± 330
Dominant wave length in water (m)	± 20	± 6.4	± 4.4
Vertical resolution (m)	± 3	± 1.6	± 1.1
Lateral resolution (m)	± 170	± 125	± 100
Average penetration limits (m)	± 700	± 500	± 500

Table 2.4: Methodologies used in the present PhD.

Characterise sedimentary facies	Revising the age models	Estimate the biogenic productivity	Trace ocean circulation patterns	Estimate the bottom current flow speed	Outline turbidite channels and fan lobes
Detailed core description	Magneto-stratigraphy	Diatom abundance	Neodymium isotope on fish teeth	Mean sortable silt of terrigenous sediment fraction	High-resolution swath bathymetry
High-resolution line scan imaging	Calcareous nannofossils biostratigraphy	Calcareous nannofossil abundance	Neodymium isotope on detrital sediments	XRF core scanning elemental proxies	Seismic profiles
Grain-size analyses	Diatom biostratigraphy	Dinoflagellate abundance	Rare Earth Element on fish teeth		
High-resolution Scan Electron microscopy	Dinoflagellates biostratigraphy	Biogenic silica content			
XRF core scanning		Carbonate content			
Magnetic susceptibility					

Analysis conducted by the PhD candidate

Analysis conducted by collaborators and coordinated/integrated by the PhD candidate

Chapter 3

Absence of a strong, deep Antarctic Circumpolar Current flow across the Tasmanian Gateway during the Oligocene-early Miocene

ABSTRACT

The vigorous eastward flow of the Antarctic Circumpolar Current (ACC) connects all major ocean basins and plays a prominent role in the transport of heat, carbon and nutrients around the globe. However, the establishment of a deep circumpolar flow, similar to present-day ACC, remains controversial thereby obscuring our understanding of its climatic impact. Deciphering the chemical composition of Circumpolar Deep Water (CDW) within the ACC can provide critical insights. Here we present new fossil fish teeth/bone debris neodymium isotope (ε_{Nd}) records from Deep Sea Drilling Project (DSDP) Sites 278 and 274 in the southwest Pacific, with the goal to trace changes in deep water masses across the Tasmanian gateway between the early Oligocene and early Miocene (34-19 Ma). Site 274 provides the first Nd isotope record proximal to the Ross Sea during the Oligocene (34-23.5 Ma). Its Nd isotope composition shifts from $\varepsilon_{Nd(t)} = -3.1$ to $\varepsilon_{Nd(t)} \sim -4.6$ across the Eocene/Oligocene transition and from $\varepsilon_{Nd(t)} = -5.6$ to $\varepsilon_{Nd(t)} \sim -3.7$ at ~24 Ma in response to major Antarctic ice sheet expansion. A third step is observed around 30 Ma, which we link to an increased influence of upwelling proto-CDW at the site. In contrast, the Nd isotope record from Site 278 in the southern Emerald Basin shows little variability ($\varepsilon_{Nd(t)} = -6.0$ to -6.8) throughout the Oligocene and early Miocene (31.2-18.8 Ma). Comparison with previously published data, demonstrates the presence of two deep water masses in the South Pacific prior to the inferred onset of the ACC (34-30 Ma), one occupying depths between ~2500-<4000 m ($\varepsilon_{Nd(t)=}$ ~-3 to -5) and a deep/bottom water mass (>= 4000 m) with more unradiogenic Nd composition ($\varepsilon_{Nd(t)=}$ ~ -6). Following the onset of the ACC, Site 278 located close to the proto-polar front (proto-PF) indicates that deep waters bathing the southern Emerald Basin remained more radiogenic compared to proto-CDW along the proto-PF in the South Atlantic and Indian Ocean ($\varepsilon_{Nd(t)=}$ ~ -8.1), indicating a prominent offset in Nd composition of deep waters along the proto-PF across the Tasmanian Gateway. This opposes the modern relatively homogenous (lateral and vertical) Nd isotopic composition of CDW along the main flow path of the ACC in all oceanic basins in the Southern Ocean. We attribute the offset in the Nd isotope composition of deep waters across the Tasmanian Gateway to reflect a less deep reaching and weaker ACC (proto-ACC) than today. Our findings suggest that the modern strong and deep-reaching ACC flow must have been developed at a later point in the Neogene.

3.1 Introduction

The Antarctic Circumpolar Current (ACC) is the world´s largest and strongest ocean current, transporting ~ 136-147 x 10^6 m^3 s^{-1} of water along a ~20,000 km long path around Antarctica (Rintoul and Sokolov, 2001; Legeais et al., 2005; Merredith et al., 2011). The absence of continental barriers around 60°S permits the vigorous eastward flow of the ACC, which is driven by the strong westerly winds (westerlies) and buoyancy forcing (Olberns et al., 2004). Most of the circumpolar flow of the ACC takes place along the Polar and the Subantarctic Fronts (PF and SAF, respectively), which extend from the surface to the seafloor (i.e. deep-reaching), connecting the Atlantic, Pacific and Indian Oceans and thus, actively modulates the global ocean circulation (Orsi et al., 1995; Rintoul et al., 2001; Rintoul, 2018). This interbasin connection of the ACC is a critical feature of the modern global overturning circulation, which carries heat, carbon and nutrients around the globe. It modulates the exchange of heat, moisture and carbon dioxide (CO_2) between the ocean and the atmosphere and controls local and global marine primary productivity (Sarmiento et al., 2004; Marshall and Speer, 2012; Rintoul, 2018).

Despite the critical role of today´s strong deep-reaching ACC flow in the global ocean circulation and Earth´s climate, there is still an ongoing debate regarding the timing of its onset and evolution towards a modern-like configuration throughout the Cenozoic period. Major changes in paleogeography and seafloor paleobathymetry related to tectonic activity through time, as well as changes in climate are likely to have controlled the initiation and evolution of the ACC during the Cenozoic. For example, it is widely accepted that the ACC only initiated after the opening of the two last major land barriers within its circum-Antarctic flow, the Drake Passage and the Tasmanian Gateway, and their respective deepening to bathyal depths (>2000 m). Dating the time when the Drake Passage reached this depth is controversial, spanning from the middle Eocene to the late Miocene (see Barker et al., 2007; Dalziel, 2014 for discussion).

In contrast, the opening of the Tasmanian Gateway is better constrained (Exon et al., 2001; Stickley et al, 2004). Prior to 35 Ma, a shallow current flowing westward across the Tasmanian Gateway (from the Pacific to the Indian Ocean) was proposed based on marine microfossils, organic geochemical records and model simulations (Huber et al., 2004; Bijl et al., 2013). Initial opening was followed by intensified deepening of the seaway between ~35.5 and 30.2 Ma as indicated by the analysis of sedimentological, micropaleontological and paleomagnetic data (Stickley et al., 2004). Chemical water mass reconstructions suggest a westward flowing (i.e., from the Pacific to the Indian Ocean) deep water current connecting both sides of the northern parts of the Tasmanian Gateway between 32 and 30 Ma (Scher et al., 2015). A deep eastward flowing water connection between the Indian and Pacific sectors of the Southern Ocean, was only established after 30 Ma, probably due to alignment of the Tasmanian Gateway within the latitudinal band of the westerlies (Scher et al., 2015). The characteristics of this nascent ACC, however, remain unclear.

One possible way to reconstruct past connectivity along the ACC is to track the evolution of Circumpolar Deep Water (CDW), using neodymium (Nd) isotope composition ($^{143}Nd/^{144}Nd$ ratio) of ambient seawater in fossil fish teeth and bones (e.g. Scher and Martin, 2004). Circumpolar Deep Water is the most voluminous water mass in the Southern Ocean, occupying the shallow to deep layers of the ACC in the Southern Ocean (Orsi et al., 1995). Today, CDW has a vertically and horizontally homogenous Nd isotopic isotope composition, probably due to the strong vertical and horizontal mixing along the frontal systems (e.g., Carter et al., 2012; Stichel et al., 2012; Lambelet et al., 2018). These findings indicate that the evolution of the Nd isotope composition of CDW in the past may provide important insights into interbasin connections/circulation in the Southern Ocean.

Neodymium is incorporated into fish teeth at the sediment-water interface at the time of deposition, remineralisation and burial (Shaw and Wasserburg, 1985). Post-burial alteration is generally negligible relative to the early diagenetic rare earth element (REE) uptake, allowing retention of the Nd isotope composition of bottom water signals (e.g., Martin and Scher, 2010). Neodymium is a lithogenic element, introduced to the ocean at its interfaces with the solid earth (e.g., Frank, 2002; Goldstein and Hemming, 2003; van Flierdt et al., 2016). Water masses forming in the different oceanic basins are distinct in their Nd isotope fingerprint, due to the distribution of geological ages and lithologies around the globe, with younger volcanogenic material yielding more radiogenic (higher) Nd isotope compositions, and older cratonic rocks being characterised by less radiogenic (lower) Nd isotope compositions. ε_{Nd} denotes the deviation of a measured ^{143}Nd/^{144}Nd ratio from the chondritic uniform reservoir in parts per 10,000 (DePaolo and Wasserburg, 1976; Jacobsen and Wasserburg, 1980). Because seawater Nd has a relatively short residence time in the ocean (~500 to 1,000 years) (Tachikawa et al., 1999; 2003), Nd can be carried from one ocean basin to another, and hence trace the provenance of water masses.

Here we present new Oligocene to early Miocene neodymium isotope data obtained from fossil fish teeth and bones (fish debris) in sediments recovered by the Deep Sea Drilling Project (DSDP) at Sites 278 and 274. Site 278 is strategically located within the main path of the modern ACC in the southern Emerald Basin (Rintoul et al., 2014), while Site 274 is situated proximal to the Ross Sea in the Adare Basin (**Figs. 3.1A and 3.1B; 10.1.1**) (Orsi et al., 1999; 2002). Our new data provide critical insights into the chemical evolution of CDW in the Southwest Pacific in the time period following the initial opening of the Tasman Gateway and leading up towards the development of the modern-like ACC.

3.2 Modern oceanographic setting of drill sites DSDP 274 and 278

To study the history of the ACC, and in particular the chemical composition of deep waters through the early Oligocene and early Miocene, we used sediments recovered from the DSDP Site 278, Hole 278* (Kennett et al., 1975). Site 278 (56°33.42´S, 160°04.29´E, 3675 m water depth) is located on a pelagic contourite drift in the southern Emerald Basin (**Figs. 3.1A and 3.1B**) (Kennett et al., 1975). At present, the site is located close to the northern branch of the Polar Front (PF) and within the main pathway of the ACC (Sokolov and Rintoul, 2007; Rintoul et al., 2014). As the ACC enters the Southwest Pacific through the Tasmanian Gateway, its flow is constrained by the Macquarie Ridge, which extends from depths of 5000 m to an average depth of 1500 m between 47°S and 56°S (Rintoul et al., 2014). The ACC passes over and through narrow gaps of the Macquarie Ridge and south of the ridge crest around 56°S, before reaching the south Emerald Basin (Rintoul et al., 2014). From there, the ACC flows around the southern end of Campbell Plateau and to the Bounty Trough, reinforcing the Deep Western Boundary Current (DWBC). South of the Bounty Trough (46°S) the ACC turns to the east and continues its journey across the South Pacific, while DWBC continues north towards the equator in the Pacific Ocean basin (Carter and McCave 1997; Whitworth et al., 1999). The ACC carries CDW eastwards from the Southeast Indian Ocean into the Southwest Pacific Ocean. In the southern Emerald Basin, modern CDW extends to the seafloor, bathing Site 278 (**Figs. 3.1B; 10.1.1-10.1.2**) (Rintoul et al., 2014; Lambelet et al., 2018).

Site 274 (68°59.81´S, 173°25.64´E, 3305 m water depth) was drilled on the lower continental rise, 250 km north-northeast of Cape Adare (Hayes et al., 1975) (**Fig. 3.1B**). It is currently situated south of the Southern ACC front (SACCF) (**Figs. 3.1B and 10.1.1**) (Sokolov and Rintoul, 2007) and within the main outflow path of bottom water formed in the western Ross Sea (Gordon et al., 2009). At a depth of 3305 m, the main modern water mass encountered is RSBW (**Fig. 3.1B and 10.1.1**) (Pardo et al., 2012). Today, most of the dense shelf water on the Ross Sea shelf resides in the Joides and Drygalski troughs, from where it is exported as RSBW to the abyssal plains (**Fig. 3.1B**) (Orsi and Wiederwohl, 2009). In contrast to CDW, which can be found all around Antarctica, bottom topography restricts the pathway of the AABW, including RSBW, in the Southern Ocean (Orsi et al., 1999). Only a small portion of RSBW formed in the western Ross Sea flows northward from its outlets, with most of it being diverted westward against the continental slope into the deep Australian-Antarctic Basin (Gordon et al., 2009).

Through diapycnal mixing with overlying CDW, the hydrographic properties of RSBW quickly erode along its westward pathway and are only detectable to ~140°E along the Adélie-Wilkes Coast (Rintoul et al., 1998). In contrast, there is a larger fraction of RSBW detected north of the Ross Sea, but this variety of RSBW forms predominantly in the central Ross Sea and is channelled to the continental slope by the Glomar Challenger trough and into the Hillary Canyon. Much of this bottom water enters into the southeast Pacific Basin (**Fig. 3.1B**) (Orsi et al., 1999; Bergamasco, 2002; Gordon et al., 2009).

3.2.1 Modern Nd isotope signatures of deep and bottom waters around the Tasmanian Gateway

Globally, NADW and PDW, constitute water mass endmembers in terms of their Nd isotope composition. Modern NADW is characterised by relatively negative ε_{Nd} values (ε_{Nd} ~ -13) (Piepgras and Wasserburg, 1987; Lambelet et al., 2016), resulting from the weathering of old cratonic rocks surrounding the North Atlantic. Pacific Deep Water, in contrast, carries less negative (i.e. more radiogenic) ε_{Nd} values of -4 (Piepgras and Jacobsen, 1988; Amakawa et al., 2009), due to the influence of weathering of younger volcanogenic material around the North Pacific. Modern CDW in the Southern Ocean is characterised by a relatively homogenous Nd isotope composition along the flow path of the ACC across all ocean basins and with depth (ε_{Nd} = -8.3 ± 1.5; n = 158) (**Figs. 3.2A**) (Lambelet et al., 2018 and references therein). In the western part of the Tasmanian Gateway along the ~140°E meridian, CDW exhibits ε_{Nd} values of -8.6 ± 0.4 (n=4) around 2500-4300 m (Lambelet et al., 2018). In the eastern part of the gateway, in the Macquarie Ridge region, close to Site 278, CDW has ε_{Nd} values of -9.0 ± 0.2 and -9.2± 0.2 between 3201 and 4183 m, respectively (**Figs. 3.2A; 10.1.2**) (Lambelet et al., 2018). Ross Sea Bottom Water exhibits a more radiogenic Nd isotope signature than CDW, probably acquired from Ross Sea shelf sediments and mixing with shelf waters (□$_{Nd}$ = -6.5 to -7.5; Rickli et al., 2014; Basak et al., 2015) (**Fig. 3.2B**).

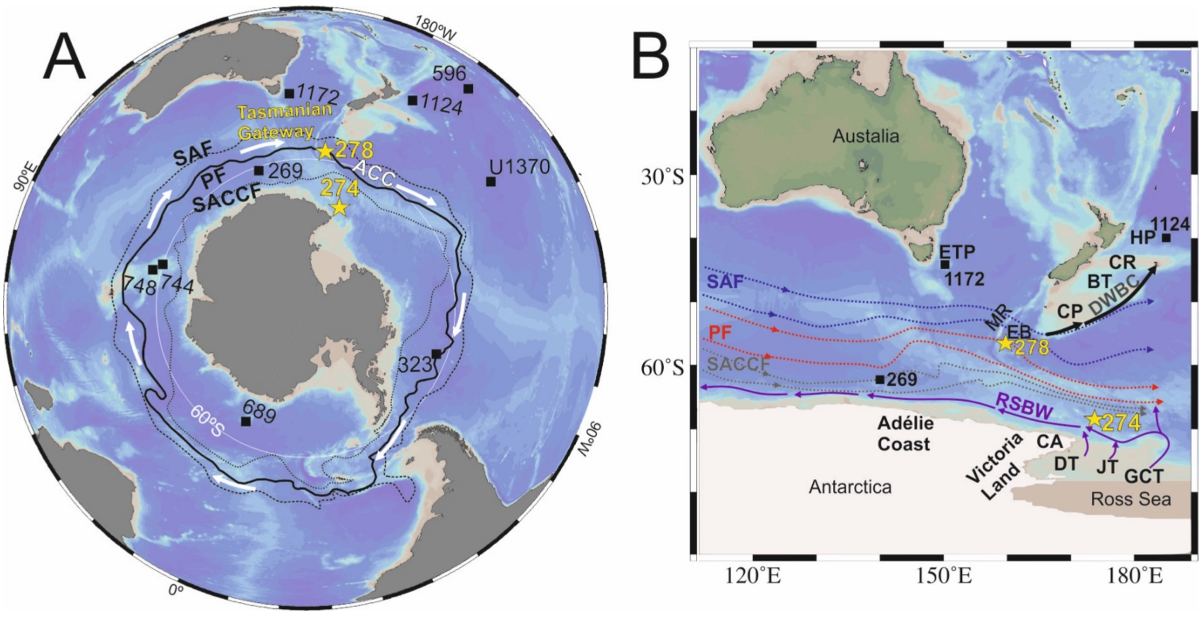

Figure 3.1: Overview map of modern Southern Ocean configuration (Ocean Data View, (Schlitzer, 2016; version 4.79; http://odv.awi.de). **A:** Antarctic Circumpolar Current (ACC) frontal system, study sites (DSDP Sites 274 and 278) (yellow stars) and sites referred to in this study (black squares). SAF: Subantarctic front (black dashed line), PF: Polar front (black line), SACCF: Southern Antarctic Circumpolar Current front (black dotted line) adapted from Orsi et al. (1995). **B:** Major modern deep ocean water circulation paths across the Tasmanian Gateway adapted from Gordon et al. (2009), Orsi and Wiederwohl, (2009) and Sokolov and Rintoul (2007). The main transport of Circumpolar Deep Water along the ACC takes place around the PF and SAF, Ross Sea bottom water (RSBW) (magenta). Deep Western Boundary Current (DWBC) (black arrows), MR: Macquarie Ridge, EB: Emerald Basin, ETP: East Tasman Plateau, CP: Campbell Plateau, BT: Bounty Trough, CR: Chatham Rise, HP: Hikurangi Plateau, CA: Cape Adare, JB: Joides Trough, DB: Drygalski Trough, GCT: Glomar Challenger Trough.

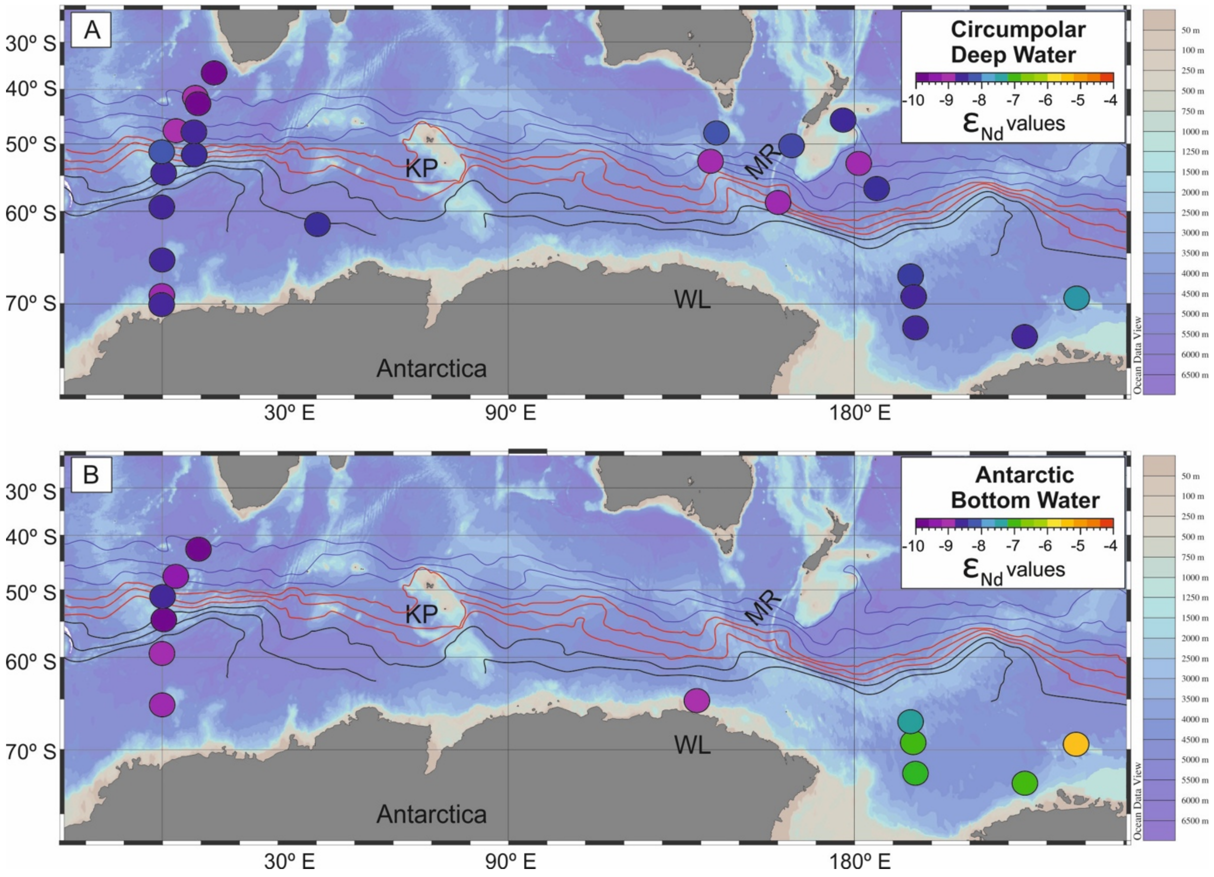

Figure 3.2: Modern neodymium (Nd) isotope composition for deep and bottom waters in the Southern Ocean (between 0°E and 110°W). Figures are made with Ocean Data View (Schlitzer, 2016; version 4.79; http://odv.awi.de). **(A):** Nd isotope composition of Circumpolar Deep Water (CDW). **(B):** Nd isotope composition of Antarctic Bottom Water (AABW) (Stichel et al., 2012; Garcia-Solsona et al., 2014; Rickli et al., 2014; Basak et al., 2015; Lambelet et al., 2018; Amakawa et al., 2019). Antarctic Circumpolar Current (ACC) fronts (mean positions) adapted from Sokolov and Rintoul, 2007. SAF (blue), PF (red), SACCF (black), MR: Macquarie Ridge, WL: Wilkes Land, KP: Kerguelen Plateau

3.3 Material and Methods

3.3.1 Study sites, age models, and paleodepths

Our study focuses on the lower part of Hole 278* at DSDP Site 278 (Cores 34-26, 429-329 meters below sea floor (mbsf)). Sediments from this core interval consist of (i) siliceous nannofossil chalk (429-386 mbsf), and (ii) detrital and nannofossil-bearing radiolarian-diatom ooze, alternating with siliceous oozes (386-329 mbsf) (Kennett et al., 1975). A new age model for the studied sections of Site 278 has been established based on the integration of new magnetostratigraphic data with revised diatom and calcareous nannofossil biostratigraphy, calibrated to the Geological Time Scale (Gradstein et al., 2012; Ogg et al., 2016) (Supplementary Text **10.1.1; Fig. 10.1.3; Tables 10.1.1-10.1.4**). Studied sediments at Site 278 are dated between ~31.2 and 18.8 Ma, similar to the initial shipboard ages, suggesting mid-Oligocene to the early Miocene sediments (Kennett et al., 1975).

For DSDP Site 274, we focus on two distinct intervals (313.5-408.5 mbsf and 180.5-199.5 mbsf). Shipboard core descriptions report that sediments between 328 and 415 mbsf are composed of silty claystones with local presence of chert layers. Sediments between 180.5 and 323 mbsf consist of diatom-detrital silty clay and minor silty clay diatom ooze (Hayes et al., 1975). Based on the initial age model, sediments between 415 and 180.5 mbsf are early to late Oligocene in age (Hayes et al., 1975). More recently, Cande et al. (2000) showed an agreement with this age range using paleomagnetic data collected in the Adare Basin, which indicate that the ocean crust close to Site 274 is not older than earliest Oligocene (Chron 13; ~34 Ma). New dinocyst constraints combined with new magnetostratigraphic data and revised diatom biostratigraphy calibrated to the most recent Geological Time Scale provide a more precise age range for the studied sediments at Site 274 from ~34 to 23.5 Ma (Hoem et al., *in prep*.).

We reconstructed the paleoposition of Sites 278 and 274 using the G-plates geodynamic modeling (http://www.gplates.org ; Müller et al., 2018), utilizing the plate circuit of Müller et al. (2016). Paleodepths for the sites were obtained from the paleo-bathymetry grids generated by the Earthbyte group (Scotese and Wright, 2018), incorporating the reconstructed paleolocation of the two sites (**Fig. 10.1.4**). Our reconstructions show that Site 278 migrated northwards from ~62.84^{o}S (~30 Ma) to 61.4^{o}S (~23 Ma); its paleodepth varied between 3500-4000 m throughout the Oligocene and early Miocene. Site 274 has migrated south from a position of ~70.22^{o}S in the early Oligocene (~33 Ma) to ~69.57^{o}S at the end of the Oligocene-Miocene transition (~23 Ma) and remained in ~2500-3000 m water depth throughout the Oligocene.

3.3.2 Neodymium isotope analyses

Fish teeth and bones (fish debris) were handpicked from the > 63 µm sediment fractions isolated by wet sieving. A total number of 33 samples were selected for fish debris Nd isotope analyses (21 samples from Site 278 and 12 samples from Site 274) (**Table 10.1.5**). All samples were treated with ultraclean 18 □Ω water (MQ water) and methanol to remove debris from surfaces and cavities following Martin and Haley (2000) in the MAGIC laboratories at Imperial College London (see also Huck et al., 2017). Cleaned fish debris samples were subsequently transferred into cleaned microcentrifuge tubes and dissolved overnight in 50 µL of 2M HCl. Dissolved fish debris were loaded on Biorad cation exchange resin (200-400 µm mesh) to separate the REEs from the sample matrix and Eichrom Ln-Spec resin (50-100 µm bead size) to separate Nd from the other REEs.

Furthermore, seven samples were selected (two from Site 278 and five from Site 274; **Table 10.1.5**) to determine the detrital Nd isotope composition in order to evaluate potential contribution of the detrital sediments to the porewaters or overlying bottom water signature. Samples were dried and gently homogenised using mortar and pestle. Approximately 500 mg of homogenised material was subjected to a carbonate leaching procedure to remove biogenic carbonate using 30 ml of 1.5% buffered acetic acid (modified from Biscaye (1965)). Due to the significant carbonate content of the samples from Site 278 (38 to 43 %), approximately 1.5 g of dried sample and 70-75 ml of 1.5% buffered acetic acid were used. Exchangeable ions were subsequently removed using 10ml 1M $MgCl_2$ solution. In a third step, ferromanganese oxides and oxyhydroxides were removed using a weak reductive solution of 0.005 M Hydroxylamine Hydrochloride (NH_2OH) 1.5% acetic acid and 0.03M Na_2-EDTA for 1 hour, followed by a stronger leaching step utilising 0.05 M NH_2OH for 17 hours. 50 mg of leached and water washed detrital sediment was subsequently dried, weight and digested on a hotplate using a mixture of 1ml of concentrated HNO_3, 0.8ml $HClO_4$ and 2ml HF. The detrital samples were processed using the same ion chromatography as the fish debris samples.

Neodymium isotope ratios of fish debris and detrital sediment samples were determined on a high-resolution Nu Plasma multiple collector inductively coupled plasma mass spectrometer (MC-ICP-MS) at Imperial College London, operated in static mode. Instrumental mass bias was corrected using the $^{146}Nd/^{144}Nd$ ratio of 0.7219. All reported $^{143}Nd/^{144}Nd$ ratios are corrected to a nominal JNd_i value of 0.512115 (Tanaka et al., 2000) using bracketing standards. JNd_i standards were also used to monitor external reproducibility, and accuracy was evaluated by processing USGS BCR-2 rock standards, which yielded average $^{143}Nd/^{144}Nd$ ratios of 0.512107 ± 0.000012 (n=121; 2s.d.), in agreement with the published BCR-2 $^{143}Nd/^{144}Nd$ ratio of 0.512638 ± 0.000015 (Weis et al., 2006) (**Table 10.1.5**).

3.3.3 Rare earth element analyses

To correct for the decay of ^{147}Sm to ^{144}Nd within the fossil fish teeth over time, we used the average Sm and Nd concentrations obtained from two fish debris samples for Site 278 samples that yielded $^{147}Sm/^{144}Nd$ ratios of 0.1275 and 0.1256 ($^{147}Sm/^{144}Nd_{average} = 0.1266$). Measured $^{147}Sm/^{144}Nd$ ratios from Site 274 were $^{147}Sm/^{144}Nd = 0.1532, 0.1921, 0.2663$ ($^{147}Sm/^{144}Nd_{average} = 0.2038$). The range of Sm/Nd ratios reported here are consistent with values from Oligocene to Miocene fossil fish debris material elsewhere (Martin and Scher, 2006; Huck et al., 2017; Evangelinos et al., submitted [Chapter 5]). These $^{147}Sm/^{144}Nd$ ratios yielded Nd isotope corrections of 0.18 to 0.28 ε_{Nd} units for Site 278 and 0.02 to 0.13 ε_{Nd} units for Site 274; (t) denotes samples that have been corrected for in situ decay of ^{147}Sm (**Table 10.1.5**). To investigate whether the Nd in the fish teeth is of authigenic nature (i.e. seawater-derived), the full suite of REE concentrations were determined on one fish teeth sample from Site 278 and three fish teeth samples from Site 274 (**Table 10.1.6**).

Rare earth element analysis was performed at the Open University using an Agilent Technologies 8800 Triple-Quad Inductively Coupled Plasma-Mass Spectrometer (ICP-MS). Analyses were standardized via a suite of seven synthetic multi-element standards made up with certified plasma standard solutions. An intermediate synthetic multi-element monitor standard, a fossil bone standard (Chavagnac et al. 2007) and a 2% HNO3 blank were run every 5th sample to monitor instrument drift and precision. Precision was generally better than ±2% (1 s.d.). Both oxide interferences (CeO^+/CeO^-) (<0.5%) and doubly charged species (Ce^{++}/Ce^+) (<1.2%) were kept low. All REE data were normalised to Post Archean Shale (PAAS) concentrations (Taylor and McLennan, 1985).

3.4 Results

3.4.1 Fossil fish teeth Nd isotope compositions

Fish debris Nd isotope data from Site 278 show little variability, ranging from $\varepsilon_{Nd(t)}$ = -6.0 ± 0.2 to 6.8 ± 0.3 from the early Oligocene to the early Miocene (~ 31.2-18.8 Ma) (**Fig. 3.3; Table 10.1.5**). The average $\varepsilon_{Nd(t)}$ throughout the record is -6.4 ± 0.2 (n=20). In contrast, fish debris Nd isotope data from Site 274 show more variability, and reach from maximum values of -3.1 ± 0.3 at ~33.5 Ma and -3.7 ± 0.3 at ~24 Ma to relative minima of -5.0 ± 0.3, at ~33-30.5 Ma, -6.2 ± 0.3 at ~30 Ma, -7.3 ± 0.3 and -6.8 ± 0.3 at ~24.4 and 24.2 Ma, respectively (**Fig. 3.3; Table 10.1.5**). The late Oligocene time period shows a shift of ~2.5 epsilon units over a time period of ~ one million years (24.4-23-5 Ma).

3.4.2 Bulk sediment Nd isotope compositions

The detrital samples at Site 278 exhibit $\varepsilon_{Nd(t)}$ values of -10.4 ± 0.3 (~ 29.8 Ma) and -7.9 ± 0.3 (~ 18.7 Ma), respectively (**Fig. 3.3; Table 10.1.5**). Early Oligocene detrital sediment Nd isotope compositions from Site 274 range between $\varepsilon_{Nd(t)}$= -4.3 ± 0.3 (~33.8 Ma), -7.6 ± 0.3 (~33 Ma) and -8.5 ± 0.3 (~29.8 Ma). Two additional late Oligocene detrital sediment samples yielded $\varepsilon_{Nd(t)}$ values of -10.3 ± 0.3 and -8.5 ± 0.3 at ~24.2 Ma and 24 Ma, respectively (**Fig. 3.3; Table 10.1.5**).

3.4.3 Fossil fish teeth REE patterns

Five fossil fish teeth samples from Site 278 and Site 274 yielded middle-REE enriched patterns (**Fig. 3.4; Table 10.1.6**). However, only one sample (Site 278, Core 33-6) showed a negative Ce anomaly, which together with the middle-REE enriched patterns represent a diagnostic feature of seawater-derived Nd in fish teeth samples (Scher et al., 2011). The other sample from Site 278 and the fossil fish teeth patterns from Site 274 show an enrichment in mid-REEs with a slight positive Ce anomaly (**Fig. 3.4; Table 10.1.6**).

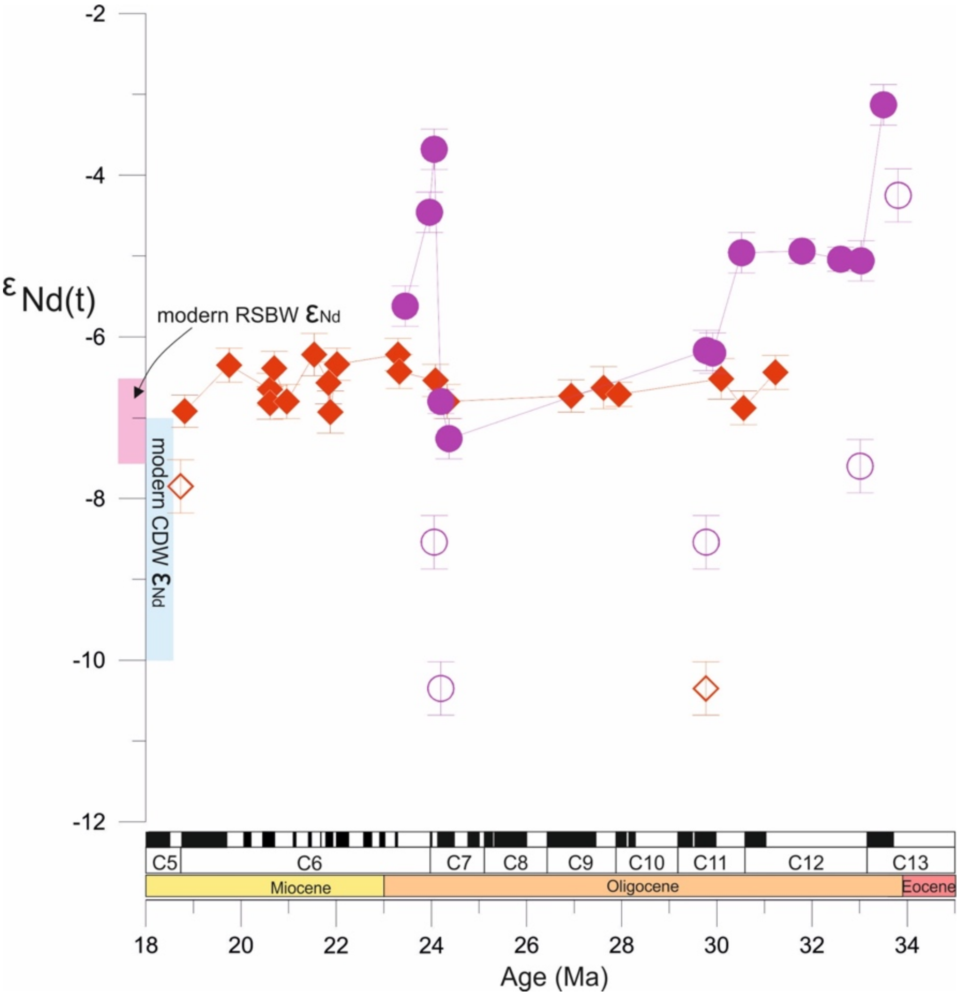

Figure 3.3: Fossil fish teeth $\varepsilon_{Nd(t)}$ records generated in this study from DSDP Sites 274 (magenta circles) and 278 (red diamonds). Detrital sediment $\varepsilon_{Nd(t)}$ values from DSDP Sites 274 (magenta open circles) and 278 (red open diamonds). Present-day Ross Sea Bottom Water (RSBW) ε_{Nd} endmember ranges shown in magenta (Rickli et al., 2014; Basak et al., 2015). Present-day Circumpolar Deep Water (CDW) ε_{Nd} endmember ranges shown in blue (Lambelet et al., 2018 and references therein).

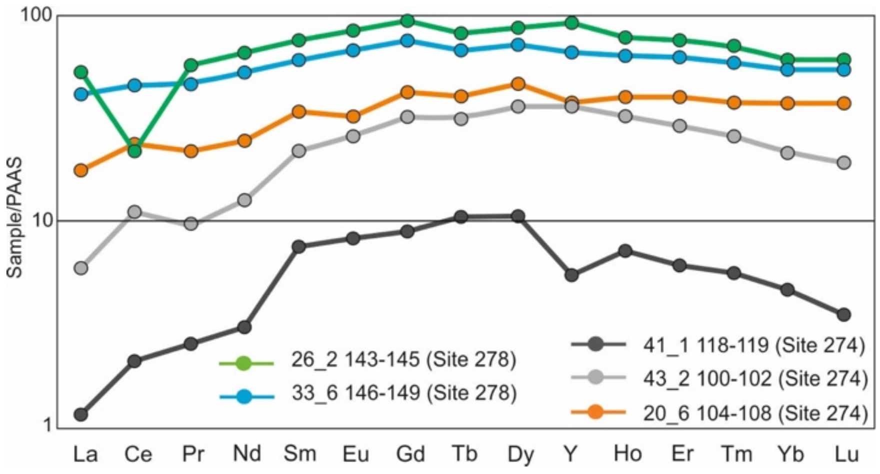

Figure 3.4: Rare earth element (REE) patterns normalised to PAAS (Taylor and McLennon, 1985) for DSDP Sites 278 and 274.

3.5. Discussion

3.5.1 Reliability of Nd isotopes signal extract at Sites 278 and 274

Results of Oligocene to Miocene-aged fish debris samples at Site 278 (paleodepth: 3500-4000 m) are more radiogenic (less negative) in their Nd isotope composition ($\varepsilon_{Nd(t)}$ = -6.0 to -6.7) than modern CDW in the south Emerald Basin (ε_{Nd} = ~ -9) at ~3200-4200 m water depth (Lambelet et al., 2018). Results for Site 274 ($\varepsilon_{Nd(t)}$ = -3.1 to -7.3) overlap with ambient RSBW (ε_{Nd} = -6.5 to -7.5; Rickli et al., 2014; Basak et al., 2015), but also extend to more radiogenic values (**Fig. 3.3**). The first question to address is hence, whether there is indication for a non-authigenic nature of the observed signal in fish debris.

Site 278 is located near the Macquarie Ridge, a relict volcanic mid-ocean ridge (Conway et al., 2012), characterised by basalts and peridotites with an ε_{Nd} value of +7 to +11 (Kamenetsky et al., 2000; Dijkstra et al., 2009). Seafloor spreading at the Macquarie Ridge occurred between ~52 and 12.5 Ma (Lamarche, 1997). Interaction of volcanic sediments and/or hydrothermal products with ambient seawater could have altered the ε_{Nd} values at Site 278 towards more radiogenic values. However, hydrothermal activity has been shown to be a sink rather than a source of Nd near ridges (Halliday et al., 1992; Stichel et al., 2018). Moreover, fossil fish teeth records from the Kerguelen Plateau show no changes in their Nd isotopic composition associated with the local volcanic activity during the timing of the northern Kerguelen Plateau emplacement (Wright et al., 2018). Volcanic glass and rock fragments have been reported from close to the base of siliceous nannofossil chalk at Site 278 (Kennett et al., 1975) (~31-30 Ma based on our new age model). However, the insignificant variability in our fish teeth Nd record makes it difficult to reconcile any major volcanic contribution to the porewater and hence to the fossil fish teeth Nd isotope signature (**Figs. 3.3; 10.1.5A**).

To further evaluate the potential interaction between detrital sediments and pore water/seawater Nd isotope composition, we can turn to the results from two detrital sediment samples from the siliceous chalk unit (core 33R-6) and from the nanno-bearing diatom ooze unit (core 26R-2) at Site 278. The detrital samples exhibit $\varepsilon_{Nd(t)}$ values of -10.4 ± 0.3 and -7.9 ± 0.3, respectively (**Fig. 3.3; Table 10.1.5**), within the range of terrigenous inputs from Paleozoic granites and metasedimentary rocks ($\varepsilon_{Nd(t)}$= -4.9 to -13.9) of the South Island, New Zealand (Pickett and Wasserburg 1989). This observation is in line with the general deep water flow in the area, suggesting that terrigenous sediments in the Southern Emerald Basin are predominantly derived from the erosion of the New Zealand´s Southern Alps via the Solander Channel (Carter and McCave, 1997; Schuur et al., 1998). Importantly, the measured detrital sediment composition is more unradiogenic (i.e. more negative ε_{Nd} values) than the almost contemporaneous fish teeth signatures and hence cannot be responsible for the observed more radiogenic values. In addition, REE patterns from a fish teeth sample from core 33R-6 (29.8 Ma) exhibits a pattern enriched in middle-REEs and a prominent negative cerium (Ce) anomaly, which represent diagnostic features of uncontaminated seawater origin in the fish teeth (**Fig. 3.4; Table 10.1.6**) (Scher et al., 2011; Huck et al., 2016, 2017). The fish teeth sample from core 26R-2 (18.7 Ma) exhibits also a typical middle-REEs enriched pattern, but records a slightly positive Ce anomaly (**Fig. 3.4**). Positive Ce anomalies in fossil fish teeth have been linked to anoxic seawater and/or pore water conditions, resulting in remobilization of REEs from authigenic or organic matter coatings (Elderfield and Pagett, 1986; Wright et al., 1987; Freslon et al., 2014; Huck et al., 2016). High biogenic productivity at Site 278 associated with proto-polar front upwelling processes (Kennett et al., 1975) may have led to anoxic conditions at the seafloor.

Similar to Site 278, bulk sediment results from Site 274 exhibit a less radiogenic (i.e. lower) Nd isotope fingerprint than fossil fish debris when comparing results for the same samples and samples picked very closely. The difference in $\varepsilon_{Nd(t)}$ for three pairs of fish debris-detrital sediment samples analyzed is -4.9, -3.5 and -2.4 ε_{Nd} units, while adjacent samples show differences in $\varepsilon_{Nd(t)}$ of -2.5 and -1.1 (**Figs. 3.3; 10.1.5B; Table 10.1.5**). This pronounced difference between the $\varepsilon_{Nd(t)}$ values of the fish debris and the detrital sediment samples at Site 274 strongly supports the absence of significant exchange between the detrital sediments and the fossil fish teeth. Overall, the more radiogenic $\varepsilon_{Nd(t)}$ values of the fish teeth, compared to the more unradiogenic $\varepsilon_{Nd(t)}$ values of the detrital samples, argues against a contribution of Nd from the detrital sediments.

Furthermore, REE patterns of three fish teeth samples at Site 274 yielded middle-REE bulge patterns, including a slightly positive Ce anomaly (**Figs. 3.4; Table 10.1.6**). The close proximity of Site 274 to the Antarctic continental margin and the high biogenic fraction in the sediment (Hayes et al., 1975) may have caused the observed positive Ce anomaly resulting from increased weathering inputs and/or remobilized REEs from authigenic or organic matter coatings due to anoxic conditions in the pore waters (Elderfield and Pagett, 1986; Wright et al., 1987; Freslon et al., 2014; Huck et al., 2016). Further work is required to fully understand the positive Ce anomaly in our fish teeth samples. Nevertheless, REE patterns from Site 278 and 274 are similar to REE patterns from Eocene-Oligocene fish teeth records from around the Tasmanian Gateway, which have been interpreted to preserve a predominantly seawater signature, despite positive Ce anomalies (Huck et al., 2016, 2017). We therefore suggest an authigenic nature of the fish debris record from Sites 278 and 274 and will use our new data in the following to explore the chemical fingerprint of proto-CDW and RSBW across the Tasman Gateway, and its implications for the ACC evolution.

3.5.2 Early Oligocene epoch (34 -30 Ma): Prior to the onset of the ACC

Neodymium isotope values from our deeper Site 278 (paleodepth: ~4000 m) between 31-30 Ma, indicate that the south Emerald Basin was bathed by an unradiogenic deep water mass ($\varepsilon_{Nd(t)}$ = ~-6.3) (**Figs. 3.3 and 3.5**). These values converge with published Nd isotope records from the deep South Pacific (Site U1370, paleodepth ~5000 m, Site 596 paleodepth ~5000 m and Site 323, paleodepth ~4000 m; $\varepsilon_{Nd(t)}$ = ~-6.3) (Thomas et al. 2014; McKinley et al., 2019), suggesting that abyssal sites in the South Pacific were likely influenced by a common deep/bottom water mass, such as South Pacific Deep Water (SPDW) (**Fig. 3.5**). McKinley et al. (2019) have proposed that a deep/bottom water mass characterised by $\varepsilon_{Nd(t)}$ of ~ -6 was a persistent feature of the deep South Pacific from 70 to 20 Ma. Temporal and spatial Nd isotope patterns and modelling results suggest that SPDW was likely formed in the Ross Sea region (Thomas et al., 2003; Thomas, 2004; Houben et al., 2014; Thomas et al., 2014; Huck et al., 2017; McKinley et al., 2019).

Our $\varepsilon_{Nd(t)}$ values from Site 274, located proximal to the Ross Sea, however, range from -3.1 to -5.1 between 33.5 and 30.5 Ma and albeit of low resolution are more radiogenic (less negative), compared to both the present-day RSBW Nd isotopic composition (ε_{Nd}= -6.4 to -7.5; Rickli et al., 2014; Basak et al., 2015) and the deep record from Site 278 (**Figs. 3.3 and 3.5**). The average $\varepsilon_{Nd(t)}$ value of ~ -4.6 for the early Oligocene (~ 33.5-30.5 Ma) at Site 274 (paleodepth: ~ 2500-3000 m) overlaps with published data from the Eastern Tasman Plateau (Site 1172; average $\varepsilon_{Nd(t)}$ =~ -3.9 paleodepth: ~ 2400 m) and Hikurangi Plateau (Site 1124; average $\varepsilon_{Nd(t)}$ = ~-4.8; paleodepth: ~3800 m) (Scher et al., 2015) (**Fig. 3.5**). Similarities between our new Nd record from Site 274 and the published records from Scher et al. (2015) suggest that these sites may have been influenced by a common water mass, occupying water depths between ~ 2500-3800 m. Prior to the onset of the ACC, the major oceanographic feature in the Pacific side of the Tasmanian Gateway was the proto-Ross Sea gyre/Tasman Current, which flowed along Antarctica´s Pacific margin and extended northward along the east side of the Tasmania and Australia turning to the east north of the New Zealand (Huber et al., 2004; Stickley et al., 2004; Sijp et al., 2011; Bijl et al., 2013). We therefore suggest that the Ross Sea gyre transported deep waters with a more equatorial-Pacific-like Nd isotope signature to the Adare Basin (Site 274), the Eastern Tasman Plateau (Site 1172) and Hikurangi Plateau (1124) (**Fig. 3.6**).

Our results point therefore to the presence of two distinct deep water masses in the late Eocene/early Oligocene South Pacific, one occupying depths between ~2500-4000 m with Nd composition ($\varepsilon_{Nd(t)=}$ ~-3 to -5) and a second deep/bottom water mass (>= 4000 m) with more unradiogenic Nd composition ($\varepsilon_{Nd(t)=}$ ~-6), which its source remains unknown (**Fig. 3.5**).

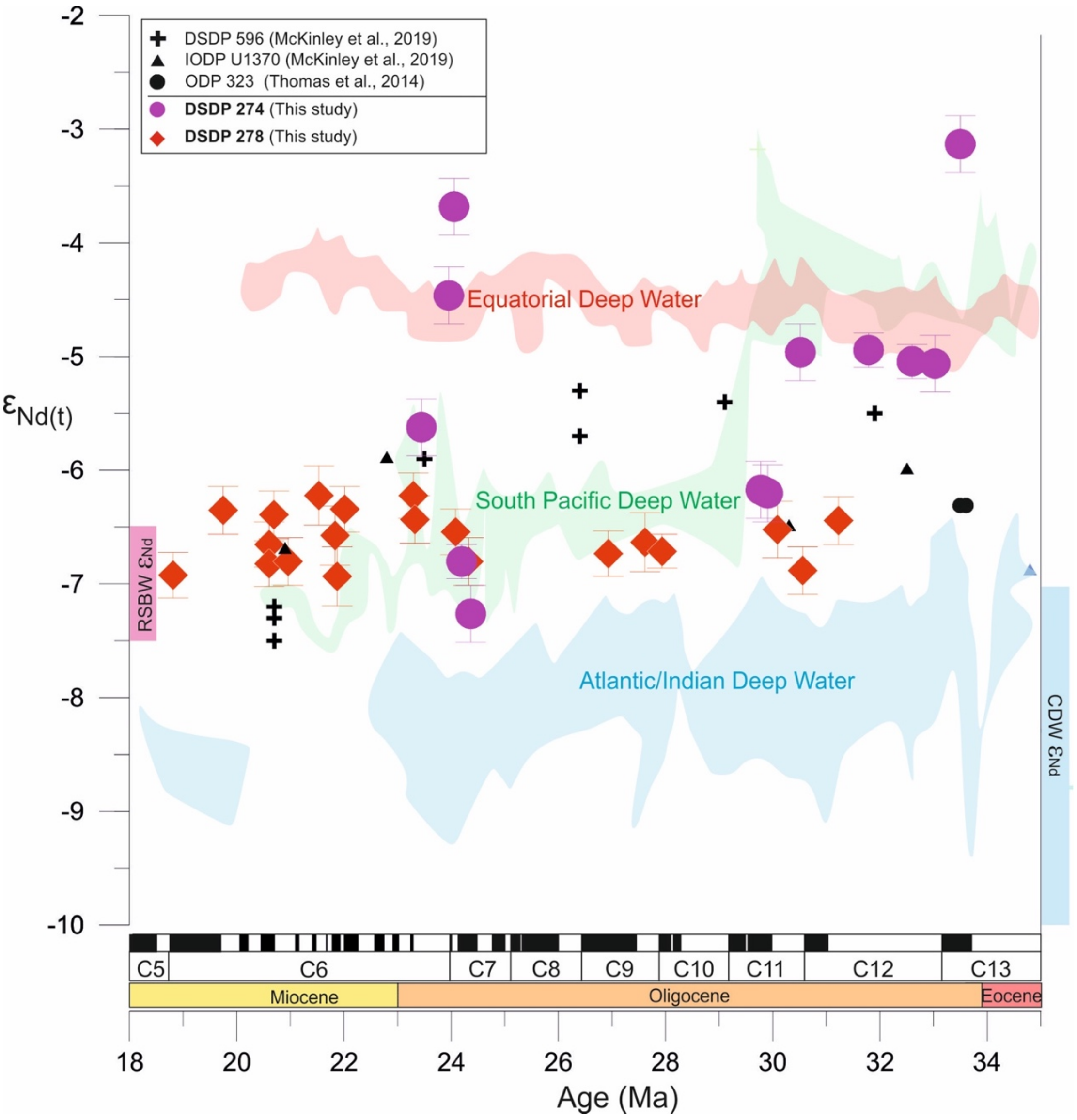

Figure 3.5: Comparison of fossil fish tooth εNd records generated in this study from DSDP Sites 274 and 278 with those derived from sites along the proto-CDW path in the Atlantic, Indian and Pacific sectors of the Southern Ocean. Atlantic/Indian Ocean locations include ODP Site 689 (Maud Rise; Scher and Martin, 2004), ODP Sites 748 and 744 (Kerguelen Plateau; Wright et al., 2018), and DSDP Site 269 (off Adélie Coast; Evangelinos et al., submitted [Chapter 5]) (light blue shading). ODP Site 1124 (Hikurangi Plateau) and ODP Site 1172 (East Tasmanian Plateau; Scher et al., 2015) are combined in the green shading. Pacific Equatorial Age Transect (PEAT) Nd isotope results from the Equatorial Pacific are based on IODP Sites U1331, U1332, U1333, U1334, and U1335 (Scher et al., 2014). The only data shown as individual symbols other than our new results are South Pacific DSDP 596, IODP Site U1370 (McKinley et al., 2019) and ODP Site 323 (Thomas et al., 2014). Blue shaded ranges refer to the present-day Nd signature of the CDW and magenta shaded rangers refer to the present-day Nd isotopic composition of the RSBW (Rickli et al.,2014; Basak et al., 2015; Lambelet et al., 2018 and references therein).

3.5.3 Early Oligocene to early Miocene epoch (30-20 Ma): After the onset of the ACC

Neodymium isotope values at Site 274 show a shift towards less radiogenic values ($\varepsilon_{Nd(t)}$ = -6.2 ± 0.3) at ~30 Ma. Slightly less radiogenic $\varepsilon_{Nd(t)}$ values are observed around 24.4 Ma and 24.2 Ma (-7.3 ± 0.25 and -6.8 ± 0.15, respectively) (**Figs. 3.3; 3.5**), resembling modern RSBW values (ε_{Nd}= -6.4 to -7.5; Rickli et al., 2014; Basak et al., 2015). The shift at 30 Ma at Site 274 took place slightly earlier than the shift observed in the two Nd isotope records in the East Tasman Plateau (Site 1172 $\varepsilon_{Nd(t)}$ = -3.8 to -7) and the Hikurangi Plateau (Site 1124 $\varepsilon_{Nd(t)}$ = -4.7 to 6) between 29.3 and 29 Ma, respectively (Scher et al., 2015) (**Fig. 3.5**). This latter shift has been linked to the northward migration and alignment of the Tasmanian Gateway with the westerly winds (Scher et al., 2015). The change in the $\varepsilon_{Nd(t)}$ values at Site 274 at ~ 30 Ma does not coincide with any significant known change in the Antarctic ice sheet that would have influenced the sediment input around the Ross Sea. Instead, given that Site 274 was located south of the proto-PF during this period, we posit that the shift to more unradiogenic Nd contribution is probably attributed to the onset of proto-CDW upwelling reaching the Adare Basin and Site 274 (**Fig. 3.6**).

Site 278, on the other hand, was located close to the proto-PF and proto-SAF between 30 Ma and 20 Ma and thus in the main pathway of the proto-ACC and proto-CDW (**Fig. 3.6**), explaining its invariant Nd isotope fingerprint (average $\varepsilon_{Nd(t)}$ = -6.4) throughout the early Oligocene to early Miocene (30-19 Ma) (**Figs. 3.3; 3.5**). These values are matched by the two published Nd isotope records ($\varepsilon_{Nd(t)}$ ~-6.5) from the eastern side of Tasmanian after the onset of ACC influence at this northern location (Scher et al., 2015) (**Fig. 3.5**). All three records do show more radiogenic Nd isotope compositions than modern CDW in the Emerald Basin with ε_{Nd} of -9 (Lambelet et al., 2018) (**Figs. 3.2A; 10.1.2**). They furthermore differ from records to the west of the Tasmanian Gateway. Throughout the Oligocene (30-23 Ma) Nd isotope records along the proto-PF in the South Atlantic and South Indian Ocean suggest the presence of proto-CDW with Nd isotopic composition between ~ -7 and -9 (Scher and Martin, 2004, 2006, 2008; Wright et al., 2018; Evangelinos et al., submitted [Chapter 5]) (**Figs. 3.5; 3.6**). Such values are similar to modern CDW (ε_{Nd}=-8.3 ± 1.5, n=158) (Lambelet et al., 2018) (**Fig. 3.5**)

Comparison between our new and previously published data along the proto-ACC pathway around the Tasmanian Gateway therefore reveal a provinciality in seawater Nd isotopes with more radiogenic proto-CDW on the Pacific side ($\varepsilon_{Nd(t)}$ = -6 to -7.5) of the Tasmanian gateway than in the Indian and Atlantic sector ($\varepsilon_{Nd(t)}$= -7 to -9) (**Figs. 3.5**). This implies an absence of a homogenous deep water mass across the Tasmanian Gateway during the Oligocene and early Miocene period suggesting a more complex evolution of the deep ocean circulation across the gateway than previously assumed. We suggest that the provinciality across the gateway was due to a less deep reaching and probably also weaker proto-ACC flow during the Oligocene to early Miocene (**Fig. 3.6**). A shallower and weaker ACC flow entering the South Pacific would have increased the amount of time that Pacific deep water could have mixed with the proto-CDW, allowing for acquisition of a more radiogenic isotopic composition of proto-CDW. These inferences are consistent with numerical simulations showing limited throughflow of the proto-ACC due to Australasian paleogeography during the Oligocene (Hill et al., 2013) and weaker global overturning circulation due to weaker westerly winds from the early to mid-Miocene (Herold et al, 2012).

Recent sedimentological data, microfossil assemblages and past reconstructions of sea surface temperatures from the Antarctic-Australian Basin and around the Tasmanian Gateway, also infer a weaker proto-ACC frontal system, characterised by intrusions of warm waters from northern latitudes from the Oligocene to the middle Miocene (34-11 Ma) (Bijl et al., 2018b; Hartman et al., 2018; Sangiorgi et al., 2018; Salabarnada et al., 2018; Evangelinos et al., submitted [Chapter 5]). The question remains when the modern-like ACC was established. Our data suggest that this may have occurred sometime during the Neogene, but future work is necessary to address the timing of its establishment and the wider implications of a weaker Oligocene to Miocene ACC.

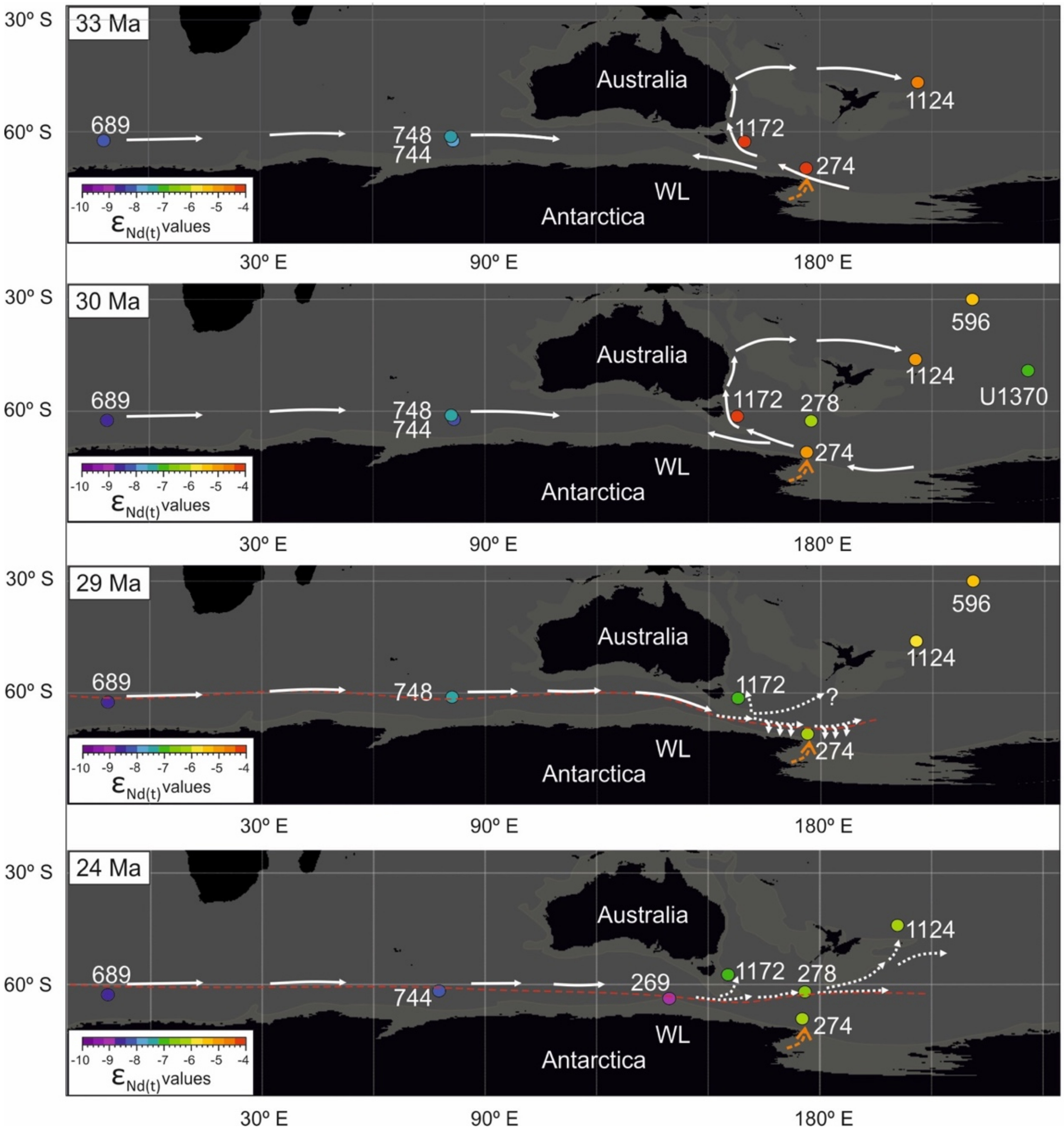

Figure 3.6: Deep water mass circulation in the Southern Ocean at 33 Ma, 30 Ma, 29 Ma and 24 Ma**.** Plate tectonic reconstructions and paleolocation of study sites 278 and 274, and other sites discussed in the main text were adapted from G-plates, based on the global plate motion model from Muller et al. (2016). Continent with present-day coastlines (black), grey boundary around continents shows areas of non-oceanic crust (e.g. continental shelves). Circles represent site locations and are coloured based on their average $\varepsilon_{Nd(t)}$ values for each period considered. Orange arrow represents Ross Sea Bottom Water (RSBW). Red dotted line denotes the reconstructed position of the proto-PF position based on Nelson and Cooke (2001).

3.5.4 Evidence of glacial weathering event in Site 274 during the Latest Oligocene (24 Ma)

The major ε_{Nd} excursion observed at Site 274 (from -6.8 ± 0.3 to -3.7 ± 0.3) at ~24 Ma is a peculiar feature of our new record and may reflect locally changing seawater composition due to a major glacial weathering advance (**Figs. 3.2; 3.5**). Considering the relative invariant Nd isotope compositions of Oligocene Pacific deep water (Scher, 2014; McKinley et al., 2019) and proto-CDW (this study; Wright et al., 2018) during the Oligocene, we propose two potential causes for the radiogenic excursion at Site 274: (i) increased boundary exchange/volcanic activity, (ii) glacial pulses in Antarctica leading to increased glacial weathering inputs to local seawater.

While volcanic activity and deposition of volcanic materials has been reported around the Ross Sea at ~24 Ma related to the McMurdo volcanic group (McIntosh, 2000; Roberts et al., 2013), there is little evidence of volcanic contribution in the sediments at Site 274 (Hayes et al., 1975). In addition, the pronounced difference between the detrital sediment ε_{Nd} value ($\varepsilon_{Nd(t)}$ = -8.5 ± 0.3) and the fish teeth ε_{Nd} value ($\varepsilon_{Nd(t)}$ = -3.7 ± 0.3) and the REE patterns indicate that fish teeth predominantly preserve a seawater signature at 24 Ma (**Figs. 3.3; 3.4**). Nevertheless, the measured detrital sediment composition is more unradiogenic than the contemporaneous fish teeth signature and hence it should result in a shift in $\varepsilon_{Nd(t)}$ value of the fish teeth towards a more unradiogenic value. We therefore exclude the possibility of boundary exchange/volcanic activity. A more promising connection of the prominent excursion observed at Site 274 can be made with the timing of a major expansion of marine ice sheet across the Ross Sea continental shelf between 24.5 and 24 Ma (Kulhanek et al., 2019; Levy et al., 2019). Antarctic weathering has previously been shown to influence the chemistry of local seawater and its Nd isotope composition as evidenced by records from the Prydz Bay area covering late Eocene and Eocene Oligocene Transition (EOT) Antarctic glacial weathering pulses (Scher et al., 2011; 2014; Wright et al., 2018).

The Cape Roberts Project cores in the Ross Sea provide further support for delivery of glaciomarine sediment to the area during the latest Oligocene (from 24 Ma), as evidenced by an increased content in volcanic glass, primarily controlled by weathering and erosion of McMurdo Volcanic group rocks (McIntosh, 2000; Roberts et al., 2013). The late Cenozoic McMurdo Volcanic group is characterised by $\varepsilon_{Nd} > 0$ (Cook et al., 2013, 2017) and thus could easily provide a source for more radiogenic Nd isotope compositions of seawater during the late Oligocene. We posit that surges of weathering associated with ice growth at 24.5-24 Ma may have changed the seawater chemistry in the Ross Sea, resulting in more radiogenic local ε_{Nd} values in the fish teeth at Site 274.

Although it is only one data point, the very radiogenic value ($\varepsilon_{Nd(t)}$ = -3.1 ± 0.3) at ~ 33.5 Ma coincides with the major expansion of Antarctic ice sheets during the second large step of the EOT (**Fig. 3**) (33.7 Ma, Zachos et al., 2001; Scher et al., 2011) and thus may also be associated with a glacial weathering event. Given the absence of McMurdo volcanic group during the early Oligocene (Kyle and Muncy, 1989), we postulate that a possible source of very radiogenic values during the early Oligocene is the Granite Harbour Intrusives (GHI) in the Gabbro Hills (ε_{Nd} =~ -2.3 ± 1.6, n=4; Borg et al., 1990). However, more data is needed to support or dispute our hypotheses.

3.6 Conclusions

Neodymium isotope data from Site 274 in the Adare Basin report the first proximal Nd isotope record to the Ross Sea during the Oligocene (~34-23.5 Ma) and reveals two major shifts through time in response to major steps in Antarctic ice sheet expansion at the Eocene/Oligocene and at ~24 Ma. A third shift around 30 Ma seems more closely related to broader changes in the Nd isotope signature of seawater in the Pacific sector of the Southern Ocean, related to changes in the westerlies and upwelling proto-CDW. In contrast, Site 278 in the southern Emerald Basin shows an invariant Nd isotopic composition ($\varepsilon_{Nd(t)}$ = -6.0 to -6.8) throughout the Oligocene and early Miocene (31.2-18.8 Ma). Comparing our Nd isotopic records with previously published data, we suggest the presence of two deep water masses in the South Pacific prior to the onset of the ACC (34-30 Ma), one occupying depths between ~2500-4000 m with Nd composition ($\varepsilon_{Nd(t)=}$ -3 to -5) and a deep/bottom water mass (>= 4000 m) with more unradiogenic Nd composition ($\varepsilon_{Nd(t)=}$ ~-6). Following the onset of the ACC and the opening of the Tasman Gateway (30-18.9 Ma), the seawater Nd isotope record at Site 278, located close to the proto-polar front (proto-PF), remained more radiogenic than the proto-CDW Nd isotope composition along the proto-PF in the South Atlantic and Indian Ocean. This observation manifests a prominent offset in Nd composition of proto-CDW along the proto-PF across the Tasmanian Gateway. In the modern Southern Ocean, CDW along the PF is characterised by relative homogenous (lateral and vertical) Nd isotope compositions in all oceanic basins. We attribute the offset in the Nd isotope composition of deep waters across the Tasmanian Gateway to a weaker, less deep reaching ACC (proto-ACC) than today. Our finding implies that the modern strong and deep-reaching ACC flow must have been developed at a later point in the Neogene.

Chapter **4**

Establishment of the modern Antarctic Circumpolar Current

ABSTRACT

The vigorous eastward-flowing Antarctic Circumpolar Current (ACC) is the largest current in the world. As it connects all the main ocean basins, it plays a fundamental role in the global ocean circulation, cryosphere, biogeochemical cycles and the climate system as a whole. Notwithstanding the relevance of the ACC in Earth´s climate system, the time when the ACC formed and evolved to reach its present characteristics (e.g., vigorous and deep-reaching current) remains highly controversial. This represents a major gap for our understanding of its role in the evolution and stability of the ice sheet and in the global climate system. Here we show evidence for the establishment of the modern vigorous and deep-reaching ACC at ~4 million years ago. We base our interpretation on a permanent shift in the: 1) neodymium isotopic composition of bottom water masses; 2) mean grain-size of sortable silt and, 3) biogenic silica, recorded in pelagic sediments from the Southwest Pacific sector of the Southern Ocean. A progressive intensification of the ACC since 19 Ma is recorded by the sortable silt. This is accompanied by a progressive decrease towards less radiogenic values of the neodymium isotopic composition of bottom water masses, suggesting higher influx of North Atlantic Deep Water in the Southwest Pacific. From 4 Ma, neodymium isotopes show the homogenization of Southern Ocean deep waters along the ACC pathway, coinciding with a sharp increase in ACC flow speeds and siliceous productivity related to stronger upwelling activity within the polar frontal system. Our findings imply that the ACC attained characteristics that are comparable to the modern ~4 million years ago, long after the Tasmanian and Drake Gateway had opened and deepened. These findings prevent the previously attributed direct link between the onset of a modern-like ACC and the opening of these gateways. The potential links between the establishment of the modern-like ACC and the closure of the Panama seaway, also dated at ~4 Ma, and the late Neogene global cooling that followed (3.5-3 Ma) deserve further investigation.

4.1 Introduction

The ACC is the planet´s largest ocean current transporting about 137 – 147 ± 10 x 10^6 m^3s^{-1} from the west to the east along a roughly 20,000 km long path around Antarctica (Rintoul and Sokolov, 2001; Cunningham et al., 2003; Legeais et al., 2005). The ACC flow is affected by the interplay between the westerly winds (westerlies) and buoyancy forcing, eddy fluxes and interactions between its flow and bathymetry (Rintoul et al., 2001; Olberns et al., 2004; Rintoul, 2018). Today, most of the transport of the ACC is centered in three major deep-reaching (i.e., extending to the seafloor) circumpolar oceanic fronts: the Sub-Antarctic Front (SAF) and the Polar Front (PF) (Orsi et al., 1995; Sokolov and Rintoul, 2007; **Fig. 4.1**). The deep layers of the ACC within the PF and SAF are occupied by Circumpolar Deep Water (CDW) (Orsi et al., 1995). By connecting the Atlantic, Indian and Pacific basins, the ACC permits the existence of the global overturning circulation, which actively modulates the transport of heat, moisture, carbon and nutrients around the globe and thereby strongly influences 1) the global climate (Marshall and Speer, 2012; Talley, 2013; Rintoul 2018), 2) the regional and remote marine ecosystems (Sarmiento et al., 2004) and 3) isolates thermally the Antarctic continent from subtropical ocean surface warmth (Martinson, 2012).

Despite the importance of ACC in the Earth´s Climate system and Antarctic ice sheet stability, the establishment of the modern-like, strong and deep-reaching ACC remains controversial. This knowledge is nevertheless fundamental for our understanding of the long-term paleoceanographic and climate evolution throughout the Cenozoic, but also for assessing the response of ACC to ongoing climate change, and its influence in the stability of the Antarctic ice sheet (Rintoul et a., 2018; Escutia et al., 2019; Meredith et al. 2019). It has been argued that the inception of a strong deep-reaching ACC depended on the deep opening of the two last Southern Ocean seaways during the break-up of Gondwana: the Tasmanian Gateway and Drake Passage (Barker et al., 2007; Sijp et al., 2014). The development of a deep (bathyal depths) oceanic passage in the Tasmanian Gateway has been proposed to occur between 33.5-30.2 Ma (Stickley et al., 2004). In contrast, the timing of the opening of the Drake Passage remains uncertain, with the development of the deep opening ranging from early Oligocene to late Miocene (~34-10 Ma) (Livermore et al., 2005; Barker et al., 2007; Dalziel, 2014).

Estimates from the ACC development based on marine sediment records suggest also a wide range of ages between 41 Ma and <10 Ma (e.g., Pfuhl and McCave, 2005; Scher and Martin, 2006; Scher et al., 2015; Bijl et al., 2018b). Neodymium (Nd) isotope records used as water mass tracer, revealed an influx of shallow Pacific waters into the South Atlantic Ocean via the Drake Passage at around 41 Ma (Scher and Martin, 2006). Between the Eocene and late Oligocene (36-23 Ma), a deep proto-CDW might have circulated in the South Atlantic and South Indian sectors, along the proto-polar front (Scher and Martin, 2008; Wright et al., 2018; Evangelinos et al., in press [Chapter 5]). The first evidence of an eastward deep water flow from the South Indian Ocean into the Southwest Pacific Ocean via the Tasmanian Gateway has been reported only at 30 Ma linked to the alignment of the Tasmanian Gateway with the westerlies (Scher et al., 2015). However, a prominent offset in Nd composition of deep waters along the proto-polar front across the Tasmanian Gateway until at least the early Miocene (~19 Ma), points to the absence of a modern-like homogenous CDW across the Gateway (Evangelinos et al., *in prep.* [Chapter 3]). This has been interpreted to result from a weaker than present-day ACC (*Evangelinos et al., in prep.* [Chapter 3]). Grain-size records from the south Tasman Rise and current-reworked sediments containing a hiatus from the south Pacific have been reported to document the initiation of a strong deep current flow between the late Oligocene and early Miocene (~25-23 Ma) linked to the onset of the modern deep ACC (Pfuhl and McCave, 2005; Lyle et al., 2007). In contrast, sedimentological and microfossil assemblages (i.e., dinocysts, calcareous nannofossils and diatoms) records from the western side of the Tasmanian Gateway indicate a weaker proto-polar front with a less intensive upwelling activity than today and thus a weak ACC at least until the late Miocene (10 Ma) (Bijl et al., 2018b; Sangiorgi et al., 2018; Salabarnada et al., 2018; Evangelinos et al., in press [Chapter 5]). This is further supported by sea surface temperature reconstructions recording a warmer-than-today ocean offshore Wilkes Land between the Oligocene and Miocene, and reduced temperature gradients within the proto-ACC (Hartman et al., 2018; Sangiorgi et al., 2018). Numerical simulations support these interpretations showing the absence of a coherent ACC due to the paleo-geography of the Tasmanian Gateway during the Oligocene (Hill et al., 2013) and the presence of weak westerlies in the Miocene (Herold et al, 2012).

Altogether, these findings indicate the presence of a weak ACC (proto-ACC) at least until the late Miocene (i.e., 10 Ma). They also imply that the onset of a modern-like ACC must have taken place at a later point when it acquired its present diagnostic characteristic features: (i) the homogenisation of

CDW in the Southern Ocean, (ii) the permanent inception of strong deep-reaching ACC flow, and (iii) the establishment of a ACC frontal system characterised by strong deep water upwelling.

In order to more precisely date the establishment of the strong and deep-reaching ACC, we trace changes in its water mass composition (i.e., CDW), bottom current speed and regional upwelling activity over the last 19 Ma. For this, we combine fossil fish teeth ε_{Nd} values, mean sortable silt, and biogenic silica records from the relatively well-dated Deep Sea Drilling Project (DSDP) Site 278 (56^{o} 33.42´S, 160^{o} 04.29´E, 3300 m water depth) (**Fig. 4.1**) (see Supplementary Information [Chapter 10.2]). Today, the site is located in the South Pacific Southern Emerald Basin within the main pathway of the ACC, close to the northern branch of the Polar Front (PF) and is bathed by CDW (Sokolov and Rintoul, 2007; Rintoul et al., 2014; Lambelet et al., 2018). Site 278 remained around 60^{o}S close to the proto-polar front and at ~3500 m water depth over the last 20 Ma (Supplementary information [Chapter 10.2]), (Nelson and Cooke, 2001; Cooke et al., 2002). It thus provides unique opportunity, when combined with other existing reconstructions, to scrutinize past ACC changes.

Our revised age model reveals that Site 278 is characterized by a nearly continuous sediment deposition during the last 20 Ma. The exception is an unconformity recording a 6 Ma hiatus, where much of the late Miocene and earliest Pliocene is missing (~ 10 to 4 Ma) (Supplementary information [Chapter 10.2]; **Fig. 10.2.1**). This unconformity has been attributed to intensification of bottom currents around the Emerald Basin due to a newly formed gateway in the Macquarie Ridge complex at 53.5^{o}S (Schuur et al., 1998). Sediments at Site 278 consists of alternations between calcareous and siliceous oozes (Kennett et al., 1975; Supplementary information [Chapter 10.2]; **Fig. 10.2.1**).

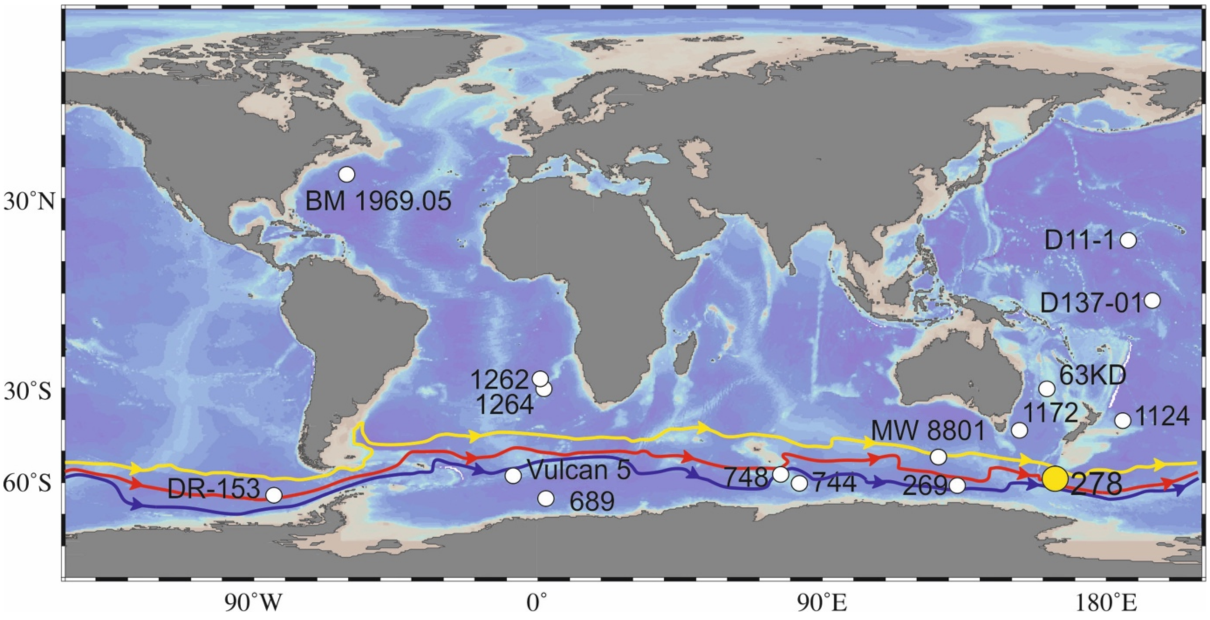

Figure 4.1: Location map of Site 278 and other sites discussed in the text. Figure is made with Ocean Data View (Schlitzer, 2016; version 4.79; http://odv.awi.de). Mean Antarctic Circumpolar Current front position: Sub-Antarctic front (SAF; yellow), Polar front (PF; red), Southern ACC front (SACCF; blue) adapted from Sokolov and Rintoul, (2007).

4.2 The establishment of modern-CDW Nd composition in the Southern Ocean

Our fossil fish teeth ε_{Nd} values at Site 278 show an overall decrease by ~2 ε_{Nd} units from -6.27 (± 0.25) to -8.12 (± 0.28) between the early Miocene and the late Pleistocene interval (i.e., from ~18.7 Ma to 500 Ka). However, short-term shifts to more radiogenic values are superimposed on this trend. (**Fig. 4.2; Table 10.2.2**). These results indicate an overall increasing influence of a source of unradiogenic Nd in the southern Emerald Basin over the last 18.7 Ma, with ε_{Nd} values converging with that of the modern CDW (i.e, deep waters from the South Atlantic, South Indian and Southeast Pacific) along the ACC from ~4 Ma (**Fig. 4.3**). Because seawater ε_{Nd} values in fossil fish teeth can be altered by a change in weathering/volcanic input, or sea water mixing (Scher and Martin, 2006), we looked into potential sources that could alter the values in our record. Sediments delivered to the southern Emerald basin are mainly sourced from the New Zealand´s South Island (Carter and McCave, 1997). New Zealand Phanerozoic granitoids and sedimentary rocks of the South Island are characterised by a wide range of Nd isotopic composition ($\varepsilon_{Nd(t)}$ = +2.7 to -11; Pickett and Wasserburg, 1989) and thus may constitute a potential source of unradiogenic Nd signature in our study area. However, the pronounced difference between the $\varepsilon_{Nd(t)}$ values of the fish teeth and the very radiogenic $\varepsilon_{Nd(t)}$ values of the two detrital sediment samples measured at Site 278 ($\varepsilon_{Nd(t)}$ = -4.31 ± 0.33 at 2.8 Ma, and -4.25 ± 0.33 at 12 Ma) indicates that detrital material was not the source of unradiogenic Nd signature of the fossil fish teeth (**Fig. 4.2; Table 10.2.2**). Our results are consistent with Oligocene-early Miocene fish teeth from Site 278, which have been shown to preserve predominantly sea water signature (Evangelinos et al., *in prep* [Chapter 3]). Moreover, the nearby Macquarie Ridge (relict volcanic mid-ocean ridge; Conway et al., 2012) located at the vicinity of Site 278, is characterised by basalts and peridotites with an ε_{Nd} value of +7 to +11 (Kamenetsky et al., 2000; Dijkstra et al., 2009). Hence, it is also excluded as a potential source of the unradiogenic signal.

The decreasing trend towards unradiogenic Nd values reconstructed at Site 278 is therefore best explained to reflect changes in the water mass mixing. Given its location, in the main pathway of the ACC close to the proto-polar front over the studied period, as well as its paleodepth (~3500 m), our data suggest that the overall decreasing trend is related to either: (1) an increasing contribution of unradiogenic Nd signature from North Atlantic deep waters (NADW) via the Tasmanian Gateway, or (2) gradually less influence of radiogenic Pacific deep waters (PDW). Available Nd isotope records from the south and equatorial Pacific document a gradual trend towards more radiogenic values from ~20 to 3-5 Ma, which opposes the increasing unradiogenic influence at Site 278 (Ling et al., 1999; van Flierdt et al., 2004; **Fig. 4.3**). The increase in radiogenic values in the Pacific Ocean has been attributed to the gradual strengthening of the Pacific circulation since 17 Ma likely related to the: 1) buildup of the East Antarctic ice sheet, and/or 2) Indonesian Gateway closure (van Flierdt et al., 2004), and/or 3) progressive restricted access of Atlantic deep waters to the central Pacific via the Panama gateway (Ling et al., 1999).

Based on the above, the increasing influence of unradiogenic Nd at Site 278 indicates a Southern Ocean source via the Tasmanian Gateway. Early Oligocene to present-day deep waters flowing along the proto-polar front in the South Atlantic and Indian Ocean exhibited unradiogenic ε_{Nd} values (-7.5 to -9) (Frank et al., 2002; Scher and Martin, 2004; Lambelet et al., 2018; Wright et al., 2018; Evangelinos et al., in press [Chapter 5]), resembling modern-CDWε_{Nd} signature (-6.8 to -10; Lambelet et al., 2018 and references therein; **Fig. 4.3**). However, the persistent offset between the South Atlantic/Indian deep waters and South Pacific deep waters across the Tasmanian Gateway between the Oligocene and early Miocene (30-19 Ma) has been attributed to reflect a weaker than present-day ACC (Evangelinos et al., *in prep*. [Chapter 3]; **Fig. 4.3**).

We posit that the overall decreasing trend at Site 278 likely reflects the increasing influence of NADW flowing across the Tasmanian Gateway into the southern Emerald Basin. The short-term changes in our record might be associated to different contribution of PDW and NADW in the study area. The first time our Nd isotope values converge with South Atlantic, South Indian and Southeastern Pacific deep waters along the main pathway of the ACC is at ~ 4 Ma (within the age uncertainties). This suggests a strengthening in NADW supply into the Southwest Pacific across the Tasmanian Gateway and homogenisation of the CDW Nd signature along the proto-polar front at that time. This supported by a decrease in Nd values reported from the central Pacific from 3-4 Ma to present-day, interpreted to reflect intensification of NADW in the Pacific (Burton et al., 1997; Ling et al., 1999; **Fig. 4.3**). We therefore infer that the increasing influence of NADW in the southern Emerald Basin from ~18.7 to ~4 Ma may indicate a gradual strengthening of the ACC, while the establishment modern homogenous CDW Nd isotopic composition in the Southern Ocean from ~4 Ma points to the full development of the modern strong deep-reaching ACC (**Fig. 4.6**).

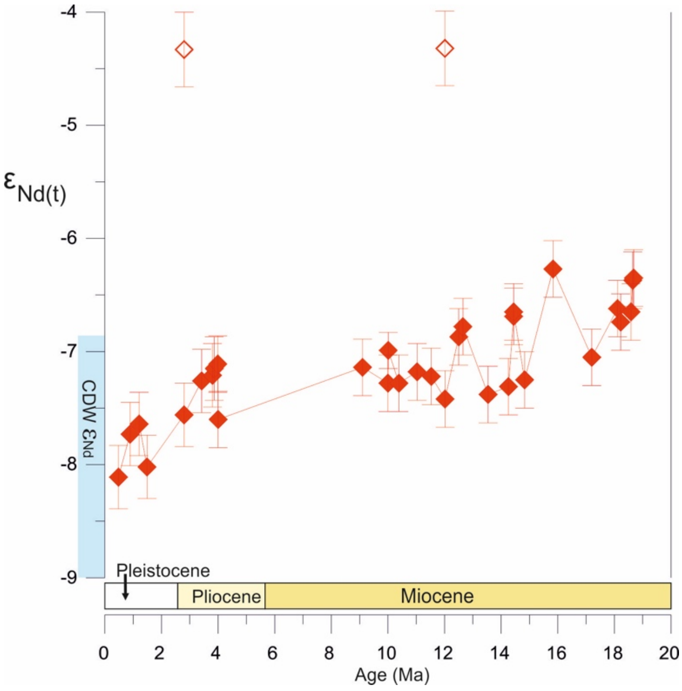

Figure 4.2. Neodymium isotopic composition ($\varepsilon_{Nd(t)}$) of fossil fish teeth (red filled diamonds) and bulk sediment $\varepsilon_{Nd(t)}$ values (red open diamond) at Site 278. Blue shaded ranges refer to present-day CDW ε_{Nd} endmember values in the Southern Ocean (Lambelet et al., 2018 and references therein).

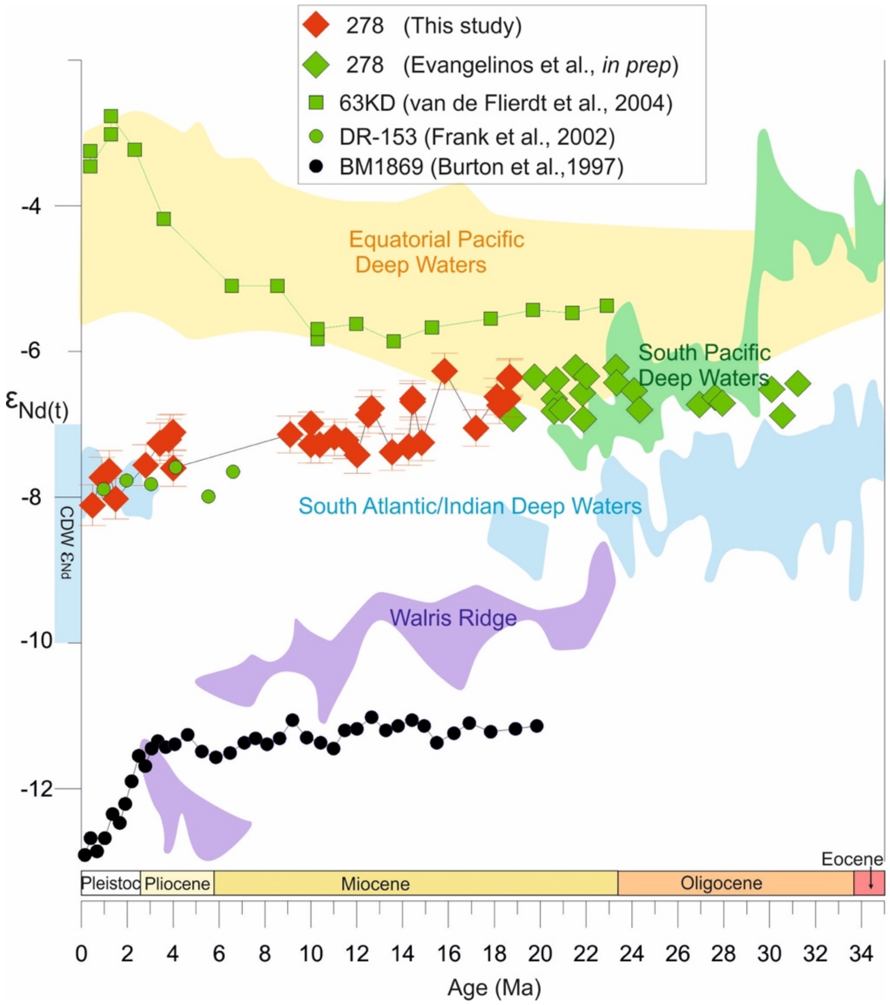

Figure 4.3: Comparison of fossil fish tooth ε_{Nd} records generated in this study from DSDP Site 278 (red filled diamonds) with those derived from Nd records in the Atlantic, Indian and Pacific Oceans. The Atlantic and Indian endmember in the Southern Ocean (blue shading) is based on sites ODP Site 689 (Maud Rise; Scher and Martin, 2004), Vulcan 5 (Frank et al., 2002), ODP Sites 748 and 744 (Kerguelen Plateau; Wright et al., 2018), MW8801 (Frank et al., 2002) and DSDP Site 269 (off Adélie Coast; Evangelinos et al., *in prep.* [Chapter 3]). Walvis Ridge endmember is based on Site 1262 and 1264 (Walvis Ridge; Via and Thomas, 2006, magenta shading). Site BM1969 (San Pablo seamount; black open dots; Burton et al., 1997). The South Pacific endmember (green shading) is based on ODP Site 1124 (Hikurangi Plateau; Scher et al., 2015) and ODP Site 1172 (East Tasmanian Plateau; Scher et al., 2015). Other South Pacific sites includes Site 278 (southern Emerald Basin; this study, red filed diamonds; and Evangelinos et al., *in prep.* [Chapter 3], green filed diamonds) and DR153 (Frank et al., 2002, green filled circles), 63KD (green filled rectangles; van de Flierdt et al., 2004). The Equatorial Pacific endmember is based on Sites D11-1 (Ling et al., 1999) and D137-01 (Nova Canton Trough; van de Flierdt et al., 2004).

4.3 The increasing deep ACC flow strength

To assess if the increasing contribution of NADW in the South Pacific sector of Southern Ocean is related to strengthening of the deep ACC flow, we reconstruct variations in the ACC flow speed through time by using changes in grain-size in sediments from Site 278. We focus on the mean $\overline{SS}$ size (10-63μm) of the terrigenous sediment fraction, which is a well-established proxy for estimating relative changes in the near-bottom flow speed in deep sea sediments (McCave et al., 1995). The $\overline{SS}$ records show an overall increasing trend superimposed by short-term fluctuations during the last 19 Ma. Similar to the Nd isotope record, the $\overline{SS}$ data record a prominent shift to higher values (from ~18.6 μm up to

~28.1 µm) from 4 Ma (**Fig. 4.4; Table 10.2.4**). Changes in $\overline{SS}$, fine-sand content (63-150 µm) and weight percentage of SS are positively correlated, which is a strong evidence of primarily current-controlled grain-size changes at Site 278 (Lamy et al., 2015; McCave et al., 2014; **Fig. 10.2.4**). The increasing trend in $\overline{SS}$ data therefore indicate strengthening of the bottom current flow speeds over the last 19 Ma, coinciding with the increasing influence of NADW in the southern Emerald Basin (**Fig. 4.6**). We therefore suggest that the gradual strengthening of the ACC would have reduced the amount of time that NADW mixed with PDW, allowing the preservation (less dilution) of NADW unradiogenic isotopic signature into the Southwest Pacific Ocean over the last 19 Ma.

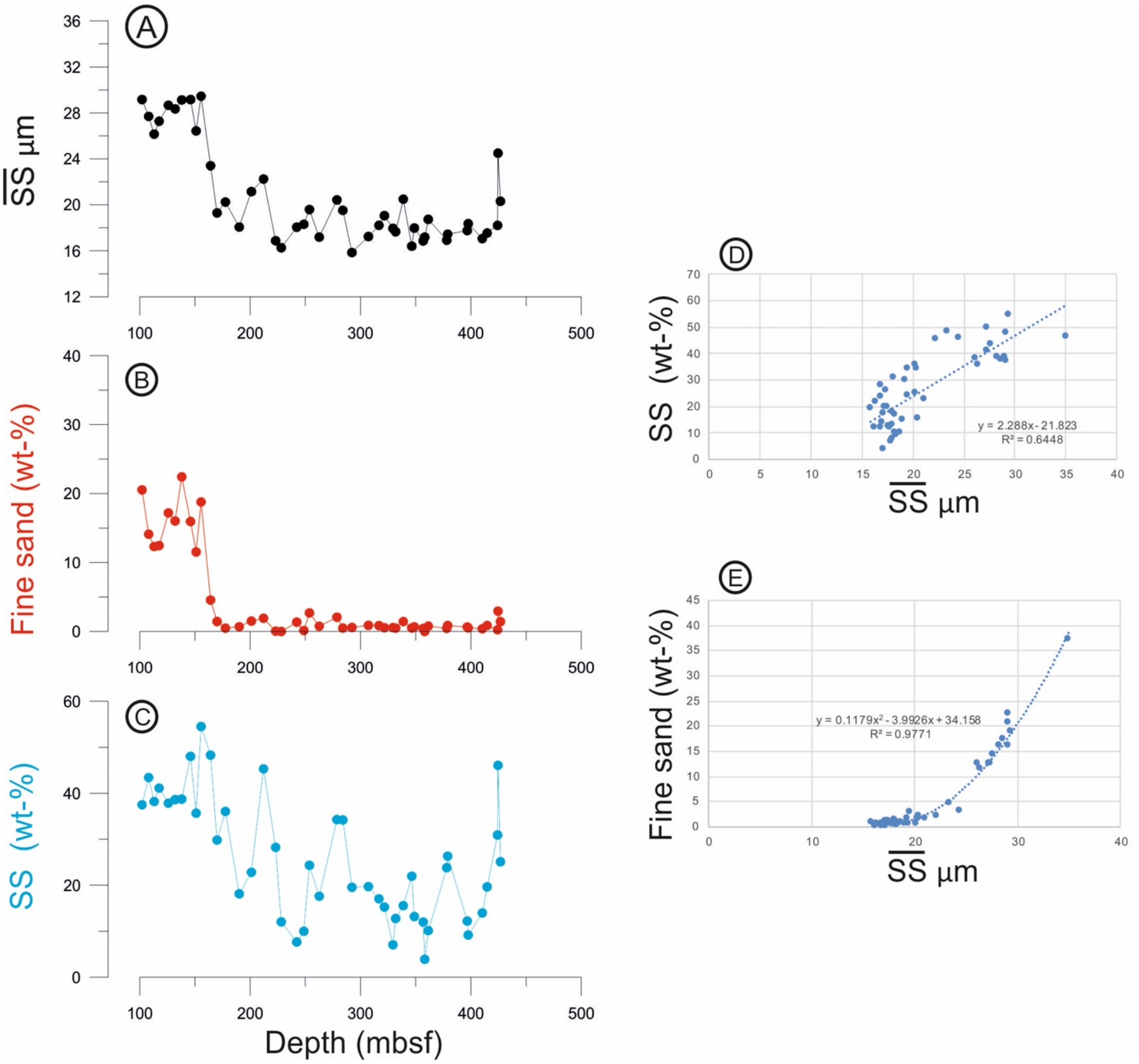

Figure 4.4: Down-core grain size data from Site 278. **A:** Mean sortable silt ($\overline{SS}$; black), **B:** fine-sand content (red), **C:** sortable silt (SS) percentage (blue). **D:** Linear relation between SS percentage and SS. **E:** Polynomial regression between fine sand.

4.4 The intensification of the upwelling activity

To assess changes in the wind-driven open water upwelling activity that today characterises the polar frontal zone area, and the response of the biological production to the associated nutrient supply, we used the biogenic silica (BSi) percentage in sediments from Site 278 as tracer of past primary productivity in the ACC pathway (e.g., Cortese et al., 2004). BSi values between 19 Ma and 4 Ma average ~27.9 % but at 4 Ma a sharp increase to average values almost doubling up to ~58 % is recorded (**Fig. 4.6**). Because changes in the BSi record are positively correlated to the diatom abundance, we argue that our proxy mirrors the siliceous primary productivity (**Fig. 4.5**) (Supplementary information [Chapter 10.2]). Moreover, the excellent preservation of siliceous biogenic components (Kennett et al., 1975) indicate that changes in the BSi record were not controlled by dissolution of biogenic material during deposition. This further supports that the BSi record at Site 278 is predominantly driven by changes in primary productivity. As the Macquarie Ridge was a prominent topographic obstacle in the ACC flow forcing minimum frontal migrations, the changes observed reflect predominantly changes in the intensification of the upwelling at the polar front (Kennet et al., 1977). The relative low sedimentation rates before the Pliocene suggests slugging upwelling (**Fig. 10.2.1**). After 4 Ma, the prominent increase in BSi % accompanied by higher sedimentation rates suggest the establishment of a strong upwelling.

The concurrent shift to permanent enhanced primary productivity/upwelling and stronger bottom currents flow speeds ($\overline{SS}$) from 4 Ma indicates a causal relationship between the enhanced productivity and the increase in bottom current flow speed (**Fig. 4.6**). We suggest that the establishment of a strong deep-reaching ACC would have brought more nutrient-rich waters to the surface leading to enhanced siliceous productivity. Our results are in line with opal data from sediment cores around the globe showing that from around 4.5 Ma the Southern Ocean became a main silica sink (widespread opal deposition) as a result of a large-scale oceanic circulation reorganisation causing the main dissolve silica pool to move from the Atlantic to the Pacific Ocean (Cortese et al., 2004 and references therein).

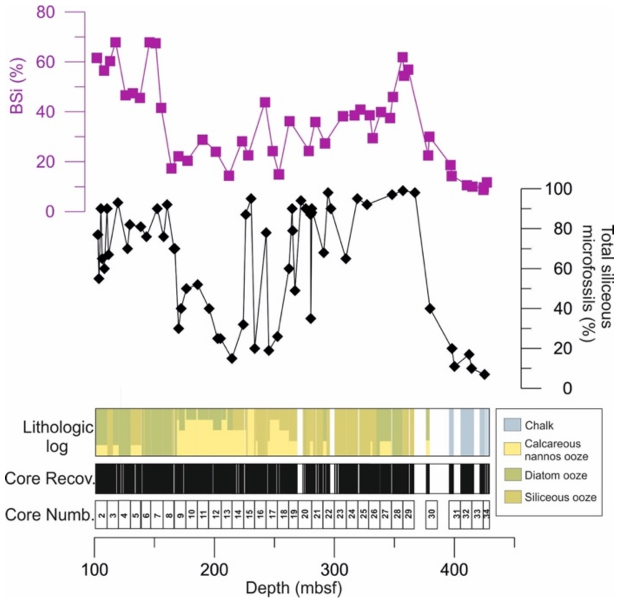

Figure 4.5: Comparison between Biogenic Silica (BSi) % (magenta filled diamonds) and total siliceous microfossils (%) (black filled diamonds) and lithology at Site 278 versus depth (meters below seafloor: mbsf).

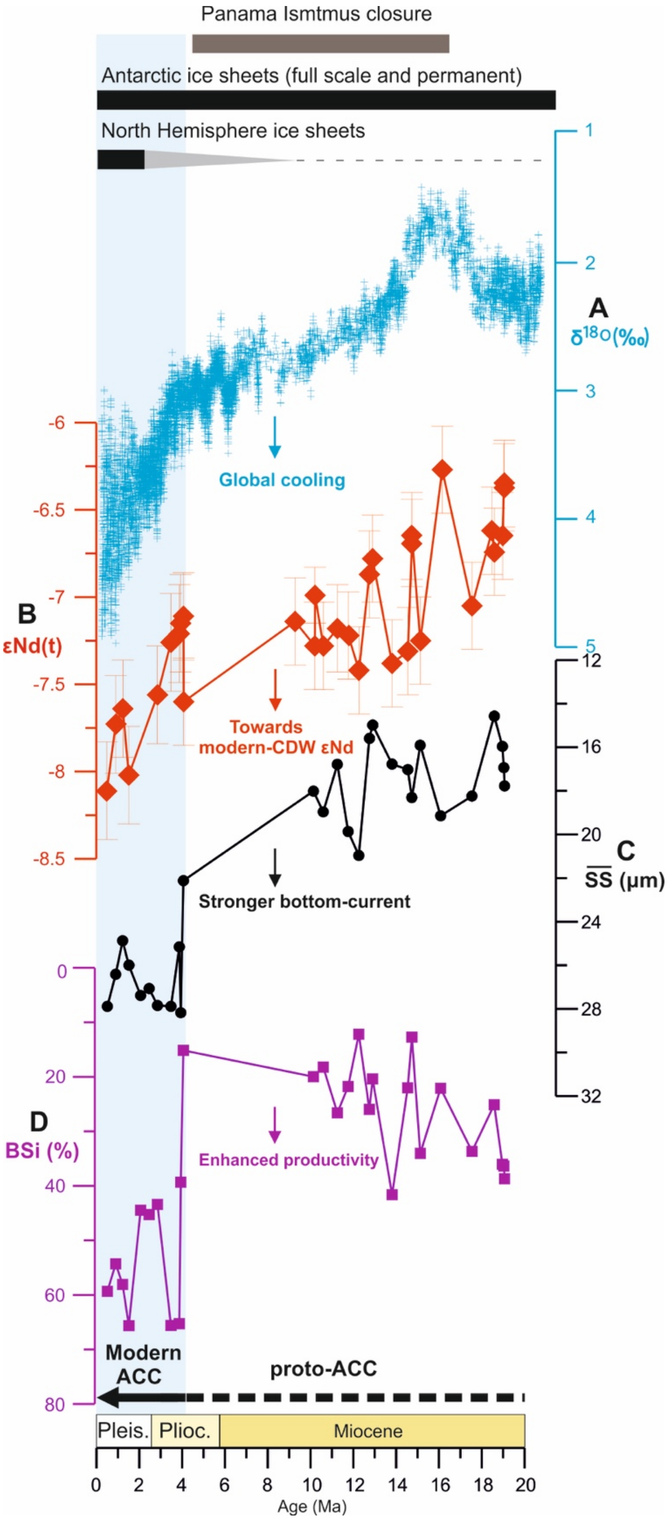

Figure 4.6: Evolution of the Antarctic Circumpolar Current over the last 20 Myr. **A:** global benthic δO_{18} records (Zachos et al., 2008; blue). **B:** Neodymium isotopic composition ($\varepsilon_{Nd(t)}$) of fossil fish teeth values at Site 278 (red filled diamonds). **C:** Mean sortable silt record from Site 278 ($\overline{SS}$; black dots). D: Biogenic silica record from Site 278 (BSi %; magenta squares).

4.5 Development of the modern ACC

Despite their low resolution, the trend recorded in our Nd isotopes and sortable silt records parallel the global benthic $\delta^{18}O$ isotope records. This suggests a strong link between the progressive strengthening of the ACC and the gradual homogenization of the composition of Southern Ocean deep water masses with the global climate cooling during the Neogene (**Fig. 4.6**). The global cooling increased the meridional atmospheric and surface ocean temperature differences, cooled surface waters and subsequently led to stronger westerlies and invigorated Southern Ocean geostrophic circulation (Cortese et al., 2004). This could have triggered the gradual strengthening of the ACC and the homogenization of the Southern Ocean water masses.

The permanent shift to stronger bottom current flow regime from 4 Ma onwards follows a major erosion in the southern Emerald Basin, evidenced by a hiatus in the sediments at Site 278. This hiatus is attributed to erosion by the ACC during the development of gateway through the Macquarie Ridge at 53.5°S (Schuur et al., 1998), which is today, the path for a major filament of the ACC entering the Emerald Basin (Carter and McCave 1997; Rintoul et al., 2014). Using the latest calibration of $\overline{SS}$ with North Atlantic current meter data (Thornalley et al., 2013), $\overline{SS}$ values of ~28.1 translate to speeds of ~17 cm/s, consistent with modern velocity measurements around the Macquarie Ridge (~20 cm/s) (Rintoul et al., 2014). Before the shift, the average $\overline{SS}$ is 18.6 µm, indicating a weaker ACC (reduced by ~76 % (~4cm/s)). Although bottom current measurements at the location of site are missing, our data indicate that modern bottom current strength in the southern Emerald Basin established after 4 Ma. This was followed by the convergence of the ε_{Nd} values at Site 278 with the south Atlantic and Indian deep waters in the main pathway of the ACC, pointing to the establishment of homogenous modern CDW Nd composition in the Southern Ocean (**Fig. 4.6**).

Our findings imply that the modern strong deep-reaching ACC flow established from 4 Ma ago, during the early Pliocene, even though further studies are needed to more precisely define the exact timing. This timing is long after the Tasmanian and Drake Gateway had opened and deepened, preventing the previously attributed direct link between the opening of these gateways and the onset of a modern-like ACC (Barker et al., 2007; Dalziel, 2014). The main known tectonic event that could be related to the establishment of the modern-like ACC at approximately 4 Ma is a major step in the closure of the Panama seaway around 4.6 Ma (Haug and Tiedemann, 1998). This tectonic event has been linked to the intensification of the Gulf Steam, strengthening of NADW flow, and the establishment of today´s general patterns of ocean circulation (Burton et al., 1997; Haug and Tiedemann, 1998). We therefore suggest that the modern deep ACC fully developed only when the modern distribution of oceans and land masses established. Our results show that the onset of the strong deep-reaching ACC precedes a major Southern Ocean cooling, pronounced sea ice extent around Antarctica and Antarctic ice-sheet expansion between 3.5 and 3 Ma (Escutia et al., 2009; Hillebrand and Cortese, 2006; McKay et al., 2012). Further studies are needed to explore the potential contribution of the establishment of the modern ACC around 4 Ma to the thermal isolation of the Antarctica, preconditioning the global cooling of the last 3 Ma and the stabilisation of the present-day icehouse climate state. Altogether, our results may reclaim the role of the Southern Ocean and ACC in the global climate evolution and development of the bipolar-glaciated world.

Chapter **5**

Late Oligocene-Miocene proto-Antarctic Circumpolar Current dynamics off the Wilkes Land margin

Based on: Evangelinos, D., Escutia, C., Etourneau, J., Hoem, F., Bijl, P., Boterblom, W., van de Flierdt, T., Valero, L., Flores, J. A., Rodriguez-Tovar, F. J., Jimenez-Espejo, F., Salabarnada, A., and López-Quirós. *Late Oligocene-Miocene proto-Antarctic Circumpolar Current dynamics off the Wilkes Land margin, East Antarctica*. Global and Planetary Change (in press)

ABSTRACT

At present, the Southern Ocean plays an important role in the global climate system and in modern Antarctic ice sheet dynamics. Past Southern Ocean configurations are however poorly understood. This information is yet important as it may provide important insights into the climate system and past ice-sheet behavior under warmer than present day climates. Here we study Southern Ocean dynamics during the Oligocene and Miocene when reconstructed atmospheric CO_2 concentrations were similar to those expected during this century. We reconstruct snapshots of late Oligocene to earliest Miocene (~24.2–23 Ma) paleoceanographic conditions in the East Antarctic Wilkes Land abyssal plain. For this, we combine marine sedimentological, geochemical (X-ray fluorescence, $TEX_{86,}$), palynological and isotopic (ε_{Nd}) records from ocean sediments recovered at Deep Sea Drilling Project (DSDP) Site 269. Overall, we find that sediments, delivered to the site by gravity flows and hemipelagic settling during glacial–interglacial cycles, were persistently reworked by a proto-Circumpolar Deep Water (CDW) with varying strengths that result from climatically controlled frontal system migrations. Just prior to 24 Ma, terrigenous input of predominantly fine-grained sediments deposited under weak proto-CDW intensities and poorly ventilated bottom conditions dominates. In comparison, 24 Ma marks the start of episodic events of enhanced proto-CDW current velocities, associated with coarse-grained deposits and better-ventilated bottom conditions. In particular, the dominance of P-cyst and low Calcium (Ca) in the sediments between ~24.2 Ma and 23.6 Ma indicate the presence of an active open ocean upwelling associated with high nutrient conditions. This is supported by TEX_{86}-derived sea surface temperature (SST) data pointing to cool ocean conditions. From ~23.6 to 23.2 Ma, our records reveal an enrichment of Ca in the sediments related to increased calcareous microfossil preservation, high amounts of G-cysts and increasing TEX_{86}-SSTs. This implies warmer water masses reaching the Antarctic margin as the polar front migrated southward. Together with the radiogenic Nd isotope data indicating modern-like CDW values, our records suggest a prominent poleward expansion of proto-CDW over our study site and reduced AABW formation during the latest Oligocene (i.e. ~23.2 Ma ago). Our findings support the notion of a fundamentally different Southern Ocean, with a weaker proto-ACC than present during the late Oligocene and the earliest Miocene.

5.1 Introduction

The Antarctic Circumpolar Current (ACC) is the Earth´s strongest ocean current (137-162 sverdrup (Sv)) flowing eastward along a 20,000 km pathway around Antarctica (Rintoul et al., 2001; Sokolov and Rintoul, 2009). Owing to the absence of land barriers, the ACC is the only ocean current connecting the Pacific, the Atlantic and the Indian oceans, and consequently influences the entire global ocean circulation (Rintoul, 2018). The ACC pathway is constrained by ocean gateways (i.e. Drake Passage) and the bathymetry of the Southern Ocean. Its strength is mainly controlled by the seafloor topography (Olbers et al., 2004), and the position and intensity of the Southern Westerly Winds (SWW) (Thompson and Solomon, 2002, Aoki et al., 2005; Toggweiler and Russell, 2008; Rignot et al., 2019). At present, the vigorous zonal flow of the ACC prevents the intrusion of warm waters from lower latitudes to penetrate the Antarctic margin and, together with sea-ice presence, contributes to maintain the cold and arid glacial state of Antarctica (e.g., Olbers et al., 2004; Ferrari et al., 2014). The deep layers of the

ACC are occupied by a relatively warm and saline water mass, the Circumpolar Deep Water (CDW) (Orsi et al., 1995). Recently, an increasing incursion of CDW into the continental margins has been shown to favor melting and thinning of the Antarctic ice shelves through basal melting (Pritchard et al., 2012; Liu et al., 2015; Nakayama et al., 2018; Rignot et al., 2019). Despite its importance for the Antarctic and the global climate, little is known about the onset and past dynamics of the ACC, as well as its linkages with the Antarctic Ice sheet (AIS) dynamics. This knowledge is especially relevant from past times when climatic conditions were close to the modern and future ones in terms of warmth and atmospheric CO_2 concentration.

One of these times was the late Oligocene (i.e., ~24.5 Ma), when the reconstructed atmospheric CO_2 concentrations dropped below 600 ppm (600-400 ppm) (Zhang et al., 2013). These values are similar to the modern and projected atmospheric CO_2 concentrations within this century (IPCC, 2013; Meredith et al., 2019). Foster and Rohling (2013) argued that the global ice volume is supposedly less sensitive to CO_2 fluctuations between 600 to 400 ppm. In contrast, benthic foraminiferal oxygen isotope records (e.g., Liebrand et al., 2017) suggest highly fluctuating ice volumes at this time. The drop in CO_2 concentration in the late Oligocene (~24.5 Ma) likely led to climate cooling and ice sheet advance across the Antarctic continental shelves, connecting large areas of marine-based ice with the ocean (Pekar and Christie-Blick, 2008; Levy et al., 2019). Ice-proximal geological records (Barrett, 1975; Naish et al., 2008; Kulhanek et al., 2019; Levy et al., 2019) and seismic data (Anderson and Bartek, 1992; Sorlien et al., 2007) provide direct evidence for a major expansion of marine ice sheets across the Ross Sea continental shelf between 24.5 and 24 Ma. However, the oceanographic and climatic conditions leading to the maximum growth of the ice sheet remain poorly known.

The global deep-sea benthic $\delta^{18}O$ records maximum expansion of the AIS between 23.2 and 23 Ma (Zachos et al., 2001; Beddow et al., 2016; Liebrand et al., 2017). However, deep-sea benthic $\delta^{18}O$ records reflect a combination of ice-volume and bottom water temperature and their location (low to mid-latitude versus Antarctic proximal records) determines the different water masses influencing the record and thus masking information from the Antarctic glaciation (e.g., Pekar et al., 2006). Thus, most of the ice volume estimates based on deep-sea benthic $\delta^{18}O$ records should be taken with caution. Variations in the Southern Ocean circulation and ocean heat transport across the Antarctic continental margin driven by obliquity forcing have been suggested to play a significant role on ice sheet sensitivity during the late Oligocene and Miocene (Salabarnada et al., 2018; Sangiorgi et al., 2018; Levy et al., 2019). This is especially true in times when ice sheets extended into the marine environments (e.g., Jovane et al., 2019; Levy et al., 2019). Sedimentary archives strategically located along latitudinal transects across the main ACC pathway and at the vicinity of the Antarctic ice sheet are however needed to provide direct links between changes in the ocean circulation and ice sheet dynamics (Escutia et al., 2019).

Sedimentary records across the Tasman Gateway (Pfuhl and McCave, 2005) and from the South Pacific (Lyle et al., 2007) document a shift to higher velocity bottom currents between 25-23 Ma. This shift has been interpreted to result from the onset of a strong, deep-reaching ACC during the late Oligocene. However, recent comparisons between the dinocysts preserved in sediments from the Integrated Ocean Drilling Program (IODP) Site U1356 off the East Antarctic Wilkes Land margin and strata from Tasmania and south of New Zealand indicate a weaker than present day ACC, at least until the middle Miocene (Bijl et al., 2018b). Oligocene and Miocene paleoceanographic reconstructions off the Wilkes Land margin based on sedimentological data (Salabarnada et al., 2018), dinoflagellate biogeography (Bijl et al., 2018a, b; Sangiorgi et al, 2018) and temperature reconstructions (Hartman et al., 2018) suggest a different oceanographic configuration from that of today in this part of the Southern Ocean. These authors report from multiple lines of evidence warm-temperate sea surface temperatures (SST), limited sea ice expansion and reduced formation of Antarctic bottom waters, linked to a weaker oceanic frontal system, which allowed the intrusion of warmer waters from low latitudes towards the Antarctic margin. These data are consistent with Oligocene numerical simulations, which show weaker global overturning and gyre circulation because of weaker SWW (Herold et al, 2012). In addition, modeling results indicate a limited throughflow of the ACC due to the Australasian paleogeography during the Oligocene (Hill et al., 2013).

To decipher the characteristics and dynamics of the ACC and CDW that can then be related to East Antarctic Ice Sheet (EAIS) behavior off Wilkes-Adélie Land during the late Oligocene-Miocene, we report new data from a sediment record recovered by the Deep Sea Drilling Project (DSDP) Leg 28 at Site 269. This site was drilled on the Wilkes Land abyssal plain (Hayes et al., 1975) along the main pathway of the ACC. We focus on the study of the late Oligocene to earliest Miocene (~24.2-23 Ma) record. This record is partly compromised by debris flows at IODP Site U1356, located on the continental rise (Escutia et al., 2011), ~280 km landward from Site 269, and is missing in most sedimentary archives around the rest of Antarctica. Because of discontinuous drilling at Site 269, we investigate snapshots of the late Oligocene and early Miocene. Sediment, palynological, geochemical and isotopic data are used to describe and characterise the main changes in sedimentation related to proto-CDW dynamics. The findings at DSDP Site 269 are then compared to results from IODP Site U1356 (Escutia et al., 2011, 2014; Salabarnada et al., 2018) (**Fig. 5.1**). This latitudinal comparison provides important insights into changes in proto-ACC dynamics that can in turn be related to the evolution of the ice sheet in this region of the East Antarctic margin.

5.2 Site description and oceanographic setting

DSDP Leg 28 Site 269 is located on the abyssal plain off the Wilkes Land (61°40.57´S, 140°04.21´E, 4282 m water depth) (Hayes et al., 1975) (**Fig. 5.1**). Two holes were discontinuously drilled at this site. Our study focuses on Hole 269A, specifically the interval between 655 to 956 meters below sea floor (mbsf) (cores 7R to 13R). Recovered sediments were interpreted shipboard to be mostly turbidites, but evidence of winnowing by bottom currents was also documented (Hayes et al., 1975). Facies were identified within the frame of the DSDP Leg 28 expedition mainly based on the lithology, bioturbation and bed contacts (Piper and Brisco, 1975).

At present, Site 269 is located between the modern southern branch of the Polar Front (PF) and the northern branch of the Southern ACC Front (SACCF). In comparison, Site U1356 (63°18.6138´S, 135°59.9376´E, 3992 m water depth) lies south of the SACCF, near the Antarctic Divergence (Sokolov and Rintoul, 2002) (**Fig. 5.1**). Both sites are today covered by the Adélie Land Bottom Water (ALBW) (Rintoul, 1998), which forms in winter time along the Adélie-Wilkes Land Coast (Orsi et al., 1995). Our reconstruction of the paleoposition of Site 269 and Site U1356 is adapted from G-plates geodynamic modeling (http://www.gplates.org; Müller et al., 2018), and uses the plate circuit of Seton et al. (2012). It shows that Site 269 has migrated south since the Oligocene but remained located at

~60°S between the late Oligocene-early Miocene, while the paleolatitude of Site U1356 was around 62°S. Geological evidence derived from the analysis of microfossil assemblages from sedimentary records around Antarctica suggest that the proto-Polar Front (PF) was situated close to 60°S between the late Oligocene-early Miocene (Nelson and Cooke, 2001; Cooke et al., 2002).

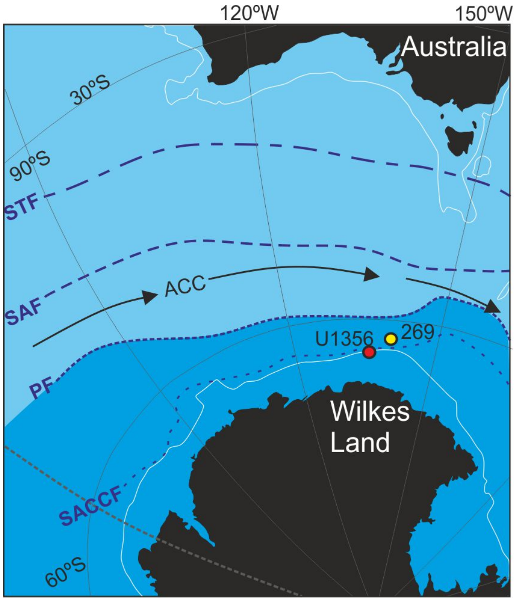

Figure 5.1: Oceanic frontal system between Antarctica and Australia**.** Dark Blue dashed lines schematically represent oceanic fronts today (Sokolov and Rintoul, 2009). Polar water south of the PF are shaded in darker blue. Map derived from Gplates software (Müller et al., 2018). Site 269 is marked with yellow symbol and Site U1356 is marked with red symbol. White lines indicate the continental lithosphere boundary. Black arrows show the pathway of the ACC today (Rintoul et al., 2001). STF: Subtropical front, SAF: Subantarctic front, PF: Polar Front, SACCF: Southern ACC front, ACC: Antarctic Circumpolar Current.

5.3 Revising the initial age model

We established a new age model based on the integration of new magnetostratigraphic data, dinocyst and calcareous nannofossil biostratigraphy, calibrated using the GTS 2012 Astronomic Age Model (Gradstein et al., 2012) (**Figs. 5.2; 10.3.1; 10.3.2** and **Tables 10.3.1; 10.3.2**). The presence of *Operculodinium janduchenei* in the sediment between ± 753-955 (mbsf) (Cores 9R 3W to 13R) is assigned to the lower Southern Ocean Dinocyst Zone (SODZ) SODZ8 (Bijl et al., 2018a). This suggests that the bottom of Hole 269A cannot be older than late Oligocene (24.2 Ma). Moreover, the last occurrence of *Operculodinium janduchenei* between 753.27-752.32 mbsf (9R 3W 125-129 cm - 9R 3W 30-33 cm) marks the boundary between dinocysts zones SODZ8 and SODZ9. This boundary is calibrated to 23.6 Ma at U1356 (Bijl et al., 2018a) and is correlated to the reversed polarity found at the bottom of chron C6C (C6Cr). This is corroborated by the presence of *Cyclicargolithus abisectus* at 752.9 mbsf indicating that this interval corresponds to the zone NP 25 (Martini, 1971), which implies a latest Oligocene age. The latter however, must be taken with caution given the scarce amount of calcareous nannofossils, as well as the absence of other conventional markers. The presence of *Impagidinium aculeatum* at 658.82 mbsf (7R 4W 30-34 cm) is assigned to the mid- of SODZ10 or older (~23 Ma) (Bijl et al., 2018a). This is correlated with the normal polarity of the geomagnetic chron C6n.2n suggesting also an age of 23 Ma. In addition, based on the biostratigraphic datums we assigned the paleomagnetic reversal at ~ 857.5 mbsf to chron C7n.1n (24 Ma) and at ~703 mbsf to chron C6n.3n (23.23 Ma). Our updated age model suggests an age range for the studied interval from ~24.2 to ~23 Ma (**Fig. 5.2**). Initial shipboard data had dated this interval to be of middle Eocene to early Oligocene age (Hayes et al., 1975). We acknowledge that the age model still has large uncertainties due to discontinuous coring, incomplete recovery and the low preservation of microfossils. However, the integration of the well-established Southern Ocean Oligocene-Miocene dinocyst stratigraphy, which was developed at the nearby Site U1356 along with the good correspondence with the magnetostratigraphic data allow us to be relatively confident in our age model.

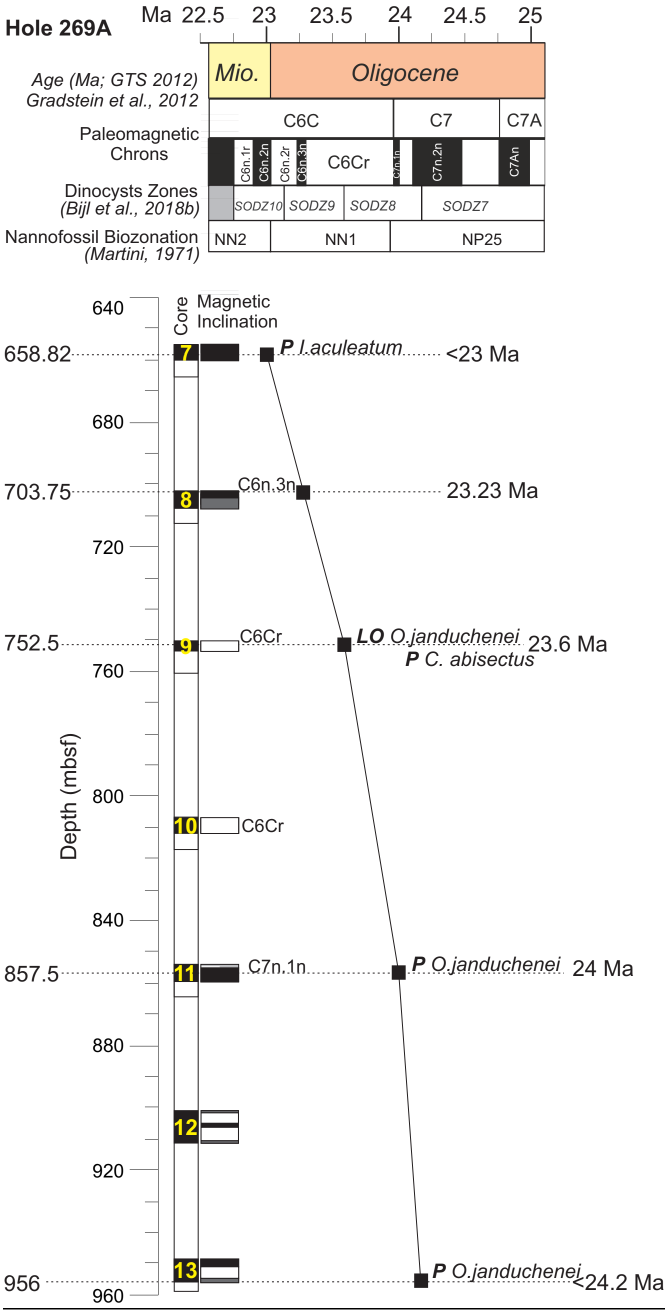

Figure 5.2: Age model for Deep Sea Drilling Project Hole 269A based on magnetostratigraphy constrained by dinocyst and calcareous nannofossil biostratigraphy. **LO:** Last Occurrence. **P:** Presence. Age model has been calibrated to GTS2012 of Gradstein et al. (2012).

5.4 Methods

5.4.1 Facies analysis

A detailed facies analysis was performed on sediment from Hole 269A to determine depositional processes and aid paleoenvironmental reconstructions. We conducted a detailed description of the cores using standard sedimentological techniques (i.e., lithological characterization, contacts, sedimentary structures and textures) in order to produce the lithostratigraphic log in Figure 3 and Supplementary Figure 3. Visual descriptions were aided by high-resolution digital images obtained on the archive halves using a Nikon 60mm camera lens mounted on a custom-built line scanner at the Coast Gulf Repository (CGR), in College Station (Texas, USA). High-resolution images were also used for ichnological analysis (i.e., type and degree of bioturbation) performed to characterise the paleoenvironmental conditions prevailing in the seafloor. Ichnological analysis was based on the digital treatment of the high-resolution images following previous researches (Dorador and Rodríguez-Tovar, 2014, 2018; Dorador et al., 2014a, 2014b; Rodríguez-Tovar and Dorador, 2015). It was conducted at the Department of Stratigraphy and Paleontology at the University of Granada (Spain). Further characterisation of the biogenic and terrigenous material within each of the lithofacies defined was achieved by: 1) Bulk grain-size analyses that was performed at EPOC (Environnements et Paléoenvironnements Océaniques et Continentaux) (Bordeaux, France). In total 44 sediment samples (dried overnight in an oven at 40ºC) were measured in a laser microgranulometer Malvern mastersizer hydro 2000G with automatic samples (0.020 to 2000 µm). 2) Wet sieving and High-Resolution Scanning Electron Microscope (HR-SEM) analysis conducted at the Instituto Andaluz de Ciencias de la Tierra, (CSIC, Spain) and at the Centro de Instrumentación Científica (University of Granada, Spain), respectively. Moreover, continuous measurements of magnetic susceptibility (MS) were taken from the archive half sections of the core. For this, the core sections were left out of the refrigerator overnight to acquire a room temperature before scanning. MS measurements were taken every 2 cm using a Bartington MS2 mounted in a Geotek Multi-Sensor Core Logger (MSCL) at the GCR. Core void measurements were removed from the data set.

5.4.2 Major and Trace Element content

The elemental composition of sediments derived from X-Ray Fluorescence (XRF) core scanners has been used as an indicator of past climate changes in proximal and distal records from the Antarctic margin. For example, titanium (Ti), aluminium (Al), iron (Fe) versus calcium (Ca) have been interpreted to show changes between terrigenous and biogenic $CaCO_3$ deposition (e.g., Grützner et al., 2005; Hepp et al., 2006; Escutia et al., 2009; Salabarnada et al., 2018). In addition, zirconium-based proxies (e.g. Zr/Ti ratios) have previously been used as an indicator of semiquantitative assessment of bottom current velocities in Oligocene sediments from Site U1356 off Wilkes Land (Salabarnada et al., 2018). This is based on the relative enrichment of heavy minerals such as zircon over less dense minerals (e.g., aluminosilicates) that result from hydrodynamic winnowing and sorting of heavy minerals (e.g., Bahr et al., 2014). Bromine (Br)/Ti ratios have been used as indicator of organic matter in the sediments (Bahr et al., 2014; Salabarnada et al., 2018). The Br content is associated to total organic carbon (TOC) concentration in the sediments (Seki et al., 2019), and TOC is mainly related to changes in productivity (organic carbon flux in the sediments) and/or changes in the redox state of the sediment (e.g., Jimenez-Espejo et al., 2007). Br is not biased by lithological changes (i.e. mudstones/sandstones), but is affected by organic matter degradation (Bahr et al, 2014).

XRF core scanning measurements were conducted at 10kV and 30 kV on the archive split sections from Cores 7R to 13R using an Avaatech XRF core scanner at the GCR. The surface of core sections was cleaned carefully for any gypsum and salts, which might have precipitated and then adjusted manually to form an even surface. A 4µm thick ultralene plastic film was used to cover the core surface in order to avoid contamination while scanning. Due to the presence of cracks in many core sections, spot measurements were taken rather than scan the section continuously.

To decipher the different processes influencing the geochemical composition of the sediment, we conducted a Principle Component Analysis (PCA). We used the PAST version 2.10 software package (Hammer et al., 2001) following the data pre-treatment in Bahr et al. (2014), including normalization of the data to reduce the signal artefacts related to changes in lithology. For the PCA, we only selected and show elements with a robust signal quality, i.e., Al, Si, K, Ca, Ti, Fe, Ba, Br, Rb, Sr, and Zr. In this study we report on the following elements and elemental ratios Ca, Ti, Zr/Ti ratios and Br/Ti ratios.

5.4.3 Neodymium isotopes

Neodymium (Nd) is delivered to the ocean through the weathering of continental crust, and by exchange with sediment on the continental margin (known as boundary exchange; e.g., Frank et al., 2002, Wilson et al., 2013). Consequently, water masses forming in different geological basins will be isotopically distinct. Because of its short oceanic residence time in the ocean (~400-1,000 yr) relative to oceanic mixing (1,500 yr) (Tachikawa et al., 2003) records of Nd isotopes allow us to reconstruct past ocean circulation and changes in the weathering inputs. Neodymium isotopes in fossil fish debris are a robust tool to reconstruct changes in ocean circulation by identifying distinct water masses (e.g. Goldstein and Hemming, 2003; Martin and Scher, 2004; van de Flierdt et al., 2016). Neodymium is incorporated into the fish teeth during the fossilization processes at the sediment-water interface and reflects the isotopic composition of seawater in contact with the seafloor at the time of fish tooth deposition, remineralisation and burial (Shaw and Wasserburg, 1985). Neodymium isotope ratios in fossil fish teeth are considered to be resistant to changes in post-burial alteration (Martin and Scher, 2004; Scher et al., 2011). Neodymium isotope ratios ($^{143}Nd/^{144}Nd$) are expressed as ε_{Nd}, which denotes the deviation of a measured $^{143}Nd/^{144}Nd$ ratio from the chondritic uniform reservoir in parts per 10,000 (DePaolo and Wasserburg, 1976; Jacobsen and Wasserburg, 1980).

Fish debris was handpicked from the >63 µm sediment fractions that were prepared by wet sieving. Four samples were prepared for fish-tooth and bone debris Nd isotope analyses in the MAGIC laboratories at Imperial College London following the sample preparation detailed in supplementary materials. In addition, to account for a potential influence of the detrital sediment towards the Nd isotope composition of pore waters or overlying bottom water, we also measured the Nd isotope compositions of two detrital sediment samples. Sample preparation for these analyses was conducted in the MAGIC laboratories at Imperial College London as detailed in supplementary materials. The detrital samples were processed using the same ion chromatography as the fish debris.

Neodymium isotope ratios for fish debris and detrital sediment samples were determined on a Nu Plasma multiple collector inductively coupled plasma mass spectrometer (MC-ICP-MS) at Imperial College London, operated in static mode. Instrumental mass bias was corrected using the $^{146}Nd/^{144}Nd$ ratio of 0.7219. A JNdi-1 isotope standard was run after every sample and all reported $^{143}Nd/^{144}Nd$ ratios are corrected to a JNd_i value of 0.512115 (Tanaka et al., 2000) using bracketing standards. External reproducibility was monitored using the JNd_i standards, and accuracy was confirmed by measuring USGS BCR-2 rock standards, which yielded average $^{143}Nd/^{144}Nd$ ratios in agreement with the published BCR-2 $^{143}Nd/^{144}Nd$ ratio of 0.512638±0.000015 (Weis et al., 2006).

To correct for the decay of ^{147}Sm to ^{144}Nd within the fish teeth over time we used Sm and Nd concentrations obtained from two samples, which were in good agreement with $^{147}Sm/^{144}Nd$ ratios reported from fossil fish teeth in other marine sedimentary records (e.g., Martin and Scher, 2006; Moiroud et al., 2013; Huck et al., 2017; Wright et al., 2018). When no values available, an average of 0.1286 from the measured samples was applied to calculate $\varepsilon_{Nd(t)}$ values. The $^{147}Sm/^{144}Nd$ ratios yielded Nd isotope corrections of 0.19 to 0.21 ε_{Nd} units; (t) denotes samples have been corrected for in situ decay of ^{147}Sm.

5.4.4 TEX_{86}

The TetraEtherindeX of 86 carbon atoms (TEX_{86}) is a proxy for sea surface temperature (SST). The TEX_{86} paleothermometer employs the temperature-dependent relative abundance of a suite of thaumarchaeotal membrane lipids; glycerol dibiphytanyl glycerol tetraethers (GDGTs) (Schouten et al., 2002, 2013). In short, this method involves lipid extraction from powdered and freeze-dried sediments using accelerated solvent extraction. Lipid extracts were separated into an apolar, ketone and polar fraction by Al_2O_3 column chromatography using hexane:DCM (9:1), hexane:DCM (1:1) and DCM:MeOH (1:1) as respective eluents. 99 ng of a synthetic C_{46} (mass-to-charge ratio, m/z = 744) GDGT standard was added to the polar fraction, which then was dissolved in hexane:isopropanol (99:1, v/v) to a concentration of ~3 mg ml^{-1} and filtered over a 0.45-µm polytetrafluoroethylene filter. The dissolved polar fractions were injected and analysed by high-performance liquid chromatography–mass spectrometry (HPLC–MS), using the double column technique for improved separation of co-eluding compounds (Hopmans et al., 2015). GDGT peaks in the HPLC chromatograms were integrated using ChemStation software. Several calibrations have been proposed to translate TEX_{86} into SST. We employ the TEX_{86} linear calibration ($SST = 81.5 \times TEX_{86} - 26.6$ with a calibration error of ± 5.2 ∘C) by Kim et al. (2010), to enable adequate comparison to existing data, and following elaborate discussions in Hartman et al. (2018). We provide the GDGT peak areas and R-script in the online supplementary materials.

Before interpreting the TEX_{86} results into SST reconstructions samples with overprint, which may affect the reliability of the SST proxy, must be discarded. Terrestrial GDGT input has been reconstructed using the branched and isoprenoid tetraether (BIT) index (Hopmans et al., 2004) as a proxy. Samples with a high BIT index may be biased by soil- and river-derived GDGTs (Hopmans et al., 2004), although the high BIT index may also stem from a decrease in marine crenarchaeol production, as the BIT index is a closed sum between terrestrial GDGTs and the exclusively marine crenachaeol. Several indices for a potential biased source of GDGTs was investigated and outliers discarded. Namely, methane index (Zhang et al., 2011), flagging overprint by sedimentary methanogenic activity, GDGT-2/GDGT-3 ratio (Taylor et al., 2013), potentially signalling overprint by archaeal communities dwelling deeper into the water column, GDGT-0/Crenarchaeol ratio (Blaga et al., 2009; Damsté et al., 2009; Taylor et al., 2013), flagging overprint by in situ production of isoprenoidal GDGTs in lakes and rivers, and ring index (Zhang et al., 2016), which assesses an overall pelagic character for the different GDGTs within the TEX86 index. High-latitude TEX_{86} SST reconstructions might be skewed towards summer temperatures (Ho et al., 2014; Schouten et al., 2013; Hartman et al., 2018) and potentially incorporate a subsurface signal (0-200 mbsl) (Hernández-Sánchez et al., 2014; Ho and Leapple, 2015). However, there is a general agreement that TEX_{86} captures the relative SST trend (Richey and Tierney, 2016).

5.4.5 Palynology – dinoflagellate cyst paleoenvironment reconstruction

In total 19 sediment samples (~15g) were processed for palynology and counted at Utrecht University using standard palynological processing and analytical procedures previously described by Bijl et al. (2013, 2018b). Modern dinoflagellate (unicellular planktonic protists) distribution are sensitive to small changes in nutrient availability, SST, salinity, bottom water oxygen, primary productivity and sea-ice cover (Dale, 1996; Prebble et al., 2013; Zonneveld et al., 2013). Approximately 13-16% produce an organic-walled cyst, dinocysts, that can preserve in the fossil record (Head, 1996). Assuming the habitat affinities and feeding strategies of most dinoflagellates can be extrapolated to the fossil assemblages, we can utilize ‘deep-time’ dinocysts assemblages as a paleoceanographic proxy (Bijl et al., 2013; Crouch et al., 2014; Sluijs et al., 2005). In the Southern Ocean, protoperidinioid (P) cysts originate from hetrotrophic dinoflagellates and proliferate under increased nutrient conditions, while gonyaulacoid (G) cysts originate from autotrophic or mixotrophix dinoflagellates and reflect oligotrophic conditions (Esper and Zonneveld, 2002). Thus, the relative P/G-cyst ratio can indicate glacial/interglacial variability and ocean frontal movement migrations. Today, the surface sediments at Site 269A consists almost exclusively of P-cysts, specifically the sea-ice affiliated species Selenopemphix antarctica (Prebble et al., 2013).

5.5 Results

5.5.1. Sedimentation at Hole 269A

Sediment from Hole 269A from 655 to 956 mbsf consists of alternations between bioturbated and laminated intervals of terrigenous-rich sediment (**Figs. 5.3a, 5.3b, 5.4 and 10.3.3**). Textural analyses show a low clay content (4 to 20%), a high silt fraction (40 to 80%) and a sand content between <5 and 60 % (**Fig. 10.3.3**). Microfossil preservation is generally low throughout the study interval. Higher preservation of calcareous microfossils was found in the carbonate-cemented beds (**Figs. 5.3a and 5.5**) and within the sediments between 753.5-702.5 mbsf (~23.6 to 23.23 Ma) (**Fig. 10.3.4**). The higher calcareous carbonate preservation is depicted in Ca peaks in Fig. 3d. Higher preservation of diatoms is also observed in the carbonate-cemented facies (**Fig. 5.5**) and in Core 7 (660-655.5 mbsf) (~23 Ma).

The main observed differences within the bioturbated and laminated intervals are the variations in the silt/sand content, ichnological features, including amount of bioturbation, and carbonate content (carbonate-cemented intervals). Based on this, we differentiate the following sedimentary facies (**Figs. 5.3c and 5.4**): (1) Bioturbated silty claystones to clayey siltstones (Bioturbated mudstone; F1a), bioturbated siltstones to sandy siltstones (F2a), and bioturbated carbonate-cemented facies (F3a). (2) Laminated silty claystones to clayey siltstones (Laminated mudstone; F1b), laminated siltstones to sandy siltstones (F2b), and laminated carbonate-cemented facies (F3b).

Bioturbated facies (F1a, F2a and F3a; **Figs. 5.3c, 5.4 and 5.5**) generally exhibit a structureless and/or mottled texture. Bioturbation varies from low, dominated by *Chondrites* and *Phycosiphon,* to high with abundant and diverse trace fossils, including *Planolites*, *Thalassinoides, Nereites, Zoophycos* and likely *Scolicia* (**Fig. 5.4**). The occurrence of coarser bioturbated facies (F2a) becomes more frequent up-section starting at 858 mbsf, but is also present in the lowermost part of the site at ~ 955.3 mbsf (**Fig. 5.3c**).

Laminated facies (F1b, F2b and F3b; **Figs. 5.3c, 5.4 and 5.5**) are characterised by faint and/or distinct sub-mm to mm silty-sandy laminations. Laminated intervals can contain a single or a group of laminae with various sedimentary structures, including continuous and discontinuous planar, wavy, lenticular, ripple and cross laminations (e.g., **Fig. 5.4a**). Small soft-sedimentary deformation structures such as convoluted, ball and pillow structures are often observed within the laminations (**Fig. 5.4k**). Scarce traces of *Chondrites* may be present.

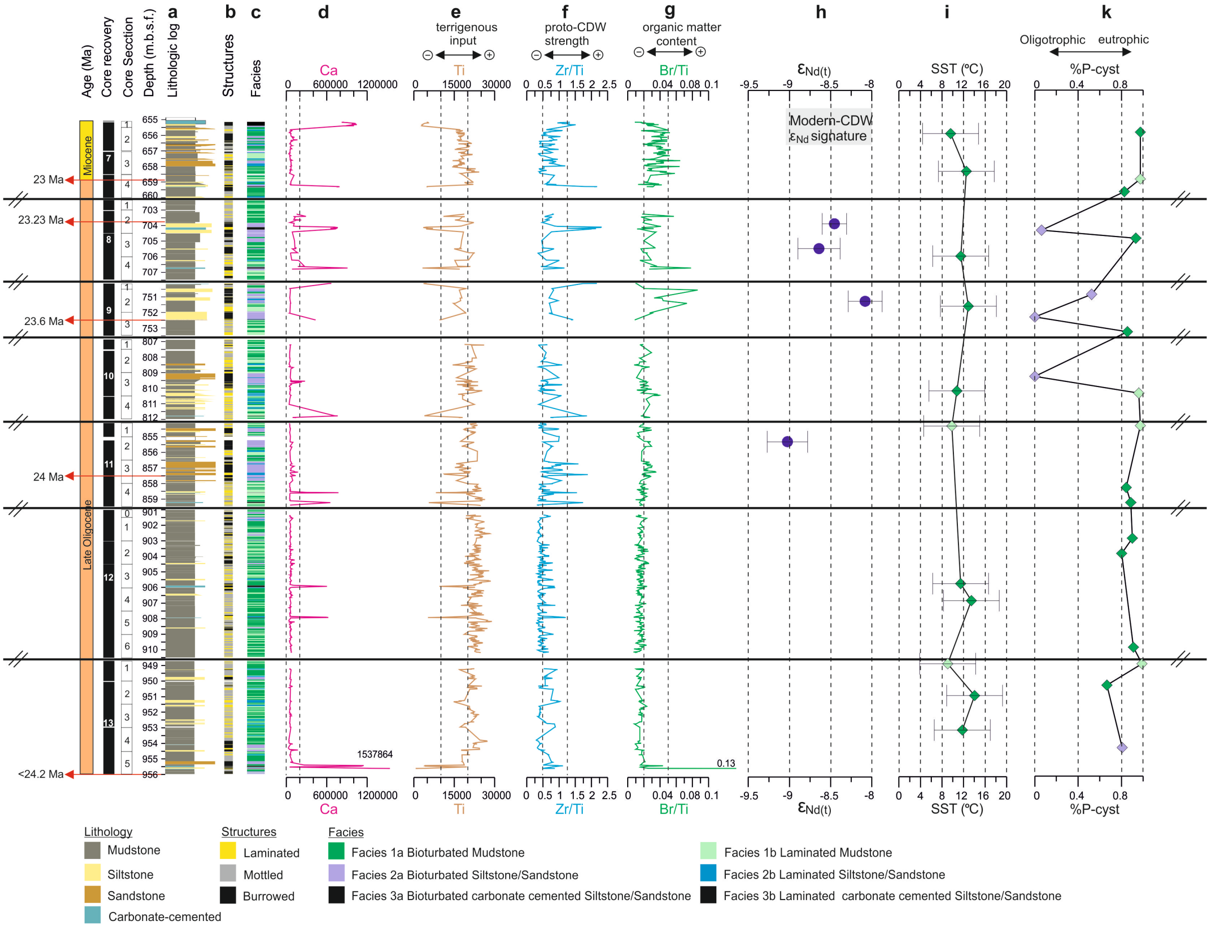

Figure 5.3: Sedimentological, paleontological and geochemical (XRF scanning data and $\varepsilon_{Nd(t)}$) data of DSDP Hole 269A, all plotted versus depth **a:** Graphic lithological log, **b:** sedimentary structures (see legend), **c:** main facies distribution (see legend), **d:** total Ca counts, **e:** total Ti counts, **f:** Zr/Ti ratios, **g:** Br/Ti ratios, **h:** ε_{Nd}, **i:** TEX_{86}-derived sea surface temperature **k:** %P-cyst=P-cyst/(P-cyst + G-cyst).Colors of TEX_{86}-derived SST and P-cyst vs G-cyst values reflect the sedimentary facies. Note core gaps between the cores were removed from the plot (gaps indicated with //).

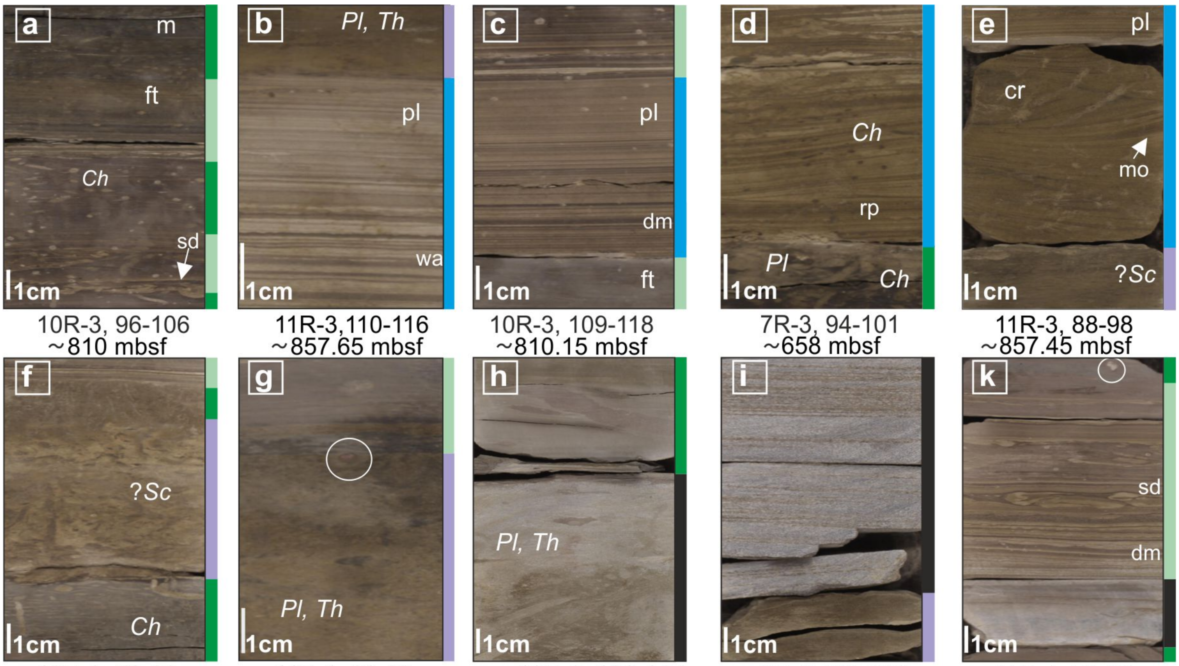

10R-3, 96-106
~810 mbsf

11R-3,110-116
~857.65 mbsf

10R-3, 109-118
~810.15 mbsf

7R-3, 94-101
~658 mbsf

11R-3, 88-98
~857.45 mbsf

10R-3, 76-86
~809.8 mbsf

11R-1, 93-99
~854.45 mbsf

12R-3, 136-147
~905.9 mbsf

8R-2,119-130
~704.25 mbsf

11R-4, 51-62
~857.45 mbsf

Figure 5.4: Representative core photographs from facies assemblages in DSDP Hole 269A, showing main structures and bed contacts referred to in the text. Facies colour code in the sidebar to the right of each core image is according to the legend in Figure 3. ft: faint laminations, pl: planar laminations, wa: wavy laminations, *dm:* double mud layers, rp: ripple, cr: cross-laminations, mo: mud-offshoots, sd: soft-sedimentary structures, m: mottled, *Ch: Chondrites, Pl: Planolites, Th: Thalassinoides, Scolicia: Sc.* Note single granule

Despite the diagenetic processes associated with the bioturbated and laminated carbonate-cemented facies (F3a, F3b), thin section analyses integrated with HR-SEM images show preservation of microfossils in both facies, including silicified planktonic foraminifers and diatoms (**Figs. 5.5f-h**). This observation is noteworthy since the sediments of the study sections were considered almost barren in microfossil (Hayes et al., 1975). The presence of benthic foraminifera with siliceous test suggests diagenetic dissolution and confirms the biogenic origin of these carbonates (**Fig. 5.5**). HR-SEM images reveal that the contact between F3b and F3a is sharp and erosive and inverse grading characterizes F3b (**Fig. 5.5e**). In total thirteen carbonate-cemented beds were observed, with the thickest ones at 704.2 mbsf and at 655.3 mbsf (e.g., **Figs. 5.3c and 5.3d**).

The intercalation of bioturbated and laminated facies is characterized by both gradational and sharp contacts. More than 90 sharp contacts were identified (**Fig. 10.3.3**). A common ichnological feature that appears associated with at the sharp contact between the coarse and the fine-grained facies is the presence of pseudo-borings, characterized by well-defined shapes, undeformed, with sharp contacts, infilled with different material to the host sediment (**Figs. 5.4 d-f**).

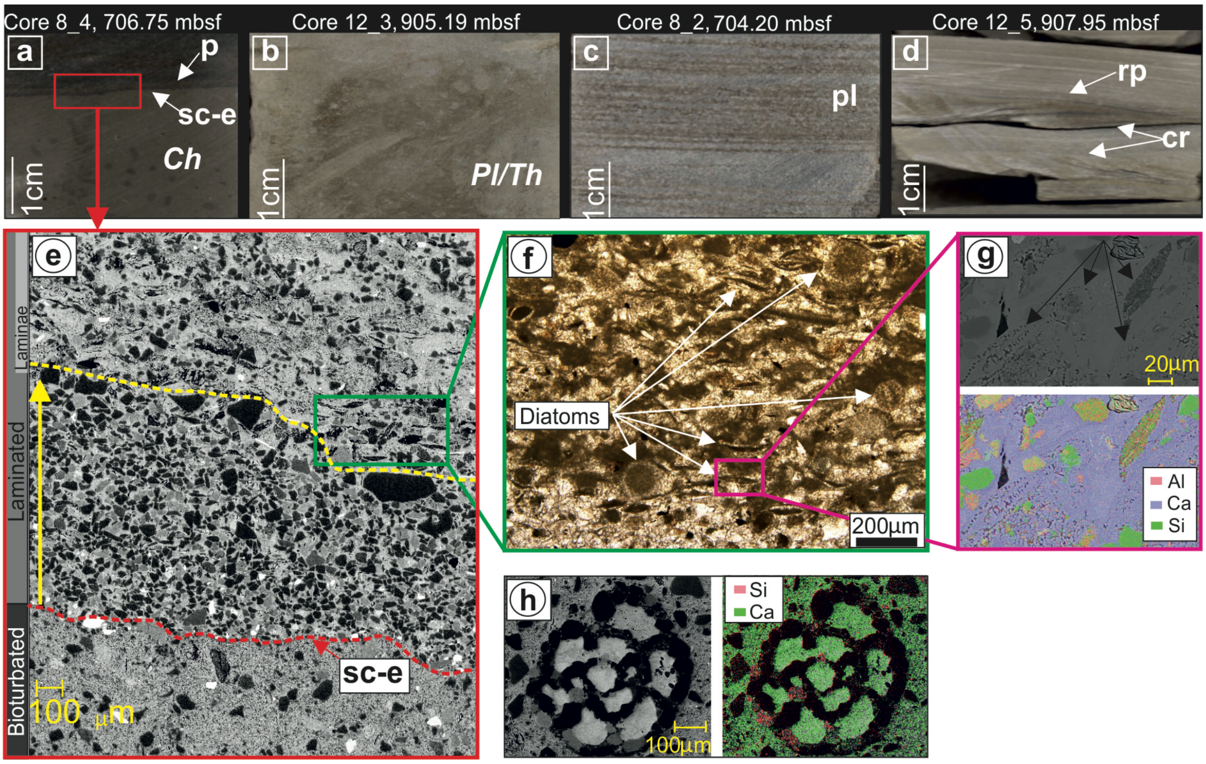

Figure 5.5: Detailed images of carbonate-cemented facies. **a**: A sharp erosive contact (sc-e) between bioturbated (F3b) and laminated (F3a) carbonate-cemented facies. **b, c, d:** A carbonate-cemented bioturbated and laminated facies. **e:** Back-scattered electron photomicrograph showing blow-up example of a sharp erosive contact (sc-e) between bioturbated and laminated carbonate-cemented facies (red dotted line) and inverse grading pattern (yellow arrow) above the contact. **f:** Thin section photomicrograph, plain-polarized light of carbonate-cemented facies showing diatom assemblages within the laminae of facies F3a. **g:** HR-SEM micrograph and corresponding elemental map of Al, Ca, Si showing diatom skeletal remains within the carbonate cementation matrix. **h:** foraminifera with siliceous tests. *Ch: Chondrites*, *Pl: Planolites, Th: Thalassinoides,* pl: planar laminations, rp: ripple, cr: cross-laminations.

5.5.2 Geochemistry at Hole 269A

Down-core variations of Ca content clearly track the 13 carbonate-cemented beds (**Fig. 5.3d**). In these beds, the dissolution of calcareous microfossils results in carbonate cementation/re-precipitation, as shown by the HR-SEM analyses (**Fig. 5.5h**). Additionally, we observe an interval of increased Ca values within the non-carbonate-cemented sediments between 706.8-703.28 mbsf (~23.23 Ma) (**Fig. 5.3d**). This increase is also associated with the preservation, even if scarce, of calcareous microfossils (i.e., planktonic, benthic foraminifers and calcareous nannofossils, **Fig. 10.3.4**).

In comparison, Ti variations show negative excursions in the carbonate-cemented facies (**Fig. 5.3e**). Ti decreases after 858 mbsf (~24 Ma), and more pronounced between 752.5 to 655 mbsf (~23.6 to 23 Ma) (**Fig. 5.3e**).

A principal component analyses (PCA) yielded one major principal component ($PC1_{TOT}$) that explains 63.8 % of the total variance in the XRF data (Table S4). $PC1_{TOT}$ is characterised by negative loadings for Ca and positive loading for all the other elements (Al, Si, K, Ti, Fe, Br, Ba, Sr, Zr) (**Fig. 5.6a**). Prominent negative excursions in $PC1_{TOT}$, are associated with the carbonate-cemented beds. In addition, $PC1_{TOT}$ decreases after 752.5 mbsf (~23.6 Ma) (**Fig. 10.3.5**).

Because of the distinct lithological/geochemical characteristics of carbonate-cemented beds compared to the rest of the sediments in our record, we ran another PCA, excluding the carbonate-cemented sediment. The first PC, named PC1 describes the 34.7% of the total variance, with main negative loadings for Zr and Ca and in lesser degree Sr, Br and Si and positive loading for all the other detrital elements (Al, Si, K, Ti, Fe, Ba, Rb) (**Table 10.3.3; Fig. 5.6b**). This pattern suggests accumulation of heavy elements (e.g., Zr) due to sediment sorting likely by bottom currents.

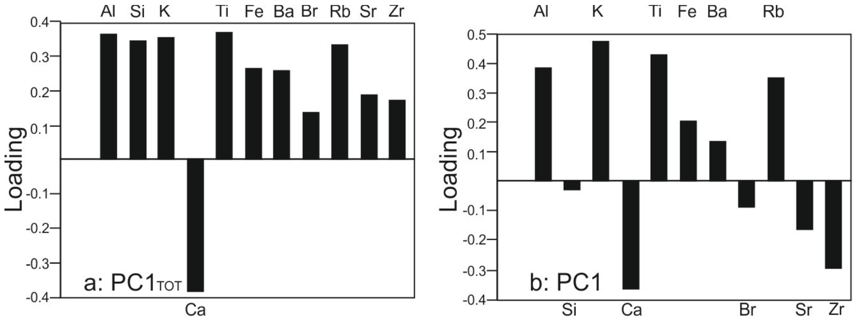

Figure 5.6: Principal Component Analysis (PCA) between XRF-scanner data through the study core section. **a:** $PC1_{TOT}$ with carbonate-cemented facies and **b:** PC1 without carbonate-cemented facies.

Down-core variations of Zr/Ti ratios show high short-term variability (**Fig. 5.3f**). In general, Zr/Ti show similar patterns with PC1 (**Fig. 10.3.5**) supporting further that both proxies reflect the accumulation of heavy minerals, due to the sorting of bottom currents and/or gravity flows. Zr/Ti ratios show less pronounced variability in fine-grained sediments between 910.5 and 901 mbsf. In general, above 858 mbsf (~24 Ma), Zr/Ti ratios show higher values (**Fig. 5.3f**). At 856.75 and 857.5 mbsf (~24 Ma) two prominent peaks of high Zr/Ti ratios, are recorded in ripple cross-laminated sandy siltstones, which indicate the strongest episodes of bottom current velocities within our study interval (**Fig. 10.3.5b**). In addition, high Zr/Ti ratios are shown between 752.5 to 750.17 mbsf (~23.6 Ma) (**Fig. 5.3f**).

Br/Ti ratios also increase slightly above 858 mbsf (~24 Ma). It is however between 752.5 and 655 mbsf (~23.6 Ma and 23 Ma) that ratios show increased values, which coincide with the higher preservation of microfossils in the non-carbonate cemented sediment (**Fig. 5.3g**).

The $\varepsilon_{Nd(t)}$ data from fish debris range from -9.03 ± 0.25 to -8.07 ± 0.21 (average $\varepsilon_{Nd(t)}$ values -8.54 ± 0.22) during the late Oligocene (~24 to 23.23 Ma) (**Fig. 5.3h**).

Late Oligocene detrital sediment samples from Site 269 have $\varepsilon_{Nd(t)}$ values of -12.14 ± 0.33 and $\varepsilon_{Nd(t)}$= -13.33 ± 0.33, at 854.72 mbsf (~24 Ma) and 751.34 mbsf (~23.6 Ma), respectively, and are within the range of local bedrock composition of proximal areas east of the Metz glacier, within the Wilkes Subglacial Basin (Early Paleozoic granite outcrops; ε_{Nd}= -11.2 and -19.8; Bertram, et al., 2018; Cook et al., 2013, 2017).

5.5.3 TEX_{86}

Of the 15 samples processed, 4 were flagged as outliers with potential for a biased source and thus they were not suitable for TEX_{86} analysis. The remaining 11 samples had normal values in the indices signaling overprints as mentioned in the methods. SST values were calibrated between 9-14°C, ± 5.2°C, with bioturbated facies characterized by higher SST values, compared to the laminated facies (**Fig. 5.3i**). The relative temperature variability of 3-5°C between laminated and bioturbated sediments, respectively at Hole 269A, is consistent with sedimentological features, glacial-interglacial variability and TEX_{86}-derived SST reported from Site U1356 (Hartman et al., 2018; Salabarnada et al., 2018).

5.5.4 Palynology

All examined samples yielded well to moderately preserved palynomorphs assemblages with *Leiosphaera* (70-80%), in-situ dinocyst (20%) and pollen, while spores and reworked dinocyst are a minor component (**Table 10.3.2**). As is common in high polar latitudes, the absolute abundances of dinocysts remain low throughout the examined succession, and do not exceed 400 cysts/g sediment. Assemblages are dominated by P-cysts, with *Brigantedinium* spp. as most abundant (45-90% of the in situ dinocyst sum), *Lejeunecysta* (<10%) showing no clear trend throughout the section and *Selenopemphix* with its largest abundance at between 955-909 mbsf (30%) (**Fig. 5.3k**). Even if less abundant (rarely >5%), the samples yielded a G-cyst assemblage that mainly consists of *Batiacasphaera, Pyxidinopsis, Operculodinium* and *Impagidinium*. Similar G-cyst assemblages are present throughout the Oligocene-Miocene record from the U1356 (Bijl et al., 2018b). G-cyst are notably common between 954.3-950.3 mbsf (~24.2 Ma) and around 23.6 Ma, with additions of *Spiniferites spp*. (sample 9R 3W 125-129 cm) and *G. inflata* (sample 9R 2W 26-30 cm). Bioturbated facies contain more G-cyst compared to the laminated facies (**Fig. 5.3k**).

5.6 Discussion

5.6.1 Glacial-interglacial sedimentation and short-term polar frontal system dynamics

Repeated alternations between laminated and bioturbated facies like those described at Hole 269A (**Figs. 5.3c and 5.4**), are common in deep-water settings around Antarctica and are interpreted to result from changes in sedimentation related to glacial-interglacial cycles, respectively (e.g., Hepp et al., 2006; Lucchi and Rebesco, 2007; Escutia et al., 2009, 2011; Patterson et al., 2014; Salabarnada et al., 2018).

Terrigenous laminated deposits at Hole 269A (F1b, F2b, **Figs. 5.3c and 5.4**) are interpreted to form by a complex interplay between sediments delivered by gravity flows (e.g., debris flows and turbidity currents) and bottom currents, during glacial times. Even when laminated deposits preserve turbidite affinity (e.g., sharp/erosional bases, normal grading depicted by visual observations and Zr/Ti variability) (e.g., **Figs. 10.3.6a and 10.3.6c**), we find evidence suggesting that these intervals were continuously reworked by bottom currents. This evidence include internal structures such as mud drapes, double mud layers, lenticular laminations, mud-offshoots and a rhythmic character between the intercalation of the muddy/sandy couplets with varying thicknesses (e.g., **Figs. 5.4b, e and k**). These structures are typical in contourite deposits and are interpreted to indicate both traction and suspension processes during deposition (Shanmugam et al., 1993; Rebesco et al., 2014). Additionally, the absence or scarcity and low diversity of trace fossils such as *Chondrites* and *Phycosiphon* in the laminated facies can suggest a poorly oxygenated/ventilated environment at seafloor, changes in nutrient availability and likely high sedimentation rates that promote unfavorable conditions for trace markers to thrive (e.g., Lucchi and Rebesco, 2007; Rodríguez-Tovar and Dorador, 2014, Rodríguez-Tovar et al., 2014; 2015a, b, 2019; Hodell et al., 2017). Poorly ventilated conditions at the seafloor where also reported from late Oligocene laminated facies at Site U1356, during glacial times (Salabarnada et al., 2018).

In comparison, bioturbated facies (F1a, F2a, **Figs 5.3c and 5.4**) are interpreted to result from mainly hemipelagic sedimentation during interglacial times with continued reworking by bottom currents. The inverse and bi-gradational grading patterns shown by Zr/Ti ratios and MS variations, when resolution is sufficient (**Fig. 10.3.6**) is a strong evidence of bottom current control, suggesting winnowing by bottom currents with fluctuating intensities (e.g., Stow and Faugéres, 2008). The diverse trace fossil assemblage, indicate more oxygenated/better ventilated conditions, likely higher nutrient content in the seafloor and lower sedimentation favorable to microbenthic trace marker proliferation than during glacial times (e.g., Lucchi and Rebesco, 2007; Rodríguez-Tovar et al., 2015a, b). Late Oligocene bioturbated deposits from Site U1356 also record an increase in oxygenation at the seafloor when compared with laminated deposits of the same age at the site (Salabarnada et al., 2018).

The carbonate-cemented laminated and bioturbated facies (facies: F3a, F3b; **Figs 5.3c and 5.5**) are interpreted to result from sedimentation during the warmest interglacials recorded by our sediments. This is indicated by the high Ca content (**Fig. 5.3d**) associated with dissolution of calcareous microfossils, which strongly supports the biogenic origin of these carbonate beds (**Figs. 5.5f, 5.5g and 5.5h**).

Our interpretation of sediments recovered at Site 269 from 956 to 858 mbsf (before 24 Ma) is supported by similar late Oligocene (26-25 Ma) bioturbated and laminated sediments recovered at the more proximal IODP Site U1356. Nearly continuous recovery of this interval at Site U1356, allowed for a detailed study of glacial-interglacial cyclicity that is paced by obliquity (Salabarnada et al., 2018). These authors interpreted the changes between laminated and bioturbated facies at Site U1356 to be driven by oceanic frontal migrations forced by glacial-interglacial cycles. In detail, during interglacial times, southward migration of the SWW and the surface oceanic fronts facilitated proto-CDW intrusions closer to the Antarctic margin. This allowed better preservation of calcareous microfossils and enhanced ventilation at the seafloor. The opposite occurred during the glacial times. In addition, even when the interval from 26 and 25 Ma was generally warm as indicated by the prevalence of open water conditions (Bijl et al., 2018b), TEX_{86}-derived SST variations (between 1.5 and 3 ºC) (Hartman et al., 2018) correlate with the glacial-interglacial cyclicity reported by Salabarnada et al. (2018). In fact, our more distal TEX_{86}-based SST data and dinocyst assemblages, compared to those from Site U1356 (Hartman et al., 2018; Bijl et al., 2018b) support further the oceanic frontal migrations forced by glacial-interglacial cycles. The relative SST variability of 3-5°C at Site 269 may be slightly higher than the glacial-interglacial TEX_{86}-derived SST variability from Site U1356 during the Oligocene-Miocene (Hartman et al., 2018), although a full representation of the glacial-interglacial variability at either site might not have been captured. Additionally, the high abundance of *Brigantedinium spp* (P-cyst) reflect open ocean upwelling and high-nutrient conditions (Harland and Pudsey, 1999; Zonneveld et al., 2013) at Site 269, perhaps even more than at U1356. In addition, the lower amounts of G-cysts compared to Site U1356 indicate that Site 269 was located closer to the upwelling/divergence zone during the glacial times. In contrast, SST increase and higher amounts of G-cysts (lower P/G cyst ratios) similar to modern temperate (interglacial), oligotrophic waters from around Tasmania and southern New Zealand (Prebble et al., 2013) indicate the southward migration of the oceanic fronts during the interglacial times. Our results are consistent with dinocyst assemblages at Site U1356, which show similar changes between oligotrophic, temperate dinocyst assemblages during interglacials, to eutrophic, colder dinocysts during glacial times (Bijl et al., 2018b). The difference in dinocyst assemblages between the two sites may be attributed to a closer proximity of Site 269 to the Antarctic Divergence.

Deposition of large stacked debris flow deposits at Site U1356 between ~24.76 Ma and 23.23 Ma (Escutia et al., 2011; Passchier et al., 2018) provide limited information regarding ocean configurations during the late Oligocene-early Miocene in this region of the East Antarctic margin. This gap is recorded at Site 269 despite the limitations related to the discontinuous drilling and low-resolution age model. Our sedimentological, geochemical and palynological analyses show that the climate-related ocean polar frontal movement migrations continued throughout the late Oligocene and into the early Miocene. We also note an increase in the frequency of siltstones and sandstones beds between 24 and 23.23 Ma. These sediments could result from local inputs from structural highs depicted nearby in seismic lines that cross the site (De Santis et al., 2003). We note however that Oligocene and the Miocene deposition around these highs is dominated by contourite deposition forming mounded deposits against the highs (De Santis et al., 2003), which could prevent direct delivery of sediment to where Site 269 is located. The correlations previously established between sedimentation at Sites 269 and U1356, argues for a regional source of sediments to Site 269 rather than a local one. We therefore argue that these coarse sediments likely correspond to the distal reaches of the debris flow deposits recovered at Site U1356. At this site these deposits have been interpreted to result from ice sheet advances into the continental shelf (Escutia et al., 2011, 2014).

5.6.2 Bottom water signatures at Site 269

Geological evidence derived from microfossil assemblages from sedimentary records around Antarctica, including evidence from Site 269, suggest that the proto-Polar Front (PF) was placed close to 60°S between the late Oligocene-early Miocene (Nelson and Cooke, 2001; Cooke et al., 2002). This is further supported by dinocyst assemblage data from Hole 269A indicating that the site was influenced by nutrient-rich upwelling and ice-free waters, with occasionally southward latitudinal transport of waters during the late Oligocene and early Miocene. Fish debris neodymium isotope results from Site 269 (**Fig. 5.3h**) are consistent with late Oligocene proto-CDW $\varepsilon_{Nd(t)}$ values recorded along the proto-PF on the Kerguelen Plateau (Indian Ocean) (average $\varepsilon_{Nd(t)} = -7.8$; Wright et al., 2018) and around Maud Rise (Atlantic Ocean) (average $\varepsilon_{Nd(t)} = -8.5$; Scher and Martin, 2004). The combined dataset suggests that a common bottom water mass (proto-CDW) was bathing the South Atlantic and South Indian Ocean along the proto-PF. The pronounced difference between the $\varepsilon_{Nd(t)}$ values of the fish debris and the detrital sediment samples from Site 269 ($\varepsilon_{Nd(t)}$= -12.14 ± 0.33, -13.33 ± 0.33 (~24 Ma and ~23.6 Ma, respectively) confirm the water mass signal in the fish debris samples (**Fig. 10.3.7**). Bathymetric reconstructions show that the Southern Indian Ocean basin was already sufficiently deep during the Oligocene and did not contain any large topographic barriers that prevented the flow of proto-CDW from the Kerguelen Plateau to the abyssal plain off the Australian-Antarctic basin (Scotese and Wright, 2018). Based on the above, we conclude that at least during the latest Oligocene (~24 to ~23.23 Ma), Site 269 was covered by a proto-CDW with a Nd signature similar to the present day CDW in the Australian sector of Southern Ocean (ε_{Nd} = -8.1 to -9.1; Lambelet et al., 2018). This observation contrasts with the present-day bottom water mass configuration at the location of Site 269, which is bathed by Adélie Land Bottom Water (ALBW) (Rintoul, 1998), suggesting a reduced export of ALBW during the late Oligocene. These results are consistent with previous inferences for reduced sea ice in the region (Bijl et al., 2018b; Hartman et al., 2018) diminishing production of ALBW at the Oligocene and Miocene on the Wilkes Land shelf. The less radiogenic $\varepsilon_{Nd(t)}$ value around 24 Ma ($\varepsilon_{Nd(t)}$ = -9.03 ± 0.25) may suggest mixing between proto-CDW and Adélie Coast Bottom Water (ACBW; Oligocene ACBW $\varepsilon_{Nd(t)}$ = - 10.6 ± 0.8; Huck et al., 2017). However, more data are needed to confirm this hypothesis.

5.6.3 Long-term changes in the proto-ACC dynamics during the late Oligocene to earliest Miocene

We provide new insights into the ocean configuration during four distinct periods between the late Oligocene-early Miocene from ~24.2 to 24 Ma, at ~24 Ma, from ~23.6 to 23.23 Ma, and at ~23 Ma.

A remarkable shift in sedimentation occurs at ~24 Ma (858 mbsf) (**Fig. 5.3a**). Before 24 Ma, predominantly fine-grained sediment deposited under enhanced terrigenous inputs and an overall weak proto-CDW. This interpretation is supported by the high Ti values and low Zr/Ti ratios, respectively, and their low variability, in particular between 910 to 901 mbsf (**Figs. 5.3e and 5.3f**). Furthermore, less frequent bioturbated facies and low Br/Ti ratios suggest a less ventilated environment and low nutrient content at the seafloor (**Figs. 5.3b and 5.3g**). The high abundance of G-cyst assemblages between 954.3 to 950.3 mbsf (**Fig. 5.3k**), together with high SST (11.5 to 14°C) (**Fig. 5.3i**), indicate that the polar front system was located south of the Site 269. However, the concomitant SST drop to 9°C and the absence of G-cysts at 948 mbsf (**Figs 5.3i and 5.3k**) indicate northward migration of the polar front, which likely reached Site 269.

Around 24 Ma, our data document the strongest proto-CDW velocities recorded at Hole 269A during the late Oligocene and earliest Miocene, as indicated by the high Zr/Ti peaks associated with cross-sandy laminated intervals that are not preserved elsewhere in the sedimentary record (**Figs. 5.3f and 5.4e**).

After 24 Ma, there is an increase in the frequency of deposition of coarser-grained material interbedded with fine-grained sediment (**Fig. 5.3a**). Overall Zr/Ti ratios are higher suggesting periods of proto-CDW strengthening, with Zr/Ti peaks associated with Ca enrichment (**Figs. 5.3f and 5.6b**). In addition, more abundant and diverse bioturbation (**Figs. 5.3b and 5.3c**) point to episodes of better ventilated bottom conditions, and likely higher nutrient content at the seafloor, as indicated by a small increase in Br/Ti ratios (**Fig. 5.3g**). Between ~24 and 23.6 Ma, the frontal system migrated northward, as indicated by the lower SST (9.8-10.8°C) and the dominance of P-cysts, suggesting cool and euthrophic ocean conditions. In addition, the sheer absence of dinocysts may have resulted from low preservation associated to oxidation at sea floor, transport by bottom currents and/or reduced productivity. Given the warmth as reconstructed for the surrounding time intervals (e.g., Bijl et al., 2018b; Hartman et al., 2018), we rule out a permanent ice cover during this time.

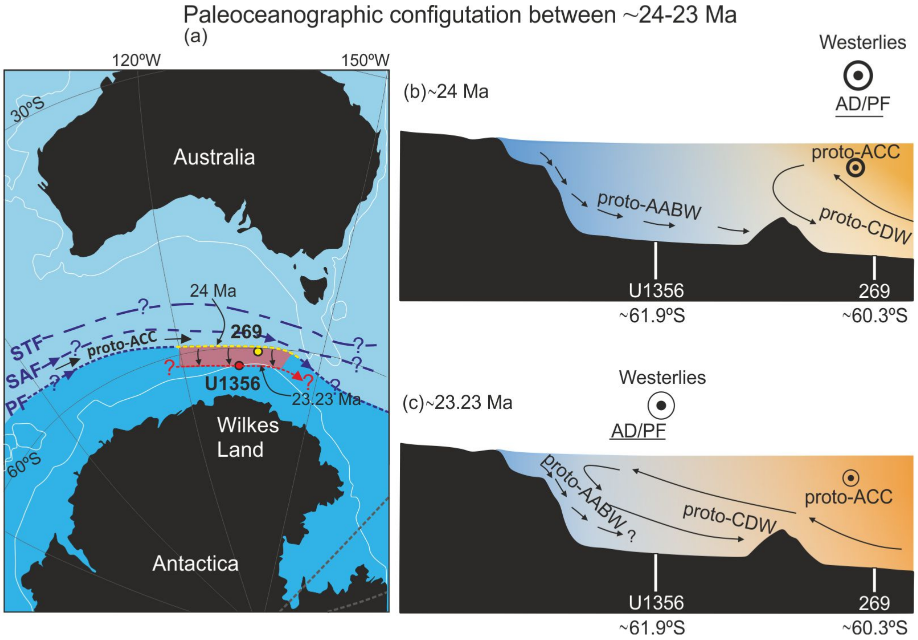

Figure 5.7: Paleoceanographic configuration offshore the Wilkes Land margin around 24-23 Ma. **a:** Reconstructed ocean frontal system between Antarctica and Australia around 24-23 Ma. Reconstruction of tectonic plates around Tasman Gateway and paleoposition of sites based on Seton et al., 2012 global plate motion model derived from Gplates software (Müller et al., 2018). White lines indicate the continental lithosphere boundary. Polar water south of the PF are shaded in darker blue. Boundary between polar and subantarctic waters during the 23.23 Ma (red dashed line) and during the 24 Ma (yellow dashed line). Frontal constraints west and east of the Wilkes Land region are from reconstructions of Nelson and Cooke (2001); Cooke et al. (2002). STF: Subtropical front, SAF Subantarctic front, PF: Polar front. Black arrows show the pathway of the proto-ACC. Schematic illustrations of the proto-CDW dynamics for the 24 Ma (b) and 23.23 Ma (c). **b:** At ~ 24 Ma, Westerlies and PF were located close to Site 269 resulting strong proto-ACC. There is likely enhanced proto-AABW production. **c:** At ~ 23.23 Ma, Westerlies and PF migrated southwards close to Site U1356. Proto-ABBW formation is reduced. This allowed the relative warmer surface water and proto-CDW to penetrate closer to Antarctic continent.

We infer that the observed shift in depositional environment at 24 Ma was driven by atmospheric and oceanic frontal changes. SWW northward migration due to the major expansion of the AIS between 24.5 and 24 Ma (see Levy et al., 2019 for discussion) is thought to have forced the northward migration of the SWW prior to 24 Ma (Fig. 5.7a and 5.7c). This would have resulted in a weak proto-CDW, reduced water mass mixing, and a less ventilated seafloor. In contrast, the increase in proto-CDW intensification after 24 Ma, inferred from the higher Zr/Ti amplitudes, likely indicate times when SWW migrated southwards, aligned with the proto-ACC. This promoted enhanced mixing and better ventilation of the seafloor and likely higher organic matter deposition, in times when the AIS retreated. Our SST and dinocyst data further support the warmer temperatures and dominance of G-cysts, which indicate the stronger influence of warm oligotrophic waters.

Between ~23.6 and ~23.23 Ma, sediments record a prominent southward polar frontal system migration, which allowed warmer water to penetrate further southwards (**Figs. 5.7a and 5.7c**). This interval is characterized by high Zr/Ti ratios (at ~23.6 Ma, **Fig. 5.3f**), high Ca, high SST (11.5-12.9°C) (**Fig. 5.3i**) and a reduction in terrigenous input (low Ti values) (**Figs. 5.3d and 5.3e**). In addition, there is higher preservation of calcareous microfossils in some intervals (Fig. S2), and dominance of G-cysts (**Fig. 5.3k**), similar to those in modern temperate (interglacial), oligotrophic waters from around Tasmania and southern New Zealand (Prebble et al., 2013), high Br/Ti ratios (**Fig. 5.3g**) and a thick carbonate cemented bed at ~23.23 Ma (**Fig. 5.3a**). Today, calcareous organisms rarely reach the seafloor within and south of the polar front zone. This is because of the presence of the corrosive (CO_2-rich) Antarctic deep waters (Whitehead and Bohaty 2003 and references therein) and strong upwelling (Olbers et al, 2004), which dissolve calcareous rain. A thick carbonate cemented bed is present at Site U1356 dated at 23.23 Ma (Escutia, et al., 2011). The synchronous deposition of these carbonate-cemented beds at Sites U1356 and 269 strongly supports a wide southward expansion of proto-CDW offshore Wilkes Land at ~23.23 Ma. Our ε_{Nd} data, despite their low resolution, also suggest a greater influence of proto-CDW during this period compared to ~24 Ma (**Fig. 5.3h**). Similar processes occur today, when a reduction in the volume of AABW is compensated by the expansion of the CDW (van Wijk and Rintoul, 2014). Our interpretation is further supported by the absence of sea-ice-related dinocyst species (i.e. *Selenopemphix antarctica*) at both Sites 269 and U1356 (Bijl et al., 2018b), which suggests a weaker than modern sea ice season during the Oligocene and Miocene. In addition, the new SST reconstruction at Site 269, similar to those at Site U1356, report warmer surface water conditions than today and argue for a decrease in the potential formation of Antarctic bottom waters (Hartman et al, 2018).

At ~23 Ma, high Br/Ti ratios indicate an increase in the organic content in the sediment (**Fig. 5.3**), coinciding with the first evidence (scarce) of diatoms at Site 269. A shift from calcareous dominated microfossils to siliceous (e.g., diatomaceous and cherty clay sediments) has also been reported at Site U1356 (Escutia et al., 2011, Escutia et al., 2014; Passchier et al., 2018) arguing for a major regional event likely related to the AIS expansion during the early Miocene, northward expansion of the polar front system and more influence of siliceous productivity. This is supported by the high amount of P-cyst at Site 269 at ~23 Ma, which indicate cool, nutrient-rich upwelling conditions (**Fig 5.3k**). After 23 Ma, deposition of the thickest carbonate cemented bed would imply this period was followed by a southward migration of the frontal system (**Fig. 5.3a**).

In summary, our combined sedimentological, geochemical and palynological data between ~24.2 and ~23 Ma show a dynamic proto-ACC off the Wilkes Land margin during the late Oligocene-Miocene. In addition, the carbonate preservation and low siliceous microfossil preservation at Site 269 (located within the polar front zone) contrasts with modern sedimentation near the Polar Front. This is supported by the presence of oligotrophic, temperate dinocyst assemblages at Sites 269 and U1356 that are similar to the ones found today north of the Polar Front around Tasmania and the Southern New Zealand (Bijl et al., 2018b). Our data therefore suggest a weaker frontal system, characterized by reduced upwelling, which probably allowed southward transport of warm surface waters from lower latitude. This is consistent with numerical modelling results indicating a weaker than present-day proto-ACC (Herold et al., 2012; Hill et al, 2013). These findings argue against the onset of a modern-like ACC during the latest Oligocene (ca 25-23 Ma) based on sedimentary records across the Tasman Gateway (Pfuhl and McCave, 2005) and the South Pacific (Lyle et al., 2007).

5.7 Conclusions

Our integrated sedimentological, geochemical, isotopic and palynological data sets from DSDP Site 269 provide new insights into the proto-ACC dynamics during the late Oligocene-early Miocene (~24.2 to 23 Ma) off the eastern Wilkes Land margin. We show that sedimentation at Site 269 is controlled by the persistent reworking of gravity flows and hemipelagic sedimentation by proto-CDW that is characterised by fluctuating current intensities driven by the migration of the frontal system in response to climatic changes. We detail four distinct snapshots (from ~24.2 to 24 Ma, at ~24 Ma, from ~23.6 to ~23.23 Ma, and at ~23 Ma) that we link to changes in the proto-ACC and deep proto-CDW dynamics. Just before 24 Ma, fine-grained sediments were deposited under enhanced terrigenous inputs and weak proto-CDW intensities that resulted in low ventilated bottom conditions and probably low organic content and preservation. At 24 Ma, episodic events of stronger proto-CDW current velocities started, associated with coarser-grained deposits, and better ventilated bottom conditions and slightly higher organic matter content. In addition, TEX_{86}-derived SST data varied between 9 to 13.5°C, while the dominance of P -cysts indicate relatively cool ocean temperatures, upwelling and high-nutrient conditions between ~24 and 23.6 Ma. Together, these evidences suggest that the polar front at this time was located near the site. At ~23.6 Ma, and more pronounced at ~23.23 Ma, a prolonged expansion of proto-CDW closer to the Wilkes Land margin is indicated by the higher Ca values, better preservation of calcareous microfossils, higher Br/Ti ratios, high SST (from 11.5 to 12.9°C), high amounts of G-cysts similar to modern temperate and oligotrophic waters, and ε_{Nd} data resembling modern-like CDW ε_{Nd} signature at Site 269. Given that the record between ~24.9 and 23.23 Ma was masked by debris flow deposition at the more proximal IODP Site U1356, our results provide the first record of ocean configuration for this margin for this time interval. When compared with results from Site U1356 and with numerical modelling, our findings support the notion of a fundamentally different Southern Ocean with a weaker proto-ACC than today during the late Oligocene and earliest Miocene. A weaker frontal system permitted the incursion of warm waters from lower latitude closer to the Antarctic margin and the preservation of carbonate. The synchronous deposition of thick carbonate-cemented beds both at Site 269 and U1356 at 23.23 Ma indicates a regional event of poleward proto-CDW expansion.

Chapter **6**

Late Quaternary climatic control of Lake Baikal (Russia) turbidite systems

Based on: Evangelinos, D., Nelson, C. H., Escutia, C., De Batist, M., Khlystov, O., 2016. *Late Quaternary climatic control of Lake Baikal (Russia) turbidite systems: Implications for turbidite systems worldwide*. Geology. 45 (2):179-182. doi: 10.1130/G38163.

ABSTRACT

Lake Baikal (Russia) contains a variety of turbidite systems in different tectonic and depositional settings that provide tests for the role of Quaternary climatic change on turbidite system growth. During Pleistocene glacial climates, all types of systems exhibit increased sediment supply (high sedimentation rates, high net sand percent, thick sand turbidites) and progradation. During Holocene interglacial climate, all systems exhibit reduced sediment supply and retreat. Seismic profiles from the large Selenga Fan and small Tompuda Fan show (1) maximum fan growth during the late Pleistocene glacial melt time, where lobes and large channels reached the distal outer fan, and (2) fan retreat during the transition to the fully developed Holocene interglacial climate. For example, the Selenga Fan surface lobes backstepped ~55 km from the distal outer fan to the distal inner fan, and the large outer fan surface channel (~750 m wide, ~20 m levee relief) evolved to a smaller surface channel (~450 m wide, ~13 m levee relief) that extended only to the end of the inner fan. These results show that Quaternary climate controls the growth of the Lake Baikal turbidite systems in a setting where there are no significant water-level changes, which often are cited as the main control on turbidite system growth. The Lake Baikal and other marine turbidite systems suggest that climatic control of sediment supply, unrelated to sea-level lowering and tectonic effects, may have been a much more important control for turbidite systems than previously believed, not only during the Pleistocene, but perhaps also for ancient systems.

6.1 Introduction

Lake Baikal (Russia), the world´s oldest and deepest lake, formed in the rift zone between the Siberian platform and the fold belts of Mongolia, Asia (**Fig. 6.1A**) (Hutchinson et al., 1992). The lake is a unique natural laboratory for turbidite system research, because it contains a variety of depositional systems, such as sand-rich fans, mud-rich fans, and base-of-slope sand-rich aprons (Nelson et al., 1995, 1999; Colman et al., 2003). The tectonic setting is the primary control for these types of turbidite systems because it determines the size of drainage systems and the type of sediment supply they receive (Nelson et al., 1999). These systems include the small base-of-slope aprons developed on the northwest border fault margin with small drainages; the small sand-rich Tompuda Fan fed by a local glaciated valley river; and the large mud-rich Selenga Fan on the eastern ramp margin fed by the Selenga River, which has a large drainage area (Back and Strecker, 1998; Nelson et al., 2009).

During Pleistocene glacial time the growth rate of most turbidite systems in marine environments was greater than in interglacial time because of lower sea level and reduced base level of river drainages, increased sediment supply, and larger grain size (e.g., Nelson, 1976; Nelson and Nilsen, 1984). Most prevailing conceptual models attribute turbidite system growth to sea-level lowering, erosion related to river incision, and sediment delivery directly into canyon heads feeding the turbidite systems (e.g., Vail et al., 1977). Some recent models neglected to consider climate change, apart from eustasy, as a controlling factor for turbidite system growth (e.g., Brackenridge et al., 2011). Like most marine turbidite systems (e.g., Nelson and Nilsen, 1984), those in Lake Baikal exhibit, at ca. 13 ka (e.g., Carter and Colman, 1994), a transition from many thick sand turbidites in the late Pleistocene deposits to a few thin sand and silt lamina turbidites in a Holocene mud drape (Nelson et al., 1995). Average sedimentation rates (turbidites and mud interbeds) during the late Pleistocene (75 cm/k.y.) were ~3–4 times higher than those during the Holocene (20 cm/k.y.) in all basins of Lake Baikal (Nelson et al., 2009). The average net sand percentage changed from 21% in the late Pleistocene to 7% in the Holocene in all basins and was 5 times greater during the late Pleistocene in the North Basin, which was most affected by Pleistocene glaciation (Back and Strecker, 1998; Nelson et al., 2009).

Lake Baikal, however, did not undergo late Quaternary lake-level fluctuations sufficient to affect sediment supply because of base-level lowering. Colman (1998) stated that the climate-induced lake-level change was <~2 m during the late Quaternary, and Khlystov et al. (2008) estimated that lake levels were close to that of today, except for inferred short term changes in the lake level (to 40–45 m) during the period 24–18 ka. Even if this latter questionable lake-level change occurred, sediment access continues at any lake level (Nelson et al., 1999). In addition, high sedimentation rates, high net sand percent, thick sand turbidites, and coarser grain size are found before and after the inferred 24–18 ka lake-level lowering, and extend to the end of the Pleistocene, ca. 13 ka (Nelson et al., 2009). Therefore, our hypothesis is that changes associated with glacial climates (e.g., vegetation changes, glacial meltwater fluxes) were the key factors controlling the Pleistocene growth of the Baikal turbidite systems.

Our study mainly focuses on the Selenga Fan in the Central Basin of Lake Baikal using high-resolution swath bathymetry and reflection seismic data (**Fig. 10.4.1**) (Colman et al., 1996; De Batist et al., 2006). With these data we outline the evolution of turbidite channel and lobe distribution related to the increased growth of the Selenga Fan during Pleistocene glacial climates and the retreat of these features during the transition to Holocene climate (**Fig. 6.1**). The effects of climatic changes on the evolution of the Selenga Fan in the Central Basin are then compared to those on the Tompuda Fan in the North Basin (Nelson et al., 1995, 2009) and then to other marine turbidite systems such as the Rhône Fan and Ebro turbidite systems (Droz and Bellaiche, 1985; Nelson, 1990).

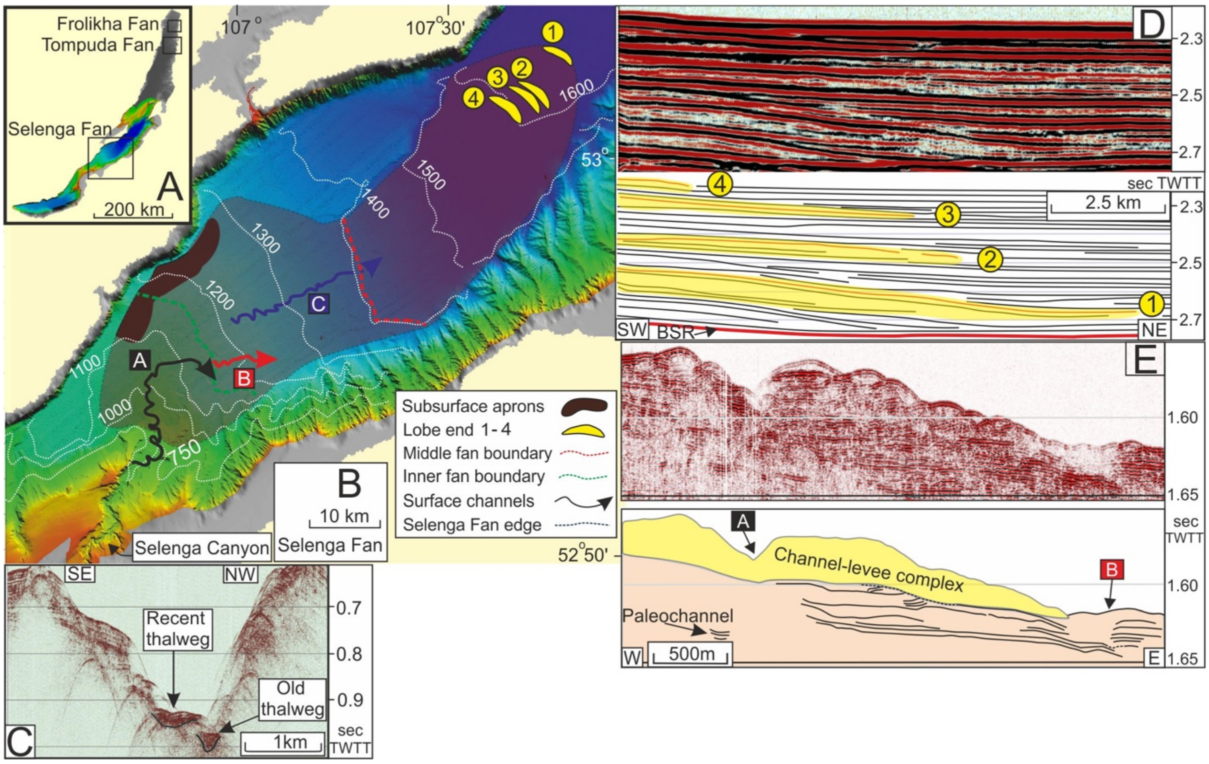

Figure 6.1: A: Location of the Selenga, Tompuda, and Frolikha Fans in Lake Baikal (Russia). B: Swath bathymetric map of the Selenga Fan (shaded area) with 100 m contour interval (De Batist et al., 2006), including the locations of canyons, channels, subsurface aprons, and depositional lobes. C: Seismic profile of the Selenga Canyon feeding the fan. D: Seismic profile interpretation showing oldest (1) to youngest (4) outer fan lobe backstepping. BSR—bottom-simulating reflection. E: Seismic profile interpretation showing younger channel levee complex A onlapping older larger channel B.

6.2 Characteristics of Selenga Canyon, Fan, Channels and Lobes

The sediment transported by the Selenga River, which feeds the Selenga Canyon, is predominantly sourced from the large Siberian-Mongolian drainage basin and in part from nearby mountain areas, which were glaciated during Marine Isotopic Stage (MIS) 2 (Osipov and Khlystov, 2010). The Selenga Canyon extends northeast into the Central Basin from the Selenga River delta (**Figs. 6.1A and 6.1B**) and feeds the Selenga Fan through the most recent active Holocene channel A (**Fig. 6.1B; Fig. 10.4.2**). The larger buried channel thalwegs of the canyon indicate that the canyon was more active in the past (**Fig. 6.1C**). The Selenga Fan extends from a depth of ~900 m to 1600 m in the Central Basin, is as wide as 26 km, and as long as 80 km (**Fig. 6.1B**). The fan interfingers laterally with western border fault aprons, as well as short stream inputs from the eastern ramp margin (**Fig. 6.1B**). The fan is at least 300 m thick; however, aprons and the presence of a bottom-simulating reflection (BSR) related to gas hydrate–bearing sediment underlying the Selenga Fan make it difficult to estimate the exact thickness (**Figs. 6.1B and 6.1D**) (Vanneste et al., 2001).

A progressive decrease in the Selenga Fan growth pattern through time is shown by the morphology of the surface channel-levee complexes (C, B, and A in **Fig. 6.1B**). Only one distributary channel was connected with the Selenga Canyon and therefore active at any given time (**Fig. 6.1B**). The oldest and largest surface channel C (~750 m wide, ~20 m levee relief) is observed for 24 km on the surface of the middle and proximal outer fan (**Fig. 6.1B; Fig. 10.4.2**). Its proximal part is buried under the younger channel-levee complexes A and B. At the inner fan to middle fan boundary, near the end of channel A, another segment of an older surface channel B is observed that has a width of 570 m and levee relief of 8–18 m (**Fig. 6.1B; Fig. 10.4.2**). Channel B extends 11 km across the Selenga middle fan, where it decreases to 3–5 m of levee relief and 350 m width and then is buried (**Fig. 6.1B; Fig. 10.4.2**). The proximal part of channel B is partially buried by the channel-levee complex of channel A. This confirms that channel B is older than channel A and that channel B is twice the size of the distal channel A at the same location (**Figs. 6.1B and 6.1E**). In the inner Selenga Fan, the youngest channel A has a surface expression for 24 km and terminates at the end of the inner fan (**Fig. 6.1B**). The proximal channel A is ~450 m wide, with levee heights of 12–13 m, but the width decreases at the end of inner fan to 200 m and levee heights decrease to 4–5 m (**Fig. 6.1B; Fig. 10.4.2**).

The longest surface lobe (4) developed in the late Pleistocene (MIS 2) and ends 69 km from the Selenga Canyon mouth (**Fig. 6.1B**) (Nelson et al., 1995). Older subsurface lobes 1, 2, and 3 extend as much as 80 km from the canyon mouth (**Figs. 6.1B and 6.1D**). Any possible lobe at the end of channel A cannot be defined because of the overlapping lateral slope failures from the eastern ramp margin and the interfingering of a network of channel-levee complexes (**Figs. 6.1B and 6.1E**).

6.3 Climatic control of the Lake Baikal turbidite systems

Late Pleistocene glacial advance and retreat, plus development of tundra and/or steppe landscapes, increased the rates of erosion and sediment supply to the Baikal turbidite systems, and glacial meltwater dominated the sediment transport processes in the Baikal region (Shichi et al., 2009; Vologina and Sturm, 2009). All turbidite systems exhibit a decrease of sediment supply, channel size, and length of outer lobes during the transition to Holocene climate, when vegetation changed from tundra to birch and pine forests as glaciers receded (**Figs. 6.1 and 6.2; Fig. 10.4.2**) (Shichi et al., 2009).

6.3.1 Central Basin

The Selenga Fan had its last maximum growth during the late Pleistocene MIS 2, as shown by the increased sedimentation rates and maximum extent of the surface lobe 4, 69 km from the canyon mouth (**Figs. 6.1B and 6.1D**) (Nelson et al., 1995, 2009). While climate ameliorated after the Last Glacial Maximum (ca. 20 ka) (Osipov and Khlystov, 2010), the outer fan surface lobe 4 retreated ~55 km to a position at the end of the youngest channel A as sediment supply decreased (e.g., 75% reduction in sediment rates) (**Figs. 6.1B and 6.1D**) (Nelson et al., 2009). The longer and older subsurface Selenga outer fan lobes 1–3 apparently developed during previous Pleistocene glacial climatic episodes. Except for surface lobe 4, there are no ages for the subsurface lobes, but the lobes repeat every ~120 ms (two-way travel time) in the seismic data, or ~90–100 m (**Fig. 6.1D**). Assuming a typical average Pleistocene turbidite system sedimentation rate of ~100 cm/k.y. (Nelson and Nilsen, 1984), which is also observed in some Lake Baikal cores (Nelson et al., 2009), increased lobe growth (i.e., length) would occur every ~100 k.y. These growth stages appear to correlate with orbital eccentricity–driven glacial climatic cycles and increased sediment supply.

Like lobe backstepping, during the transition from MIS 2 to MIS 1 channel C, the largest surface channel on the Selenga Fan, retreated and became the smaller surface channel B (**Fig. 6.1B; Fig. 10.4.2**). Channel B then shrank to the shortest, smallest, and youngest channel A (**Figs. 6.1B and 6.1E**). Similar to this pattern for the oldest surface channels, the largest and oldest subsurface channels also extended furthest out to the distal outer fan lobes (**Fig. 10.4.2**). The change from a larger, older subsurface Selenga Canyon thalweg to the smaller surface thalweg parallels the channel changes on the fan surface that are related to the transition from Pleistocene to Holocene climate (**Fig. 6.1C**).

6.3.2 North Basin

In the North Basin of Lake Baikal, the small sand-rich Frolikha and Tompuda Fans, as well as the base-of-slope aprons, exhibit the same Pleistocene to Holocene depositional trends as the Selenga Fan (**Fig. 6.1A**). The maximum Pleistocene glacial extent and two recessional moraines have been dated at the Frolikha River mouth. At 40–35 ka (MIS 3) the glacier reached its maximum extent, 3–4 km offshore, and by 26–13 ka (MIS 2) the glacier had receded ~9 km inshore from its maximum extent (Back and Strecker, 1998). During the early Holocene, the glaciers in the valleys of both the Frolikha and Tompuda Rivers retreated and finally disappeared (Osipov and Khlystov, 2010). Like the Frolikha Fan, the Tompuda Fan growth was controlled by the North Basin glacial history (Back and Strecker, 1998; Osipov and Khlystov, 2010). The late Pleistocene turbidites of the Tompuda Fan and the base-of-slope aprons exhibit coarser grain sizes, numerous thick sand beds, and net sand content up to 8 times greater during the MIS 2 Pleistocene glacial climate compared to the mud drape with thin silt lamina of the Holocene (Nelson et al., 1995, 2009). Nelson et al. (2009) inferred that the oldest Tompuda Fan lobe reached its maximum extent from the youngest channel during the MIS 2 late Pleistocene glaciation of the Tompuda Valley; we now conclude that the progressive reduction of channel size and backstepping of lobes from 1 to 4 are linked to the regression of the Tompuda Valley glacier (**Fig. 6.2**).

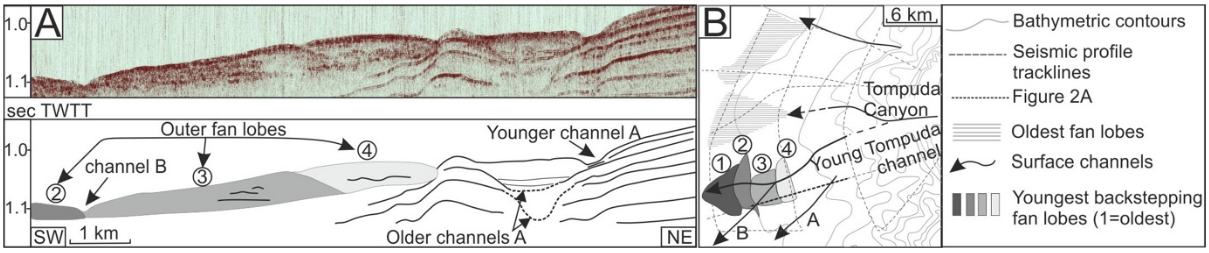

Figure 6.2: The Tompuda Fan (Russia). A: Airgun seismic profile showing lobe backstepping and change from older larger channels to younger, smaller channel A (dashed lines). B: Map view of backstepping from oldest (1) to youngest (4) outer fan lobes of Tompuda Fan. Dashed line in B shows profile A location. Modified from Nelson et al. (2009).

6.4 Implications for marine turbidite systems

The sand-rich Tompuda Fan and base-of-slope aprons in the North Basin, as well as the mud-rich Selenga Fan in the Central Basin, are different types of turbidite systems, but they all exhibit the same depositional history related to climate change effects on vegetation and glaciation. These Baikal turbidite systems all show evidence of maximum size and growth rates and greater sediment supply during the late Pleistocene glacial climate (**Figs. 6.1 and 6.**; Nelson et al., 1995). Other turbidite systems worldwide exhibit similar climatic-driven control on sediment supply and fan growth. The number of turbidite systems on the present seafloor doubled during the Pleistocene (Nelson and Nilsen, 1984); this emphasizes the importance of climate-related sediment supply. Like the Lake Baikal climatic control, most marine systems show thick turbidite deposition in the latest Pleistocene MIS 2 until the mainly hemipelagic deposition beginning in MIS 1 (ca. 13 to 12 ka), even while sea level was rising ~70 m (e.g., Nelson and Nilsen, 1984; Nelson et al., 1995).

When the Mediterranean Sea underwent significant sea-level lowering during Pleistocene glacial climates, the sediment supply of the Ebro turbidite systems from the Ebro River was an average of 15 × 106 t/yr, whereas during the Pliocene and Holocene times of high sea level and warmer climates it supplied an average of 5–6 × 106 t/yr (Nelson, 1990). Although the effects of climate and sea level are combined in these systems, pollen records show that during the Pleistocene glacial climates, the Pyrenean pine forests and Ebro Basin oak forests changed to grasslands. During the Holocene warm climate the forests returned, until humans deforested the Ebro drainage basin, similar to Pleistocene climate change, and the sediment supply reached 22 × 106 t/yr.

The Rhône Fan exhibits a reduced MIS 2 to MIS 1 sediment supply, because the youngest fan lobe (Neo fan), fed by the youngest Rhône Fan channel, ends on the inner fan (Droz and Bellaiche, 1985) just like the Selenga Fan channel A (**Fig. 6.1B**). This retreat of the Rhône Fan channel, similar to channel A, indicates the importance of Pleistocene to Holocene climate change on sediment supply and turbidite system growth.

System growth is mainly unrelated to lower sea levels, because sea level lowering contributes a <10% increase in sediment supply from river incision (Blum and Tornqvist, 2000). Although lower sea level results in more direct sediment access to marine turbidite systems, this low sediment input from river incision suggests that glacial climate change, causing increased sediment supply, is a significant controlling factor for Pleistocene lowstand fan growth.

6.5 Conclusions

This study emphasizes the importance of Pleistocene climatic control on sediment supply to deep-water turbidite system growth that is unrelated to lowered sea level. The depositional history of Lake Baikal turbidite systems shows that maximum sedimentation rates, net sand percent, turbidite bed thickness, channel size, and fan lobe extent occurred during the late Pleistocene glacial melt period. In contrast, smaller and shorter channels evolved and lobes backstepped as the warmer Holocene climate developed, glaciers disappeared, and forests grew. The importance of climatic control for the robust development of Pleistocene turbidites in Lake Baikal is shown, because with nearly constant lake level, the late Pleistocene to Holocene lithologic changes in Baikal are the same as marine turbidite systems with ~120 m of sea-level lowering. Marine turbidite systems also show the importance of climate as a key driver of turbidite system development, because of the doubled number of Pleistocene- age submarine fans on the present seafloor, significant turbidite deposition during rising MIS 2 sea level, and Pleistocene to Holocene reduction in sediment supply from rivers (e.g., the Ebro). The dominant glacial climatic control on Lake Baikal turbidite system growth suggests that climatic control on vegetation changes, glacial erosion, and glacial meltwater fluxes unrelated to sea-level changes may have been much more important than previously believed, not only in Pleistocene turbidite systems, but perhaps also for ancient turbidite systems.

Chapter 7

Synopsis & General Discussion

The results of this PhD Thesis advance our understanding on the evolution of the Antarctic Circumpolar Current and its interactions with the cryosphere during past warm climates and major climate transitions of the Cenozoic. Here, we first discuss our findings regarding the evolution of the Antarctic Circumpolar Current (ACC) from the time of its initiation to the establishment of the present-day vigorous, deep-reaching ACC flow. We then discuss our major results focusing on the Southern Ocean - ice sheet interactions offshore the Wilkes Land margin between (24-23 Ma) and across the second major glaciation in Antarctica (23.03 Ma). In addition, we discuss sea level and climate controls on deep-water deposition in these two sectors of the Antarctic margins and in the glaciated Lake Baikal basin.

7.1 The Antarctic Circumpolar Current evolution

Our study on sediments from the Deep Sea Drilling Project (DSDP) Sites 269, 274 and 278 across both sides of the Tasmanian Gateway provides key insights into the evolution of the Antarctic Circumpolar Current (ACC) from its development to the formation of an ACC similar to the present-day: vigorous and deep-reaching (**Chapters 3, 4 and 5**). We focused our analyses on tracking the evolution of Circumpolar Deep Water (CDW), using Neodymium (Nd) isotopes of ambient seawater in fossil fish teeth and bones. CDW is the most voluminous water mass in the Southern Ocean, occupying the shallow to deep layers of the ACC (Orsi et al., 1995). Today, CDW has a vertically and horizontally homogenous Nd isotopic isotope composition, probably due to the strong vertical and horizontal mixing along the ACC frontal systems (e.g., Carter et al., 2012; Stichel et al., 2012; Lambelet et al., 2018). Therefore, the evolution of the Nd isotope composition of CDW in the past provides critical insights regarding ACC interbasin connections/circulation in the Southern Ocean. Based on our studies we determine three major phases of the ACC evolution: from 34 to 30 Ma, from 30 Ma to 4 Ma, and from 4 Ma to present.

7.1.1 The late Eocene-early Oligocene epoch (41-30 Ma): Before the formation of the Antarctic Circumpolar Current

Despite the controversies regarding the timing of the opening of the Drake Passage ranging from ~ 49 to 11 Ma (Barker et al., 2007; Dalziel, 2014), the first influx of shallow Pacific waters into the South Atlantic Ocean via the Drake Passage and the formation of a proto-polar front (PF), are reported during the late Eocene between 41 and 37 Ma (Diester-Haass and Zahn, 1996; Scher and Martin, 2006). To the west of the Tasmanian Gateway, a Neodymium (Nd) isotope signature resembling that of the modern CDW was reported along the proto-PF in the South Atlantic and South Indian Oceans as far as the Kerguelen Plateau between the late Eocene and early Oligocene (37.8-30 Ma) (Scher and Martin, 2004, 2006, 2008; Scher et al., 2014; Wright et al., 2018). This suggested the existence of an eastward flowing proto-CDW to the west of the Kerguelen Plateau at that time. However, to the east of the Kerguelen Plateau, data from offshore the Wilkes Land margin, located south and near the proto-PF on the western side of the Tasmanian Gateway, indicate the presence of westward flowing bottom waters before ~28 Ma (Salabarnada, 2020). This was attributed to the presence of proto-Antarctic bottom waters bathing this region, which points to proto-CDW not extending to the seafloor in this margin before 28 Ma.

Neodymium isotope records from the South Pacific Ocean also report on the existence of a westward flowing deep water interbasin connection in the northern parts of the Tasmanian Gateway between 32 and 30 Ma (Scher et al., 2015). This was interpreted to result from intermediate/deep waters from the Pacific Ocean flowing westwards into the Indian Ocean, under the influence of the Antarctic Counter Current (Houben et al., 2013, Scher et al., 2015; Houben et al., 2019). Altogether, these findings argue against an eastern flow of deep waters from the Indian Ocean into the Southwest Pacific before 30 Ma.

Our neodymium isotope records at Sites 274 and 278, located directly on the eastern side of the Tasmanian Gateway and covering a depth range of ~2500-4000 m (**Chapter 3**), do not record an eastward transport of proto-CDW across the gateway and into the Southwest Pacific between 34-30 Ma, supporting the results from Scher et al. (2015). In addition, the similarities between our Nd isotope values from Site 278 (Southern Emerald Basin, paleodepth: ~4000 m) and those published from the deep/abyssal South Pacific (paleodepth~4000-5000 m) between 31-30 Ma, show the presence of a common deep/bottom water mass in the deep/abyssal Southwest Pacific, such as South Pacific Deep Water (SPDW).

In contrast, our Nd isotope data from Site 274 (Adare Basin, paleodepth: ~ 2500-3000 m), located proximal to the Ross Sea, overlap with the values reported from the north side of the Tasmanian Gateway (paleodepth~2500-3800 m) (Scher et al., 2015). This suggests that these sites may have been influenced by a common water mass with a more equatorial-Pacific-like Nd signature. Prior to the onset of the ACC, the major oceanographic feature in the Pacific side of the Tasmanian Gateway was the proto-Ross Sea gyre/Tasman Current, which flowed along Antarctica´s Pacific margin and extended northward along the east side of Tasmania and Australia turning to the east north of the New Zealand (Huber et al., 2004; Stickley et al., 2004; Sijp et al., 2011; Bijl et al., 2013). We suggested that the Ross Sea gyre transported deep waters to the Adare Basin (Site 274), and the northern side of the Tasmanian Gateway.

Altogether, these findings indicate the absence of an eastward deep water connection in the Southern Ocean via the Tasmanian Gateway between 41-30 Ma, implying that an ACC did not exist prior to 30 Ma. In addition, we found the presence of two distinct deep water masses in the late Eocene/early Oligocene South Pacific (34-30 Ma), one occupying depths between ~2500-4000m and a second deep/bottom water mass at >= 4000m.

7.1.2 Onset and evolution of a proto-Antarctic Circumpolar Current (30-4 Ma)

Neodymium isotope values at Site 274 record a major change at ~30 Ma, related to the influx of deep waters (i.e. proto-CDW) via the Tasmanian Gateway into the Pacific (**Chapter 3**). Our results are consistent with the Nd isotope records from the northern side of the Tasmanian Gateway, also suggesting the onset of eastward flowing deep waters across the Gateway at around 29-30 Ma (Scher et al., 2015). This shift has been linked to the northward migration and alignment of the Tasmanian Gateway with the westerly winds (Scher et al., 2015). Given that Site 274 was located south of the newly formed proto-PF in the South Pacific around 30 Ma, we link this change to the onset of proto-CDW upwelling reaching the site location.

Site 278, on the other hand, was located along the proto-PF and proto-SAF between 30 Ma and 20 Ma and thus, in the main pathway of the proto-ACC and proto-CDW. Comparison between our new and previously published Nd data in the Southwest Pacific Ocean and Nd isotope records along the proto-PF in the South Atlantic and South Indian Ocean (Scher and Martin, 2004, 2006, 2008; Wright et al., 2018) shows a disparity in Nd values (**Chapter 3**). We interpreted this prominent offset in the Nd composition of deep water composition across the Tasmanian Gateway to result from a shallower and weaker ACC flow entering the Southwest Pacific. Our inferences are consistent with numerical simulations showing limited throughflow of the proto-ACC due to topographic constrains in the Australasian basin during the Oligocene (Hill et al., 2013). Numerical models also point to a weaker global overturning circulation due to weaker westerly winds from the early to mid-Miocene (Herold et al, 2012). Model simulations are supported by sedimentological data, microfossil assemblages and past reconstructions of sea surface temperatures from the Antarctic-Australian side of the Tasmanian Gateway, which also infer a weaker proto-ACC frontal system, allowing intrusion of warm waters from northern latitudes from the Oligocene to the middle Miocene (34-11 Ma) (Bijl et al., 2018b; Hartman et al., 2018; Salabarnada et al., 2018; Sangiorgi et al., 2018) (**Chapter 3**).

In summary, our findings indicate the existence of an eastward connection in the Southern Ocean via the Tasmanian Gateway. However, the circulation was characterized by the presence of a shallower and weaker ACC (proto-ACC) than today at least until the early Miocene (~19 Ma). As a result, a disparity in Nd values across the Tasmanian gateway is recorded instead of the homogeneous values that characterize the modern CDW around Antarctica. This implies that the modern strong and deep-reaching ACC flow must have been developed at a later point in the Neogene (i.e., after 19 Ma).

As Site 278 remained in the main pathway of the ACC through the Neogene, its sediments have allowed to provide key insights into the evolution of the ACC in the Southwest Pacific from the early Miocene to the late Pleistocene (20 Ma-500 kyr) (**Chapter 4**). Our Nd isotope record reports a gradual increased contribution of NADW into the proto-CDW in the Southwest Pacific between 20 Ma and 4 Ma. This long-term trend coincides with a progressive increase of deep water current flow speeds during the same period, demonstrated by sortable silt analyses at Site 278. Based on the above we suggest that the gradual strengthening of the proto-ACC flow allowed the higher preservation of NADW-like Nd into the proto-CDW along the proto-PF in the Southwest Pacific. We link the progressive strengthening of the proto-ACC to the gradual global cooling during the Neogene, resulting in increased meridional atmospheric and surface ocean temperature differences, cooled surface waters and subsequently led to stronger westerlies and invigorated Southern Ocean geostrophic circulation (Cortese et al., 2004).

7.1.3 The establishment of the modern-like, strong deep Antarctic Circumpolar Current 4 million years ago

Sediments from Site 278 record a major reorganisation of the ACC at ~4 Ma (**Chapter 4**). This is the first time when the South Pacific deep water Nd isotope values (i.e. Site 278) converge with those from the South Atlantic and South Indian Nd records along the main pathway of the ACC. This suggests a homogenization of CDW in the Southern Ocean ~ 4 Ma. At the same time, grain-size analyses demonstrate a permanent shift to stronger deep ACC flow speeds, with values resembling the modern bottom current flow in the area. In addition, the onset of enhanced siliceous productivity at Site 278 is related to stronger upwelling activity within the polar frontal system. We interpret the combination of these marked changes in our record to reflect the establishment of the modern homogeneous and vigorous deep-reaching ACC around 4 Ma ago.

To our knowledge this is the youngest age estimate for the onset of the modern-like ACC, which contrasts with other estimates linking it to the final development of the deep opening of the Southern Ocean gateways (41- 6 Ma) (e.g., Barker et al, 2007; Dalziel, 2014). Although a weak frontal system (proto-ACC) developed as a result of the separation of the two last land barriers forming the Tasmanian and the Drake Passages, the last step towards the establishment of the modern ACC does not appear related to any known tectonic event in these Gateways (Barker et al., 2007; Dalziel, 2014). However, the observed onset of the modern-like ACC takes place following a major tectonic step in the closure of the Panama seaway reported to occur between 4.7 and 4.2 Myr ago (Haug and Tiedemann, 1998; Haug et al., 2001). The gradual emergence of the Central American seaway forced the intensification of the global meridional overturning circulation and North Atlantic Deep waters production (Haug and Tiedemann, 1998; Ravelo and Andreasen, 2000; Haug et al., 2001; Osborne et al., 2014). This new tectonic-driven ocean re-organisation likely forced the intensification of the ACC.

Given the relevance of the ACC in the global climate system today (Olberns et al., 2004; Rintoul, 2018), we attempt here to decipher the effects that the establishment of the modern vigorous ACC must have had in the global climate and ocean circulation. We posit that the establishment of the strong deep ACC at ~4 Ma led to the thermal isolation of Antarctica from warm surface subtropical waters, strong upwelling of CDW in the Southern Ocean and intensified teleconnections with lower latitudes. Previous studies have reported summer sea surface temperature cooling in the Southern Ocean of more than 5°C recorded during the warm Pliocene interglacials (i.e., 4.8 to 3.7 Ma) (Whitehead and Bohaty, 2003; Escutia et al 2009) to ~2.5°C at 3.5 Ma (Escutia et al., 2009). Further cooling of 2°C between 3.3-3 Ma was accompanied by sea ice and Antarctic ice sheet expansion (McKay et al., 2012; Hillenbrand and Cortese, 2006; Karas et al., 2019). There is therefore evidence for cooling around Antarctica starting at 3.7 Ma may have been pre-conditioned by the onset of the vigorous modern-like ACC. Further studies may reveal the potential relationship between this strengthening of the ACC with the onset of permanent Northern Hemisphere glaciation and the shift to a bipolar-glaciated world at 2.75 Ma (Zachos et al., 2001).

Moreover, stronger CDW upwelling in the Southern Ocean has been linked to increased primary productivity (Cortese et al., 2004; Kara et al., 2019). This is supported by numerical modelling showing drastic changes in the ACC and CDW at the Pliocene-Pleistocene transition (3.2-2.6 Ma), which likely led to the convergence of deep water mas properties in the North Atlantic and North Pacific Ocean as

CDW became the common source (Hill et al., 2017). Evidence from sediments in the Southwest Atlantic detect that the modern Antarctic Intermediate Water properties gradually established over the last 3 Ma, resulting from stronger vertical mixing in the polar front and pronounced CDW upwelling (Karas et al., 2019). Additionally, the onset of the modern-like ACC likely forced the increased subsurface delivery of cooler and nutrient-rich waters from the Southern Ocean via Antarctic Intermediate Water to major lower-latitudes coastal upwelling areas, driving enhanced primary productivity in these regions (Etourneau et al., 2009, 2012).

Based on the above, the drastic changes reported in the Southern Ocean and at low latitudes, (Haug and Tiedemann, 1998; Ravelo et al., 2004; Etourneau et al., 2012; McKay et al., 2012) could have been related to the onset of the modern-like ACC. Our findings therefore reclaim the role of ACC in the global climate evolution and development of the bipolar-glaciated world.

7.2 Ocean-Cryosphere interactions

Past ocean-cryosphere interactions are one of the main unknowns today even though they are very relevant to our understanding the future stability of the Antarctic ice sheets and to inform models that are used to forecast future changes. Our study on the eastern Wilkes Land margin sector between 24-23 Ma provide key insights into the interactions between the ocean and the cryosphere prior to the second major Antarctic glaciation (Mi-1 event 23.03 Ma) (**Chapter 5**).

7.2.1 Antarctic ice sheet and Southern Ocean interactions during the late Oligocene (24-23 Ma)

Previous studies on sediments from the continental rise off the eastern Wilkes Land margin (IODP Site U1356) 250 km landward from Site 269, suggest that the East Antarctic ice sheet was retreated into the continent and did not reached the coast during the late Oligocene (26-25 Ma) (Salabarnada et al., 2018). Moreover, temperate sea surface temperature and absence or reduced sea ice prevailed over this period (Bijl et al., 2018b; Hartman et al., 2018; Salabarnada et al., 2018). In addition, oceanic frontal system migrations followed glacial-interglacial cyclicity, driven by obliquity forcing (Salabarnada et al., 2018). The presence of carbonated sediments at Site U1356 suggests reduced AABW production and expansion of proto-CDW closer to the Antarctic margin during warm interglacial periods between 26-25 Ma (Salabarnada et al., 2018). In contrast, during glacial times, more AABW occupied the continental rise offshore the Wilkes Land margin and intrusion of proto-CDW decreased (Salabarnada et al., 2018). Deposition of large stacked debris flow deposits at Site U1356, between ~24.76 Ma and 23.23 Ma (Escutia et al., 2011; Passchier et al., 2018, Salabarnada, 2020) provide limited information regarding changing ocean configurations in this margin during the latest Oligocene-early Miocene. This interval includes a climate threshold that led to the development of the second major glaciation in Antarctica in this margin (Mi-1 event; 23.03 Ma; Miller et al., 1991; Zachos et al., 2001). In addition, ocean configuration reconstructed at Site U1356 are based on a single location. Therefore, additional sites ideally in a latitudinal transect, are needed to determine the regional configuration of the oceanic frontal system and its variability during the Cenozoic. This information is key for example, to better understand ocean-cryosphere configuration/interactions during the warm late Oligocene and during the cooling trend that culminated in the Mi-1 event.

Our multi-proxy analysis at Site 269 including sedimentological, palynological, geochemical and isotopic data, provides the first record of ocean configuration for the eastern Wilkes Land margin during the late Oligocene (24-23 Ma) (**Chapter 5**). This section includes the paleoenvironmental record that at Site U1356 is masked by massive debris flow deposition. Our results show that during the latest Oligocene the proto-ACC frontal system remained weaker compared to that of the present-day, allowing warm subtropical waters to continue to reach close to the Antarctic margin, while upwelling was sluggish. In addition, sea surface temperatures were higher and sea ice was reduced or absent. Moreover, reduced AABW export caused proto-CDW expansion closer to the Wilkes Land margin. We identified three major changes in this sector of the Southern Ocean: (i) at 24 Ma, (ii) 23.6 to 23.2 and (iii) 23.23 to 23.03 Ma that can be linked to major changes in the ice sheets on the Wilkes Land.

As shown in **Chapter 5**, at 24 Ma sediments from Site 269 record a northward migration of the ACC frontal system, coinciding with the initiation of stronger bottom flow velocities in the abyssal plain. Neodymium isotopes from fossil fish teeth at Site 269 identify proto-CDW was bathing the site with some contribution of Antarctic Bottom Waters produced in the Adélie Coast during glacial times. In addition, at 24 Ma a marked shift in sedimentation is shown by the start of deposition of coarse-grained deposits at Site 269. We correlate the start of coarse-grained sediment depositions at Site 269 with the start of mass transport deposits at Site U1356, resulting from sediment instability at the outer shelf and upper slope as ice sheets advanced into the outer Wilkes Land continental shelf (Escutia et al., 2011, 2014; Salabarnada, 2020). Site 269 provides therefore an age constraint for the start of ice sheet expansion into the Wilkes Land continental shelf at 24 Ma coinciding with the beginning of cooling trend leading to the Mi-1 isotopic event in the Southern Ocean. The timing of this major ice sheet advance in the Wilkes Land margin, coincides with the expansion of the ice sheet in the Ross Sea sector and the transition from continental to marine-based ice sheets, reported at around 24.5-24 Ma (Kulhanek et al., 2019; Levy et al., 2019). This concurrent expansion to marine-based ice sheet in Wilkes Land and Ross Sea sector suggests a major expansion of the East Antarctic Ice sheet. The expansion of the ice sheets into the marine system has been linked to intensification of the ocean-ice sheet dynamics driven by obliquity forcing, influencing the ocean heat transport (i.e., proto-CDW intrusions) across the Antarctic continental margins (Levy et al., 2019).

Between 23.6 and more pronounced at 23.2 Ma we find evidence of a prominent poleward ACC frontal system migration and expansion of proto-CDW close to the Antarctic margin. This observation, implies warmer waters closer to the Antarctic margin within an overall climate cooling when frontal migrations are expected northward. The poleward migration actually occurs at 23.23 Ma towards the end of the sharp cooling depicted in the benthic isotopic record and just prior to the Mi-1 event (23.03 Ma; Miller et al., 1991; Zachos et al., 2001). This is one of the most prominent intrusions of proto-CDW during the late Oligocene (24-23 Ma), as indicated by the high preservation of carbonate in the sediments at Site 269 and *in situ* sediments intercalated between the debris flows at Site U1356 (Salabarnada, 2020).

Between 23.23 to 23.03 Ma, seismic profiles and sediments from Site U1356 record a permanent shift from debris flow-dominated sedimentation to predominantly turbidite deposits, which is accompanied by a drastic decrease in sedimentation rates (Escutia et al., 2011; Tauxe et al., 2012;

Salabarnada, 2020). This change in depositional style has been linked to the onset of marine-based ice sheets in this margin as a result of the deepening of the Wilkes Subglacial Basin due to isostatic loading and elevated erosional rates during successive ice advances (Salabarnada, 2020). These results ground-truth and constrain the timing of modelled bedrock topography reconstructions indicating major erosion and deepening of the Wilkes Subglacial Basin during the Oligocene (Paxman et al., 2019). The timing of this event coincides with the cooling and ice sheet expansion leading to the Mi-1 event as documented in the δ^{18}O isotopic deep-sea records (e.g., Zachos et al., 2001; Beddow et al., 2016; Liebrand et al., 2011) and a drop in SST values (from 12.5 °C to 9.5 °C) measured in sediments from Site U1356 (Hartman et al., 2018).

In the absence of data, we can only hypothesize about a likely a causal relationship between the prominent expansion of proto-CDW close to the Antarctic margin just prior to the Mi-1 glacial expansion. A feedback mechanism has been suggested that links the poleward transport of warmer water masses, increased precipitation in the Antarctic continent, and buildup of the continental Antarctic ice sheet during the Pliocene (Billups et al., 1998), late Miocene (Kong et al., 2010) and Pleistocene times (Suganuma et al., 2014). However, additional data are needed to confirm or not if that similar mechanisms forced ice sheet expansion across the Oligocene Miocene Transition (~23.2-23 Ma).

7.3 Controls on deep-water deposition on glaciated margins

Our study on development of the Lake Baikal turbidite systems during the late Quaternary improve our understanding on the climate control on deep sea sedimentary processes and their sedimentary products in glaciated margins (**Chapter 6**).

Deposition of the studied deep-water sedimentary sections across the Tasmanian Gateway is the result of the interplay between different processes. As discussed in the different chapters of this thesis, deposition at Sites 269 and 274, is greatly influenced by the evolution of the Antarctic ice sheet and oceanic bottom currents, which in turn is controlled by climatic changes. The effects of the evolution of the Antarctic continental ice sheet in deep-water deposition are complex, which go beyond the control exerted by advances and retreats in the delivery of terrigenous sediment to the margin. For example, the topography of Antarctica during the Late Eocene and Oligocene was very different to the one today (e.g., Wilson et al., 2011). Low-lying lands characterized areas during the Eocene and part of the Oligocene that are now below sea level. As discussed in the previous section, successive advances of the ice sheets during the Oligocene eroded and transported materials from land to the ocean contributing to the deepening of these basins. Moreover, since the first expansion of a continental-size Antarctic ice sheet around 34 Ma, Glacial Isostatic Adjustment has also played a major role in deepening the topography of the Antarctic margins (e.g., Stocchi et al., 2013) causing deepening of onland basins and the continental shelf to acquire its reverse sloping profile (i.e., deeper areas of the Antarctic continental shelf are deeper than the outer shelf). Glacial isostatic adjustment has also had an important role in the delivery of sediment to the Antarctic margins. As ice sheets grow the increase weight causes the crust below the ice to sink and, as these massive ice sheets reach the coast, they also exert a gravitational attraction in the water mass of the ocean causing, near the Antarctic coasts, the sea level to rise instead of the expected sea level lowering (e.g., Stochhi et al., 2013). The opposite is true during ice sheet retreat, when around the Antarctic margins sea level is lowered contrary to the global sea level rise. All these processes have an effect in the volume and type of sediment delivered to the deep sea, both because sediment availability and through the creation/destruction of depocenters.

Of the processes above, sea level lowering is often cited as the main control on the delivery of sediments to the deep-sea (i.e., turbidity flows, mass transport systems, etc). However, given the different patterns of sea lowering/rising around the Antarctic margins due to the gravitational attraction of the ice sheet on the ocean, it is necessary to further investigate water level control in deep-sea sedimentation.

Lake Baikal is a perfect natural laboratory to study the climatic and ice sheet influences on different types of turbidite systems, because (i) although it has experienced relative changes in lake levels of hundreds of meters in the Quaternary, these changes can be linked to the well constrained tectonic history, (ii) during glacial times glaciers extend to the lake, and (iii) is part of one of the most active continental rifts in the world and abundant evidence show the large-amplitude tectonic movements (Hutchinson et al., 1992; Mats, 1993; Back and Strecker, 1998; Colman et al., 1998). Ongoing tectonic activity has been suggested to be sufficient to account for the lake level changes by displacements of lake outlet and nearshore features. However, the morphology and hydrology of lake Baikal make its water level insensitive to climate changes (Colman et al., 1998). From the documented lake level fluctuations, less than about 2m has been driven solely to climate change (Colman et al., 1998). Therefore, studying deep sea deposition on lake Baikal can provide key insights into the glacial climate influence on sedimentation that can be used to other complex setting where changes in sea level due to climate are difficult to separate from other factors controlling sedimentation, such as in Antarctica.

Our analysis of high-resolution bathymetry and reflection seismic data compared with records from sediment cores shows that during Pleistocene glacial climates, turbidite systems exhibit increased sediment supply (high sedimentation rates, high net sand percent, thick sand turbidites) and progradation (**Chapter 6**). In contrast, during Holocene interglacial climate, all systems exhibit reduced sediment supply and retreat (**Chapter 6**). These changes are similar to other deep sea marine turbidite systems developed in margins with ~120 m of sea level lowering during glacial times. Hence, our study emphasizes the importance of Pleistocene climatic control on sediment supply to deep water turbidite system growth that is unrelated to sea level and tectonics. The Lake Baikal and other marine turbidite systems in major river system in the Mediterranean Sea (Nile, Rhone and Ebro) (Nelson et al., 1990) suggest that climate may have been a much more important control for turbidite systems than previously believed, not only during the Pleistocene, but perhaps also for ancient systems.

Our results have important implications for deep sea sedimentation and evolution of depositional system in glaciated margins such as offshore the Antarctic margin, which are governed by a complex interplay between ice sheet dynamics, sea level changes and tectonic control.

Chapter **8**

Summary & Conclusions

The overarching aim of this PhD thesis is to advance our understanding on the evolution of the Antarctic Circumpolar Current (ACC) and its interactions with the cryosphere during past warm climates and major climate transitions of the Cenozoic using the sedimentary record across the Tasmanian Gateway.

The results presented in this PhD thesis highlight novel and significant insights into the evolution of the Antarctic Circumpolar Current since the Oligocene (34 Ma) and the establishment of vigorous deep-reaching ACC, similar to today´s during the Pliocene (4 Ma). In addition, we provide new constrains into ocean-ice sheet interactions offshore the Wilkes Land margin between (24-23 Ma) prior and during the second major glaciation in Antarctica that culminated at 23.03 Ma. Lastly, our results from the study Lake Baikal turbidite systems highlight the role of climate control unrelated to sea level changes and tectonic effects on the development of deep-water turbidite systems in glaciated margins. Below, we summarize the major findings of this PhD Thesis within the framework of the four research objectives presented in the thesis outline

Objective 1: *Reconstruct the evolution of Circumpolar Deep Water (CDW) across both sides of the Tasmanian Gateway between the Oligocene and early Miocene (34-19 Ma) (Chapter 3).*

- We provide with the first constraints on the evolution of proto-CDW in the Southwest Pacific during the Oligocene and early Miocene (34-19 Ma) based on neodymium isotopes data from fossil fish teeth in sediments from Sites 278, 274, and comparisons with published Nd records from the Indian Ocean side of the Gateway (e.g., Site 269).

- We report the first Nd isotope record close to the Antarctic margin in the Ross Sea (Site 274) during the Oligocene (~34-23 Ma). This record reveals two major shifts through time in response to major steps in Antarctic ice sheet expansion: at the Eocene-Oligocene (33.7 Ma) and at the late Oligocene (24.5-24 Ma). A third shift around 30 Ma seems more closely related to upwelling proto-CDW in the Southwest Pacific.

- We report the first Nd isotope data from a site (Site 278) located in the abyssal plain along the proto Polar front (proto-PF) between 31-30 Ma. This record indicates that abyssal sites in the South Pacific were not bathed by a proto-CDW at this time, instead they were likely influenced by South Pacific Deep Water.

- Comparing our Nd isotopic records with previously published data, we suggest the presence of two deep water masses in the South Pacific prior to the inferred onset of the ACC (34-30 Ma): one occupying Site 274 at depths between ~2500-4000m (Equatorial-like Pacific Deep Water) and a deep/bottom water mass occupying Site 278 at depths >= 4000m (South Pacific Deep Water).

- Oligocene-early Miocene deep water Nd composition measured along the proto-PF and across the Tasmanian Gateway (i.e., Site 269 in the Indian Ocean, and Sites 274 and 278 in the Pacific Ocean) record different Nd values. This contrasts with the modern homogenous CDW neodymium isotope signature recorded in all the Southern Ocean resulting from the strong vertical and horizontal mixing of the ACC. We attribute the offset in the Nd isotope composition of deep waters across the Tasmanian Gateway to a weaker, less deep reaching ACC (proto-ACC) than today.

- Our finding implies that the modern strong and deep-reaching ACC flow must have been developed at a later point in the Neogene, supporting previous studies claiming the onset before < 11 Ma.

Objective 2: Determine the timing of the establishment of the modern-like, strong, deep-reaching Antarctic Circumpolar Current (Chapter 4).

- We determine that the modern deep-reaching ACC fully established ~4 million years ago. Our interpretation is based on a coeval shift recorded in the sedimentary record at Site 278 towards values/signatures of the modern ACC. At ~4 Ma we record for the first time: (i) the establishment of modern homogenous Circumpolar Deep Water neodymium isotopic composition in the Southern Ocean, (ii) the permanent shift to stronger deep ACC flow speeds, comparable to modern current speed values, and (iii) enhanced siliceous productivity related to stronger upwelling activity such as the one in today´s polar frontal system.

- The onset of the modern-like ACC at ~4 Ma is long after the Tasmanian and Drake Gateway had opened and deepened (~50-10 Ma). This time offset prevents the previously proposed direct link between the opening of these gateways and the onset of a modern-like ACC causing thermal isolation of Antarctica and the growth of the first continental-size ice sheet. It does not prevent however, that water mass exchanges across the gateways as they opened and deepened had an effect on global climate and ice sheet evolution.

- We relate the development of the modern-like ACC at ~4 Ma may be linked to a major step in the closure of the Panamian Seaway between 4.7-4.2 Ma, which has been proposed to trigger the intensification of the global meridional overturning circulation and North Atlantic Deep waters production.

- Our results indicate that the establishment of the modern-like, strong deep-reaching ACC was likely the tipping point that led to the thermal isolation of the Antarctic continent. In this context, we hypothesise that the formation of the modern vigorous ACC could have triggered the Southern Ocean sea surface cooling reported from 3.7 to 3 Ma.

- Further studies are needed to determine any potential link between the onset of the modern-ACC and the shift to bipolar-glaciated world at 2.75 Ma. Our findings therefore reclaim the role of ACC in the global climate evolution and development of the bipolar-glaciated world.

Objective 3: Determine the proto-Antarctic Circumpolar Current dynamics offshore the eastern Wilkes Land margin and its link with the Antarctic ice sheet during the late Oligocene-early Miocene (Chapter 5)

- We determine for the first time the oceanographic configurations in the East Antarctic Wilkes Land abyssal plain during the late Oligocene (~24.2-23 Ma).

- Overall, our results show that during the late Oligocene-early Miocene the proto-ACC frontal system was weaker compared to that of the present-day, allowing warm subtropical waters to reach close to the Antarctic margin. In addition, upwelling was sluggish. Sea surface temperatures were higher than present and sea ice was reduced or absent. Moreover, proto-CDW was circulating closer to the Wilkes Land margin especially during interglacial times (e.g., 23.23 Ma) likely due to reduced AABW export.

- When compared with results from Site U1356 and with numerical modelling, our findings support the notion of a fundamentally different Southern Ocean with a weaker proto-ACC than today during the late Oligocene and earliest Miocene.

- We provide with four snapshots of Southern Ocean evolution between the late Oligocene (from ~24.2 to 24 Ma, at ~24 Ma, from ~23.6 to ~23.23 Ma, and at ~23 Ma) that we link to major changes in the proto-ACC and proto-CDW dynamics.

- Between 24.2 and 24 Ma, proto-CDW was characterised by weak velocities that resulted in low ventilated bottom conditions and likely low organic content. This ocean configuration characterises the warm latest Oligocene a time when ice sheets in Antarctica were retreated to the continent.

- At 24 Ma, and coinciding with the beginning of the cooling trend leading to the Mi-1 isotopic event in the Southern Ocean, a northward migration of the ACC frontal system is recorded. Neodymium isotope signature from fossil fish teeth at Site 269 reveals the presence of proto-CDW and suggest some contribution of Adélie Coast Bottom Water. Proto-CDW currents become stronger resulting in better ventilated bottom conditions and slightly higher organic matter content. This oceanic configuration is coeval with the increase in deposition of coarser-grained material at Site 269, which has been linked with reported ice sheet advances into the continental shelf in this margin.

- At ~23.6 Ma, and more pronounced at ~23.23 Ma, a prolonged expansion of proto-CDW closer to the Wilkes Land margin is indicated by neodymium isotope data, carbonate preservation, and higher Ca values in the sediments. This event represents the most prominent intrusions of proto-CDW during the late Oligocene (24-23 Ma). This observation, implies warmer waters closer to the Antarctic margin within an overall climate cooling when frontal migrations are expected northward.

Objective 4: Decipher climate influence versus other factors controlling deep-water deposition in glaciated margins (Chapter 6).

- We determine that the main control on sediment supply to deep-water turbidite systems in Lake Baikal is controlled by climate and it is unrelated to lowered sea level and tectonic effect.

- Lake Baikal turbidite systems shows that maximum sedimentation rates, net sand percent, turbidite bed thickness, channel size, and fan lobe extent occurred during the late Pleistocene glacial melt period. In contrast, smaller and shorter channels evolved and lobes backstepped as the warmer Holocene climate developed, glaciers disappeared, and forests grew.

- The late Pleistocene to Holocene lithologic changes in Baikal are the same as marine turbidite systems with ~120 m of sea-level lowering.

- The dominant glacial climatic control on Lake Baikal turbidite system growth suggests that climatic control on vegetation changes, glacial erosion, and glacial meltwater fluxes unrelated to sea-level changes and tectonics may have been much more important than previously believed, not only in Pleistocene turbidite systems, but perhaps also for ancient turbidite systems.

Chapter 9

Unsettled issues & Future research directions

The results of this PhD thesis arise new questions that can serve as new research hypotheses for future studies. Because we have studied three sedimentary archives in different time intervals, we present remarks on unsettled issues and limitations, as well as potential future directions for each sedimentary archive.

9.1 Deep Sea Drilling Project (DSDP) Leg 28 Site 269

DSDP Site 269 provides the first record of ocean configuration for the eastern Wilkes Land margin during the late Oligocene (~24-23 Ma) (**Chapter 5**). However, DSDP Site 269 was drilled discontinuously (spot coring), and thus captures only snapshots of the ocean configuration during the late Oligocene (24-23 Ma). Despite the discontinuous core recovery and consequently the challenges in dating the cores, our results provide novel information on the Southern Ocean configurations and the interactions of the Southern Ocean and the Antarctic ice sheet in this margin, during the warm latest Oligocene and prior to one of Earth's main climate transitions that culminated in the development of the second major Antarctic glaciation (Mi-1 event; 23.03 Ma; Zachos et al., 2001).

One unanswered but critical question has arisen from our study on sediments at Site 269. We found that one of the most prominent expansions of proto-CDW close to the Wilkes Land margin in the late Oligocene (24-23 Ma) took place at ~23.2 Ma. Did this pronounced proto-CDW expansion at ~23.2 Ma play a role in preconditioning the second major Antarctic glaciation at 23.03 Ma (Zachos et al., 2001)? Previous studies have suggested that poleward transport of warmer water masses can increase precipitation in the Antarctic continent, and buildup of the continental Antarctic ice sheet (Billups et al., 1998; Kong et al., 2010; Suganuma et al., 2014). This mechanism has been also documented in the North Hemisphere and the establishment of the permanent North Hemisphere glaciation (Haug and Tiedemann, 1998).

The only other deep sea sedimentary archive that recovers the late Oligocene-early Miocene epoch is the Integrated Ocean Drilling Program (IODP) Expedition 318 Site U1356 located on the continental rise of the eastern Wilkes Land margin (Escutia et al., 2011, 2014). While the deposition of large stacked debris flow deposits recovered at Site U1356 between ~24.76 Ma and 23.23 Ma (Escutia et al., 2011; Passchier et al., 2018) provided evidence for the first development of marine ice sheets in this margin as a result of the deepening of the Wilkes Subglacial Basin, it recorded only limited information regarding ocean configurations during the late Oligocene-early Miocene (Bijl et al., 2018b; Hartman et al., 2018; Salabarnada, 2020).

To shed light into the ocean-ice sheet interactions during this major climate transition and address the unanswered question from our study, a future strategy is to obtain (i) new sedimentary archives with better core recovery (continuous coring) in a latitudinal transect across the present-day Antarctic Circumpolar Current fronts offshore the Wilkes Land margin, (ii) sedimentary archives from the continental shelf, and (iii) subglacial drilling. The offshore records can provide a continuous record of the proto-ACC and proto-CDW configurations and frontal migrations through glacial-interglacial cycles and better constraints on time of proto-CDW expansion in this region of the East Antarctic margin. Records from the continental shelf can trace proto-CDW intrusions into the continental shelf that can be linked to grounding line advances and retreats of the ice sheet. The continental shelf records are bound to be discontinuous, but the recovered snapshots of time, if dated, can be then correlated with the records from the continental rise. Subglacial drilling underneath the ice also can provide with valuable snapshots on continental conditions and ice sheet dynamics that can be linked with the continental shelf and offshore records to better reconstruct the ocean-ice sheet dynamics in this margin.

A similar multi-proxy analysis as at Site 269 including sedimentological, micropaleontological, geochemical, biomarkers, palynological and isotopic data sets is suggested, in order to obtain a better understanding of interactions between the East Antarctic ice sheet and the Southern Ocean. IODP Expedition 373 is scheduled, although pending dates, aiming to collect Cretaceous to Oligocene sedimentary archives close to the Antarctic coastline in front of the Wilkes Subglacial Basin. In addition, a proposal has been submitted to collect a transect of sites from north of Sites 269 and U1356 to close to the Australian margin. These programs, when implemented will certainly increase our understanding the role of interactions between the East Antarctic ice sheet and Southern Ocean in their evolution and their relation to the global climate.

9.2 Deep Sea Drilling Project (DSDP) Leg 28 Site 274

DSDP Site 274 was located directly at the nascent deep opening of the Tasmanian Gateway (35-30 Ma (Stickley et al., 2004; Scher et al., 2015) on the Southwest Pacific side and proximal to the Ross Sea. Our results suggest a link between the two major excursions in the neodymium isotope record at Site 274 at ~33.7 and ~23.1 Ma, and the two largest expansions of the Antarctic ice sheet in Cenozoic (Oi-1 event at ~34 Ma and Mi-1 event at 23.03 Ma; Zachos et al., 2001) (**Chapter 3**). This relationship rises new fundamental questions regarding a potential change in the seawater neodymium signature of Ross Sea Bottom Water (RSBW) during major ice sheet expansions due to glacial weathering events delivering terrigenous sediments from different provenances in the Ross Sea shelf. Resampling for fossil fish teeth at higher resolution across both transitions can provide important insights into the timing and duration of these excursions.

Moreover, new sedimentary archives from the continental shelf of the Ross Sea are necessary, in order to capture directly the neodymium isotope composition of RSBW in the Ross Sea shelf during the Oligocene and compare them with results at Site 274. IODP expedition 374 to the Ross Sea has recently recovered a Neogene sequence of sediments in a transect from the continental shelf to the continental rise in the Ross Sea, aiming to trace changes of RSBW in the past (McKay et al., 2018). Although they did not obtain Oligocene sediments, unravelling the Neogene neodymium signature of RSBW during other major glaciations (e.g during the mid-Miocene) might provide important information regarding potential changes in the seawater neodymium signature of RSBW during major glaciations. This information is certainly valuable for the understanding the link between Oligocene major glaciations and potential changes in RSBW neodymium endmember signature. In addition, IODP expedition 378 in the South Pacific recovered Oligocene sections that can be compared with our results (Thomas et al., 2018).

9.3 Deep Sea Drilling Project (DSDP) Leg 29 Site 278

Results from Site 278 provide key insights into the evolution of the ACC over the last ~31 Ma (**Chapter 3 and 4**). Based on our multi-proxy analysis we proposed a new age estimate for the establishment of a strong deep-reaching ACC similar to the present-day at ~ 4 Ma. In addition, our study suggests that the formation of the modern-like ACC at ~4 Ma might have driven major changes in Southern Ocean cooling from 3.7 to 3.5 Ma (Whitehead and Bohaty, 2003; Escutia et al., 2009) and between 3.3-3 Ma (McKay et al., 2012; Karas et al, 2019), resulting in major changes in global climate likely preconditioning the onset of bipolar glaciated world at ~2.7 Ma (Lisiecki and Raymo et al., 2005). Sediments at Site 278 were continously drilled and core recovery was very good (85%) (Kennett et al., 1975). Recovered sediments are dominated by biogenic material (i.e., calcareous nannofossils, siliceous diatoms and radiolarians, and foraminifera). We updated the age model for the Oligocene-early Miocene sections, combining biostratigraphy with new paleomagnetic constraints (**Chapter 3**). However, paleomagnetic data are missing for the upper sections of the site (between the middle Miocene and late Pleistocene) (**Chapter 4**). Our study was based on a low-resolution sampling, aiming to determine long-term changes in the evolution of the ACC. The aforementioned issues did not allow us to determine precisely the timing of the major shift at ~4 Ma and limit our understanding regarding the link between the establishment of the modern-like ACC at ~4 Ma and the major changes observed in the Southern Ocean (3.3-3 Ma) (McKay et al., 2012; Karas et al, 2019).

To address these crucial issues, a future strategy should include: first, the improvement of the age model at Site 278. This is fundamental for obtaining a more precise constraints across the major shift at ~4 Ma. Sampling for paleomagnetic analysis combined with biostratigraphic analysis on diatoms and radiolarians in higher resolution is essential for a robust age model in the upper sections of Site 278. Second, resampling the late Pliocene-Pleistocene (4-2 Ma) sediments at higher-resolution is critical to better determine the timing of the shift. Lastly, it is necessary to conduct similar multi-proxy analysis on other sites from the South Atlantic, South Indian and South Pacific that remained along the ACC and recover Pliocene and the Pliocene-Pleistocene sediments to compare with our results. New sedimentary archives from recent IODP expeditions such as IODP expedition 378 (Thomas et al., 2018) and IODP expedition 387 (Lamy et al., 2019) in the South Pacific and IODP expedition 382 in the Drake Passage region -Iceberg Alley (Weber and Raymo, 2019) will certainly provide new and complementary information that will help to address our outstanding questions.

References

Amakawa, H., Sasaki, K., and Ebihara, M., 2009. Nd isotopic composition in the central North Pacific. Geochimica et Cosmochimica Acta, 73(16), 4705–4719. https://doi.org/10.1016/j.gca.2009.05.058

Anderson, J. B., and Bartek, L. R., 1992. Cenozoic glacial history of the Ross Sea revealed by intermediate resolution seismic reflection data combined with drill site information, The Antarctic Paleoenvironment: A Perspective on Global Change: Part One, p. 231-263. https://doi.org/10.1029/AR056p0231.

Anderson, J. B., Warny, S., Askin, R. A., Wellner, J. S., Bohaty, S. M., Kirshner, A. E., Livsey, D. N., Simms, A. R., Smith, T. R., Ehrmann, W., Lawver, L. A., Barbeau, D., Wise, S. W., Kulhanek, D. K., Weaver, F. M., and Majewski, W., 2011. Progressive Cenozoic cooling and the demise of Antarctica's last refugium: Proceedings of the National Academy of Sciences, v. 108, no. 28, p. 11356- 11360.

Aoki, S., Bindoff, N.L., Church, J.A., 2005. Interdecadal water mass changes in the Southern Ocean between 30^{O}E and 160^{O}E, Geophys. Res. Lett., 32, L07607. doi:10.1029/2004GL022220.

Back, S., and Strecker, M.R., 1998, Asymmetric late Pleistocene glaciations in the North Basin of the Baikal Rift, Russia: Journal of the Geological Society [London], v. 155, p. 61–69, doi: 10 .1144 /gsjgs .155 .1 .0061.

Badger, M.P.S., C.H. Lear, R.D. Pancost, G.L. Foster, T.R. Bailey, M.J. Leng, and H.A. Abeis. 2013. CO2 drawdown following the middle Miocene expansion of the Antarctic Ice Sheet. Paleoceanography and Paleoclimatology 28:42–53, https://doi.org/10.1002/palo.20015.

Bahr, A., Jiménez-Espejo, F.J., Kolasinac, N., Grunert, P., Hernández-Molina, F.J., Röhl, U., Voelker, A.H.L., Escutia, C., Stow, D.A.V., Hodell, D., Alvarez-Zarikian, C.A., 2014. Deciphering bottom current velocity and paleoclimate signals from contourite deposits in the Gulf of Cádiz during the last 140 kyr: An inorganic geochemical approach, Geochem. Geophy. Geosy., 15, 3145-3160. https://doi.org/10.1002/2014GC005356.

Barker, P., and Kennett, J., 1988, Proceedings of the Ocean Drilling Program, scientific results Leg 113: Ocean Drill. Program, v. 774.

Barker, P.F., 2001. Scotia Sea regional tectonic evolution: implications for mantle flow and palaeocirculation. Earth Science Reviews 55, 1 39.

Barker, P.F., Barrett, P., Camerlenghi, A., Cooper, A.K., Davey, F., Domack, E., Escutia, C., Jokat, W., and. O'Brien, P., 1998. Ice sheet history from Antarctic continental margin sediments: The ANTOSTRAT approach. Terra Antarctica 5: 737–760.

Barker, P.F., Burrell, J., 1977. The opening of Drake Passage. Marine Geology 25, 15–34.

Barker, P.F., Filippelli, G.M., Florindo, F., Martin, E.E., Scher, H.D., 2007. Onset and role of the Antarctic Circumpolar Current. Deep-Sea Research II 54, 2388-2398.

Barrett, P. J., 1989, Antarctic Cenozoic history from the CIROS-1 drill hole, McMurdo Sound, Wellington, DSIR Publishing, DSIR Bulletin.

Barrett, P. J., 2013. Resolving views on Antarctic Neogene glacial history – the Sirius debate: Earth and Environmental Science Transactions of the Royal Society of Edinburgh, v. 104, no. 01, p. 31-53.

Barrett, P., 1975. Textural characteristics of Cenozoic preglacial and glacial sediments at Site 270, Ross Sea, Antarctica: Initial Reports of the Deep Sea Drilling Project, v. 28, p. 757-767.

Barrett, P., 2007. Cenozoic climate and sea level history from glacimarine strata off the Victoria Land coast, Cape Roberts Project, Antarctica, in Hambrey, M. J., Christoffersen, P., Glasser, N., and Hubbard, B., eds., Glacial sedimentary processes and products, Volume 39: Oxford, Blackwell Publishing, p. 259-287.

Barron, J., B. Larsen, J. Baldauf, C. Alibert, S. Berkowitz, J.-P. Caulet, S. Chambers, A. Cooper, R. Cranston, W. Dorn, and others. 1989. Proceedings of the Ocean Drilling Program, Initial Reports, Volume 119. College Station, TX, https://doi.org/10.2973/odp.proc.ir.119.1989.

Barron, J., Larsen, B., and Baldauf, J.G., 1991. Evidence for late Eocene to early Oligocene Antarctic glaciation and observations on late Neogene glacial history of Antarctica: results from Leg 119. In Barron, J., Larsen, B., et al., Proc. ODP, Sci. Results, 119: College Station, TX (Ocean Drilling Program), 869–891. doi:10.2973/odp.proc.sr.119.194.1991

Bart, P. J., and De Santis, L., 2012. Glacial Intensification During the Neogene: A Review of Seismic Stratigraphic Evidence from the Ross Sea, Antarctica, Continental Shelf: Oceanography, v. 25, no. 3, p. 166-183.

Basak, C., Pahnke, K., Frank, M., Lamy, F., & Gersonde, R., 2015. Neodymium isotopic characterization of Ross Sea Bottom Water and its advection through the southern South Pacific. Earth and Planetary Science Letters, 419, 211–221. https://doi.org/10.1016/j.epsl.2015.03.011.

Beddow, H. M., Liebrand, D., Sluijs, A., Wade, B. S., and Lourens, L. J., 2016. Global change across the Oligocene- Miocene transition: High-resolution stable isotope records from IODP Site U1334 (equatorial Pacific Ocean), Paleoceanography, 31, 81–97, doi:10.1002/2015PA002820.

Beerling, D. J., and Royer, D. L., 2011, Convergent Cenozoic CO2 history: NatureGeosci, v. 4, no. 7, p. 418-420.

Bergamasco, A., Defendi, V., Zambianchi, E., & Spezie, G., 2002. Evidence of dense water overflow on the Ross Sea shelf-break. Antarctic Science, 14(03). doi:10.1017/s0954102002000068

Bertram, R.A., Wilson, D.J., van de Flierdt, T., McKay, R.M., Patterson, M.O., Jimenez-Espejo, F.J., Escutia, C., Duke, G.C., Taylor-Silva, B.I., Riesselman, C.R., 2018. Pliocene deglacial event timelines and the biogeochemical response offshore Wilkes Subglacial Basin, East Antarctica. Earth and Planetary Science Letters 494, 109-116. https://doi.org/10.1016/j.epsl.2018.04.054.

Bijl P. K, Schouten, S., Sluijs, A., Reichart, G. J., Zachos, J., and Brinkhuis, H., 2009. Early Palaeogene temperature evolution of the southwest Pacific Ocean. Nature 461(7265):776–779.

Bijl, P. K., Bendle, A. P. J., Bohaty, S. M., Pross, J., Schouten, S., Tauxe, L., Stickley, C. E., McKay, R. M., Röhl, U., Olney, M., Sluijs, A., Escutia, C., Brinkhuis, H., and Expedition 318 scientists, 2013. Eocene cooling linked to early flow across the Tasmanian Gateway, P. Natl. Acad. Sci. USA, 110, 9645–9650.

Bijl, P. K., Houben, A. J. P., Hartman, J. D., Pross, J., Salabarnada, A., Escutia, C., and Sangiorgi, F., 2018b. Paleoceanography and ice sheet variability offshore Wilkes Land, Antarctica – Part 2: Insights from Oligocene–Miocene dinoflagellate cyst assemblages, Clim. Past, 14, 1015–1033, https://doi.org/10.5194/cp-14-1015-2018.

Bijl, P.K., Bendle, J.A., Bohaty, S.M., Pross, J., Schouten, S., Tauxe, L., Stickley, C.E., McKay, R.M., Rohl, U., Olney, M., Sluijs, A., Escutia, C., Brinkhuis, H., and Expedition 318 Scientists., 2013. Eocene cooling linked to early flow across the Tasmanian Gateway. Proceedings of the National Academy of Sciences, 110 (24), pp. 9645-9650.

Bijl, P.K., Houben, A.J.P., Bruls, A., Pross, J., Sangiorgi, F., 2018a. Stratigraphic calibration of Oligocene–Miocene organic-walled dinoflagellate cysts from offshore Wilkes Land, East Antarctica, and a zonation proposal, J. Micropalaeontol., 37, 105–138. https://doi.org/10.5194/jm-37-105-2018.

Birkenmajer, K., Gazdzicki, A., Krajewski, K. P., Przybycin, A., Solecki, A., Tatur, A., and Yoon, H. I., 2005, First Cenozoic glaciers in West Antarctica: Polish Polar Research, v. 26, no. 1, p. 3-12.

Biscaye, P.E., 1965. Mineralogy and sedimentation of recent deep-sea clay in the Atlantic Ocean and adjacent seas and oceans. Geol. Soc. Am. Bull.76 (7), 803–832.

Blaga, C.I., Reichart, G.-J., Heiri, O., Damsté, J.S.S., 2009. Tetraether membrane lipid distributions in water-column particulate matter and sediments: a study of 47 European lakes along a north–south transect. Journal of Paleolimnology, 41(3), 523-540

Blum, M.D., and Tornqvist, T.E., 2000, Fluvial responses to climate and sea-level change: A review and look forward: Sedimentology, v. 47, p. 2–48, doi: 10 .1046 /j .1365 -3091 .2000 .00008 .x.

Bohaty, S. M., Zachos, J. C., and Delaney, M. L., 2012, Foraminiferal Mg/Ca evidence for Southern Ocean cooling across the Eocene–Oligocene transition: Earth and Planetary Science Letters, v. 317, p. 251-261.

Borg, S. G., Depaolo, D. J., and Smith, B. M., 1990. Isotopic structure and tectonics of the central Transantarctic Mountains. Journal of Geophysical Research: Solid Earth, 95(B5), 6647-6667.

Bouma, A. H., 1962. Sedimentology of some Flysch Deposits. A graphic Approach to Facies Interpretation, Elsevier, Amsterdam, 168 pp.

Brackenridge, R., Stow, D.A.V., and Hernández-Molina, F.J., 2011, Contourites within a deep-water sequence stratigraphic framework: Geo-Marine Letters, v. 31, p. 343–360, doi: 10 .1007 /s00367 -011 -0256 -9.

Breza, J. R., and Wise, S. W., 1992. Lower Oligocene ice-rafted debris on the Kerguelen Plateau: Evidence for East Antarctic continental glaciation, in Wise, S. W., Jr., Schlich, R., et al., 1992 Proceedings of the Ocean drilling Program, Scientific Results, vol. 120.

Burke, K. D., Williams, J. W., Chandler, M. A., Haywood, A. M., Lunt, D. J., and Otto-Bliesner, B.L., 2018. Pliocene and Eocene provide best analogs for near-future climates. Proceedings of the National Academy of Sciences, 115 (52), pp. 13288-13293.

Burton, K.W., Ling, H-F., & O´Nions, R. K., 1997. Closure of the Central American Isthmus and its effect on deep-water formation in the North Atlantic. Nature, Vol 386. 382-386.

Caballero, R. & Huber, M., 2013. State-dependent climate sensitivity in past warm climates and its implications for future climate projections. Proceedings of the National Academy of Sciences, 110 (35) 14162-14167.

Cande, S. C., Stock, J. M., Mueller, R. D., and Ishihara, T., 2000. Cenozoic motion between East and West Antarctica,Nature, 404, 145–150.

Carter, A., Curtis, M., and Schwanethal, J. 2014. Cenozoic tectonic history of the South Georgia microcontinent and potential as a barrier to Pacific-Atlantic through flow. Geology v. 42 (4), p: 299-302.

Carter, A., Riley, T. R., Hillenbrand, C. D. & Rittner, M., 2017. Widespread Antarctic glaciation during the late Eocene. Earth and Planetary Science Letters, 458, 49-57.

Carter, J., and Colman, S.M., 1994, Biogenic silica in Lake Baikal sediments: Results from 1990–1992 American cores: Journal of Great Lakes Research, v. 20, p. 751–760, doi: 10 .1016 /S0380 -1330 (94)71192–8.

Carter, L., McCave, I.N., 1997. The sedimentary regime beneath the Deep Western Boundary Current infow to the Southwest Pacific Ocean. J. Sediment. Res. 67, 1005-1017.

Carter, P., Vance, D., Hillenbrand, C. D., Smith, J. A., and Shoosmith, D. R., 2012. The neodymium isotopic composition of waters masses in the eastern Pacific sector of the Southern Ocean. Geochimica et Cosmochimica Acta, 79, 41–59. https://doi.org/10.1016/j.gca.2011.11.034.

Chavagnac, V., Milton, J., Green, D., Breuer, J., Bruguier, O., Jacob, D., Jong, T., Kamenov, G., Le Huray, J., and Liu, Y., 2007. Towards the development of a fossil bone geochemical standard: An inter-laboratory study, Analytica Chimica Acta, 599(2), 177-190.

Colman, S.M., 1998, Water-level changes in Lake Baikal, Siberia: Tectonism versus climate: Geology, v. 26, p. 531–534, doi: 10 .1130 /0091 -7613 (1998)26 <0531: WLCILB> 2 .3 .CO;2.

Colman, S.M., Foster, D.S., and Hatton, J., 1996, High-resolution seismic-reflection surveys of Lake Baikal, Siberia, 1990–1992: U.S. Geological Survey Open- File Report 96–274, 21 p.

Colman, S.M., Karabanov, E.B., and Nelson, C.H., 2003, Quaternary sedimentation and subsidence history of Lake Baikal, Siberia, based on seismic stratigraphy and coring: Journal of Sedimentary Research, v. 73, p. 941–956, doi: 10 .1306 /041703730941.

Contreras, L., Pross, J., Bijl, P. K., Koutsodendris, A., Raine, J. I., van de Schootbrugge, B., & Brinkhuis, H., 2013. Early to Middle Eocene vegetation dynamics at the Wilkes Land Margin (Antarctica). Review of Palaeobotany and Palynology, 197, 119–142. doi:10.1016/j.revpalbo.2013.05.009

Conway, C. E., Bostock, H. C., Baker, J. A., Wysoczanski, R. J., & Verdier, A., 2012. Evolution of Macquarie Ridge Complex seamounts: Implications for volcanic and tectonic processes at the Australia-Pacific plate boundary south of New Zealand. Marine Geology, 295-298, 34–50. https://doi.org/10.1016/j.margeo.2011.11.009

Cook, C.P., Hemming, S.R., van de Flierdt, T., Pierce Davis, E.L., Williams, T., Galindo, A.L., Jiménez-Espejo, F.J., Escutia, C., 2017. Glacial erosion of East Antarctica in the Pliocene: a comparative study of multiple marine sediment provenance tracers. Chem. Geol. 466, 199–218.

Cook, C.P., van de Flierdt, T., Williams, T., Hemming, S.R., Iwai, M., Kobayashi, M., Jimenez-Espejo, F.J., Escutia, C., Gonzalez, J.J., Khim, B.-K., McKay, R.M., Passchier, S., Bohaty, S.M., Riesselman, C.R., Tauxe, L., Sugisaki, S., Galindo, A.L., Patterson, M.O., Sangiorgi, F., Pierce, E.L., Brinkhuis, H., Klaus, A., Fehr, A., Bendle, J.A.P., Bijl, P.K., Carr, S.A., Dunbar, R.B., Flores, J.A., Hayden, T.G., Katsuki, K., Kong, G.S., Nakai, M., Olney, M.P., Pekar, S.F., Pross, J., Rohl, U., Sakai, T., Shrivastava, P.K., Stickley, C.E., Tuo, S., Welsh, K., Yamane, M., 2013. Dynamic behaviour of the East Antarctic ice sheet during Pliocene warmth. Nat. Geosci.6 (9), 765–769. https://doi .org /10 .1038 /ngeo1889.

Cooke, P.J., Nelson, C.S., Crundwell, M.P., Spiegler D., 2002. Bolboforma as monitors of Cenozoic palaeoceanographic changes in the Southern Ocean, Palaeogeography, Palaeoclimatology, Palaeoecology, 188(1), 73-100.

Cooper, A. K., and O'Brien, P. E., 2004. Leg 188 synthesis: transitions in the glacial history of the Prydz Bay region, East Antarctica, from ODP drilling, in Proceedings Proc. ODP, Sci. Results, Volume 188, College Station Texas, p. 1-42.

Cortese, G., Gersonde, R., Hillenbrand, C.-D., and Kuhn, G., 2004. Opal sedimentation shifts in the World Ocean over the last 15 Myr, Earth Planet. Sc. Lett., 224, 509–527.

Coxall, H. K., Wilson, P. A., Palike, H., Lear, C. H., and Backman, J., 2005, Rapid stepwise onset of Antarctic glaciation and deeper calcite compensation in the Pacific Ocean: Nature, v. 433, no. 7021, p. 53-57.

Cramer, B. S., Miller, K. G., Barrett, P. J., and Wright, J. D., 2011, Late Cretaceous– Neogene trends in deep ocean temperature and continental ice volume: Reconciling records of benthic foraminiferal geochemistry (δ18O and Mg/Ca) with sea level history: Journal of Geophysical Research: Oceans, v. 116.

Crouch, E.M., Willumsen, P.S., Kulhanek, D.K., Gibbs, S.J., 2014. A revised Paleocene (Teurian) dinoflagellate cyst zonation from eastern New Zealand. Review of Palaeobotany and Palynology, 202, 47-79.

Cunningham, S. A., Alderson, S. G., King, B. A., and Brandon M. A., 2003. Transport and variability of the Antarctic Circumpolar Current in Drake Passage, J. Geophys. Res., 108, 8084, doi:10.1029/2001JC001147.

Dale, B., 1996. Dinoflagellate cyst ecology: modeling and geological applications. Palynology: principles and applications, 1249-1275.

Dalziel, I. W. D.,2014. Drake Passage and the Scotia arc: A tortuous space-time gateway for the Antarctic Circumpolar Current. Geology, 42(4), 367–368. doi:10.1130/focus042014.

Dalziel, I.W.D., Lawver, L.A., Pearce, J.A., Barker, P.F., Hastie, A.R., Barfod, D.N., Schenke, H.-W., and Davis, M.B., 2013. A potential barrier to deep Antarctic circumpolar flow until the late Miocene?: Geology, v. 41, p. 947–950, doi:10.1130/G34352.1.

Damsté, J.S.S., Ossebaar, J., Abbas, B., Schouten, S., Verschuren, D., 2009. Fluxes and distribution of tetraether lipids in an equatorial African lake: constraints on the application of the TEX86 palaeothermometer and BIT index in lacustrine settings. Geochimica et Cosmochimica Acta, 73(14), 4232-4249.

De Batist, M., Canals, M., Sherstyankin, P., Alekseev, S., and INTAS Project 99–1669 Team, 2006, A new bathymetric map of lake Baikal: Deutsches GeoForschungsZentrum GFZ, doi: 10 .1594 /GFZ .SDDB .1100.

De Santis, L., Brancolini, G., & Donda, F., 2003. Seismo-stratigraphic analysis of the Wilkes Land continental margin (East Antarctica): influence of glacially driven processes on the Cenozoic deposition. Deep Sea Research Part II: Topical Studies in Oceanography, 50(8–9), 1563–1594. https://doi.org/10.1016/S0967-0645(03)00079-1

DeConto, R. M., & Pollard, D., 2016. Contribution of Antarctica to past and future sea-level rise. Nature, 531(7596), 591–597. doi:10.1038/nature17145

DeConto, R.M., and Pollard, D., 2003. Rapid Cenozoic glaciation of Antarctica induced by declining atmospheric CO2. Nature 421(6920):245–249, https://doi.org/10.1038/nature01290.

DePaolo, Wasserburg, G.L., 1976. Nd isotopic variations and petrogenetic models, Geophys. Res. Lett. 3, 249–252.

Diester-Haass, L., & Zahn, R., 2001. Paleoproductivity increase at the Eocene–Oligocene climatic transition: ODP/DSDP sites 763 and 592. Palaeogeography, Palaeoclimatology, Palaeoecology, 172(1-2), 153–170. doi:10.1016/s0031-0182(01)00280-2

Diester-Haass, L., Robert, C., & Chamley, H., 1996. The Eocene-oligocene preglacial-glacial transition in the atlantic sector of the Southern Ocean (ODP site 690). Marine Geology, 131(3-4), 123–149. doi:10.1016/0025-3227(95)00174-3

Dijkstra, A. H., Sergeev, D. S., Spandler, C. A., Pettke, T., Meisel, T., and Cawood, P. A., 2009. Highly refractory peridotites on Macquarie Island and the case for anciently depleted domains in the Earth' s mantle. Journal of Petrology, 51(1-2), 469–493. https://doi.org/10.1093/petrology/ egp084

Dorador, J., Rodríguez-Tovar, F.J., 2014. A novel application of digital image treatment by quantitative pixel analysis to trace fossil research in marine cores. PALAIOS 29 (10), 533–538.

Dorador, J., Rodríguez-Tovar, F.J., 2018. High-resolution image treatment in ichnological core analysis: initial steps, advances and prospects. Earth-Sci. Rev. 177, 226–237.

Dorador, J., Rodríguez-Tovar, F.J., IODP Expedition 339 Scientists, 2014a. Digital image treatment applied to ichnological analysis of marine core sediments. Facies 60 (1), 39–44.

Dorador, J., Rodríguez-Tovar, F.J., IODP Expedition 339 Scientists, 2014b. Quantitative estimation of bioturbation based on digital image analysis. Mar. Geol. 349, 55–60.

Droz, L., and Bellaiche, G., 1985, Rhone deep-sea fan: Morphostructure and growth pattern: American Association of Petroleum Geologists Bulletin, v. 69, p. 460–479.

Ehrmann, W. U., and Mackensen, A., 1992. Sedimentological evidence for the formation of an East Antarctic ice sheet in Eocene/Oligocene time: Palaeogeography, Palaeoclimatology, Palaeoecology, v. 93, no. 1, p. 85-112.

Ehrmann, W., 1998. Implications of late Eocene to early Miocene clay mineral assemblages in McMurdo Sound (Ross Sea, Antarctica) on paleoclimate and ice dynamics: Palaeogeography, Palaeoclimatology, Palaeoecology, v. 139, no. 3–4, p. 213-231.

Ehrmann, W., Hillenbrand, C.-D., Smith, J. A., Graham, A. G. C., Kuhn, G., & Larter, R. D., 2011. Provenance changes between recent and glacial-time sediments in the Amundsen Sea embayment, West Antarctica: clay mineral assemblage evidence. Antarctic Science, 23(05), 471–486. doi:10.1017/s095410201100032

Ehrmann, W., Setti, M., and Marinoni, L., 2005. Clay minerals in Cenozoic sediments off Cape Roberts (McMurdo Sound, Antarctica) reveal palaeoclimatic history: Palaeogeography, Palaeoclimatology, Palaeoecology, v. 229, no. 3, p. 187-211.

Elderfield, H., and Pagett, R., 1986. Rare earth elements in ichthyoliths: variations with redox conditions and depositional environment, Science of the Total Environment, 49, 175-197.

Escutia, C., and Brinkhuis, H., 2014. From Greenhouse to Icehouse at the Wilkes Land Antarctic Margin: IODP Expedition 318 Synthesis of Results, in Ruediger Stein, D. K. B. F. I., and Hans-Christian, L., eds., Developments in Marine Geology, Volume Volume 7, Elsevier, p. 295-328.

Escutia, C., Bárcena, M.A., Lucchi, R.G., Romero, O., Ballegeer, A.M., Gonzalez, J.J., Harwood, D.M., 2009. Circum-Antarctic warming events between 4 and 3.5 Ma recorded in marine sediments from the Prydz Bay (ODP Leg 188) and the Antarctic Peninsula (ODP Leg 178) margins, Glob. Planet. Change, 69,170–184. https://doi.org/10.1016/j.gloplacha.2009.09.003.

Escutia, C., Brinkhuis, H., 2014. From Greenhouse to Icehouse at the Wilkes Land Antarctic Margin, in earth and Life Processes Discovered from Subseafloor Environments: A Decade of Science Achieved by the Integrated Ocean Drilling Program (IODP), vol. 7, edited by: Stein, R., Blackman, D.K., Inagaki, F., and Larsen, H.-C., 295–328, Elsevier, Amsterdam.

Escutia, C., Brinkhuis, H., Klaus, A., and IODP Expedition 318 Scientists, 2011. IODP Expedition 318: From Greenhouse to Icehouse at the Wilkes Land Antarctic Margin: Scientific Drilling, v. 12, p. 15-23.

Escutia, C., DeConto, R., Dunbar, R., De Santis, L., Shevenell, A., & Nash, T., 2019. Keeping an Eye on Antarctic Ice Sheet Stability. Oceanography, 32(1), 32–46. doi:10.5670/oceanog.2019.117

Escutia, C., Donda, F. Lobo, F. J., & Tanahashi, M., 2007. Extensive debris flow deposits on the eastern Wilkes Land margin: a key to changing glacial regimes. In U. A. K., Cooper and C. R. Raymond et al. (Ed.), Online Proceedings of the 10th ISAES pp. 2000–2003.

Esper, O., Zonneveld, K.A.F., 2002. Distribution of organic-walled dinoflagellate cysts in surface sediments of the Southern Ocean (eastern Atlantic sector) between the Subtropical Front and the Weddell Gyre, Mar. Micropaleotol., 46, 177–208.

Etourneau, J., Sgubin, G., Crosta, L., Swingedouw, D., Willmott, V., Barbara, L., Houssais, M.-N., Schouten, S., Sinninghe Damsté, J., Goose, H., and others, 2019. Ocean temperature impact on ice shelf extent in the eastern Antarctic Peninsula. Nature Communications 10:304, https://doi.org/10.1038/ s41467-018-08195-6.

Evangelinos D., Escutia, C., Etourneau, J., Hoem, F., Bijl, P., Boterblom, W., van de Flierdt, T., Valero, L., Flores, J. A., Rodriguez-Tovar, F., Jimenez-Espejo, F., Salabarnada, A., López-Quirós, A., 2020. Global and Planetary Change

Exon, N., Kennett, J. P., Malone, M. J., and the Expedition 189 Scientists, 2001. The Tasmanian Gateway: Cenozoic Climatic and Oceanographic Development, Sites 1168-1172Rep., Ocean Drilling Program.

Expedition 318 Scientists, 2011. Methods. In Escutia, C., Brinkhuis, H., Klaus, A., and the Expedition 318 Scientists, Proc. IODP, 318: Tokyo (Integrated Ocean Drilling Program Management International, Inc.). doi:10.2204/iodp.proc.318.102.2011

Ferrari, R., Jansen, M.F., Adkins, J.F., Burke, A., Stewart, A.L., Thompson, A.F., 2014. Antarctic Sea ice control on ocean circulation in present and glacial climates. Proceedings of the National Academy of Sciences of the United States of America, 111(24), 8753–8758. https://doi.org/ 10.1073/pnas.1323922111.

Fielding, C. R., Browne, G. H., Field, B., Florindo, F., Harwood, D. M., Krissek, L. A., Levy, R. H., Panter, K. S., Passchier, S., and Pekar, S. F., 2011. Sequence stratigraphy of the ANDRILL AND-2A drillcore, Antarctica: A long-term, ice proximal record of Early to Mid-Miocene climate, sea-level and glacial dynamism: Palaeogeography, Palaeoclimatology, Palaeoecology, v. 305, no. 1–4, p. 337-351.

Foster, G.L., and Rohling, E. J., 2013. Relationship between sea level and climate forcing by CO2 on geological timescales. Proceedings of the National Academy of Sciences of the United States of America 110(4):1,209–1,214, https://doi.org/10.1073/ pnas.1216073110.

Foster, G.L., C.H. Lear, and J.W.B. Rae. 2012. The evolution of pCO2, ice volume and climate during the middle Miocene. Earth and Planetary Science Letters 341–344:243–254, https://doi.org/10.1016/j.epsl.2012.06.007.

Francis, J. E., 2000. Fossil wood from Eocene high latitude forests: McMurdo Sound, Antarctica. Antarctic Research Series, 253–260. doi:10.1029/ar076p0253

Frank, M., 2002. Radiogenic isotopes: Tracers of past ocean circulation and erosional input: Reviews of Geophysics, v. 40, doi: 10.1029 /2000RG000094.

Freslon, N., Bayon, G., Toucanne, S., Bermell, S., Bollinger, C., Chéron, S., Etoubleau, J., Germain, Y., Khripounoff, A, and Ponzevera, E., 2014. Rare earth elements and neodymium isotopes in sedimentary organic matter, Geochimica Et Cosmochimica Acta, 140, 177-198.

Fretwell, P., H.D. Pritchard, D.G. Vaughan, J.L. Bamber, N.E. Barrand, R. Bell, C. Bianchi, R.G. Bingham, D.D., Blankenship, G., Casassa, and others., 2013. Bedmap2: Improved ice bed, surface and thickness datasets for Antarctica. Cryosphere 7:375–393, https://doi.org/10.5194/tc-7-375-2013.

Galeotti, S., DeConto, R.M., Naish, T.R., Stocchi, P., Florindo, F., Pagani, M., Barrett, P.J., Bohaty, S.M., Lanci, L., Pollard, D., and others. 2016. Clast distribution in sediment core CRP-3. PANGAEA, https://doi.org/ 10.1594/ PANGAEA.858577.

Garcia-Solsona, E., Jeandel, C., Labatut, M., Lacan, F., Vance, D., Chavagnac, V., & Pradoux, C., 2014. Rare earth elements and Nd isotopes tracing water mass mixing and particle-seawater interactions in the SE Atlantic. Geochimica et Cosmochimica Acta, 125, 351–372. https:// doi.org/10.1016/j.gca.2013.10.009

Goldstein, S.L., Hemming, S.R., 2003. 6.17 - Long-lived isotopic tracers in oceanography, paleoceanography, and ice-sheet dynamics. In: Holland, H.D, Turekian, K.K. (Eds.), Treatise on Geochemistry. Pergamon, Oxford, pp. 453–489.

Gradstein, F.M., Ogg, J.G., Schmitz, M.D., Ogg, G.M., 2012. The Geologic Time Scale 2012, The Geologic Time Scale 2012, 2, 437–1144.

Greene, C. A., Blankenship, D. D., Gwyther, D. E., Silvano, A., & van Wijk, E., 2017. Wind causes Totten Ice Shelf melt and acceleration. Science Advances, 3(11), e1701681. doi:10.1126/sciadv.1701681

Greene, HG., Murai, L. Y., Watts, P., et al., 2006. Submarine landslides in the Santa Barbara Channel as potential tsunami sources. Natural Hazards and Earth System Sciences 6: 63–88.

Grützner, J., Hillenbrand, C.-D., Rebesco, M., 2005. Terrigenous flux and biogenic silica deposition at the Antarctic continental rise during the late Miocene to early Pliocene: implications for ice sheet stability and sea ice coverage. Global and Planetary Change 45, 131–149.

Halliday, A. N., Davidson, J. P., Holden, P., Owen, R. M., and Olivarez A. M., 1992. Metalliferous sediments and the scavenging residence time of Nd near hydrothermal vents, Geophysical Research Letters, 19(8), 761-764.

Hambrey, M. J., & McKelvey, B., 2000. Major Neogene fluctuations of the East Antarctic ice sheet: Stratigraphic evidence from the Lambert Glacier region. Geology, 28(10), 887. doi:10.1130/0091-7613(2000)28<887:mnfote>2.0.co;2

Hammer, Ø., Harper, D.A.T., Ryan, P.D., 2001. PAST: Paleontological statistics software package for education and data analysis, Palaeontol. Electron., 4(1), 9.

Harland, R., Pudsey, C.J., 1999. Dinoflagellate cysts from sediment traps deployed in the Bellingshausen, Weddell and Scotia seas, Antarctica, Mar. Micropaleontol., 37, 77–99.

Hartman, J. D., Sangiorgi, F., Salabarnada, A., Peterse, F., Houben, A. J. P., Schouten, S., Escutia, C., and Bijl, P. K., 2018. "Paleoceanography and Ice Sheet Variability Offshore Wilkes Land , Antarctica – Part 3 : Insights from Oligocene – Miocene TEX 86 -Based Sea Surface Temperature Reconstructions," 1275–97.

Harwood, D. M., and Levy, R. H., 2000, The McMurdo Erratics: Introduction and Overview, in Stilwel, J. D., and Feldman, R. M., eds., Paleobiology and Paleoenvironments of Eocene Rocks: McMurdo Sound, East Antarctica, Volume 76: Washington, DC, American Geophysical Union, p. 1-18.

Haug, G. H., and R. Tiedemann, R., 1998. Effect of the formation of the Isthmus of Panama on Atlantic Ocean thermohaline circulation, Nature, 393, 673–676, doi:10.1038/31447.

Haug, G. H., Tiedemann, R., Zahn, R., and Ravelo, A. C., 2001. Role of Panama uplift on oceanic freshwater balance, Geology, 29, 207 210, doi:10.1130/0091-7613(2001)029<0207: ROPUOO>2.0.CO;2.

Hayes, D. E., and Frakes, L. A., 1975. General Synthesis, Deep Sea Drilling Project Leg 28, in Initial Reports of the Deep Sea Drilling Project', US, 28, pp.19–48.

Hayes, D.E., Frakes, L.A., et al., 1975. Initial Reports of the Deep Sea Drilling Project', vol. 28, U.S. Government Printing Office, Washington, pp. 179-210. doi:10.2973/dsdp.proc.28.107.1975.

Head, M., 1996. Modern dinoflagellate cysts and their biological affinities. Palynology: principles and applications, 3, 1197-1248.

Hepp, D.A., Mörz, T., Grützner, J., 2006. Pliocene glacial cyclicity in a deep-sea sediment drift (Antarctic Peninsula Pacific Margin). Palaeogeography, Palaeoclimatology, Palaeoecology 231, 181–198.

Hernández-Sánchez, M.T., Woodward, E.M.S., Taylor, K.W.R., Henderson, G.M., Pancost, R. D., 2014. Variations in GDGT distributions through the water column in the South East Atlantic Ocean. Geochimica et Cosmochimica Acta, 132, 337–348. doi:10.1016/j.gca.2014.02.009

Herold, N., Huber, M., Müller, R.D., and M Seton, M., 2012. "Modeling the Miocene Climatic Optimum: Ocean Circulation" 27 (December 2011): 1–22. https://doi.org/10.1029/2010PA002041.

Herraiz-Borreguero, L., Coleman, R., Allison, I., Rintoul, S. R., Craven, M., & Williams, G. D., 2015. Circulation of modified Circumpolar Deep Water and basal melt beneath the Amery Ice Shelf, East Antarctica. Journal of Geophysical Research: Oceans, 120(4), 3098–3112. doi:10.1002/2015jc010697

Hill, D. J., Haywood, A.M., Valdes, P.J., Francis, J.E., Lunt, D.J., Wade, B.S., Bowman, V.C., 2013. Paleogeographic controls on the onset of the Antarctic circumpolar current, Geophys. Res. Lett., 40, 5199–5204. https://doi.org/10.1002/grl.50941.

Hillenbrand, C. D. and Cortese, G., 2006. Polar stratification: A criti-cal view from the Southern Ocean, Palaeogeogr. Palaeocl., 242,240–252.

Ho, S.L., Laepple, T., 2015. Glacial cooling as inferred from marine temperature proxies TEX^{H}_{86} and $U^{K'}_{37}$. Earth and Planetary Science Letters, 409, 15-22. doi: https://doi.org/10.1016/j.epsl.2014.10.033.

Ho, S.L., Mollenhauer, G., Fietz, S., Martínez-Garcia, A., Lamy, F., Rueda, G., Schipper, K., Méheust, M., Rosell-Melé, Stein, R., Tiedemann, R. Stein, R., 2014. Appraisal of TEX86 and TEX86L thermometries in subpolar and polar regions. Geochimica et Cosmochimica Acta, 131, 213-226.

Hodell, D.A., Nicholl, J.A., Bontognali, R.R.R., Danino, S., Dorador, J., Dowdeswell, J.A., Einsele, J., Kuhlmann, H., Martrat, B., Mleneck-Vautravers, M.J., Rodriguez-Tovar, F.J., Rohl, U., 2017. Anatomy of Heinrich Layer 1 and its role in the last deglaciation. Paleoceanography 32, 284-303.

Holbourn, A., Kuhnt, W., Kochhann, K. G. D., Andersen, N., & Sebastian Meier, K. J., 2015. Global perturbation of the carbon cycle at the onset of the Miocene Climatic Optimum. Geology, 43(2), 123–126. doi:10.1130/g36317.1

Holbourn, A., Kuhnt, W., Schulz, M., Flores, J.-A., and Andersen. N., 2007. Orbitally-paced climate evolution during the middle Miocene "Monterey" carbon-isotope excursion. Earth and Planetary Science Letters 261:534–550, https://doi.org/ 10.1016/ j.epsl.2007.07.026.

Holland, D. M., Nicholls, K. W., Basinski, A., 2020. The Southern Ocean and its interaction with the Antarctic Ice Sheet. Science, 367, 1326-1330.

Hopmans, E.C., Schouten, S., Sinninghe Damsté, J.S., 2015. The effect of improved chromatography on GDGT-based palaeoproxies, Organic Geochemistry. doi: http://dx.doi.org/10.1016/j.orggeochem.2015.12.006.

Hopmans, E.C., Weijers, J.W., Schefuß, E., Herfort, L., Damsté, J.S.S., Schouten, S., 2004. A novel proxy for terrestrial organic matter in sediments based on branched and isoprenoid tetraether lipids. Earth and Planetary Science Letters, 224(1-2), 107-116.

Houben, A. J. P., Bijl, P. K., Sluijs, A., Schouten, S., & Brinkhuis, H., 2019. Late Eocene Southern Ocean cooling and invigoration of circulation preconditioned Antarctica for full-scale glaciation. Geochemistry, Geophysics, Geosystems. doi:10.1029/2019gc008182

Houben, A.J.P., Bijl, P. K., Pross, J., Bohaty, S. M., Passchier, S., Stickley, C. E., Passchier, S., Roel, U., Sugisaki, S., Tauxe, L., van de Flierdt, T., 2013. Reorganization of Southern Ocean plankton ecosystem at the onset of Antarctic glaciation. Science 340 (6130), 341-344, https://doi.org/10.1126/ science.1223646.

Huber, M., Brinkhuis, H., Stickley, C.E., Döös, K., Sluijs, A., Warnaar, J., Schellenberg, S.A., Williams, G.L., 2004. Eocene circulation of the Southern Ocean: was Antarctica kept warm by subtropical waters? Paleoceanography 19. https:// doi .org /10 .1029 /2004PA001014.

Huber, M., Sloan, L. C., and Shellito C., 2003. Early Paleogene oceans and climate: A fully coupled modeling approach using the NCAR CCSM, in Causes and Consequences of Globally Warm Climates in the Early Paleogene, edited by S. L. Wing et al., Geol. Soc. Spec. Publ., 369, 25–47.

Huck, C. E., van de Flierdt, T., Bohaty, S. M., and Hammond, S. J., 2017. Antarctic climate, Southern Ocean circulation patterns, and deepwater formation during the Eocene, Paleoceanography, 32, 674–691, doi: 10.1002/2017PA003135

Huck, C. E., van de Flierdt, T., Jiménez-Espejo, F. J., Bohaty S. M., Röhl, U., and Hammond, S. J, 2016. Robustness of fossil fish teeth for seawater neodymium isotope reconstructions under variable redox conditions in an ancient shallow marine setting, Geochemistry, Geophysics, Geosystems.

Hutchinson, D.R., Golmshtok, A.Y., Zonenshain, L.P., Moore, T.C., Scholz, C.A., and Klitgord, K., 1992, Depositional and tectonic framework of the rift basins of Lake Baikal from multichannel seismic data: Geology, v. 20, p. 589–592, doi: 10 .1130 /0091 -7613 (1992)020 <0589: DATFOT>2 .3 .CO;2.

IPCC, 2019: IPCC Special Report on the Ocean and Cryosphere in a Changing Climate [H.-O. Pörtner, D.C. Roberts, V., Masson-Delmotte, P., Zhai, M. Tignor, E., Poloczanska, K., Mintenbeck, A., Alegría, M., Nicolai, A., Okem, J., Petzold, B., Rama, N.M., Weyer (eds.)]. In press.

IPCC: Climate Change 2013: The Physical Science Basis, Contribution of Working Group I to the Fifth Assessment Report of the Intergovernmental Panel on Climate Change, Cambridge University Press, Cambridge, United Kingdom and New York, NY, USA, 2013.

Ivany, L. C., Simaeys, S. V., Domack, E. W., & Samson, S. D., 2006. Evidence for an earliest Oligocene ice sheet on the Antarctic Peninsula. Geology, 34(5), 377. doi:10.1130/g22383.1

Jacobs, S. S., Jenkins, A., Giulivi, C. F., & Dutrieux, P., 2011. Stronger ocean circulation and increased melting under Pine Island Glacier ice shelf. Nature Geoscience, 4(8), 519–523. doi:10.1038/ngeo1188

Jacobs, S., Giulivi, C., Dutrieux, P., Rignot, E., Nitsche, F., & Mouginot, J., 2013. Getz Ice Shelf melting response to changes in ocean forcing. Journal of Geophysical Research: Oceans, 118(9), 4152–4168. doi:10.1002/jgrc.20298

Jacobsen, S. B., & Wasserburg, G. J.,1980. Sm-Nd evolution of chondrites. Earth and Planetary Science Letters, 50, 139–155. https://doi.org/ 10.1016/0012-821X(80)90125-9

Jenkins, A., Dutrieux, P., Jacobs, S., Steig, E., Gudmundsson, H., Smith, J., Heywood, K., 2016. Decadal Ocean Forcing and Antarctic Ice Sheet Response: Lessons from the Amundsen Sea. Oceanography, 29(4), 106–117. doi:10.5670/oceanog.2016.103

Jenkins, A., Shoosmith, D., Dutrieux, P., Jacobs, S., Kim, T. W., Lee, S. H., Kyung Ha, H., Stammerjohn, S., 2018. West Antarctic Ice Sheet retreat in the Amundsen Sea driven by decadal oceanic variability. Nature Geoscience. doi:10.1038/s41561-018-0207-4

Jimenez-Espejo, F.J., Martinez-Ruiz, F., Sakamoto, T., Iijima, K., Gallego-Torres, D., Harada, N.: Paleoenvironmental changes in the western Mediterranean since the last glacial maximum: High resolution multiproxy record from the Algero-Balearic basin. Palaeogeogr. Palaeoclimatol. Palaeoecol., 246, 292–306, doi:10.1016/j.palaeo.2006.10.005, 2007.

Joughin, I., Smith, B. E., & Medley, B., 2014. Marine Ice Sheet Collapse Potentially Under Way for the Thwaites Glacier Basin, West Antarctica. Science, 344(6185), 735–738. doi:10.1126/science.1249055

Jovane, L., Florindo, F., Acton, G., Ohneiser, C., Sagnotti, L., Strada, E., Verosub, K. L., Wilson, G. S., Iacoviello, F., Levy, R. H., Passchier, S., 2019. Miocene glacial dynamics recorded by variations in magnetic properties in the ADRILL-2A drill core. American Geophysical Union, doi: 10.1029/2018JB016865

Kamenetsky, V. S., Everard, J. L., Crawford, A. J., Varne, R., Eggins, S. M., and Lanyon, R., 2000. Enriched end-member of primitive MORB melts: Petrology and geochemistry of glasses from Macquarie Island (SW Pacific). Journal of Petrology, 41(3), 411–430. https://doi.org/10.1093/petrology/41.3.411

Katz, M. E., Miller, K. G., Wright, J. D., Wade, B. S., Browning, J. V., Cramer, B. S., and Rosenthal, Y., 2008. Stepwise transition from the Eocene greenhouse to the Oligocene icehouse: Nature Geoscience, v. 1, no. 5, p. 329-334.

Kennett, J. P., Houtz, R. E., Andrews, P. B., Edwards, A. R., Gostin, V. A., Hajos, M., Hampton, M., Jenkins, D. G., Margolis, S. V., Ovenshine, A. T., Perch-Nielsen, K., 1975: Cenozoic paleoceanography in the southwest Pacific Ocean, Antarctic glaciation, and the development of the Circum- Antarctic Current. Initial Reports of the Deep Sea Drilling Project 29: 1155–1169.

Kennett, J.P., 1977. Cenozoic evolution of Antarctic glaciation, the circum-Antarctic Ocean, and their impact on global paleoceanography. Journal of Geophysical Research 82(27):3,843–3,860, https://doi.org/10.1029/JC082i027p03843.

Kennett, J.P., R.E. Houtz, et al., 1975. Initial Reports of the Deep Sea Drilling Project, Volume 29. US Government Printing Office, Washington, DC, https://doi.org/10.2973/dsdp.proc.29.1975.

Khazendar, A., Rignot, E., Schroeder, D. M., Seroussi, H., Schodlok, M. P., Scheuchl, B., Mouginot, J., Sutterley, T. C., and Velicogna, I., 2016. Rapid submarine ice melting in the grounding zones of ice shelves in West Antarctica. Nature Communications, 7 13243.

Khlystov, O.M., Khanaev, I.V., and Grachev, M.A., 2008, Evidence of Lowstand of Lake Baikal during the Last Glaciation: Doklady Earth Sciences, v. 422, p. 1133–1136, doi: 10 .1134 /S1028334X08070301.

Kim, J.H., Van der Meer, J., Schouten, S., Helmke, P., Willmott, V., Sangiorgi, F., Koç, H., Hopmans, E.C., Sinninghe Damsté, J. S, 2010. New indices and calibrations derived from the distribution of crenarchaeal isoprenoid tetraether lipids: Implications for past sea surface temperature reconstructions. Geochimica et Cosmochimica Acta, 74(16), 4639-4654.

Kominz, M. A., and Pekar, S. F., 2001, Oligocene eustasy from two-dimensional sequence stratigraphic backstripping: Geological Society of America Bulletin, v. 113, no. 3, p. 291-304.

Kominz, M. A., Browning, J. V., Miller, K. G., Sugarman, P. J., Mizintseva, S., and Scotese, C. R., 2008, Late Cretaceous to Miocene sea-level estimates from the New Jersey and Delaware coastal plain coreholes: an error analysis: Basin Research, v. 20, no. 2, p. 211-226.

Kuijpers, A., Knutz, P., Moros, M., 2014. Ice-Rafted Debris (IRD) in Encyclopedia of Marine Geosciences

Kulhanek, D., Levy, R., Clowes, C.D., Prebble, J.G., Rodelli, D., Jovane, L., Morgans, H.E.G., Kraus, C., Zwingmann, H., Griffith, E.M., Scher, H.D., McKay, R.M., Naish, T.R., 2019. Revised chronostratigraphy of DSDP Site 270 and late Oligocene to early Miocene paleoecology of the Ross Sea sector of Antarctca, Global and Planetary Change, 178, 46-64.

Kyle, P. R., and Muncy, H. L., 1989. Geology and geochronology of McMurdo Volcanic Group rocks in the vicinity of Lake Morning, McMurdo Sound, Antarctica. Antarctic Science, 1(4), 345-350.

Lamarche, G., Collot, J.Y., Wood, R.A., Sosson, M., Sutherland, R., Deltail, J. 1997. The Oligocene-Miocene Pacific-Australia plate boundary: Evolution from oceanic spreading to strike-slip faulting, Earth Planet. Sci. Lett., 148, 129-139.

Lambelet, M., van de Flierdt, T., Butler, E. C. V., Bowie, A. R., Rintoul, S. R., Watson, R. J., Remenyi, T., Lannuzel, D., Warner, M., Robinson, L.F., Bostock, H.C. and Bradtmiller, L.I, 2018. The neodymium isotope fingerprint of Adélie Coast Bottom Water. Geophysical Research Letters, 45, 11,247–11,256. https://doi. org/10.1029/2018GL080074

Lambelet, M., van de Flierdt, T., Crocket, K., Rehkämper, M., Kreissig, K., Coles, B., et al., 2016. Neodymium isotopic composition and concentration in the western North Atlantic Ocean: Results from the GEOTRACES GA02 section. Geochimica et Cosmochimica Acta, 177, 1–29. https://doi.org/10.1016/j.gca.2015.12.019

Lamy, F., Arz, H. W., Kilian, R., Lange, C. B., Lembke-Jene, L., Wengler, M., Kaiser, J., Baeza-Urrea, O., Hall, I. R., Harada, N., and Tiedemann R., 2015. Glacial reduction and millennial-scale variations in Drake Passage throughflow. PNAS 112 (44) 13496-13501 https://doi.org/10.1073/pnas.1509203112

Lawver, L.A., Gahagan, L.M., 1998. Opening of Drake Passage and its impact on Cenozoic ocean circulation. In: Crowley, T.J., Burke, K.C. (Eds.), Tectonic Boundary Conditions for Climate Reconstructions. Oxford University Press, Oxford, pp. 212–223.

Lawver, L.A., Gahagan, L.M., 2003. Evolution of Cenozoic seaways in the circum-Antarctic region. Palaeogeography, Palaeoclimatology, Palaeoecology 198, 11–38.

Lear, C. H., Bailey, T. R., Pearson, P. N., Coxall, H. K., and Rosenthal, Y., 2008. Cooling and ice growth across the Eocene-Oligocene transition: Geology, v. 36, no. 3, p. 251-254.

Lear, C. H., Elderfield, H., and Wilson, P. A., 2000. Cenozoic Deep-Sea Temperatures and Global Ice Volumes from Mg/Ca in Benthic Foraminiferal Calcite: Science, v. 287, no. 5451, p. 269-272.

Lear, C. H., Rosenthal, Y., Coxall, H. K., and Wilson, P. A., 2004. Late Eocene to early Miocene ice sheet dynamics and the global carbon cycle: Paleoceanography, v. 19, no. 4.

Legeais, J. F., Speich, S., Arhan, M., Ansorge, I., Fahrbach, E., Garzoli, S., and Klepikov, A., 2005. The baroclinic transport of the Antarctic Circumpolar Current south of Africa, Geophys. Res. Lett., 32, L24602, doi:10.1029/2005GL023271.

Levy, R., Harwood, D., Florindo, F., Sangiorgi, F., Tripati, R., von Eynatten, H., Gasson, E., Kuhn, G., Tripati, A., DeConto, R., Fielding, C. R., Field, B., Golledge, N. R., McKay, R., Naish, T., Olney, M. P., Pollard, D., Schouten, S., Talarico, F., Warny, S., Willimott, V., Acton, G., Panter, K., Paulsen, T., Taviani, M., and SMS Science Teams, 2016. Antarctic ice sheet sensitivity to atmospheric CO2 variations in the early to mid-Miocene: Proceedings of the National Academy of Sciences.

Levy, R.H., Meyers, S.R., Naish, T.R., Golledge, N.R., McKay, R.M., Crampton, J.S., DeConto, R.M., De Santis, L., Florindo, F., Gasson, E.G.W., Harwood, D.M., Luyendyk, B.P., Powell, R.D., Clowes, C., Kulhanek, D.K., 2019. Antarctic ice-sheet sensitivity to obliquity forcing enhanced through ocean connections. Nature Geosciences 12, 132-137.

Lewis, A. R., Marchant, D. R., Kowalewski, D. E., Baldwin, S. L., & Webb, L. E., 2006. The age and origin of the Labyrinth, western Dry Valleys, Antarctica: Evidence for extensive middle Miocene subglacial floods and freshwater discharge to the Southern Ocean. Geology, 34(7), 513-516. https://doi.org/10.1130/G22145.1

Li, X., Rignot, E., Mouginot, J., and Scheuchl, B., 2016. Ice flowdynamics and mass loss of Totten Glacier, East Antarctica, from1989 to 2015, Geophys.Res. Lett.,43, 6366 6373, doi:10.1002/2016GL069173

Liebrand, D., De Bakker, A.T.M., Beddow, H.M., Wilson, P.A., Bohaty, S.M., Ruessink, G., Pälike, H., Batenburg, S.J., Hilgen, F.J., Hodell, D.A., Huck, C.E., Kroon, D., Raffi, I., Saes, M.JM., van Dijk, A.E., Lourens, L., 2017. Evolution of the Early Antarctic Ice Ages 114 (15): 3867–72. https://doi.org/10.1073/pnas.1615440114.

Liebrand, D., Lourens, L. J., Hodell, D. A., de Boer, B., van de Wal, R. S. W., and Pälike, H., 2011. Antarctic ice sheet and oceanographic response to eccentricity forcing during the early Miocene, Clim. Past, 7, 869–880, https://doi.org/10.5194/cp-7-869-2011.

Ling, H. F., K. W., Burton, R. K., O'Nions, B. S., Kamber, F., von Blanckenburg, A., J. Gibb, and J. R. Hein, 1997. Evolution of Nd and Pb isotopes in Central Pacific seawater from ferromanganese crusts, Earth and Planetary Science Letters, 146(1–2), 1-12.

Liu, Y., Moore, J.C., Cheng, X., Gladstone, R M., Bassis, J.N., Liu, H., Wen, J., Hui, F., 2015. Ocean-driven thinning enhances iceberg calving and retreat of Antarctic ice shelves, P. Natl. Acad. Sci. USA, 112, 3263–3268. https://doi.org/10.1073/pnas.1415137112.

Livermore, R., Eagles, G., Morris, P., Maldonado, A., 2004. Shackleton Fracture Zone: no barrier to early circumpolar circulation. Geology 32, 797–800.

Livermore, R., Nankivell, A., Eagles, G. & Morris, P., 2005. Paleogene opening of Drake passage. Earth and Planetary Science Letters, 236(1-2), 459-470.

Livermore, R.A., Hillenbrand, C.-D., Meredith, M., and Eagles, G., 2007. Drake Passage and Cenozoic climate: An open and shut case?: Geochemistry Geophysics Geosystems, v. 8, Q01005, doi:10.1029/2005GC001224.

Lucchi, R.G, Rebesco, M., 2007. Glacial contourites on the Antarctic Peninsula margin: insights for palaeoenvironmental and paleoclimatic conditions. Geol. Soc. Spec. Publi., 276, 111-127. https://doi.org/10.1144/GSL.SP.2007.276.01.06.

Lunt, D.J., Dunkley, T., Jones, Heinemann, M., Huber, M., LeGrande, A., Winguth, A., Loptson, C., Marotzke, J., Tindall, J., Valdes, P., and Winguth, C., 2012. A model-data comparison for a multi-model ensemble of early Eocene atmosphere-ocean simulations: EoMIP. Clim. Past, 8, 1717-1736, doi:10.5194/cp-8-1717-2012.

Lyle, M., Gibbs, S., C. Moore, T.C., Rea, D.K., 2007. Late Oligocene Initiation of the Antarctic Circumpolar Current: Evidence from the South Pacific. Geology 35 (8): 691–94. https://doi.org/10.1130/G23806A.1

Marshall, J., and K. Speer, K., 2012. Closure of the meridional overturning circulation through Southern Ocean upwelling, Nat. Geosci., 5, 171–180, doi:10.1038/NGEO1391.

Martin, E. E., and Scher, H. D., 2006. A Nd isotopic study of southern sourced waters and Indonesian throughflow at intermediate depths in the Cenozoic Indian Ocean, Geochem Geophy Geosy, 7.

Martin, E. E., Haley B. A., 2000. Fossil fish teeth as proxies for seawater Sr and Nd isotopes. Geochim. Cosmochim. Acta 64, 835–847. (doi:10.1016/S0016-7037(99)00376-2)

Martin, E. E., Scher, H. D., 2004. Preservation of seawater Sr and Nd isotopes in fossil fish teeth: bad news and good news, Earth Planet. Sci. Lett. 220, 25–39.

Martin, E.E., Blair, S.W., Kamenov, G.D., Scher, H.D., Bourbon, E., Bask, C., Newkirk, D.N., 2010. Extraction of Nd isotopes from bulk deep sea sediments for paleoceanographic studies on Cenozoic time scales. Chem. Geol. 269, 414–431.

Martin, E.E., Scher, H.D., 2006. A Nd isotopic study of southern sourced waters and Indonesian Throughflow at intermediate depths in the Cenozoic Indian Ocean, Geochemistry, Geophysics, Geosystems, 7(9). doi: 10.1029/2006GC001302

Martini, E., 1971. Standard Tertiary and Quaternary calcareous nannoplanktonzonation. In: Farinacci, A. (Ed.), Proceeding II Plankt. Conf., Roma, 1970, vol. 2,pp. 739–785.

Martinson DG, McKee, D. C., 2012. Transport of warm upper circumpolar deep water onto the western Antarctic Peninsula continental shelf. Ocean Sci 8:433–442.

Martinson, D. G., 2012. Antarctic circumpolar current's role in the Antarctic ice system: An overview. Palaeogeography, Palaeoclimatology, Palaeoecology, 335-336, 71–74. doi:10.1016/j.palaeo.2011.04.007

McCave I.N., Crowhurst, S.J., Kuhn, G., Hillenbrand, C-D., Meredith M.P., 2014. Minimal change in Antarctic Circumpolar Current flow speed between the last glacial and Holocene. Nature Geoscience 11(7):113–116.

McIntosh, W. C., 2000, 40Ar/39Ar geochronology of tephra and volcanic clasts in CRP-2A, Victoria Land Basin, Antarctica, Terra Antarctica, 7, 621-630.

McKay, R., Naish, T., Carter, L., Riesselman, C., Dunbar, R., Sjunneskog, C., Winter, D., Sangiorgi, F., Warren, C., Pagani, M., Schouten, S., Willmott, V., Levy, R., DeConto, R., and Powell, R. D., 2012. Antarctic and Southern ocean influences on late Pliocene global cooling. Proc. Natl. Acad. Sci. 109 (17), 6423e6428, 27.

McKay, R.M., L. De Santis, D.K. Kulhanek, and the Expedition 374 Scientists. 2018. Expedition 374 Preliminary Report: Ross Sea West Antarctic Ice Sheet History. International Ocean Discovery Program, 374, College Station, TX, https://doi.org/ 10.14379/iodp.pr.374.2018.

McKinley, C. C., Thomas, D. J., LeVay, L., Rolewicz, Z. 2019. Nd isotopic structure of the Pacific Ocean 40-10 Ma, and evidence for the reorganization of deep North Pacific Ocean circulation between 36 and 25 Ma. Earth and Planetary Science Letters 521 (2019) 139-149.

Meijers A. J. S., 2014. The Southern Ocean in the Coupled Model Intercomparison Project phase 5. Philos Trans R Soc Lond A 372(2019):20130296.

Meredith, M. P., et al., 2011. Sustained monitoring of the Southern Ocean at Drake Passage: Past achievements and future priorities, Rev. Geophys.,49, doi:10.1029/2010RG000348.

Meredith, M., M. Sommerkorn, M., Cassotta, S., Derksen, C., Ekaykin, A., Hollowed, A., Kofinas, G., Mackintosh, A., Melbourne- Thomas, J., Muelbert, M.M.C., Ottersen, G., Pritchard, H., and Schuur, E.A.G. 2019: Polar Regions. In: IPCC Special Report on the Ocean and Cryosphere in a Changing Climate).

Miller, K. G., Browning, J. V., Aubry, M.-P., Wade, B. S., Katz, M. E., Kulpecz, A. A., and Wright, J. D., 2008a. Eocene–Oligocene global climate and sea-level changes: St. Stephens Quarry, Alabama: Geological Society of America Bulletin, v. 120, no. 1-2, p. 34-53.

Miller, K. G., Kominz, M. A., Browning, J. V., Wright, J. D., Mountain, G. S., Katz, M. E., Sugarman, P. J., Cramer, B. S., Christie-Blick, N., and Pekar, S. F., 2005a. The Phanerozoic Record of Global Sea-Level Change: Science, v. 310, no. 5752, p. 1293-1298.

Miller, K. G., Wright, J. D., and Browning, J. V., 2005b. Visions of ice sheets in a greenhouse world: Marine Geology, v. 217, no. 3–4, p. 215-231.

Miller, K. G., Wright, J., Katz, M., Browning, J., Cramer, B., Wade, B. S., and Mizintseva, S., 2018b. A view of Antarctic ice-sheet evolution from sea-level and deep sea isotope changes during the Late Cretaceous–Cenozoic, in Proceedings Antarctica: A Keystone in a Changing World. Proceedings of the 10th International Symposium on Antarctic Earth Sciences, Washington, DC,The National Academies Press, p. 55-70

Miller, K.G., J.D. Wright, and R.G. Fairbanks. 1991. Unlocking the Ice House: Oligocene-Miocene oxygen isotopes, eustasy, and margin erosion. Journal of Geophysical Research 96(4):6,829–6,848, https://doi.org/10.1029/90JB02015.

Moiroud, M., Pucéat, E., Donnadieu, Y., Bayon, G., Moriya, K., Deconinck, J-F., Boyet, M., 2013. Evolution of the neodymium isotopic signature of neritic seawater on a northwestern Pacific margin: New constrains on possible end-members for the composition of deep-water masses in the Late Cretaceous ocean, Chem. Geol., 356, 160–170.

Morlinghem, M., Rignot, E., Binder, T., Blankenshio, D., Drews, R., Eagles, G., Eisen, O., Ferracioli, F., Forsberg, R., Fretwell, P., Goel, V., et al., 2019. Deep glacial troughs and stabilizing ridges unveiled beneath the margins of the Antarctic ice sheet. Nature Geoscience 13(2):1-6 https://doi.org/10.1038/s41561-019-0510-8

Mudelsee, M., Bickert, T., Lear, C. H., and Lohmann, G., 2014, Cenozoic climate changes: A review based on time series analysis of marine benthic δ18O records: Reviews of Geophysics, v. 52, no. 3, p. 333-374.

Mulder, T., & Alexander, J., 2001. The physical character of subaqueous sedimentary density flows andtheir deposits. Sedimentology, 48(2), 269–299.

Müller, R. D., Cannon, J., Qin, X., Watson, R. J., Gurnis, M., Williams, S., et al. 2018. GPlates: Building a virtual Earth through deep time. Geochemistry, Geophysics, Geosystems, 19. doi:10.1029/2018GC007584

Müller, R. D., Seton, M., Zahirovic, S., Williams, S. E., Matthews, K. J., Wright, N. M., Shephard, G. E., Maloney, K., Barnett-Moore, N. and Hosseinpour, M. 2016. Ocean Basin Evolution and Global-Scale Plate Reorganization Events Since Pangea Breakup, Annual Review of Earth and Planetary Sciences, 44(1).

Naish, T., Powell, R., Levy, R., Wilson, G., Scherer, R., Talarico, F., Krissek, L., Niessen, F., Pompilio, M., Wilson, T., and others. 2009. Obliquity-paced Pliocene West Antarctic Ice Sheet oscillations. Nature 458:322–328, https://doi.org/10.1038/nature07867.

Naish, T.R., Wilson, G.S., Dunbar, G.B., Barrett, P.J., 2008. Constraining the amplitude of Late Oligocene bathymetric changes in western Ross Sea during orbitally-induced oscillations in the East Antarctic Ice Sheet: (2) implications or global sea-level changes. Palaeogeogr. Palaeoclimatol. Palaeoecol. 260, 66–76. doi:10.1016/j.palaeo.2007.08.021.

Naish, T.R., Woolfe, K.J., Barrett, P.J., Wilson, G.S., Atkins, C., Bohaty, S.M., Backer, C.J., Claps, M., Davey, F.J., Dunbar, G.B., and others. 2001. Orbitally induced oscillations in the East Antarctic ice sheet at the Oligocene/Miocene boundary. Nature 413:719–723, https://doi.org/ 10.1038/35099534.

Nakayama, Y., Menemenlis, D., Zhang, H., Schodlok, M., Rignot, E., 2018. Origin of Circumpolar Deep Water Intruding onto the Amundsen and Bellingshausen Sea Continental Shelves. Nature Communications 9 (1): 1–9. https://doi.org/10.1038/s41467-018-05813-1.

Nelson, C. H., Escutia, C., Damuth, J. E., & Twichell, D. C., 2011. Interplay of mass-transport and turbidite-system deposits in different active tectonic and passive continental margin settings: external and local controlling factors. In Mass-Transport Deposits in Deepwater Settings (Vol. 96, pp. 39–66). Society for Sedimentary Geology.

Nelson, C. S., and Cooke, P.J., 2001. History of Oceanic Front Development in the New Zealand Sector of the Southern Ocean during the Cenozoic—a Synthesis. New Zealand Journal of Geology and Geophysics 44 (4): 535–53. https://doi.org/10.1080/00288306.2001.9514954.

Nelson, C.H., 1976, Late Pleistocene and Holocene depositional trends, processes and history of Astoria deep-sea fan, northeast Pacific: Marine Geology, v. 20, p. 129–173, doi: 10 .1016 /0025 -3227 (76)90083 -9.

Nelson, C.H., 1990, Estimated Post-Messinian sediment supply and deposition rates of the Spanish Ebro margin: Marine Geology of the Ebro continental margin, northwestern Mediterranean Sea: Marine Geology, v. 95, p. 395–418, doi: 10 .1016 /0025 -3227 (90)90126 -5.

Nelson, C.H., and Nilsen, T.H., 1984, Modern and ancient deep-sea fan sedimentation: Society for Sedimentary Geology Short Course Notes Volume 14, 403 p., doi: 10 .2110 /scn .84 .14.

Nelson, C.H., Escutia, C., Goldfinger, C., Karabanov, E., Gutierrez-Pastor, J., and De Batist, M., 2009, External controls on modern clastic turbidite systems: Three case studies, in Kneller, B., et al., eds., External controls on deep-water depositional systems: Society for Sedimentary Geology Special Publication 92, p. 57–76, doi: 10 .2110 /sepmsp .092 .057.

Nelson, C.H., Karabanov, E.B., and Colman, S.M., 1995, Late Quaternary turbidite systems in Lake Baikal, Russia, in Pickering, K.T., et al., eds., Atlas of deep- water environments Architectural style in turbidite systems: London, Chapman & Hall, p. 29–33, doi: 10 .1007 /978 -94 -011 -1234 -5_7.

Nelson, C.H., Karabanov, E.B., Colman, S.M., and Escutia, C., 1999, Tectonic and sediment supply control of deep rift lake turbidite systems, Lake Baikal, Russia: Geology, v. 27, p. 163–166, doi: 10 .1130 /0091 -7613 (1999)027 <0163: TASSCO >2 .3 .CO;2.

Nelson, C.S., Cooke, P.J., 2001. History of Oceanic Front Development in the New Zealand Sector of the Southern Ocean during the Cenozoic—a Synthesis. New Zealand Journal of Geology and Geophysics 44 (4): 535–53. https://doi.org/10.1080/00288306.2001.9514954.

O'Brien, P.E., A.K. Cooper, C. Richter, et al. 2001. Proceedings of the Ocean Drilling Program, Initial Reports, Volume 188. Texas A&M University, College Station TX, https://doi.org/10.2973/odp.proc.ir.188.2001.

Ogg, G. J., Ogg, G. M., and Gradstein, F. M., 2016. A Concise Geologic Time Scale. Elsevier, Amsterdam. https://doi.org/10.1016/C2009-0-64442-1

Olbers, D., Borowski, D., Völker, C., Wölff, J., 2004. The dynamical balance, transport and circulation of the Antarctic Circumpolar Current, Antarct. Sci., 16, 439–470.

Orejola, N., S. Passchier, and IODP Expedition 318 Scientists, 2014. Sedimentology of lower Pliocene to upper Pleistocence diamictons from IODP Site 1358, Wilkes Land margin, and implications and dynamic topography. Earth and Planetary Science Letters 387:27–33, https://doi.org/ 10.1016/j.epsl.2013.10.030.

Orsi, A. H., Johnson, G. C., & Bullister, J. L., 1999. Circulation, mixing, and production of Antarctic Bottom Water. Progress in Oceanography, 43(1), 55–109. https://doi.org/10.1016/S0079-6611(99)00004-X

Orsi, A. H., Smethie, W .M., Bullister, J. L., 2002. On the total input of Antarctic waters to the deep ocean: a preliminary estimate from chlorofluorocarbon measurements. JournalofGeophysicalResearch-Oceans107(C8),1–14.

Orsi, A. H., Wiederwohl, C. L., 2009. A recount of Ross Sea waters. Deep-Sea Research II, 56, 778-795.

Orsi, A.H., Whitworth, T., Nowlin, W.D., 1995. On the meridional extent and fronts of the Antarctic Circumpolar Current, Deep-Sea Res. Pt. I, 42, 641–673. https://doi.org/10.1016/0967-0637(95)00021-W.

Osipov, E.Y., and Khlystov, O.M., 2010, Glaciers and meltwater flux to Lake Baikal during the Last Glacial Maximum: Palaeogeography, Palaeoclimatology, Palaeoecology, v. 294, p. 4–15, doi: 10 .1016 /j .palaeo .2010 .01 .031.

Pagani, M, Liu, Z., Lariviere, J., Ravelo A. C., 2010. High Earth-system climate sensitivity

Pälike, H., Norris, R.D., Herrle, J.O., Wilson, P.A., Coxall, H.K., Lear, C.H., Shackleton, N.J., Tripati, A.K., and Wade. B.S., 2006. The heartbeat of the Oligocene climate system. Science 314:1,894–1,898, https://doi.org/10.1126/science.1133822.

Palter, J. B., Frölicher, T. L., Paynter, D., & John, J. G., 2018. Climate, ocean circulation, and sea level changes under stabilization and overshoot pathways to 1.5 K warming. Earth System Dynamics, 9(2), 817–828. doi:10.5194/esd-9-817-2018

Pardo, P. C., Pérez, F. F., Velo, A., Gilcoto, M., 2012. Water masses distribution in the Southern Ocean: Improvement of an extended OMP (eOMP) analysis. Progress in Oceanography, 103, 92-105.

Passchier, S., Bohaty, S. M., Jiménez-Espejo, F., Pross, J., Röhl, U., van de Flierdt, T., Escutia, C., and Brinkhuis, H., 2013. Early Eocene to middle Miocene cooling and aridification of East Antarctica: Geochemistry, Geophysics, Geosystems, v. 14, no. 5, p. 1399-1410.

Passchier, S., Browne, G., Field, B., Fielding, C. R., Krissek, L. A., Panter, K., Pekar, S. F., and ANDRILL-SMS Science Team, 2011. Early and middle Miocene Antarctic glacial history from the sedimentaty faceis distribution in the AND-2A drill hole, Ross Sea, Antarctica. GSA Bulletin, v. 123; no. 11/12; p. 2352–2365; doi: 10.1130/B30334.1

Passchier, S., Ciarletta, D. J., Miriagos, T. E., Bijl, P. K., & Bohaty, S. M., 2016. An Antarctic stratigraphic record of stepwise ice growth through the Eocene-Oligocene transition. Geological Society of America Bulletin, 129(3-4), 318–330. doi:10.1130/b31482.1

Passchier, S., Ciarletta, D., Henao, V., and Sekkas, V., 2018. Sedimentary processes and facies on a high-latitude passive continental margin, Wilkes Land, East Antarctica. Geological Society, London, Special Publications, 475, https://doi.org/10.1144/SP475.3

Patterson, M.O., McKay, R., Naish, T., Escutia, C., Jimenez- Espejo, F.J., Raymo, M.E., Meyers, S.R., Tauxe, L., Brinkhuis, H., Klaus, A., Fehr, A., Bendle, J.A.P., Bijl, P.K., Bohaty, S.M., Carr, S. A., Dunbar, R.B., Flores, J.A., Gonzalez, J.J., Hayden, T.G., Iwai, M., Katsuki, K., Kong, G.S., Nakai, M., Olney, M.P., Passchier, S., Pekar, S.F., Pross, J., Riesselman, C.R., Röhl, U., Sakai, T., Shrivastava, P.K., Stickley, C.E., Sugasaki, S., Tuo, S., van de Flierdt, T., Welsh, K., Williams, T., Yamane, M., 2014. Orbital forcing of the East Antarctic ice sheet during the Pliocene and Early Pleistocene, Nat. Geosci., 7, 841 847. https://doi.org/10.1038/ngeo2273, 2014.

Paull, C.K., Talling, P.J., Maier, K.L., Parsons, D., Xu, J., Caress, D.W., Gwiazda, R., Lundsten, E.M., Anderson, K., Barry, J.P., et al. Powerful turbidity currents driven by dense basal layers. Nat. Commun. 2018, 9, 4114. DOI: 10.1038/s41467-018-0625

Pekar, S. F., Christie-Blick, N., Kominz, M. A., and Miller, K. G., 2002, Calibration between eustatic estimates from backstripping and oxygen isotopic records for the Oligocene: Geology, v. 30, no. 10, p. 903-906.

Pekar, S.F., Christie-Blick, N., 2008. Resolving Apparent Conflicts between Oceanographic and Antarctic Climate Records and Evidence for a Decrease in p CO 2 during the Oligocene through Early Miocene (34 – 16 Ma), 260: 41–49. https://doi.org/10.1016/j.palaeo.2007.08.019.

Pekar, S.F., DeConto, R.M., Harwood, D.M., 2006. Resolving a late Oligocene conundrum: Deep-sea warming and Antarctic glaciation, Palaeogeogr. Palaeocl., 231, 29–40.

Pfuhl, H. A., and McCave, I. N., 2005. Evidence for late Oligocene establishment of the Antarctic Circumpolar Current. Earth and Planetary Science Letters, 235 (3-4). pp. 715-728. ISSN 0012-821X DOI https://doi.org/10.1016/j.epsl.2005.04.025

Pfuhl, H. A., McCave, I. N., Integrated age models for the early Oligocene–early Miocene, Sites 1168 and 1170–1172, in: N.F. Exon, J.P. Kennett, M.J. Malone (Eds.), Leg 189 The Tasmanian Gateway, Proc. ODP, Scientific Results, vol. 189, Ocean Drilling Program, College Station, TX, 2003, pp. 1 –21.

Pickett, D.A, Wasserburg, G . J., 1989. Neodymium and strontium isotopic characteristics of New Zealand granitoids and related rocks. Contrib. Mineral Petrol 103, 131-142

Piepgras, D. J., and Jacobsen, S. B., 1988. The isotopic composition of neodymium in the North Pacific, Geochim. Cosmochim. Acta, 52, 1373–1381.

Piepgras, D. J., and Wasserburg, G. J., 1987. Rare earth element transport in the western North Atlantic inferred from Nd isotopic observations, Geochim. Cosmochim. Acta, 51, 1257–1271.

Piper., D.J.W., Brisco, C., 1975. Deep-water continental-margin sedimentation , dsdp Leg 28, Antarctica. In Hayes D. E., Frakes, L.A., et al., 1975 Initial Reports of the Deep Sea Drilling Project, Vol. 28, U.S. Government Printing Office, Washington pp.727-755. doi:10.2973/dsdp.proc.28.121.1975.

Pole, M., Hill, B., and Harwood, D., 2000. Eocene Plant Macrofossils from Erratics, Mcmurdo Sound, Antarctica, in Stilwel, J. D., and Feldman, R. M., eds., Paleobiology and Paleoenvironments of Eocene Rocks: McMurdo Sound, East Antarctica, Volume 76: Washington, DC, American Geophysical Union, p. 243-251.

Pollard, D, DeConto, RM, Alley R. B., 2015 Potential Antarctic Ice Sheet retreat driven by hydrofracturing and ice cliff failure. Earth Planet. Sci. Lett. 412, 112–121. (doi:10.1016/j.epsl.2014.12.035)

Prebble, J., Crouch, E., Carter, L., Cortese, G., Bostock, H., Neil, H., 2013. An expanded modern dinoflagellate cyst dataset for the Southwest Pacific and Southern Hemisphere with environmental associations. Marine Micropaleontology, 101, 33-48.

Pritchard, H.D., Ligtenberg, S.R. M., Fricker, H.A., Vaughan, D.G., Van Den Broeke, M.R., Padman, L., 2012. Antarctic Ice-Sheet Loss Driven by Basal Melting of Ice Shelves." Nature 484 (7395): 502–5. https://doi.org/10.1038/nature10968.

Pritchard, H.D., Ligtenberg, S.R. M., Fricker, H.A., Vaughan, D.G., Van Den Broeke, M.R., Padman, L., 2012. Antarctic Ice-Sheet Loss Driven by Basal Melting of Ice Shelves." Nature 484 (7395): 502–5. https://doi.org/10.1038/nature10968.

Pross, J., Contreras, L., Bijl, P. K., Greenwood, D. R., Bohaty, S. M., Schouten, S., et al., 2012. Persistent near–tropical warmth on the antarctic continent during the early eocene epoch. Nature, 488(7409),73–77. https://doi.org/10.1038/nature11300

Rebesco, M., & Camerlenghi, A., 2008. Late Pliocene margin development and mega debris flow deposits on the Antarctic continental margins: Evidence of the onset of the modern Antarctic Ice Sheet? Palaeogeography, Palaeoclimatology, Palaeoecology, 260(1-2), 149–167. doi:10.1016/j.palaeo.2007.08.009

Rebesco, M., Hernández-Molina, F.J., Van Rooij, D., Wåhlin, A., 2014. Contourites and associated sediments controlled by deep-water circulation processes: State-of-theart and future considerations, Mar. Geol., 352, 111–154. https://doi.org/10.1016/j.margeo.2014.03.011.

Reese, R., Gudmundsson, G. H., Levermann, A., & Winkelmann, R., 2017. The far reach of ice-shelf thinning in Antarctica. Nature Climate Change, 8(1), 53–57. doi:10.1038/s41558-017-0020-x

Reinardy, B.T.I., Escutia, C., Iwai, M., Jimenez- Espejo, F.J., Cook, C., van de Flierdt, T., and Brinkhuis, H., 2015. Repeated advance and retreat of the East Antarctic Ice Sheet on the continental shelf during the early Pliocene warm period. Palaeogeography, Palaeoclimatology, and Palaeoecology 422:65–84, https://doi.org/10.1016/j.palaeo.2015.01.009.

Richey, J.N., Tierney, J.E., 2016. GDGT and alkenone flux in the northern Gulf of Mexico: Implications for the TEX86 and UK'37 paleothermometers. Paleoceanography, 31(12), 1547-1561.

Rickli, J., Gutjahr, M., Vance, D., Fischer-Gödde, M., Hillenbrand, C.-D., & Kuhn, G., 2014. Neodymium and hafnium boundary contributions to seawater along the West Antarctic continental margin. Earth and Planetary Science Letters, 394, 99–110 https://doi.org/10.1016/j.Bepsl.2014.03.008

Rignot, E. and Jacobs, S. S., 2002. Rapid Bottom Melting Widespread near Antarctic Ice Sheet Grounding Lines. Science, 296(5575), 2020–2023. doi:10.1126/science.1070942

Rignot, E., Jacobs, S., Mouginot, J., & Scheuchl, B., 2013. Ice-Shelf Melting Around Antarctica. Science, 341(6143), 266–270. doi:10.1126/science.1235798

Rignot, E., Mouginot, J., Scheuchl, B., van den Broeke, M., van Wessem., M., Morlighem, M., 2019. Four decades of Antarctic Ice Sheet mass balance from 1979–2017.

Rintoul S. R, Silvano, A., Pena-Molino, B., van Wijk, E., Rosenberg, M., Greenbaum, J. S., Blankenship, D. D., 2016. Ocean heat drives rapid basal melt of Totten Ice Shelf. Science Advances 2:e1601610.

Rintoul, S. R., 1998. On the origin and influence of Adélie Land Bottom Water. In Ocean, ice, and atmosphere: Interactions at the Antarctic continental margin (Vol. 75, pp. 151–171). Washington, DC: American Geophysical Union.

Rintoul, S. R., 2018. The global influence of localized dynamics in the Southern Ocean. Nature, 558(7709), 209–218. https://doi.org/10.1038/s41586-018-0182-3

Rintoul, S. R., and Sokolov S., 2001. Baroclinic transport variability of the Antarctic Circumpolar Current south of Australia (WOCE repeat section SR3), J. Geophys. Res., 106, 2795–2814, doi:10.1029/2000JC900117.

Rintoul, S. R., Chown, S. L., DeConto, R. M., England, M. H., Fricker, H. A., Masson-Delmotte, V., Naish, T.R., Siegert, M. J. and Xavier, J. C., 2018. Choosing the future of Antarctica. Nature 558, 233-241 https://doi.org/10.1038/s41586-018-0173-4.

Rintoul, S. R., Sokolov, S., Williams, M. J. M., Peña Molino, B., Rosenberg, M., & Bindoff, N. L., 2014. Antarctic Circumpolar Current transport and barotropic transition at Macquarie Ridge. Geophysical Research Letters, 41, 7254–7261. https://doi.org/10.1002/2014GL061880

Rintoul, S.R., Hughes, C., Olbers, D., 2001. The Antarctic circumpolar current system. In G. Siedler, J. Church, J. Gould (Eds.), Ocean circulation and climate. New York: Academic Press. Proc. Natl. Acad. Sci. USA, pp. 271-302.

Robert, C., Kennett, J. P., 1997. Antarctic continental weathering changes during the Eocene-Oligocene cryosphere expansion: Clay mineral and oxygen isotope evidence. Geology v25.; no 7; p. 587-590

Roberts, A. P., Sagnotti, L., Florindo, F., Bohaty, S. M., Verosub, K. L., Wilson, G. S., and Zachos, J. C., 2013. Environmental record of paleoclimate, unroofing of the Transantarctic Mountains, and volcanism in later Eocene to early Miocene glaci-marine sediments from the Victoria Land Basin, Ross Sea, Antarctica, Journal of Geophysical Research: Solid Earth, 118, 1845-186 1

Rodriguez-Tovar, F.J., Dorador, J., 2014. Ichnological analysis of pleistocene sediments from the IODP Site U1385 “Shackleton Site” on the Iberian margin: approaching paleoenvironmental conditions. Palaeogeogr. Palaeoclimatol. Palaeoecol. 409,24–32.

Rodríguez-Tovar, F.J., Dorador, J., 2015. Ichnofabric characterization in cores: a method of digital image treatment. Ann. Soc. Geol. Pol. 85 (3), 465–471.

Rodríguez-Tovar, F.J., Dorador, J., Grunert, P., Hodell, D., 2015b. Deep-sea trace fossil and benthic foraminiferal assemblages across glacial terminations 1, 2 and 4 at the “Shackleton Site” (IODP Expedition 339, Site U1385). Glob. Planet. Chang. 133, 359–370.

Rodríguez-Tovar, F.J., Dorador, J., Hodell, D.A.V. 2019. Trace fossils evidence of a complex history availability and oxygen conditions during Heinrich Event 1. Global and Planetary Change, 174, 26-34.

Rodríguez-Tovar, F.J., Dorador, J., Martin-Garcia, G.M., Sierro, F.J., Flores, J.A., Hodell, D.A., 2015a. Response of macrobenthic and foraminifer communities to changes in deep-sea environmental conditions from marine isotope stage (MIS) 12 to 11 at the “Shackleton Site”. Glob. Planet. Chang. 133, 176–187.

Rodríguez-Tovar, F.J., Nagy, J., Reolid, M., 2014. Palaeoenvironment of Eocene prodelta in Spitsbergen recorded by the trace fossil Phycosiphon incertum. Polar Res. 33, 23786.

Russell, J. L., Dixon, K. W., Gnanadesikan, A., Stouffer, R. J., and Toggweiler, J. R., 2006. The Southern Hemisphere Westerlies in a Warming World: Propping Open the Door to the Deep Ocean. Journal of Climate, v.19 6382-6390

Salabarnada, 2020. Oligocene-Miocene Ice sheet and Paleoceanographic Evolution of the Eastern Wilkes Land margin. PhD Thesis

Salabarnada, A., Escutia, C., Röhl, U., Nelson, C.H., McKay, R., Jiménez-Espejo, F.J., Bijl, P. K., Hartman, J.D., Strother, S. L., Salzmann, U., Evangelinos, D., López-Quirós, A., Flores, J.A., Sangiorgi, F., Ikehara, M., Brinkhuis, H., 2018. Paleoceanography and ice sheet variability offshore Wilkes Land, Antarctica – Part 1: Insights from late Oligocene astronomically paced contourite sedimentation, Clim. Past, 14, 991–1014, https://doi.org/10.5194/cp-14-991-2018..

Salzmann, U., Strother, S., Sangiorgi, F., Bijl, P., Pross, J., Woodward, J., Escutia, C., and Brinkhuis, H., 2016. Oligocene to Miocene terrestrial climate change and the demise of forests on Wilkes Land, East Antarctica, in: EGU General Assembly Conference Abstracts, 18, EPSC2016-2717, 2016.

Sangiorgi, F., Bijl, P. K., Passchier, S., Salzmann, U., Schouten, S., McKay, R., Cody, R. D., Pross, J., Van De Flierdt, T., Bohaty, S. M., Levy, R., Williams, T., Escutia, C., Brinkhuis, H., 2018. Southern Ocean warming and Wilkes Land ice sheet retreat during the mid-Miocene. Nature Communications. 9, 317, doi:10.1038/s41467-017-02609-7

Sangiorgi, F., Bijl, P.K., Passchier, S., Salzmann, U., Schouten, S., McKay, R., Cody, R.D., Pross, J., Flierdt, T., Bohaty, S.M. & Levy, R., 2018. Southern Ocean warming and Wilkes Land ice sheet retreat during the mid-Miocene. Nature communications, 9(1), 317.

Sarmiento, J. L., Gruber, N., Brzezinski M. A., and Dunne, J. P., 2004. High-latitude controls of thermocline nutrients and low latitude biological productivity. Nature 427, 56-59.

Sarmiento, J. L., Gruber, N., Brzezinski, M. A., and Dunne, J. P., 2004. High-latitude controls of thermocline nutrients and low latitude biological productivity. Nature 427, 56–60; corrigendum 479, 556 (2011).

Scher, H.D., Bohaty, S.M., Zachos, J. C., Delaney, M.L., 2011. Two-stepping into the icehouse: East Antarctic weathering during progressive ice-sheet expansion at the Eocene–Oligocene transition. Geology 39, 383–386.

Scher, H. D., 2014. Stacking PEAT; A stacked Nd isotope record for the Paleogene equatorial Pacific. Società Geologica Italiana, 31, 191-192 (doi: 10.3301/ROL.2014.115).

Scher, H. D., and Martin, E. E., 2006. Timing and climatic consequences of the opening of Drake Passage, Science, 312(5772), 428-430.

Scher, H. D., and Martin, E. E., 2004. Circulation in the Southern Ocean during the Paleogene inferred from neodymium isotopes. Earth Planet. Sci. Lett. 228, 391–405.

Scher, H. D., and Martin, E. E., 2008. Oligocene deep water export from the North Atlantic and the development of the Antarctic Circumpolar Current examined with neodymium isotopes, Paleoceanography, 23(1).

Scher, H. D., S. M. Bohaty, B. W. Smith, and G. H. Munn, 2014. Isotopic interrogation of a suspected late Eocene glaciation, Paleoceanography, 29(6), 628-644.

Scher, H. D., Whittaker, J., William, S., Latimer, J., Kordesch, W., Delaney, M., 2015. Onset of Antarctic circumpolar current 30 million years ago as Tasmanian Gateway aligned with westerlies. Nature 523, 580–583.

Schlitzer, R, 2016. Ocean data view. Retrieved from odv.awi.de. https://doi.org/10.1182/blood-2012-03-418400

Schouten, S., Hopmans, E.C., Rosell-Melé, A., Pearson, A., Adam, P., Bauersachs, T., Brocks, J.J., et al., 2013. An interlaboratory study of TEX86 and BIT analysis of sediments, extracts, and standard mixtures. Geochemistry, Geophysics, Geosystems, 14(12), 5263-5285.

Schouten, S., Hopmans, E.C., Schefuß, E., Damste, J.S.S., 2002. Distributional variations in marine crenarchaeotal membrane lipids: a new tool for reconstructing ancient sea water temperatures? Earth and Planetary Science Letters, 204(1-2), 265-274.

Schuur, C.L., Coffin, M.F., Frohlich, C., Massell, C.G., Karner, G.D., Ramsey, D., Caress, D.W., 1998. Sedimentary regimes at the Maquarie Ridge Complex: interaction of Southern Ocean circulation and plate boundary bathymetry. Paleoceanography 13, 646-670.

Scotese, C.R., & Wright, N., 2018. PALEOMAP Paleodigital Elevation Models (PaleoDEMS) for the Phanerozoic PALEOMAP Project, https://www.earthbyte.org/paleodem-resource-scotese-and-wright-2018.

Seki, A., Tada, R., Kurokawa, S., Murayama, M., 2019. High-resolution Quaternary record of marine organic carbon content in the hemipelagic sediments of the Japan Sea from bromine counts measured by XRF core scanner Progress in Earth and Planetary Science volume 6, Article number: 1 (2019).

Seton, M., Müller, R.D., Zahirovic, S., Gaina, C., Torsvik, T.H., Shephard, G., Talsma, A., Gurnis, M., Turner, M., Maus, S., Chandler, M., 2012. Global continental and ocean basin reconstructions since 200 Ma, Earth-Science Reviews, Volume 113, Issues 3-4, July 2012, Pages 212-270, ISSN 00128252,10.1016/j.earscirev.2012.03.002.

Shackleton, N. J., and Kennett, J. P., 1975. Paleotemperature history of the Cenozoic and the initiation of Antarctic glaciation: oxygen and carbon isotope analyses in DSDP Sites 277, 279, and 281: Initial reports of the deep sea drilling project, v. 29, p. 743-755

Shanmugam, G., 2018. Slides, Slumps, Debris Flows, Turbidity Currents, Hyperpycnal Flows, and Bottom Currents. Reference Module in Earth Systems and Environmental Sciences. doi:10.1016/b978-0-12-409548-9.10884-x

Shanmugam, G., Spalding, T.D., Rofheart, D.H.,1993. Traction structures in deep-marine, bottom-current-reworked sands in the Pliocene and Pleistocene, Gulf of Mexico, Geology, 21, 929–932. https://doi.org/10.1130/0091- 7613(1993)021<0929:TSIDMB>2.3.CO;2.

Shaw, H., and Wasserburg, G., 1985. Sm-Nd in marine carbonates and phosphates: Implications for Nd isotopes in seawater and crustal ages, Geochimica et Cosmochimica Acta, 49(2), 503-518.

Shen, Q., Wang, H., Shum, C. K., Jiang, L., Hsu, H. T., Dong, J., 2018. Recent high resolution Antarctic ice velocity maps reveal increased mass loss in Wilkes Land, East Antarctica. Scientific Reports. 8, doi:10.1038/s41598-018-22765-0

Shevenell, A. E., Kennett, J. P., & Lea, D. W., 2008. Middle Miocene ice sheet dynamics, deep-sea temperatures, and carbon cycling: A Southern Ocean perspective. Geochemistry, Geophysics, Geosystems, 9(2). https://doi.org/10.1029/2007GC00173

Shichi, K., Takahara, H., Krivonogov, S.K., Bezrukova, E.V., Kashiwaya, K., Takehara, A., and Nakamura, T., 2009, Late Pleistocene and Holocene vegetation and climate records from Lake Kotokel, central Baikal region: Quaternary International, v. 205, p. 98–110, doi: 10 .1016 /j .quaint .2009 .02.005.

Sijp, W. P., von der Heydt, A. S., & Bijl, P. K., 2016. Model simulations of early westward flow across the Tasman Gateway during the early Eocene. Climate of the Past 12(4), 807-817.

Sijp, W. P., von der Heydt, A. S., Dijkstra, H. A., Flögel, S., Douglas, P. M. J., Bijl, P. K., 2014. The role of ocean gateways on cooling climate on long time scales. Global and Planetary Change. 119, 1–22.

Sijp, W.P., England, M.H., Huber, M., 2011. Effect of the deepening of the Tasman Gateway on the global ocean. Paleoceanography 26, 4207

Silvano, A., Rintoul, S. R., Pena-Molino, B, and Williams, G. D., 2017. Distribution of water masses and meltwater on the continental shelf near the Totten and Moscow University ice shelves, J. Geophys. Res. Oceans, 122, 2050–2068, doi:10.1002/ 2016JC012115.

Slater, T., Shepherd, A., McMillan, M., Muir, A., Gilbert, L., Hogg, A. E., Konrad, H., and Parrinello, T., 2018. A new digital elevation model of Antarctica derived from CryoSat-2 alimetry. The Cryosphere, 12, 15551-1562, https://doi.org/10.5194/tc-12-1551-2018

Sluijs, A., Pross, J., Brinkhuis, H., 2005. From greenhouse to icehouse; organic-walled dinoflagellate cysts as paleoenvironmental indicators in the Paleogene. Earth-Science Reviews, 68(3-4), 281-315.

Smith, B., Flicker, H. A., Gardner, A. S., Medley, B., Nilsson, J., Paolo, F. S., Holschuh, N., Adusumilli, S., Brunt, K., Csatho, Bea, Harbeck, J., Markus, T., Neumann, T., Siegfried, M. R., Zwally, H. J., 2020. Pervasive ice sheet mass loss reflects competing ocean and atmosphere processes. Science eaaz5845 DOI: 10.1126/science.aaz5845

Sokolov, S., & Rintoul, S. R., 2007. Multiple jets of the Antarctic Circumpolar Current south of Australia. Journal of Physical Oceanography, 37(5), 1394–1412. https://doi.org/10.1175/JPO3111.1

Sokolov, S., Rintoul, S.R., 2002. Structure of Southern Ocean fronts at 140°E, J. Mar. Syst., 37, 151–184. doi:10.1016/S0924-7963(02)00200-2.

Sokolov, S., Rintoul, S.R., 2009. Circumpolar structure and distribution of the Antarctiv Circumpolar Current fronts: 1. Mean circumpolar paths. J. Geophysical Research, 14, doi:10.1029/2008JC005108.

Sorlien, C.C., Luyendyk, B.P., Wilson, D.S., Bartek, L.R., Diebold, J.B., 2007. Oligocene development of the West Antarctic Ice Sheet recorded in eastern Ross Sea strata. Geology 35, 467–470.

Spence, P., Holmes, R. M., Hogg, A. M., Griffies, S. M., Stewart, K. D., & England, M. H., 2017. Localized rapid warming of West Antarctic subsurface waters by remote winds. Nature Climate Change, 7(8), 595–603. doi:10.1038/nclimate3335

Stichel, T., Frank, M., Rickli, J., & Haley, B. A, 2012. The hafnium and neodymium isotope composition of seawater in the Atlantic sector of the Southern Ocean. Earth and Planetary Science Letters, 317-318, 282–294. https://doi.org/10.1016/j.epsl.2011.11.025

Stichel, T., Pahnke, K., Duggan, B., Goldstein, S. L., Hartman, A. E., Paffrath, R., & Scher, H. D., 2018. TAG Plume: Revisiting the Hydrothermal Neodymium Contribution to Seawater. Frontiers in Marine Science, 5. doi:10.3389/fmars.2018.00096

Stickley, C.E., Brinkhuis, H., Schellenberg, S., Sluijs, A., Roehl, U., Fuller, M., Grauert, M., Huber, M., Warnaar, J., Williams, G.L., 2004. Timing and nature of the deepening of the Tasmanian Gateway. Paleoceanography 19 (4), PA4027.

Stow, D. A.V., Tabrez, A. R., 1998. Hemipelagites: processes, facies and model. Geol. Soc. Lond. Spéc. Publ. 129, 317–337.

Stow, D., and Smillie, Z., 2020. Distinguish between Deep-Water Sediemnt Facies: Turbidites, Contourites and Hemipelagites. Geosciences, 10, 68.

Stow, D., Faugères, J.-C., 2008. Contourite Facies and the Facies Model, chap. 13, 223–256.

Stow, D.; Smillie, Z.; Pan, J.; Esentia, I., 2019. Deep-Sea contourites: Sediments and cycles. In Encyclopedia of Ocean Sciences; Elsevier BV: Amsterdam, The Netherlands, 2019; pp. 111–120.

Strand, K., Passchier, S., and Näsi, J., 2003, Implications of quartz grain microtextures for onset Eocene/Oligocene glaciation in Prydz Bay, ODP Site 1166, Antarctica: Palaeogeography, Palaeoclimatology, Palaeoecology, v. 198, no. 1–2, p. 101-111.

Strother, S. L., Salzmann, U., Sangiorgi, F., Bijl, P. K., Pross, J., Escutia, C., et al., 2017. A new quantitative approach to identify reworking in Eocene to Miocene pollen records from offshore Antarctica using red fluorescence and digital imaging. Biogeosciences, 14(8), 2089–2100. https://doi.org/10.5194/bg- 14-2089-2017

Tachikawa, K., Jeandel, C., and Roy-Barman, M., 1999. A new approach to the Nd residence time in the ocean, Earth Planet. Sci. Lett., 170, 433–446.

Tachikawa, K., Athias, ., Jeandel, C., 2003. Neodymium budget in the modern ocean and paleo-oceanographic implications, Journal of Geophysical Research: Oceans (1978–2012), 108(C8).

Talley, L. D., 2013. Closure of the Global Overturning Circulation Through the Indian, Pacific, and Southern Oceans: Schematics and Transports. Oceanography, 26(1), 80–97. doi:10.5670/oceanog.2013.07

Tanaka, T., Togashi, S., Kamioka, H., Amakawa, H., Kagami, H., Hamamoto, T., Yuhara, M., Orihashi, Y., Yoneda, S., Shimizu, H., Kunimaru, T., Takahashi, K., Yanagi, T., Nakano, T., Fujimaki, H., Shinjo, R., Asahara, Y., Tanimizu, M. & Dragusanu, C., 2000. JNdi-1: a neodymium isotopic reference in consistency with LaJolla neodymium. Chemical Geology, 168, 279-281.

Taylor, K.W., Huber, M., Hollis, C.J., Hernandez-Sanchez, M.T., Pancost, R.D., 2013. Re-evaluating modern and Palaeogene GDGT distributions: Implications for SST reconstructions. Global and Planetary Change, 108, 158-174.

Taylor, S. R., and McLennan, S. M., 1985. The continental crust: Its composition and evolution, 312 pp., Blackwell Scientific Publications, Oxford, U. K.

Thomas, D. J., 2004. Evidence for deep-water production in the North Pacific Ocean during the early Cenozoic warm interval, Nature, 430(6995), 65-68.

Thomas, D. J., Bralower, T. J., and Jones, C. E., 2003. Neodymium isotopic reconstruction of late Paleocene–early Eocene thermohaline circulation, Earth Planet. Sci. Lett., 209, 309–322.

Thomas, D.J., Korty, R., Huber, M., Schubert, J.A., Haines, B., 2014. Nd isotopic structure of the Pacific Ocean 70–30 Ma and numerical evidence for vigorous ocean circulation and ocean heat transport in a greenhouse world. Paleoceanography 29, 454–469.

Thompson, D.W.J., Solomon, S., 2002. Interpretation of recent Southern Hemisphere climate change. Science 296, 895–899.

Thornalley, D.J.R., Blaschek, M., Davies, F.J., Praectorius, S., Oppo, D.W., McManus, J.F., Hall, I.R., Kleiven, H., Renssen, H., McCave, I.N., 2013. Long-term variations in Iceland-Scotland overflow strength during the Holocene. Clim Past 9(5):2073–2084.

Toggweiler, J. R., Russell, J., 2008. Ocean circulation in a warming climate, Nature, 451, 286–288. https://doi.org/10.1038/nature06590.

Troedson, A. L., and Riding, J. B., 2002. Upper Oligocene to lowermost Miocene strata of King George Island, South Shetland Islands, Antarctica: stratigraphy, facies analysis, and implications for the glacial history of the Antarctic Peninsula: Journal of Sedimentary Research, v. 72, no. 4, p. 510-523.

Vail, P.R., Mitchum, R.M., Jr., Todd, R.G., Widmier, J.M., Thompson, S., III, Sangree, J.B., Bubb, J.N., and Hatlelid, W.G., 1977, Seismic stratigraphy and global changes of sea level, in Payton, C.E., ed., Seismic stratigraphy—Applications to hydrocarbon exploration: American Association of Petroleum Geologists Memoir 26, p. 49–51.

van de Flierdt, T., Frank, M., Halliday, A. N., Hein, J., Hattendorf, R.B., Günther, D., and Kubik, P. W., 2004. Deep and bottom water export from the Southern Ocean to the Pacific over the past 38 million years, Paleoceanography, 19(1), PA1020.

van de Flierdt, T., Griffiths, A.M., Lambelet, M., Little, S.H., Stichel, T., Wilson, D., 2016. Neodymium in the oceans: a global database, a regional comparison and implications for palaeoceanographic research. Philos. Trans. R. Soc. A 374, 20150293.

van Wijk, E.M., Rintoul, S.R., 2014. Freshening drives contraction of Antarctic Bottom Water in the Australian Antarctic Basin, Geophys. Res. Lett., 41, 1657–1664. https://doi.org/10.1002/2013GL058921.

Vanneste, M., De Batist, M., Golmshtok, A., Kremlev, A., and Versteeg, W., 2001, Multi-frequency seismic study of gas hydrate-bearing sediments in Lake Baikal, Siberia: Marine Geology, v. 172, p. 1–21, doi: 10 .1016 /S0025 -3227 (00) 00117-1.

Vologina, E.G., and Sturm, M., 2009, Types of Holocene deposits and regional pattern of sedimentation in Lake Baikal: Russian Geology and Geophysics, v. 50, p. 722–727, doi: 10 .1016 /j .rgg

Warny, S., Askin, R. A., Hannah, M. J., Mohr, B. A. R., Raine, J. I., Harwood, D. M., Florindo, F., and Team, t. S. S., 2009. Palynomorphs from a sediment core reveal a sudden remarkably warm Antarctica during the middle Miocene: Geology, v. 37, no. 10, p. 955-958.

Wei, W., Wise Jr., S.W., 1992. Selected Neogene calcareous nannofossil index taxa of the Southern Ocean: biochronology, biometrics and paleoceanography. In: Wise, Jr., S.W., Schlich, R., et al. (Eds.), Proceedings of ODP, Science Results, Vol. 120. Ocean Drilling Program, College Station, TX, pp. 523–537.

Weis, D., Kieffer, B., Maerschalk, C., Barling J., de Jong, J., Williams, G.A., Hanano, D., Pretorius, W., Mattielli, N., Scoates, J.S., 2006. High-precision isotopic characterization of USGS reference materials by TIMS and MC-ICP-MS, Geochemistry, Geophysics, Geosystems, 7(8), Q08006.

Whitehead, J.M., Bohaty, S.M., 2003. Pliocene summer sea surface temperature reconstruction using silicoflagellates from Southern Ocean ODP Site 1165, Paleoceanography, 18. https://doi.org/10.1029/2002PA000829.

Whitworth, T., Warren, B.A., Nowlin, W.D., Pillsbury, R.D., Moore, M.I., 1999. On the deep western-boundary current in the Southwest Paci¢c Basin. Prog. Oceanogr. 43, 1^54.

Wilson D.J., Piotrowski, A.M., Galy, A., Clegg, J.A., 2013 Reactivity of neodymium carriers in deep sea sediments: implications for boundary exchange and paleoceanography. Geochim. Cosmochim. Acta 109, 197–221. doi:10.1016/j.gca.2013.01.042.

Wilson, D. S., & Luyendyk, B. P., 2009. West antarctic paleotopography estimated at the Eocene-oligocene climate transition. Geophysical Research Letters, 36(16), 10–13. https://doi. org/10.1029/2009GL039297

Wilson, D.J., R.A. Bertram, E.F. Needham, T. van de Flierdt, K.J. Welsh, R.M. McKay, A. Mazumder, C.R. Riesselman, F.J. Jimenez-Espejo, and C. Escutia. 2018. Ice loss from the East Antarctic Ice Sheet during late Pleistocene interglacials. Nature 561:383–386, https://doi.org/10.1038/s41586-018-0501-8.

Wouters B, Martin-Español, A., Helm, V., Flament, T., van Wessem, J.M., Ligtenberg, S. R.M., van den Broeke, M. R., Bamber, J. L., 2015. Dynamic thinning of glaciers on the southern Antarctic Peninsula. Science 348:899–903. DOI: 10.1126/science.aaa5727

Wright, J., Schrader, H., and Holser W. T., 1987. Paleoredox variations in ancient oceans recorded by rare earth elements in fossil apatite, Geochimica et Cosmochimica Acta, 51(3), 631-644.

Wright, N., Scher, H. D., Seton, M., Huck, C. E., Duggan, B. D., 2018.No Change in Southern Ocean Circulation in the Indian Ocean From the Eocene Through Late Oligocene', Paleoceanography and Paleoclimatology, 33(2), pp. 152–167. doi: 10.1002/2017PA003238.

Zachos, J. C., Dickens, G., and Zeebe, R., 2008, An early Cenozoic perspective on greenhouse warming and carbon-cycle dynamics: Nature, v. 451, no. 7176, p. 279-283.

Zachos, J. C., Pagani, M., Sloan, L., Thomas, E., and Billups, K., 2001. Trends, Rhythms, and Aberrations in Global Climate 65 Ma to Present: Science, v. 292, no. 5517, p. 686-693.

Zachos, J.C., Breza, J., and Wise, S.W., 1992. Early Oligocene ice-sheet expansion on Antarctica: Stable isotope and sedimentological evidence from Kerguelen Plateau, southern Indian Ocean: Geology, v. 20, p. 569 573, doi: 10.1130/0091-7613(1992)020<0569:EOISEO >2.3.CO;2.

Zhang, Y. G., Pagani, M., Liu, Z., Bohaty, S. M., and DeConto, R., 2013, A 40-millionyear history of atmospheric CO2: Philosophical Transactions of the Royal Society A: Mathematical, Physical and Engineering Sciences, v. 371, no. 2001, p. 20130096.

Zhang, Y. G., Zhang, C. L., Liu, X.-L., Li, L., Hinrichs, K.-U., Noakes, J. E., 2011. Methane Index: A tetraether archaeal lipid biomarker indicator for detecting the instability of marine gas hydrates. Earth and Planetary Science Letters, 307(3-4), 525-534.

Zhang, Y.G., Pagani, M., and Wang. Z., 2016. Ring Index: A new strategy to evaluate the integrity of TEX86 paleothermometry. Paleoceanography and Paleoclimatology 31:220–232, https://doi.org/ 10.1002/ 2015PA002848.

Zonneveld, K.A., Marret, F., Versteegh, G.J., Bogus, K., Bonnet, S., Bouimetarhan, I., Crouch, E., de Vernal, A., Elshanawany, R., Edwards, L., Esper, O., Forke, S., Grøsfjeld, K., Henry, M., Holzwarth, U., Kielt, J.F., Y., Kim, S.Y., Ladouceur, S., Ledu, D., Chen, L., Limoges, A., Londeix, L., Lu, S.H., Mahmoud, M.S., Marino, G., Matsouka, K., Matthiessen, J., Mildenhal, D., Mudie, P., Neil, H., Pospelova, V., Qi, Y., Radi, T., Richerol, T., Rochon, A., Sangiorgi, F., Solignac, S., Turon, J.L., Verleye, T., Wang, Y., Wang, Z., Young M., 2013. Atlas of modern dinoflagellate cyst distribution based on 2405 data points. Review of Palaeobotany and Palynology, 191, 1-197. https://doi.org/10.1016/j.revpalbo.2012.08.003.

Chapter **10**

Appendices

Appendix 1

Supplementary Material for chapter 3

Supplementary text

Age model for Site 278

A total of 19 samples were examined for the identification of calcareous nannofossils. Only 12 of these samples contained enough amounts of nannoliths to provide biostratigraphic information (**Table10.1.3**). In most of these samples calcareous nanofossils are abundant. In addition, 7 samples were examined for diatom biostratigraphy, providing further age constraints based on Harwood and Maruyama, (1992) and Florindo et al. (2013) (**Table 10.1.2**). We established a new age model based on the integration of new magnetostratigraphic data, calcareous nannofossil and diatom biostratigraphy, calibrated using the Geological Time Scale (GPTS) 2012 (Gradstein et al., 2012) (**Fig. 10.1.3; Tables 10.1.3 and 10.1.4**).

The presence of *Cyclicargolithus floridanus* and absence of *Reticulofenestra daviesii* (very abundant in the lower part) between 329.14-331.95 mbsf, as well as the absence of *Reticulofenestra bisecta/stavensis* and other markers recorded the lower part of Site 278 is assigned to be between calcareous biozones NN2 (19-22.82 Ma) and NN1 (22.82-23.13) (Martini et al., 1970; Young et al., 2017). The first appearance datum (FAD) of *Thalassiosira spumellaroides and Raphidodiscus marylandicus is recognised* at 333.51 and 342.01 mbsf respectively, are assigned to 22.7 Ma. The FAD of *Fragilariopsis maleinterpretaria* is recognized at 348.51 mbsf, suggesting ages between 18.6-19.5 Ma. The last appearance datum (LAD) of *Bogorovia veniamini* (20 Ma) is recognized at 358.01 mbsf, while the FAD of *Bogorovia veniamini* (28.1 Ma) is recognized at 378.51mbsf. Based on the above, we correlate the magnetic reversal at 331.44 mbsf to the top of chron C6n (18.75 Ma), the reverse polarity at 338.74 mbsf to the top chron C6r (19.72 Ma), the normal polarity at 344.14 mbsf to the top of normal magnetozone 6CAn.2n (20.44 Ma), at 357.66 mbsf to the top of C6Bn.1n (21.77 Ma), at 366.28 mbsf to the top of C6Bn.2n (22.27 Ma) and at 377.94 mbsf to the top of C6Cn.3n (23.3 Ma).

A major change in the sedimentation occurs at Core 30 (378.91-379-75mbsf) marked by the first occurrence of high presence of siliceous microfossils (Kennett et al., 1975). This interval is characterized by the presence of *Reticulofenestra daviesii, Cyclicargolithus floridanus, Discoaster deflandrei*, while regular taxa recorded above, such as *Reticulofenestra bisecta/stavensis* and *Chiasmolithus altus* are absent. This assemblage is assigned to be between zones NN1 (22.82-23.13 Ma) and NP25 (23.13-26.48 Ma) (Martini et al., 1970; Young et al., 2017). Despite the weak and low inclinations of the paleomagnetic samples in this interval, we tentatively assign the normal polarity zone found at 377.94 mbsf to chron C6Cn.3n, suggesting an age of 23.3 Ma. Our interpretation is in line with the initial shipboard biostratigraphic data in this interval, which suggest an early Miocene age (Kennett et al., 1975).

Sediments between 396.95-428.45 mbsf (Cores 34-31) contain *Reticulofenestra daiviesii, Cyclicargolithus floridanus, Chiasmolithus altus, Reticulofenestra bisect/stavensis and, Cyclicargolithus abisectus* (<10um; not considered). One specimen of *Reticulofenestra umbilicus* in core 31 is interpreted as reworked, due to the absence of the taxon in the other samples. The interval between 379.5 and 414.41 mbsf is assigned to be between NP25 (23.13-26.84 Ma) and NP23 (29.62-32.02 Ma) (Martini et al. 1970; Young et al., 2017). The LAD of *Rocella vigilans* (25.4 Ma) is recognized at 408.51 mbsf. The FAD of *Cestodiscus robustus* at 411.51 suggests that sediments are younger than 33.7 Ma. Based on these ages, we correlate the normal polarity at 397.34 mbsf to C7n.2n

(24.11 Ma) and the magnetic reversal at 408.85 mbsf to the top of chron C9n (26.42 Ma). Sediments between 414.41-428.45 mbsf are assigned to NP23 (29.62-32.02 Ma) and maybe NP16 (40.4-42.87 Ma). However, initial shipboard biostratigraphic data suggest that sediments are no older than mid-Oligocene in age (Kennett et al., 1975). We therefore interpret the magnetic reversal at 425.44 mbsf as top of chron C12n (30.59 Ma).

Supplementary Figures

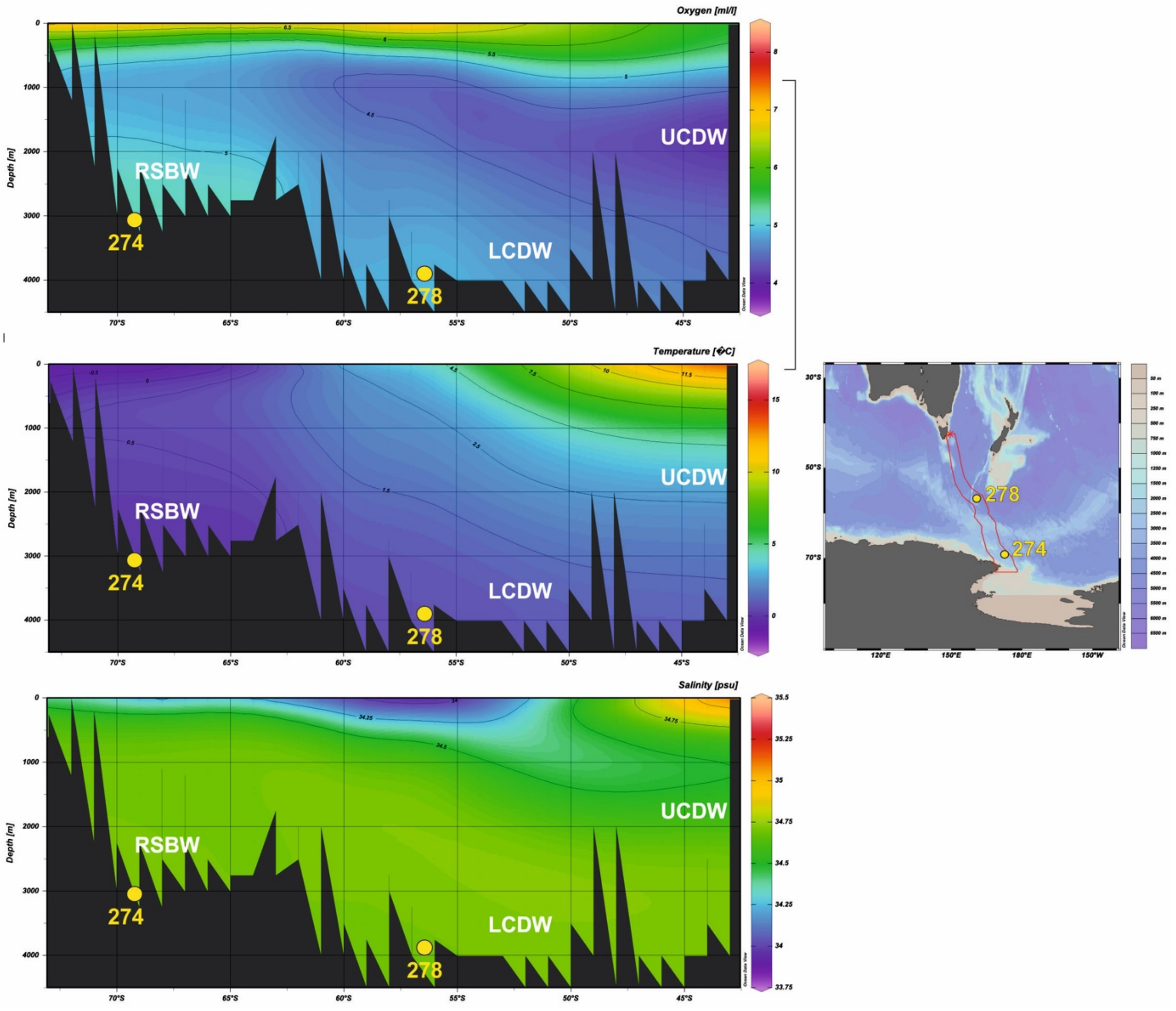

Figure 10.1.1: Maps showing the location of the sites and the distribution of dissolved oxygen, temperature and salinity versus depth along the Tasmanian to Ross Sea transect. Data derived from HYDROGRAPHIC ATLAS OF THE SOUTHERN OCEAN (Olberns et al., 1992). Maps were produced using Ocean Data View (Schlitzer, 2016). UCDW= Upper Circumpolar Deep Water; LCDW: Lower Circumpolar Deep Water; RSBW= Ross Sea Bottom Water.

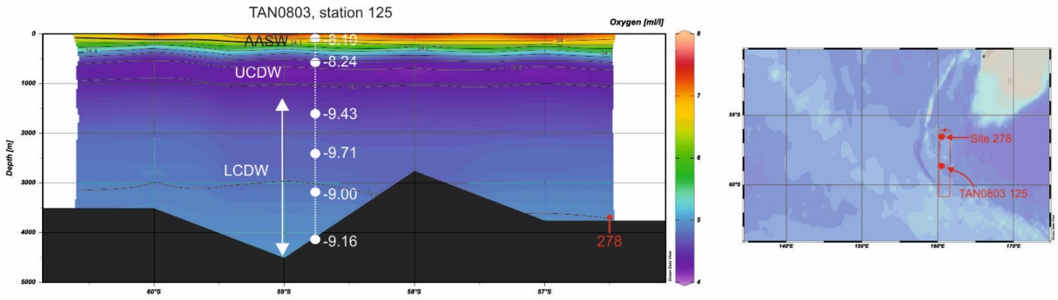

Figure 10.1.2: Neodymium isotopic composition from station TAN0803 station 125 (Lambelet et al., 2018) versus depth. Map and section were created using Ocean Data View software (Schlitzer, 2016)

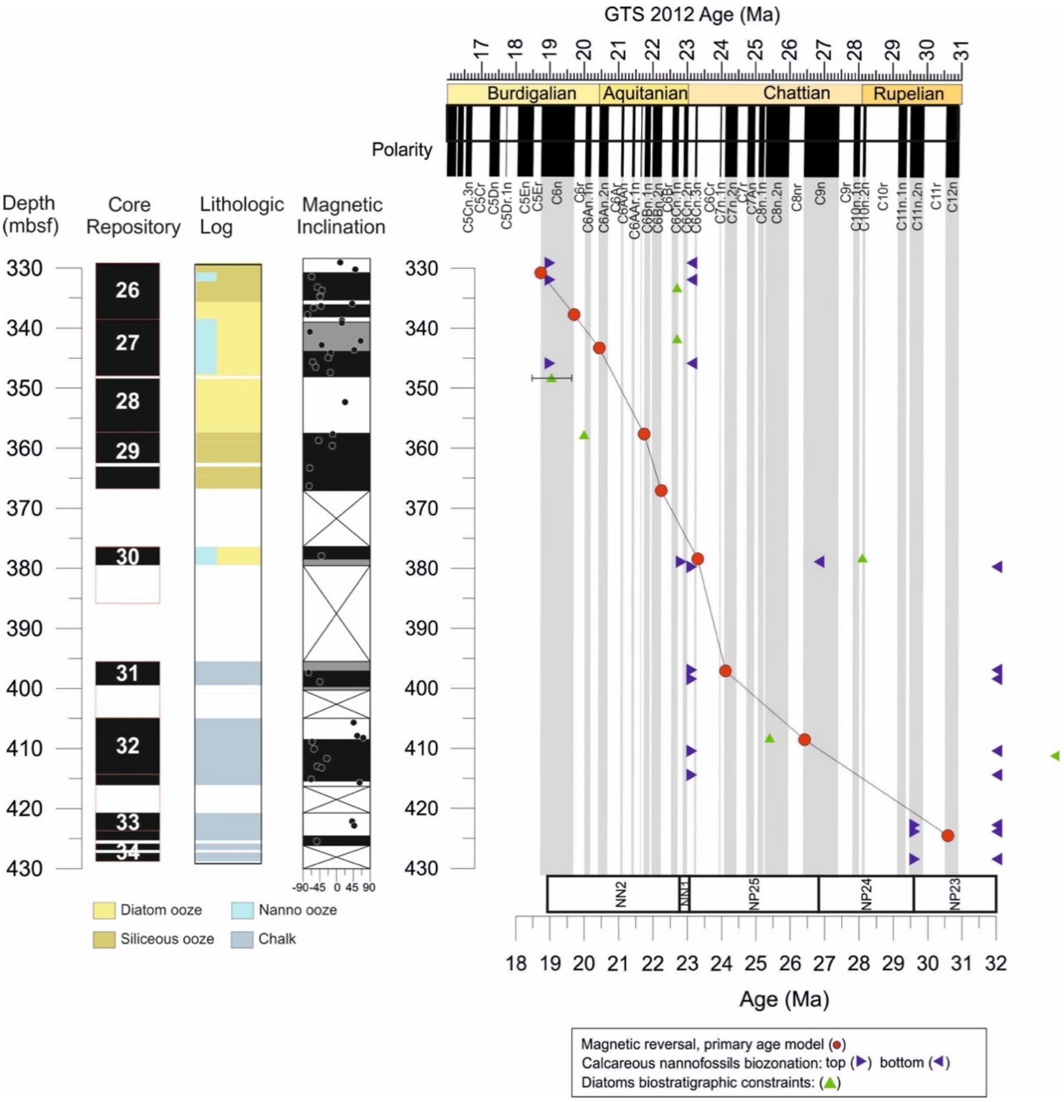

Figure 10.1.3: Revised age-depth model at Site 278. The lithologic log is based on initial shipboard sedimentological descriptions. Grey vertical boxes show normal polarity zones of the geomagnetic polarity timescale (Gradstein et al., 2012). Red dots = magnetic reversals, green triangles = diatom biostratigraphic constraints, blue triangles = time distribution interval of calcareous nannofossil bioevents. Magnetic stratigraphy: black = normal polarity, white= reverse polarity, grey undetermined.

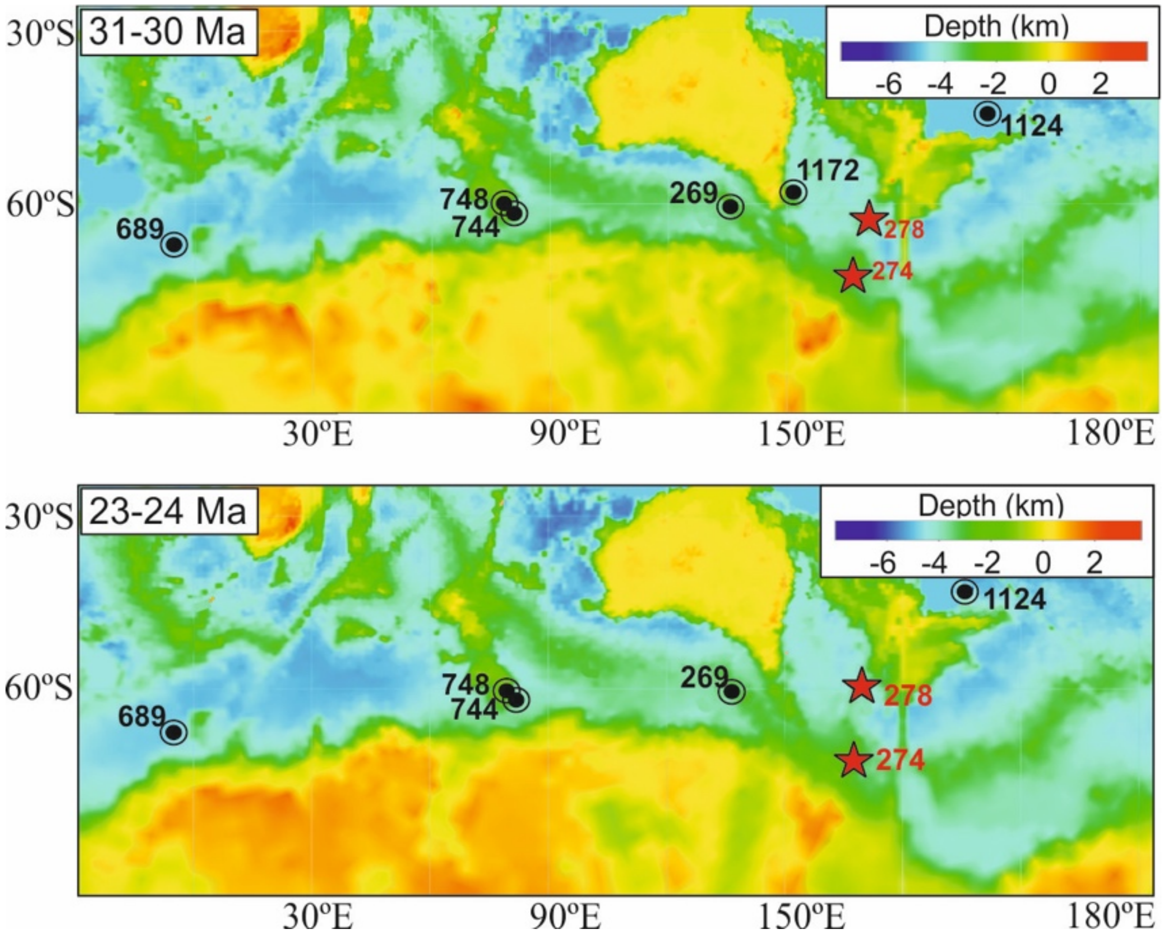

Figure 10.1.4: Paleobathymetry and Paleotopography reconstructions of the Southern Ocean derived from Paleo-digital elevation model by Scotese and Wright (2018). Reconstructions of the paleolocation of study sites and sites discussed were adapted from G-plates based on Muller et al., 2016 global plate motion model.

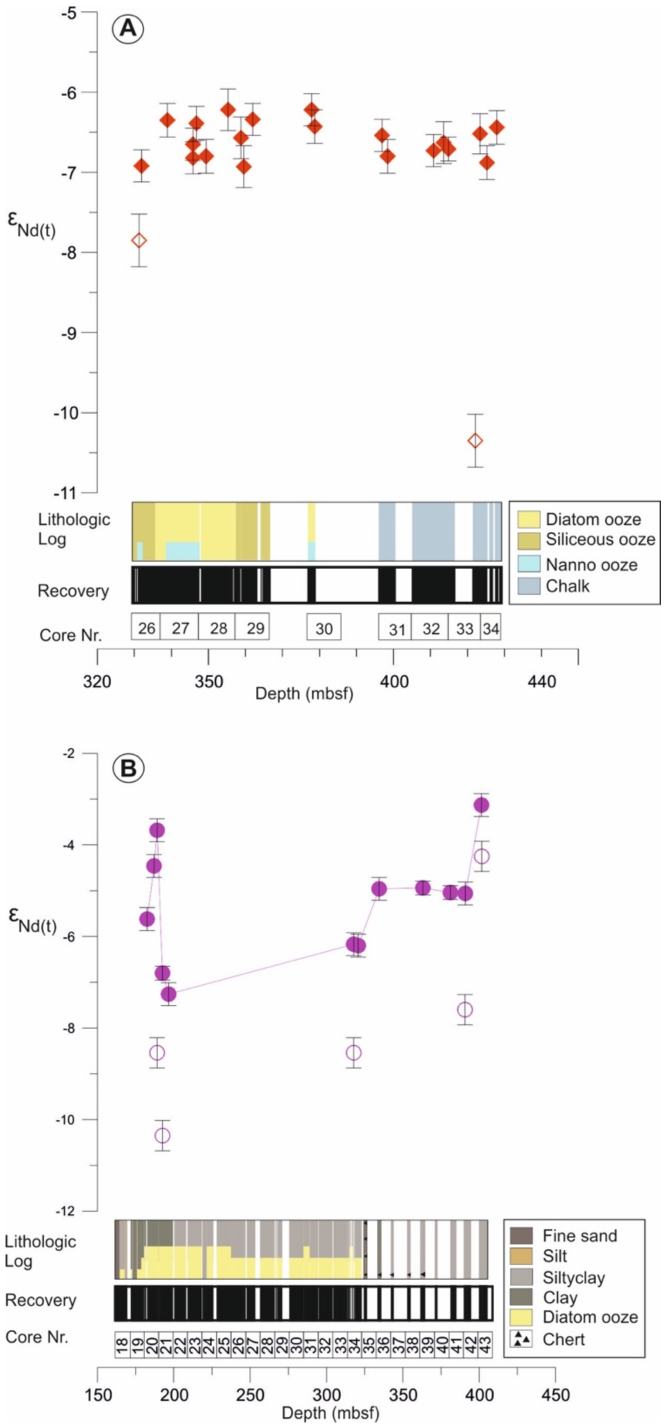

Figure 10.1.5: Neodymium isotopic composition ($\varepsilon_{Nd(t)}$) of fossil fish teeth and detrital sediment samples from this study. **A:** fossil fish teeth $\varepsilon_{Nd(t)}$ values (red diamonds) and detrital sediment $\varepsilon_{Nd(t)}$ values (red open diamonds) at Site 278. **B:** fossil fish teeth $\varepsilon_{Nd(t)}$ values (magenta circles) and detrital sediment $\varepsilon_{Nd(t)}$ values (magenta open circles) at Site 274.

Supplementary Tables

Table 10.1.1: Calcareous nannofossils from Site 278

Site	Core	Section	Intercal	ABUNDANCE	PRESERVATION	Coccolithus pelagicus	Reticulofenestra daviesii	Cyclicargolithus floridanus	Cyclicargolithus abisectus	R. bisecta/stavensis (>11)	Discoaster deflandrei	Coccolithus miopelagicus	Coronocyclus nitescens	Chiasmolithus altus	Martini 1970 (top)	Martinii 1970 (bottom)	Ma NN/NP(top
278	26	1	13-15	M	P	F	C	C/A							NN2	NN1	19.0-2
278	26	2	145-146	AM		C	C	A	R		R				NN2	NN1	19.0-2
278	27	1	44-46	barren													
278	27	5	136-138	F	p	F	F	F	F			R			NN2	NN1	19.0-2
278	27	6	80-82	barren													
278	28	1	137-139	barren													
278	28	5	132-134	barren													
278	29	1	83-85	barren													
278	29	2	40-42	barren													
278	29	3	147-149	barren													
278	30	1	140-142	A	M		A	C	R		R				NN1	NP25	22.82-
278	30	2	74-76	A	M	F	A	C	cf.	R	F				NP25	NP23	23.13-
278	31	1	144-146	A	M	C	A	A	F	cf.			R	F	NP25	NP23	23.13-
278	31	2	144-146	A	M		A	R						F	NP25	NP23	23.13-
278	32	4	140-142	A	M	F	A		R	F				F	NP25	NP23	23.13-
278	32	6	111-113	A	M	F	A	F	cf.	R		R		A	NP25	NP23	23.13-
278	33	5	123-125	A	M	C	C	F		F				C	NP23	NP16?	29.62-
278	34	1	132-134	A	M		A	R		F				A	NP23	NP16?	29.62-
278	34	3	144-146	C	M		A	F		R				A	NP23	NP16?	29.62-

Table 10.1.2: Diatom datums from Site 278

Site	Core	Section	Interval	Depth (mbsf)	datum	Taxon name	Age (Ma)
278	27	4	50-51	333.5	FAD	*Thalassiosira spumellaroides*	22.7
278	27	3	50-51	342	FAD	*Raphidodiscus marylandicus (lower)*	22.7
278	28	1	50-51	348.5	FAD	*Fragilariopsis maleinterpretaria*	18.6-19.5
278	29	1	50-51	358	LAD	*Bogorovia veniamini*	20
278	30	2	50-51	378.5	FAD	*Bogorovia veniamini*	28.1
278	32	3	50-51	408.5	LAD	*Rocella vigilans*	25.4
278	32	5	120-121	411.5	FAD	*Cestodiscus robustus*	<33.7

Table 10.1.3: Magnetic data from Site 278

Site	Core	Section	Top (cm)	Bot (cm)	Depth (mbsf)	Magnetic inclination
278	26	1	7	9	329.08	10.09669
278	26	1	123	125	330.24	50.32393
278	26	2	93	95	331.44	-66.26107
278	26	3	47	49	332.48	nan
278	26	3	118	120	333.19	-51.15978
278	26	4	23	25	333.74	-39.23275
278	26	4	113	115	334.64	-43.96
278	26	4	130	132	334.81	-44.06893
278	26	5	93	95	335.94	41.86535
278	26	5	132	134	336.33	-41.44715
278	26	6	12	14	336.63	-61.12367
278	26	6	125	127	337.76	-77.6255
278	27	1	23	25	338.74	14.48637
278	27	1	65	67	339.16	14.61735
278	27	2	67	69	340.63	-71.44009
278	27	3	62	64	342.13	64.52266
278	27	3	132	134	342.83	-39.77118
278	27	4	61	63	343.62	47.33343
278	27	4	113	115	344.14	-15.88262
278	27	5	45	47	344.96	-22.36507
278	27	5	114	116	345.65	-63.69654
278	27	6	48	50	346.49	-55.9591
278	27	6	139	141	347.4	-16.70067
278	28	3	132	134	352.32	22.95085
278	29	1	15	17	357.66	-10.27871

278	29	1	118	120	358.69	-47.73737
278	29	2	57	59	359.58	-10.99477
278	29	4	129	131	363.3	-71.80119
278	29	6	127	129	366.28	-73.67526
278	30	1	143	145	377.94	-40.46397
278	30	2	98	100	378.99	nan
278	31	2	33	35	397.34	-74.94684
278	31	3	35	37	398.86	-45.06627
278	32	1	67	69	405.68	45.54036
278	32	2	137	139	407.88	55.34094
278	32	3	18	20	408.19	72.01543
278	32	3	84	86	408.85	-65.27749
278	32	4	55	57	410.06	-60.13198
278	32	5	63	65	411.64	-26.19554
278	32	6	44	46	412.95	-51.10619
278	32	6	68	70	413.19	-40.45005
278	33	1	60	62	415.11	-67.89755
278	33	1	116	118	415.67	61.78054
278	33	2	28	30	416.29	-28.45919
278	33	2	98	100	416.99	26.90091
278	33	2	118	120	417.19	37.2319
278	33	6	9	11	422.1	41.90168
278	33	6	81	83	422.82	47.17607
278	34	1	143	145	425.44	-53.18868

Table 10.1.4: Magnetic chrons at Site 278

Site	Core	Section	Interval	Depth (mbsf)	Magnetic chron	Age (Ma)
278	26	2	93-95	331.44	C6n	18.75
278	27	1	23-25	338.74	C6r	19.72
278	27	4	113-115	344.14	C6An.2n	20.44
278	29	1	15-17	357.66	C6Bn.1n	21.77
278	29	6	127-129	366.28	C6Bn.2n	22.27
278	30	1	143-145	377.94	C6Cn.3n	23.3
278	31	2	33-35	397.34	C7n.2n	24.11
278	32	3	84-86	408.85	C9n	26.42
278	34	1	143-145	425.44	C12n	30.59

Table 10.1.5: Fish teeth and bones and detrital sediment Neodymium dat

Sample Name	Sample Depth (mbsf)	Age (Ma) (GTS 2012)	$^{143}Nd/^{144}Nd$ (a)	± 2σ S.E (b)	ε_{Nd} (c)	± 2σ S.D (d)
FISH TEETH						
Site 274						
28-274-20R-2,53-55	182.54	23.45	0.512351	0.000011	-5.60	0.25
28-274-20R-5,50-52	187.03	23.96	0.512410	0.000008	-4.44	0.25
28-274-20R-6,104-106	189.05	24.06	0.512443	0.000010	-3.81	0.25
28-274-21R-2,108-110	192.59	24.20	0.512291	0.000008	-6.78	0.15
28-274-21R-5,59-62	196.60	24.37	0.512267	0.000010	-7.23	0.25
28-274-34R-3,130-132	317.81	29.78	0.512323	0.000013	-6.14	0.25
28-274-34R-5,127-129	320.78	29.91	0.512322	0.000007	-6.17	0.25
28-274-36R-2,47-50	334.48	30.52	0.512385	0.000010	-4.93	0.25
28-274-39R-2,62-64	363.13	31.79	0.512386	0.000011	-4.91	0.15
28-274-41R-1,118-119	381.18	32.60	0.512381	0.000013	-5.01	0.15
28-274-42R-1,137-139	390.88	33.03	0.512380	0.000010	-5.03	0.25
28-274-43R-2,100-102	401.51	33.50	0.5124792	0.000009	-3.10	0.25
Site 278						
29-278-26R-2,143-145	331.94	18.82	0.512283	0.000010	-6.92	0.2
29-278-27R-1,44-46	338.95	19.75	0.512312	0.000011	-6.35	0.21
29-278-27R-5,136-138	345.87	20.61	0.512297	0.000009	-6.65	0.2
29-278-27R-5,136-138	345.87	20.61	0.512288	0.000015	-6.82	0.2
29-278-27R-6,80-82	346.81	20.70	0.512311	0.000010	-6.39	0.21
29-278-28R-1,137-139	349.38	20.96	0.512289	0.000011	-6.8	0.21

29-278-28R-5,132-134	355.33	21.54	0.512319	0.000009	-6.22	0.26
29-278-29R-1,83-85	358.84	21.84	0.512301	0.000012	-6.57	0.26
29-278-29R-2,40-42	359.61	21.88	0.512283	0.000010	-6.93	0.26
29-278-29R-3,147-149	361.98	22.02	0.512313	0.000009	-6.34	0.2
29-278-30R-1,140-142	377.91	23.30	0.512319	0.000010	-6.22	0.2
29-278-30R-2,74-76	378.75	23.33	0.512308	0.000010	-6.43	0.21
29-278-31R-1,144-146	396.95	24.09	0.512303	0.000007	-6.54	0.2
29-278-31R-2,144-146	398.45	24.33	0.51229	0.000013	-6.8	0.21
29-278-32R-4,140-142	410.91	26.94	0.512293	0.000009	-6.73	0.2
29-278-32R-6,111-113	413.62	27.62	0.512298	0.000010	-6.63	0.26
29-278-33R-1,38-40	414.89	27.94	0.512294	0.000009	-6.71	0.15
29-278-33R-6,146-148	423.47	30.09	0.5123036	0.000008	-6.52	0.25
29-278-34R-1,132-134	425.33	30.56	0.512285	0.000010	-6.88	0.21
29-278-34R-3,98-100	427.99	31.23	0.512308	0.000012	-6.44	0.21
SEDIMENTS						
Site 274						
28-274-20R-6,104-106	189.05	24.06	0.512193	0.000009	-8.67	0.33
28-274-21R-2,108-110	192.59	24.20	0.512100	0.000011	-10.49	0.33
28-274-34R-3,130-132	317.81	29.78	0.512191	0.000011	-8.71	0.33
28-274-42R-1,120-122	390.71	33.01	0.512239	0.000010	-7.79	0.33
28-274-43R-2,120-122	401.7	33.81	0.512410	0.000012	-4.45	0.33
Site 278						
29-278-26R-2,77-79	331.28	18.73	0.512229	0.000010	-7.97	0.33
29-278-33R-6,18-20	422.19	29.77	0.512098	0.000009	-10.52	0.33

Table 10.1.6: Rare earth element concentrations (ppm) for fish teeth samples

Fish teeth sample	Depth (mbsf)	Age (Ma)	La	Ce	Pr	Nd	Sm	Eu	Gd	Tb	Dy	Y
274 20_6 104-106	189.05	24.1	658.6	1869.1	189.8	759.3	183.9	34.6	195.7	30.2	195.5	1011.
274 43_2 120-122	401.71	33.8	215.7	857.1	83.4	399.8	121.4	27.5	147.8	23.6	153.8	940.
278 26_2 144-149	331.97	20.3	1527.2	3572.5	400.7	1652.0	333.1	72.8	349.3	50.3	308.3	1748.
278 33_6 18-20	422.19	30.0	1946.8	1713.2	503.3	2057.0	408.6	90.8	432.3	60.9	374.4	2411.
274 41_2 134-136	382.85	32.4	41.8	162.3	21.9	96.5	40.6	8.9	41.2	7.8	44.8	144.
	PAAS Values		38	80	8.9	32	5.6	1.1	4.7	0.77	4.4	2

Appendix 2

Supplementary Material for chapter 4

Supplementary text

Site description

Deep Sea Drilling Project (DSDP), Leg 29, Site 278 is located at 3675 m water depth on a pelagic contourite drift, on the Southern Emerald Basin (56°33.42´S, 160°04.29´E) (Kennett et al., 1975). Approximately 285 m of sediments were continuously cored in two holes (Hole 278*; 35 cores and Hole 278A; 2 cores). Recovery was 85 % in Hole * and 39% in Hole A. Our study focuses on sediments between 329 to 101 meters before sea floor-mbsf (Hole 278* cores 26R to 2R). Shipboard description divided the sediments in this sequence in three main lithological units: Unit 5 (between 329-264 mbsf) is composed of detrital and nannofossil-bearing radiolarian-diatom ooze, alternating with siliceous oozes. Unit 4 (between 264-236 mbsf) consists of alternating nannofossil-rich siliceous ooze and diatom-rich nannofossil ooze. Unit 3 (between 236-172 mbsf) is composed of siliceous nannofossil ooze. Unit 2 (between 172-101 mbsf) consists of nannofossil-rich spicule-bearing diatom ooze (Kennett et al., 1975).

Age model

Sediments within our study interval (329 to 101 meters before sea floor-mbsf) (Hole 278* cores 26R to 2R) were dated to cover from the early Miocene to the Middle Pleistocene (Kennett et al., 1975). Ages adopted for the Miocene were based on calcareous nannofossils, planktonic foraminifera and diatoms while the late Neogene ages obtained from radiolarian and calcareous nannofossis, (Kennett et al., 1975). We updated this age model by revising the diatom and calcareous nannofossil biostratigraphy (**Table 10.2.1**). Our updated age model was calibrated to the Geological Time Scale of Gradstein et al. (2012) and suggests an age range for the studied interval from ~20 to 500 ka (**Fig. 10.2.1**).

Paleolocation and paleodepth estimates for Site 278

We reconstructed the paleolatitude of the Tasmanian Gateway and the paleoposition of Sites 278 using G-plates geodynamic modeling (http://www.gplates.org ; Müller et al., 2018), utilizing the plate circuit of Müller et al. (2016). Paleodepths for Site 278 were obtained from the paleo-bathymetry grids generated by the Earthbyte group (Scotece and Wright, 2018), incorporated the reconstructed paleolocation of the site in G-plates software (**Fig. 10.2.2**). Our reconstruction of the paleoposition of Site 278 shows that the site has remained close to the ~60 °S throughout the Neogene ~59.8°S at 22 Ma, ~59.2 °S at 17 Ma and ~57.3°S between 4 Ma and 2 Ma (**Fig. 10.2.2**). Geological evidence derived from the analysis of microfossil assemblages from sedimentary records across the Tasmanian Gateway suggest that the proto-Polar Front (PF) was situated close to 60°S since the late Oligocene (Nelson and Cooke, 2001; Cooke et al., 2002; Evangelinos et al., submitted [Chapter 5]). In addition, its paleodepth was ~3500 m throughout the early Miocene to early Pleistocene (**Fig. 10.2.2**).

Methods

Fossil fish tooth sample preparation for Neodymium isotopes analyses

Fish teeth and bones (fish debris) were handpicked from the >63 µm sediment fractions isolated by wet sieving. A total of 31 samples were selected for fish debris Nd isotope analyses. All samples were treated with ultraclean 18 □Ω water (MQ water) and methanol-following Martin and Haley (2000) to remove debris from surfaces and cavities (see also Huck et al., 2017). Cleaned fish debris samples were subsequently transferred into cleaned microcentrifuge tubes and dissolved overnight in 50 µL of 2M HCl. Dissolved fish debris were loaded on Biorad cation exchange resin (200-400 µm mesh) to separate the REEs from the sample matrix and Eichrom Ln-Spec resin (50-100 µm bead size) to separate Nd from the other REEs.

Bulk sediment sample preparation for Neodymium isotopes analyses

Two samples were selected to determine the detrital sediment Nd isotope composition in order to evaluate potential contribution of the detrital sediments to the porewaters or overlying bottom water signature. Sample was dried and gently homogenised using mortar and pestle. First, 1.5g of dried sample and 70-75 ml of 1.5% buffered acetic acid solution were used to remove biogenic carbonate (carbonate leaching). Exchangeable ions were subsequently removed using 10ml 1M $MgCl_2$ solution. In a third step, ferromanganese oxides and oxyhydroxides were removed using a weak reductive solution of 0.005 M Hydroxylamine Hydrochloride (NH_2OH) 1.5% acetic acid and 0.03M Na_2-EDTA for 1 hour, followed by a stronger leaching step utilising 0.05 M NH_2OH for 17 hours. 50 mg of leached and water washed detrital sediment was subsequently digested on a hotplate using a mixture of 1ml of concentrated HNO_3, 0.8ml $HClO_4$ and 2ml HF. The detrital samples were processed using the same column chromatography as the fish debris.

Neodymium isotope measurements

Neodymium isotope ratios for fish debris and detrital sediment samples were determined on a Nu Plasma multiple collector inductively coupled plasma mass spectometer (MC-ICP-MS) at Imperial College London, operated in a static mode. Instrumental mass bias was corrected using the ^{146}Nd/^{144}Nd ratio of 0.7219. A JNdi-1 isotope standard was run after every sample and all reported ^{143}Nd/^{144}Nd ratios are corrected to a JND$_i$ value of 0.512115 (Tanaka et al., 2000) using bracketing standards. External reproducibility was monitored by using the JNd$_i$ standards, and accuracy was confirmed by measuring USGS BCR-2 rock standards, which yielded average ^{143}Nd/^{144}Nd ratios of 0.512107 ± 0.000012 (n=121; 2s.d.) in agreement with the published BCR-2 ^{143}Nd/^{144}Nd ratio of 0.512638 ± 0.000015 (Weis et al., 2006) (**Table 10.2.2**).

To correct for the decay of ^{147}Sm to ^{144}Nd within the fossil fish teeth over time we used Sm and Nd concentrations obtained from one sample yielded 0.1532 (**Table 10.2.3**). The range of Sm/Nd ratios reported here is consistent value is consistent with values other fossil fish-tooth material (Martin and Scher, 2006; Moiroud et al., 2013; Huck et al., 2017; Evangelinos et al., submitted; *in prep*; [Chapters 5 and 3, respectively]). When no values available, an average of 0.1365 from the measured samples at Sites 278 was applied to calculate $\varepsilon_{Nd(t)}$ values. The^{147}Sm to ^{144}Nd ratios would yield Nd isotope corrections of 0.01 to 0.14 ε_{Nd} units: (t) denotes samples have been corrected for in situ decay of ^{147}Sm (**Table 10.2.2**).

Rare Earth Element (REE) concentrations

A full suite of REE concentrations were determined for one sample. Major and trance analysis was performed at the Open University using an Agilent 7500s ICP-MS (Table SX). Rare earth element analysis was performed at the Open University using an Agilent Technologies 8800 Triple-Quad Inductively Coupled Plasma-Mass Spectrometer (ICP-MS). Analyses were standardized via a suite of seven synthetic multi-element standards made up with certified plasma standard solutions. An intermediate synthetic multi-element monitor standard, a fossil bone standard (Chavagnac et al. 2007) and a 2% HNO3 blank were run every 5th sample to monitor instrument drift and precision. Precision was generally better than ±2% (1 s.d.). Both oxide interferences (CeO^+/CeO^-) (<0.5%) and doubly charged species (Ce^{++}/Ce^+) (<1.2%) were kept low. All REE data were normalised to Post Archean Shale (PAAS) concentrations (Taylor and McLennan, 1985).

Grain size analyses

Grain-size analyses was performed was performed at the Environnements et Paléoenvironnements Océaniques et Continentaux (EPOC, Bordeaux, France). Bulk grain-size analyses in a total of 28 samples from Site 278 were measured in a laser microgranulometer Malvern mastersizer hydro 2000G with automatic samples (0.020 to 2000 μm). Samples were dried in the oven at 40°C overnight. 1-2 grams of sediments was subsampled to be subject to (i) carbonate, (ii) organic matter and (iii) opaline silica removal (see below for details). Grain-size measurements for all samples were performed after each removal step.

To remove the carbonate a Hydrochloric acid 37% HCl_A 4% solution was used. To control the efficiency of the reaction 1-2 mL of HCl_B 20% solution was added. When all carbonate was dissolved an addition of 50 ml of H_2Od was added to the samples. Samples were centrifuged (7 min at 3000 rpm) and then dried in the oven at 40°C. The percentage of carbonate of each sample was calculated based on its weight difference before and after carbonate removal (**Table 10.2.4**).

For the organic carbon removal, 20 ml of H_2O_2 was added and carefully mixed to resuspend the sediments. Samples were left on the bain-maire at 65°C for 6 hours, while mixed occasionally to keep sediments in suspension. After 6 hours, sediments were mixed to resuspend and 1 to 2ml H_2O_2 was added. Once the reaction was completed, 50 ml of H2Od was added and sediment were resuspended using a vortex. Samples were then centrifuged (7 min at 3000 rpm), supernatant was removed and sediment resuspended in H2Od. This step was repeated 4-5 times. Samples were then dried at 40 ^{O}C. The percentage of organic matter of each sample was calculated based on its weight difference before and after the treatment (organic matter removal) (**Table 10.2.4**).

In order to remove the biogenic silica, samples were separated into two groups (i) sediments contained low silica content and (ii) sediments contained high silica content. For the (i) 40 ml of Na_2CO_3 (2M) (Sodium carbonate) were added and left for 6 hours on the bain-marie at 90°C. Samples were mixed every 2 hours. Following this, 50 ml of H2Od were added and samples were placed on a vortex to resuspend the sediments. Samples were then centrifuged (7 min at 3000 rpm). Supernatant was removed and samples were resuspended in H_2Od. This step was repeated 5 to 6 times. Smear slides were prepared and looked under the microscope at X 500 magnification to ensure the absence of siliceous microfossil remnants (diatoms/radiolarians). If no diatoms/radiolarians were found, then samples were dried in the oven at 60°C. If there were still remains of siliceous microfossils the entire processes was repeated, but samples were place in bain-marie only for 2 hours. We calculated the percentage of carbonate of each sample based on its weight difference before and after treatment (biogenic silica removal for samples with low silica content) (**Table 10.2.4**).

For sediments with high silica content, 20 ml of NaOH (1M) (Sodium hydroxide) was added, mixed and put on the bain-marie at 70°C for 8 hours. Samples were mixed every 2 hours Following this, some extra NaOH was added to the samples and put back in the bain-marie at 70°C for another 8 hours. This step can be repeated several times. Once the reaction was completed, 50 ml of H2O was added and vortexed to resuspend the sediments. Samples were then centrifuged (7 min at 3000 rpm). Supernatant was removed and samples were resuspended in H_2Od. This step was repeated 5-6 times. Smear slides were prepared and looked under the microscope at X 500 magnification to ensure the absence of microfossil remnants. The percentage of biogenic silica of each sample was calculated based on its weight difference before and after the biogenic silica removal for samples with high silica content (**Table 10.2.4**).

In order to reconstruct the current speed we focused on the 10-63 μm terrigenous sediment fraction-the sortable silt range (SS McCave et al., 1995). Particles smaller than 10 μm deposited as aggregates due to cohesion and thus cannot be used as proxy for current velocity, whereas sediment fraction between 10-63 μm has been documented to reflect current sorting in most cases (McCave et al., 1995). The mean sortable silt size of 10-63 μm terrigenous sediment fraction ($\overline{SS}$) was calculated in the same 28 samples at Site 278 after the removal of carbonate, organic matter, and opaline silica (**Table 10.2.4**). Precision of the method was ± 3% for the d (0.5).

Supplementary figures

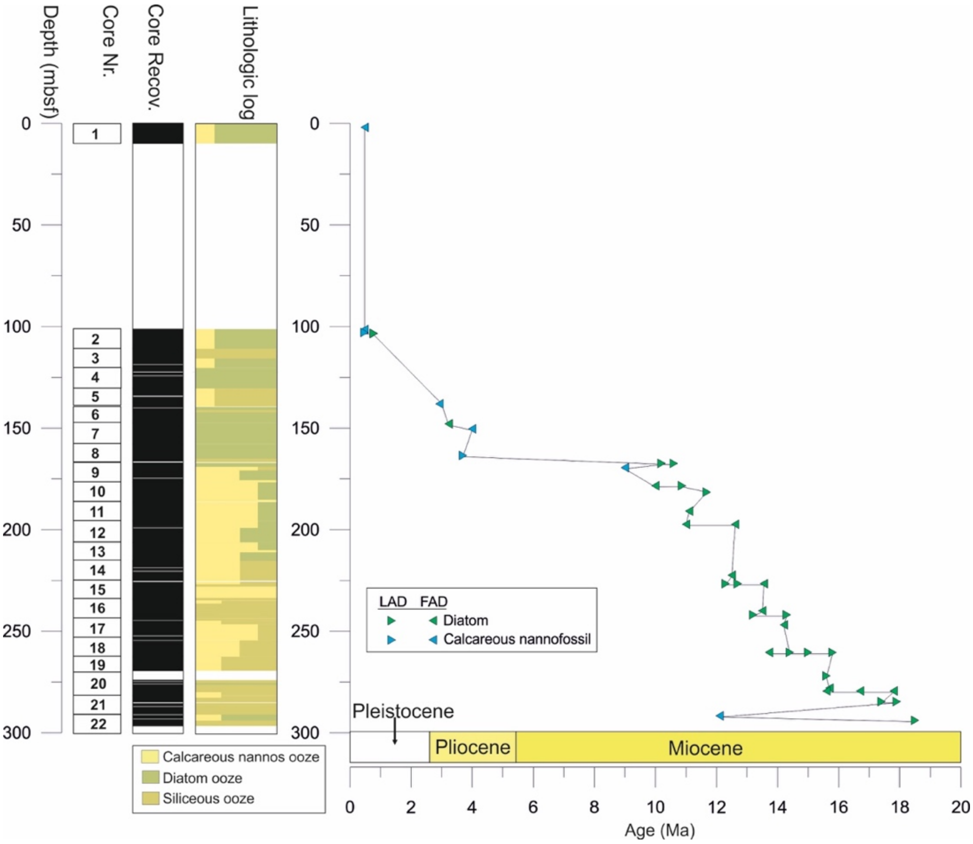

Figure 10.2.1: Revised age-depth model for Site 278 and lithology log. Green triangles=diatom bioevents, Blue triangles=nannofossil bioevents LAD: Last appearance datum, FAD: First appearance datum.

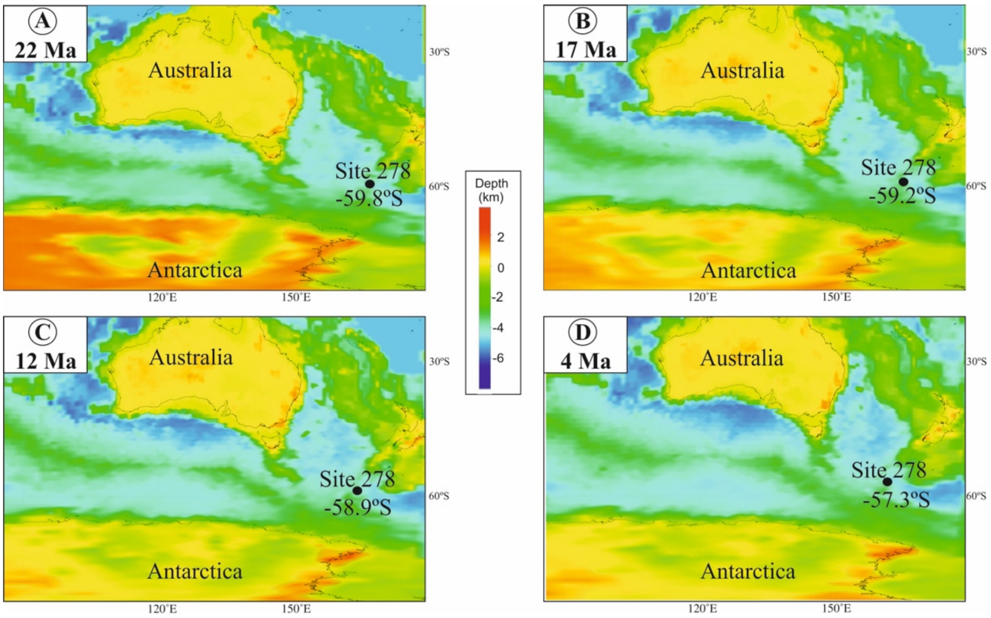

Figure 10.2.2: Paleolocation and paleodepth estimates for Site 278 at 22 Ma (A), 17 Ma(B), 12 Ma(C) and 4 Ma (D). Paleobathymetry reconstructions of the Southern Ocean derived from Paleo-digital elevation model by Scotese and Wright (2018). Reconstructions of the paleolocation of Site 278 was adapted from G-plates based on Muller et al., 2016 global plate motion model.

Supplementary tables

Table 10.2.1: Age model information for Site 278

Datum	Taxon name	Source	Age (Ma)
		CN	<0.478
		CN	<0.478
		CN	>0.478
LAD	Cycladophora davisiana	D	0.78
LAD	Anthocyrtidium pliocenica	D	0.78
LAD	Eucampia antarctica	D	0.78
		CN	<3
FAD	Cycladophora davisiana	D	3.23
		CN	<4
		CN	>3.7
LAD	Denticulopsis dimorpha	D	>10.6
LAD	Fragilariopsis claviceps	D	>10.2
		CN	<9
FAD	Thalassiosira nativa	D	<10
LAD	Actinomma golownini	D	10.87
LAD	Nitzschia denticuloides	D	11.7
FAD	N. januaria	D	11.1
FAD	F. donahuensis	D	11
FAD	Cycladophora spongothorax	D	12.61
FAD	D. dimorpha	D	12.5
LAD	C. nicobarica	D	12.3-12.7
FAD	Actinomma golownini	D	13.55
FAD	N. denticuloides	D	13.5
LAD	N. grossepunctata	D	13.2
LAD	D. maccollumii	D	14.3
FAD	D. simonseii	D	14.2
LAD	A. lewisianus	D	14.4-15.0
FAD	T. juanii	D	13.72
LAD	D. deflandrei	D	15.8
LAD	R. marylandicus (upper)	D	15.6
FAD	D. lauta	D	15.7
FAD	N. grossepunctata	D	15.6
FAD	D. maccollumi	D	16.7
FAD	A. lewisianus	D	17.8
LAD	T. praefraga	D	17.4-17.9
		CN	<12.1
LAD	T. spumellaroides	D	18.5

D: Diatoms, CN: Calcareous nannofossil, LAD: Last appearance Datum, FAD: First appearance Datum

Table 10.2.2: Fish and detrital sediment Neodymium data from Site 278

Sample Name	Sample Depth (mbsf)	Age (Ma)	$^{143}Nd/^{144}Nd$ (a)	± 2σ S.E (b)	ε_{Nd} (c)	± 2σ S.D (d)	147Sm/144 Nd (e)	$\varepsilon_{Nd(t)}$ (f)
FISH TEETH								
29-278-2R-1,60-64	101.62	0.48	0.512222	0.000009	-8.12	0.28	*0.1365*	-8.11
29-278-2R-5,100-104	108.02	0.89	0.512241	0.000011	-7.74	0.28	*0.1365*	-7.73
29-278-3R-2,100-104	113.02	1.21	0.512246	0.000010	-7.65	0.28	*0.1365*	-7.64
29-278-3R-5,100-104	117.525	1.49	0.512226	0.000013	-8.03	0.28	*0.1365*	-8.02
29-278-5R-6,100-104	138.02	2.80	0.512250	0.000009	-7.58	0.28	0.1562	-7.56
29-278-6R-5,100-104	146.02	3.42	0.512264	0.000010	-7.29	0.28	*0.1365*	-7.26
29-278-7R-2,100-104	151.02	3.80	0.512267	0.000011	-7.24	0.28	*0.1365*	-7.21
29-278-7R-5,100-104	155.52	3.86	0.512270	0.000010	-7.18	0.28	*0.1365*	-7.15
29-278-8R-5,5-9	164.07	3.99	0.5122722	0.000007	-7.14	0.25	*0.1365*	-7.11
29-278-8R-5,104-108	165.07	4.00	0.5122468	0.000006	-7.63	0.25	*0.1365*	-7.60
29-278-9R-2,30-34	169.32	9.10	0.5122684	0.000012	-7.21	0.25	*0.1365*	-7.14
29-278-9R-2,105-109	170.07	10.00	0.5122611	0.000009	-7.35	0.25	*0.1365*	-7.28
29-278-9R-2,105-109	170.07	10.01	0.512276	0.000011	-7.07	0.16	*0.1365*	-6.99
29-278-10R-1,60-64	177.62	10.39	0.5122609	0.000008	-7.36	0.25	*0.1365*	-7.28
29-278-11R-3,64-68	190.16	11.03	0.5122656	0.000009	-7.26	0.25	*0.1365*	-7.18
29-278-12R-4,64-68	201.16	11.53	0.512263	0.000009	-7.31	0.25	*0.1365*	-7.22
29-278-13R-5,70-74	212.22	12.02	0.512253	0.000009	-7.51	0.25	*0.1365*	-7.42
29-278-14R-6,60-64	223.12	12.50	0.5122810	0.000008	-6.96	0.25	*0.1365*	-6.87
29-278-15R-3,70-74	228.22	12.65	0.5122856	0.000009	-6.87	0.25	*0.1365*	-6.78
29-278-16R-6,70-74	242.22	13.54	0.5122543	0.000008	-7.48	0.25	*0.1365*	-7.38
29-278-17R-4,64-68	248.66	14.26	0.512258	0.000008	-7.42	0.25	*0.1365*	-7.31
29-278-18R-1,72-76	253.74	14.44	0.512289	0.000008	-6.80	0.25	*0.1365*	-6.69
29-278-18R-1,72-76	253.74	14.44	0.5122912	0.000007	-6.77	0.25	*0.1365*	-6.65
29-278-19R-1,12-16	262.64	14.83	0.512260	0.000009	-7.37	0.25	*0.1365*	-7.25
29-278-20R-5,68-72	278.7	15.83	0.5123103	0.000007	-6.39	0.25	*0.1365*	-6.27
29-278-21R-2,100-104	284.02	17.20	0.512270	0.000009	-7.18	0.25	*0.1365*	-7.05
29-278-22R-1,34-38	291.36	18.11	0.5122914	0.000008	-6.76	0.25	*0.1365*	-6.62
29-278-22R-1,125-129	292.27	18.22	0.5122855	0.000009	-6.88	0.25	*0.1365*	-6.74
29-278-23R-5,65-69	307.17	18.59	0.512290	0.000010	-6.79	0.25	*0.1365*	-6.65
29-278-24R-5,70-74	316.72	18.65	0.512304	0.000008	-6.51	0.25	*0.1365*	-6.37
29-278-25R-2,65-69	321.67	18.68	0.5123052	0.000010	-6.49	0.25	*0.1365*	-6.35
SEDIMENTS								
29-278-5R-6,100-104	138.02	2.80	0.512416	0.000013	-4.33	0.33	*0.1500*	-4.31
29-278-13R-5,58-62	212.1	12.01	0.512416	0.000011	-4.32	0.33	*0.1500*	-4.25

Analytical details

(a) All reported 143Nd/144Nd ratios are corrected to a JNDi value of 0.512115 (Tanaka et al., 2000) using bracketing standards.
(b) S.E. = internal precision (2s level) on sample measurement.
(c) εNd based on present-day CHUR value 143Nd/144Nd = 0.512638 expressed in parts per 10,000 (Jacobsen and Wasserburg, 1980).
(d)External error based on the reproducibility of all JNDi standards measured during run.
(e) 147Sm/144Nd ratio calculated from an average value from the measured samples at the site (italics) and direct measurements from all measured samples at that site was used and is in italics.
For the sediments an average of 0.1500 (Huck et al., 2017) was used and is reported in italic font
(f) εNd (t) were calculated using values from column (e) and CHUR values of 143Nd/144Nd 0.512638 and Sm/Nd 0.1966 from Jacobsen and Wasserburg (1980).
Replicate analyses of the Nd standard JNdi yielded 143Nd/144Nd JNDi standard ratios of 0.512107 ± 0.000012 (2.S.D., n=121).

Appendix 3

Supplementary Material for chapter 5

Supplementary text

Fossil fish tooth sample preparation for Neodymium isotopes

Fish debris was handpicked from the >63 µm sediment fractions that were prepared by wet sieving. Four samples were prepared for fish-tooth and bone debris Nd isotope analyses. All samples were treated with ultraclean 18 MΩ water (MQ water) and methanol-following Martin and Haley (2000) to remove debris from surfaces and cavities in the MAGIC laboratories at Imperial College London (see also Huck et al., 2017). Cleaned fish tooth samples were subsequently transferred into cleaned microcentrifuge tubes and dissolved overnight in 50 µL of 2M HCl. Dissolved fish debris were loaded on Biorad cation exchange resin (200-400 µm mesh) to separate the REEs from the sample matrix and Eichrom Ln-Spec resin (50-100 µm bead size) to separate Nd from the other REEs.

Bulk sediment sample preparation for Neodymium isotopes

In order to consider a potential influence of the detrital sediment towards the Nd isotope composition of pore waters or overlying bottom water, we also measured the Nd isotope compositions of two detrital sediment samples. Samples were dried and gently homogenised using mortar and pestle. Approximately 500 mg of homogenised material was subjected to a carbonate leaching procedure to remove biogenic carbonate using 30 ml of 1.5% buffered acetic acid (see Biscaye (1965) for more details). Ferromanganese oxides and oxyhydroxides were leached using a weak reductive solution of 0.005 M Hydroxylamine Hydrochloride (NH_2OH), followed by a stronger solution of 0.05 M NH_2OH. 50 mg of leached detrital sediment sample was subsequently digested on a hotplate using a mixture of 1ml of concentrated HNO_3, 0.8ml $HClO_4$ and 2 ml HF. The detrital samples were processed using the same ion chromatography as the fish debris.

Supplementary figures

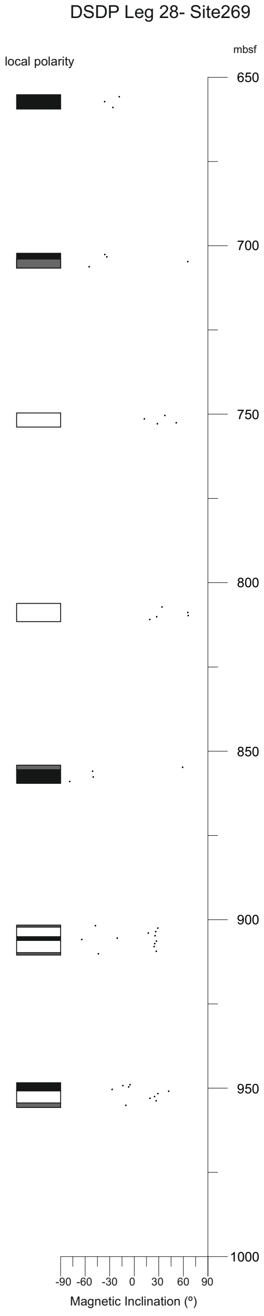

Figure 10.3.1: Stratigraphic location of the calculated Inclinations for the Site 269. A local polarity, where negative (positive) inclinations indicate normal (reversed) polarity in black (white), is also provided. Magnetozones are defined by more than one sample, otherwise they are shown in grey.

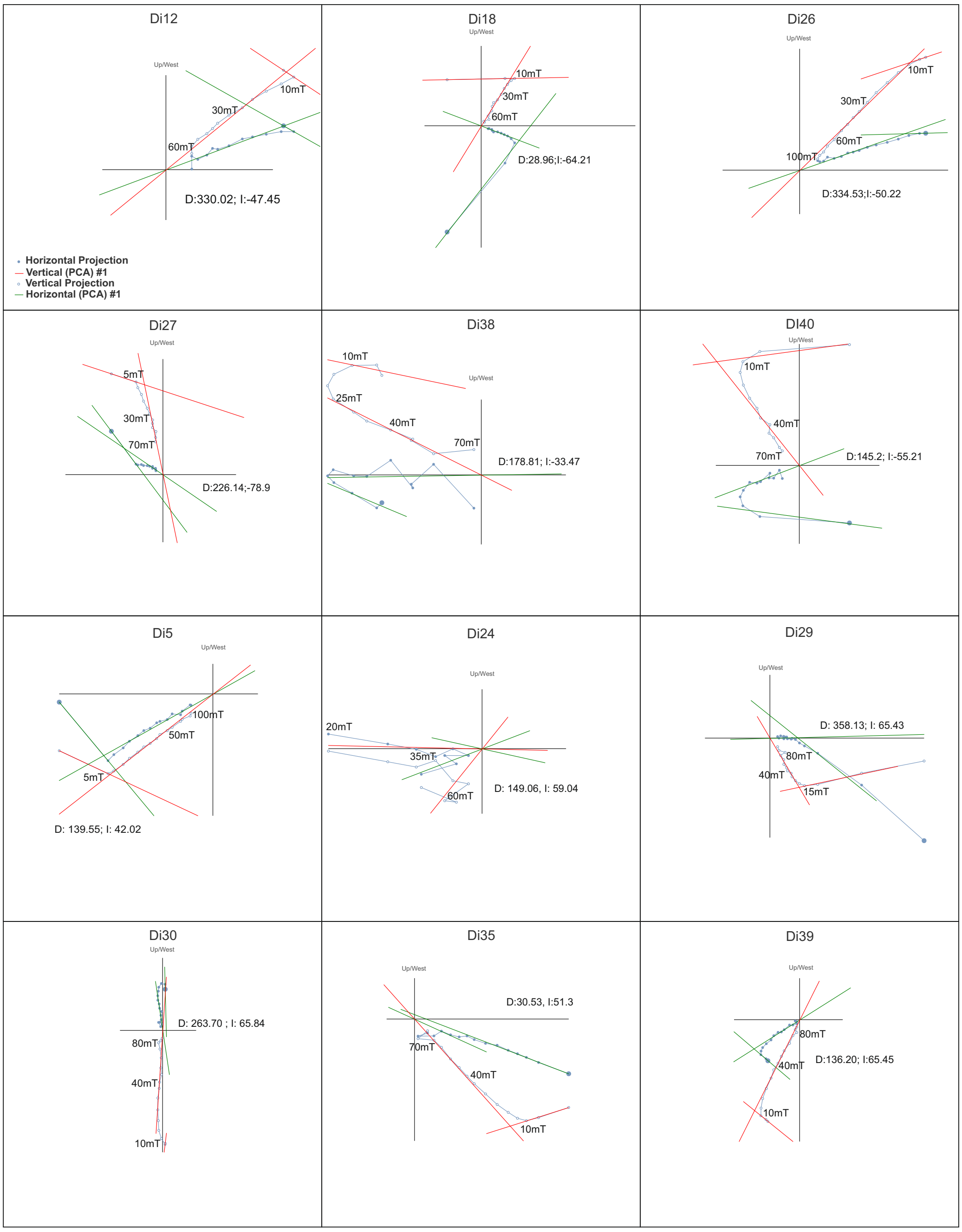

Figure 10.3.2: Orthogonal plots of the representative samples, showing two distinctive directions, both in normal samples and in reversed samples. Inclination values are also indicated. Open plots indicate inclinations (vertical projection). All calculated directions are available in Table S1. Samples were calculated by means of the Paldir and paleomagnetism.org (Koymans et al., 2016) programs.

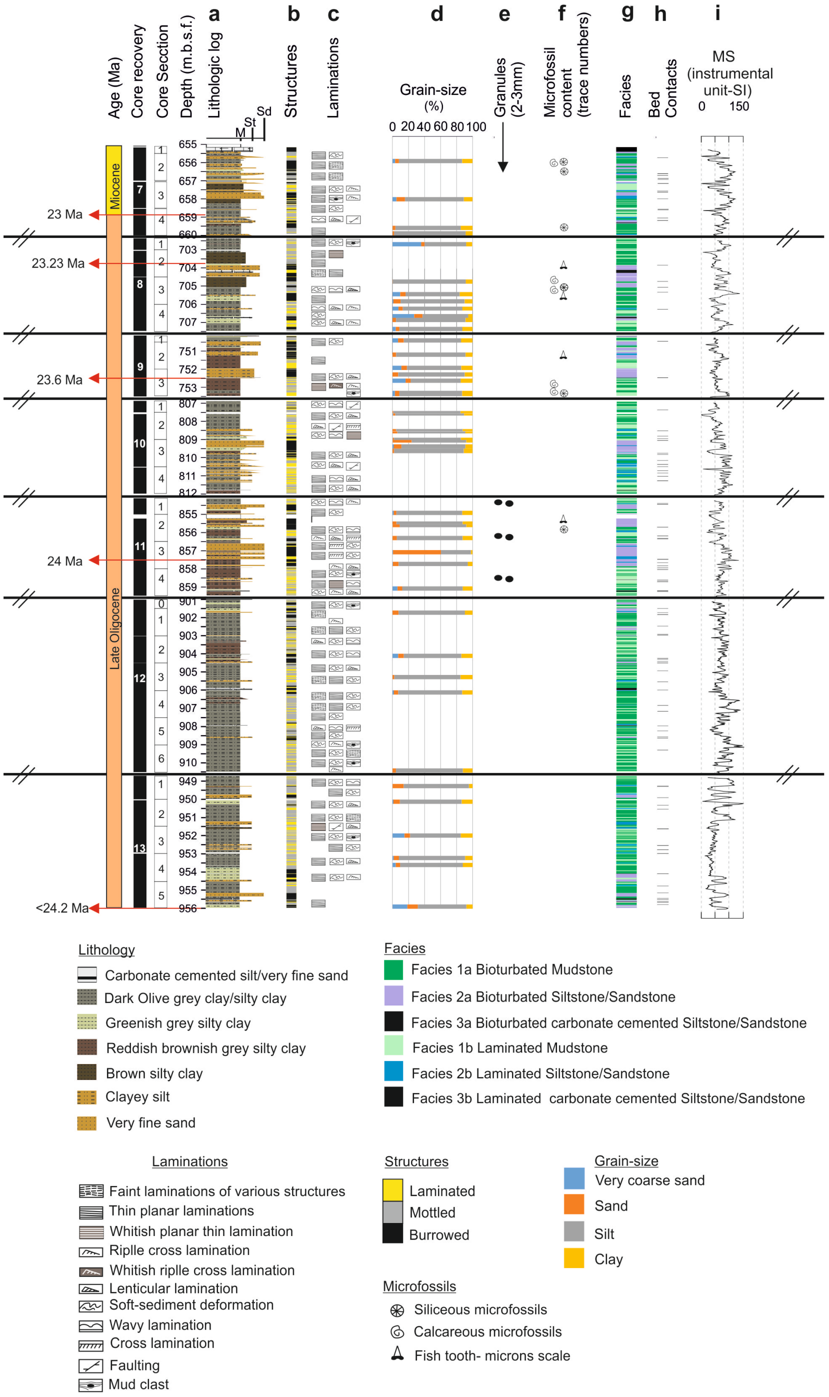

Figure 10.3.3 a: Detailed lithological log, **b:** structures, **c:** types of laminations, **d:** grain-size data, **e:** presence of granules 2-3mm, **f**: visually observed microfossils (trace amounts), **g:** main facies distribution, **h:** sharp contacts between facies, **i**: magnetic susceptibility (MS). Note core gaps between different cores due to discontinuous coring (//). M: Mudstone, St: Siltstone: Sd Sandstone.

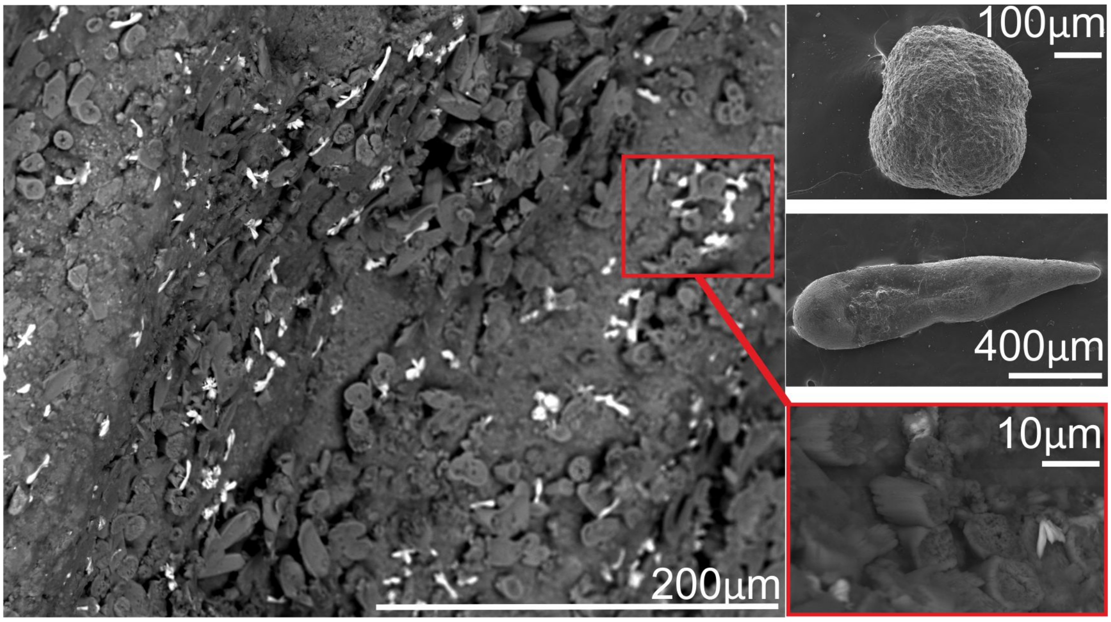

Figure 10.3.4: HR-SEM image showing calcareous microfossils associated with barite and representative species of foraminifers found in cores 8R and 9R.

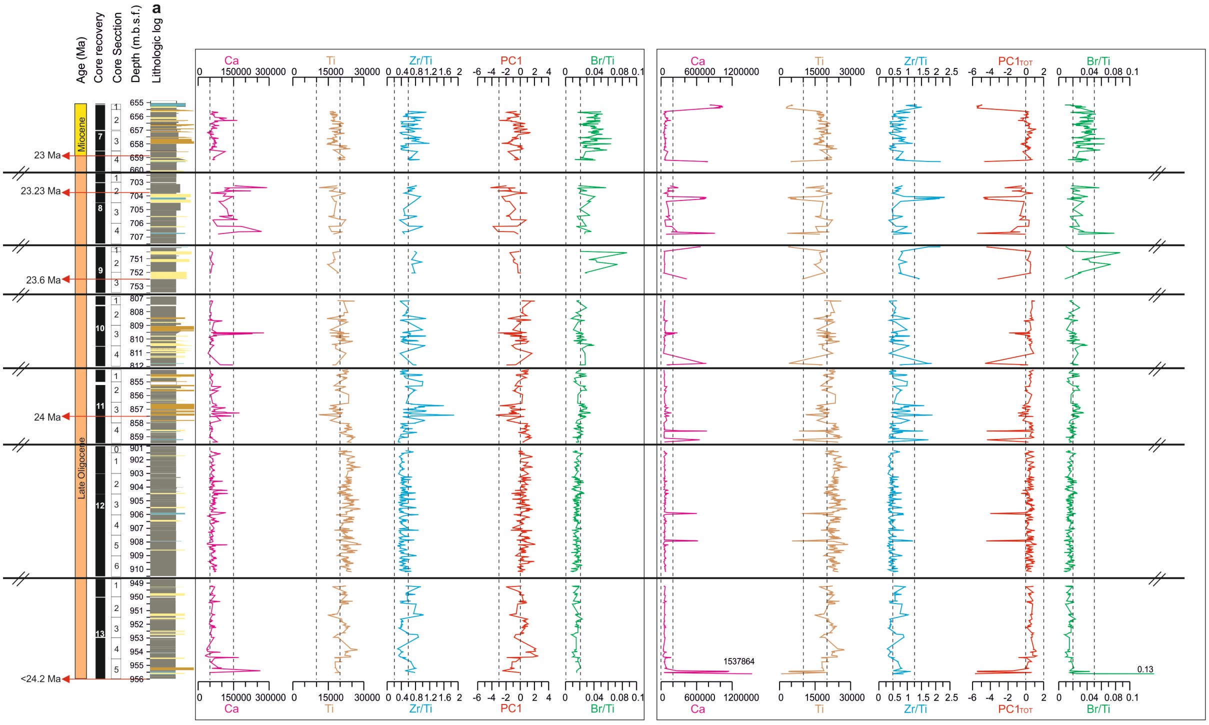

Figure 10.3.5: Lithologic log (a) and down-core variations of (i) selected XRF-scanning data (in total counts), elemental ratios and PC1 without the carbonate-cemented facies (left) and (ii) selected XRF-scanning data, elemental ratios and $PC1_{TOT}$ with the carbonate-cemented facies (right). Note core gaps between different cores due to discontinuous coring (//).

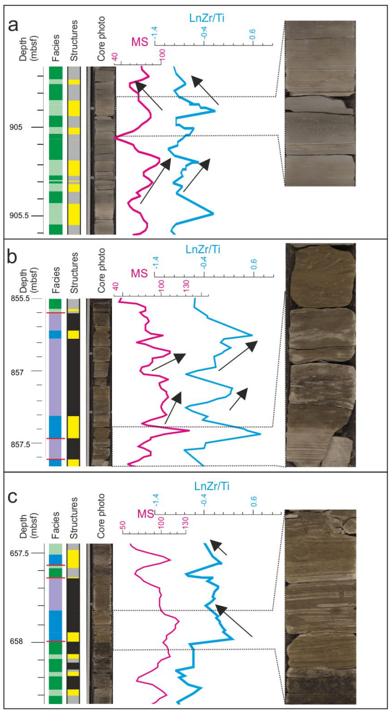

Figure 10.3.6: Representative examples of facies associations, including structures, magnetic susceptibility (MS) and Zr/Ti data. **a:** Fine-grained facies associations. **b** and **c:** Coarse-grained facies associations. Arrows indicate inverse and normal grading patterns. Red lines between facies indicate sharp bed contacts. Facies colour and structure codes are given in Figure 5.3.

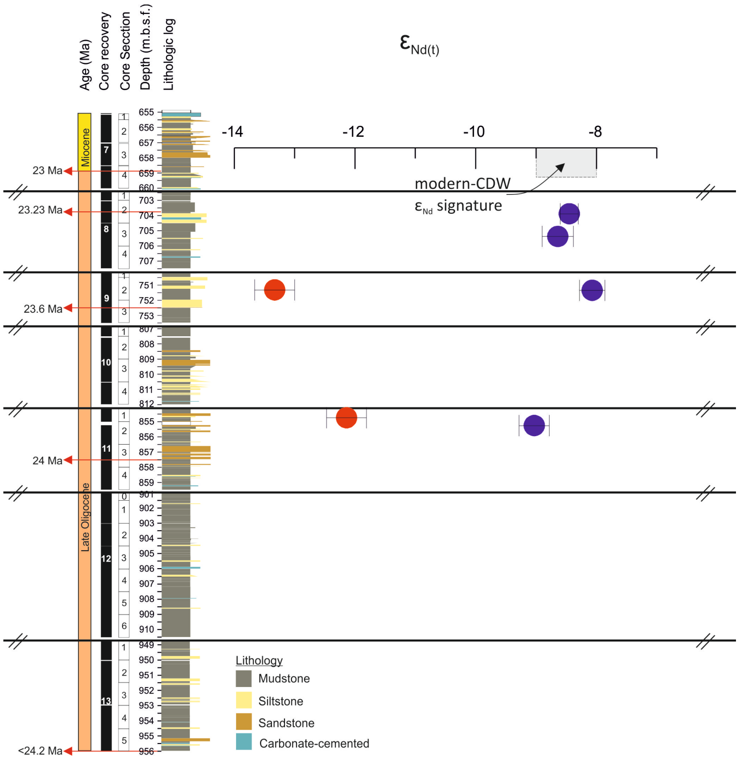

Figure 10.3.7: Neodymium isotopic composition of fish debris (blue) and bulk detrital sediment ε_{Nd} values (red) from Hole 269A

Supplementary tables

Table 10.3.1: Paleomagnetic dataset at Hole 269A Cores 7R-13R

Leg	Site	Hole	Core	Section	Top (cm)	Bot (cm)	Depth (mbsf)	Sample Name	Declination	Inclination	Intensity (A/m2)	Strat	MAD	Forced	Type	Coordinates	Bedding Strike	Bedding Dip	Num Step	Min Step	Max Step
28	269	A	13	1	53	55	949.03	di1	53.76352373	-5.199547693	12816.60013	7	4.408449078	TRUE	dir	Geographic Coordinates	90	0	5	15	35
28	269	A	13	1	76	78	949.26	di2	187.5173705	-13.90078791	6251.883574	6	3.301610054	TRUE	dir	Geographic Coordinates	90	0	11	25	100
28	269	A	13	1	114	116	949.64	di3	140.0669862	-6.894508896	6266.399988	5	1.729861671	TRUE	dir	Geographic Coordinates	90	0	12	15	90
28	269	A	13	2	44	46	950.44	di4	62.01754422	-27.06342913	16272.10342	4	1.777811659	TRUE	dir	Geographic Coordinates	90	0	12	20	100
28	269	A	13	2	95	98	950.95	di5	139.5556692	42.02077811	14790.02487	3	1.980377917	TRUE	dir	Geographic Coordinates	90	0	14	10	100
28	269	A	13	3	13	15	951.63	di6	99.02692451	28.92119504	9137.591091	2	2.41338962	TRUE	dir	Geographic Coordinates	90	0	8	25	70
28	269	A	13	3	104	106	952.54	di7	182.0068096	24.78570975	11344.96448	1	1.967135126	TRUE	dir	Geographic Coordinates	90	0	12	15	90
28	269	A	13	4	3	5	953.03	di8	222.6946459	19.20222119	5656.079284	8	2.106426055	TRUE	dir	Geographic Coordinates	90	0	9	30	90
28	269	A	13	4	82	84	953.82	di9	35.35353282	26.65869667	4713.510042	7	4.291701509	TRUE	dir	Geographic Coordinates	90	0	8	30	80
28	269	A	13	5	67	69	955.17	di10	43.23591546	-10.24051787	1349.560528	6	13.32826152	TRUE	dir	Geographic Coordinates	90	0	6	5	30
28	269	A	12	cc	108	110		di11	98.56922818	42.67535279	23715.78417	5	2.340095871	TRUE	dir	Geographic Coordinates	90	0	9	20	70
28	269	A	12	1	31	33	901.81	di12	330.0166967	-47.4554181	9962.928043	4	2.367538165	TRUE	dir	Geographic Coordinates	90	0	10	10	60
28	269	A	12	1	100	105	902.5	di13	308.9936867	28.80580856	4401.981022	3	22.37747839	TRUE	dir	Geographic Coordinates	90	0	7	30	70
28	269	A	12	2	55	58	903.55	di14	255.5246598	26.24829681	21456.26987	2	3.458319655	TRUE	dir	Geographic Coordinates	90	0	8	25	70
28	269	A	12	2	99	102	903.99	di15	43.87058825	17.08826976	33370.27581	1	1.930333287	TRUE	dir	Geographic Coordinates	90	0	10	25	90
28	269	A	12	3	31	37	904.81	di16	311.4540766	25.38271471	6261.890212	8	7.110635407	TRUE	dir	Geographic Coordinates	90	0	3	70	100
28	269	A	12	3	100	104	905.5	di17	112.8863995	-20.79215717	21881.08232	7	2.435042272	TRUE	dir	Geographic Coordinates	90	0	9	20	70
28	269	A	12	3	139	143	905.89	di18	28.96001016	-64.21128488	18086.04801	6	2.041162135	TRUE	dir	Geographic Coordinates	90	0	9	20	70
28	269	A	12	4	35	38	906.35	di19	141.8096984	27.06084292	19862.01544	5	3.18722628	TRUE	dir	Geographic Coordinates	90	0	8	25	70
28	269	A	12	4	114	116	907.14	di20	344.1505266	24.98480412	7524.080645	4	5.534615148	TRUE	dir	Geographic Coordinates	90	0	7	15	50
28	269	A	12	5	52	54	908.02	di21	69.08596658	24.27440215	17408.94553	3	2.165969334	TRUE	dir	Geographic Coordinates	90	0	9	25	80
28	269	A	12	6	43	46	909.43	di22	281.6904156	26.9239216	14765.06822	2	2.552548953	TRUE	dir	Geographic Coordinates	90	0	5	40	70
28	269	A	12	6	119	120	910.19	di23	153.9393002	-43.82377169	17273.54343	1	3.971015509	TRUE	dir	Geographic Coordinates	90	0	8	25	70
28	269	A	11	1	128	131	854.78	di24	149.0593065	59.0440706	6141721.081	8	13.68602895	TRUE	dir	Geographic Coordinates	90	0	4	50	80
28	269	A	11	2	100	102	856	di25	326.9019884	-50.97461873	289344012	7	3.08101949	TRUE	dir	Geographic Coordinates	90	0	9	30	90
28	269	A	11	3	116	119	857.66	di26	334.5364202	-50.21976757	388489949.3	6	2.845164352	TRUE	dir	Geographic Coordinates	90	0	11	25	100
28	269	A	11	4	102	104	859.02	di27	226.1544957	-78.90314623	98982659.64	5	1.643774787	TRUE	dir	Geographic Coordinates	90	0	7	30	70
28	269	A	10	1	118	120	807.18	di28	127.4962079	33.84819793	125506107.5	4	3.888959636	TRUE	dir	Geographic Coordinates	90	0	8	25	70
28	269	A	10	2	135	137	808.85	di29	358.1326336	65.43141803	34389970.9	3	4.194877001	TRUE	dir	Geographic Coordinates	90	0	9	30	90
28	269	A	10	3	79	81	809.79	di30	263.7014199	65.84537641	218693976.6	2	1.907142101	TRUE	dir	Geographic Coordinates	90	0	8	30	80
28	269	A	10	3	113	115	810.13	di31	312.9883864	27.39953287	639061206.2	1	0.796159944	TRUE	dir	Geographic Coordinates	90	0	9	30	90
28	269	A	10	4	47	49	810.97	di32	281.4697077	18.89465352	1001907661	8	1.089722914	TRUE	dir	Geographic Coordinates	90	0	9	30	90
28	269	A	9	1	140	141	750.4	di33	6.985047386	37.39524076	71105293.91	7	7.206328365	TRUE	dir	Geographic Coordinates	90	0	6	35	70
28	269	A	9	2	91	92	751.41	di34	142.4203434	12.32332113	310016716.7	6	2.480805913	TRUE	dir	Geographic Coordinates	90	0	9	35	100
28	269	A	9	3	56	57	752.56	di35	30.53633776	51.30379385	222359261.8	5	9.025097405	TRUE	dir	Geographic Coordinates	90	0	7	40	90
28	269	A	9	3	82	84	752.82	di36	148.2317044	28.23487618	320725804.9	4	2.837413	TRUE	dir	Geographic Coordinates	90	0	9	30	90
28	269	A	8	1	112	114	702.62	di37	296.5709821	-35.97232585	178226512.9	3	2.017011139	TRUE	dir	Geographic Coordinates	90	0	6	30	60
28	269	A	8	2	32	34	703.32	di38	178.8055694	-33.57064374	31276157.15	2	15.17208249	TRUE	dir	Geographic Coordinates	90	0	6	35	70
28	269	A	8	3	21	23	704.71	di39	136.2052788	65.45985345	254911417.1	1	1.883407029	TRUE	dir	Geographic Coordinates	90	0	8	30	80
28	269	A	8	4	24	26	706.24	DI40	154.1991718	-55.21781411	125870874.8	8	5.107651031	TRUE	dir	Geographic Coordinates	90	0	8	25	70
28	269	A	7	2	28	30	655.78	DI42	199.0415962	-18.28783989	71590755.93	7	6.586390491	TRUE	dir	Geographic Coordinates	90	0	3	15	25
28	269	A	7	3	21	23	657.21	DI43	193.5689914	-36.21456441	77389858.44	6	1.903325393	TRUE	dir	Geographic Coordinates	90	0	6	35	70
28	269	A	7	4	51	53	659.01	DI44	168.0187196	-26.12330831	72845114.34	5	6.719835872	TRUE	dir	Geographic Coordinates	90	0	4	40	60

Table 10.3.2: Palynomorphs assemblages at Hole 269A; Cores 7R-13R.

Sample Name	Core Section	Interval (cm)	Depth core (mbsf)	Lycopodium	Lycopodium counted	Weight (g)	Brigantedinium spp.	Brigantedinium cavate	Brigantedinium pynei	Selenopemphix spp.	Selenopemphix antarctica	Selenopemphix Nephroides	Selenopemphix Undulata	Lejeunecysta spp.	Lejeunecysta acuminata	Protoperidinium	Malvinia escutiana	Vozzhennikovia spp.	Spinidinium spp.	Spinidinium macmurdoense	Wetzellia spp.	Rhombodinium draco	Deflandrea spp.	Deflandrea antarctica	Phthanoperidinium spp.	**Total protoperidinioids**
DSDPLeg 28 Site 269A	006R 3W	100-104	610.52	20848	2549	19.4551	9												1							10
DSDP Leg 28 Site 269A	007R 2W	30-34	655.82	20848	648	18.9571	174	1	1	2		3		4	1	9										195
DSDP Leg 28 Site 269A	007R 4W	30-34	658.82	20848	1538	20.0307	127	14						2.5				10	1	2						156.5
DSDP Leg 28 Site 269A	007R 4W	113-117	659.65	20848	2533	19.4604	49	7		1						2		3.5								62.5
DSDP Leg 28 Site 269A	008R 2W	131-135	704.33	20848	2283	20.1364	1											1								2
DSDP Leg 28 Site 269A	008R 3W	28-32	704.8	20848	2243	19.3753	124	15		7				13.5				5	3							167.5
DSDPLeg 28 Site 269A	009R 2W	26-30	750.78	20848	3505	16.3358	45	4											2		1		4	1		59
DSDP Leg 28 Site 269A	009R 3W	30-34	752.32	20848	1863	19.8009																				0
DSDP Leg 28 Site 269A	009R 3W	125-129	753.27	20848	2285	18.2004	86	2		3				10			3	62.5	2	2			1			171.5
DSDP Leg 28 Site 269A	010R 3W	25-29	809.27	20848	2017	20.1234																				0
DSDP Leg 28 Site 269A	010R 4W	25-29	810.77	20848	1999	19.1668	65			3				5.5												73.5
DSDP Leg 28 Site 269A	011R 1W	75-79	854.27	20848	1766	14.4943	187			7	1			2		1										198
DSDP Leg 28 Site 269A	011R 4W	22-26	858.24	20848	2128	20.0815	82	8		7		0.5		6				4.5								108
DSDPLeg 28 Site 269A	011R 4W	125-129	859.27	20848	2100	20.0162	150	25		4								1	1							181
DSDP Leg 28 Site 269A	012R 2W	35-39	902.87	20848	1865	19.4047	88											2								90
DSDP Leg 28 Site 269A	012R 2W	125-129	903.77	20848	2018	20.0258	123	5		6				0.5			1	14	3	1		1	1		1	156.5
DSDPLeg 28 Site 269A	012R 6W	125-129	909.77	20848	2069	20.0322	169	2		20.5		14		4			3	2				1				215.5
DSDPLeg 28 Site 269A	013R 1W	33-37	948.85	20848	840	19.2824	134			19		44		1		1		1								200
DSDP Leg 28 Site 269A	013R 2W	26-30	950.28	20848	1642	20.0555	159.5			35		29.5		1	1											226
DSDP Leg 28 Site 269A	013R 4W	125-129	954.27	20848	839	18.1817	148			26	5	43.5		5					1							228.5

Achomosphaera spp.					1		2					1				1				
Aiora fenestrata		1								1							1			
Areoligera spp.							1													
Batiacasphaera spp.	8		1		1		1		1					3		2	7		1	2
Corrudinium spp.					4		1													
Cerebrocysta ssp.	2									1										
Ectosphaeropsis burdigalensis																				
Enneadocysta spp. "pale"	1	1			4,5+2	4	9	2	9	6		1	14		2.5	12	2		1	4
Enneadocysta spp. "yellow"	2		1	3			17		2	6.5	1			1	2.5	5.5	4		3	
Gelatia inflata							9		3	1				1				1	6	
Homotryblium spp.							1													
Impagidinium spp.	16		1	5	5	4	6	2	1			1		1	4	2	2		2	
Impagidinium spp. Bruin							1													
Impagidinium aculeatum			1		1	2	3	4				1								
Impagidinium pallidum	18			3		2							1	6		3			6	1
Impagidinium cf pallidum	25				6					1							1			
Impagidinium cf paradoxum																2				
Impagidinium patulum								4									2			
Impagidinium velorum	3																		2	3
Impagidinium victorianum																				
Nemat. labyrinthus	16	3			1		1					1								
Pyxidinopsis spp.	13			1					2		2			9		1			3	
Operculodinium spp.	5				3		1		1				1	1	1	3	2	1	8	3
Operculodinium centrocarpum																			3	2
Operculodinium "pale"																			8	7
Operculodinium janduchenei																4			1	
Operculodinium piaseckii	11				1															
Operculodinium polar																			32	10
Operculodinium eirikianum										1										
Operculodinium cf eirikianum							1													
Operculodinium "spiky"																			4	12
Operculodinium wannabe													2						29	10
Reticulatosphaera spp.																2				
Spiniferites spp.									3				2	1		1			5	1
Spiniferites sp A									7											
Invertocysta tabulata				1				1												
Invertocysta lacrymosa																				
Total gonyaulacoids	120	5	4	13	23	12	53.5	13	29	17.5	3	5	20	23	10	38.5	21	2	114	54.5
Total dinocysts	130	200	161	75.5	25	180	113	13	201	17.5	76.5	203	128	204	100	195	237	202	340	283

Table 10.3.3: Principal components (PC) of Hole 269A; Cores 7R-13R. **a:** PCA $_{\mathrm{TOT}}$, **b:** PCA excluding carbonate-cemented intervals.

PCA $_{\mathrm{TOT}}$			PCA		
PC	**Eigenvalue**	**Variance (%)**	**PC**	**Eigenvalue**	**Variance (%)**
PC 1	1.93	63.77	PC 1	0.95	34.72
PC 2	0.53	17.50	PC 2	0.88	31.98
PC 3	0.26	8.47	PC 3	0.27	9.73
PC 4	0.12	3.83	PC 4	0.24	8.88
PC 5	0.08	2.48	PC 5	0.17	6.19
PC 6	0.06	1.82	PC 6	0.09	3.14
PC 7	0.04	1.32	PC 7	0.07	2.55
PC 8	0.01	0.35	PC 8	0.04	1.41
PC 9	0.01	0.24	PC 9	0.02	0.78
PC 10	0.01	0.22	PC 10	0.02	0.62
PC 11	0.00	0.00	PC 11	0.00	0.00

Table 10.3.4: Concentrations of GDGTs at Hole 269A; Cores 7R-13R. All samples and corresponding depths, GDGT peak area values, TEX86 (Schouten et al., 2002) and BIT index values (Hopmans et al., 2004), Methane Index (Methzhang) values (Zhang et al., 2011), GDGT2/Crenarchaeol ratios (Weijers et al., 2011), GDGT-0/Crenarchaeol ratios (Blaga et al., 2009) and GDGT-2/GDGT-3 ratios (Taylor et al., 2013), and RING index (Sinninghe Damsté, 2016). Discarded samples (OUTLIER=TRUE) with outlier values are based on BIT > 0.4, GDGT2/GDGT3` > 5, `GDGT0/cren` > 2 and `Methzhang` > 0.3.

Sample Name	Depth(mbsf)	GDGT-0	GDGT-1		GDGT-2	GDGT-3	GDGT-4	GDGT-4'	GDGT-IIIa	GDGT-IIIa'	SUM GDGT-IIIa
		1302	1300	H1300	1298	1296	1292	1292'	1050-1	1050-2	1050-tot
28-269A-7R-2W 30-34cm	655.8	2942750.0	159364.0	0.0	62727.9	18918.3	2706500.0	45714.4	47578.7	26296.1	73874.8
28-269A-7R-3W 136-136cm	658.4	12613497.0	717051.9	119649.4	385648.6	77529.1	12553429.0	198797.5	314790.5	156020.8	470811.3
28-269A-7R-4W 127-131	659.8	28695870.0	829447.3	248715.4	461230.4	57143.8	8250699.5	231671.9	139414.0	94517.9	233931.9
28-269A-8R-3W 142-146	705.9	4760829.0	204032.7	38097.8	92975.4	29892.9	4139520.5	56135.2	167024.0	105912.6	272936.6
28-269A-9R-2W 106-110cm	753.1	17138900.0	576784.9	167579.6	251321.1	117106.8	16933678.0	174104.2	230212.3	147753.3	377965.6
28-269A-10R-3W 25-28cm	809.3	28890.9	2495.0	7904.5	2223.6	2104.2	4668.5	2071.6	5271.6	2961.4	8233.0
28-269A-10R-3W 116-120cm	810.2	6003169.0	254334.4	56686.4	86115.8	45950.0	6143775.5	83228.2	151393.5	86406.7	237800.2
28-269A-11R-1W 75-79cm	854.3	795513.0	42238.5	0.0	15689.7	5634.5	861324.0	12810.7	19932.8	10570.1	30502.9
28-269A-11R-3W 23-27cm	856.8	33051.7	2651.7	0.0	2004.7	2018.5	22133.5	2057.4	9372.8	7193.4	16566.2
28-269A-12R-2W 40-43cm	902.9	194355.7	10943.2	0.0	3960.4	2268.3	183369.7	4365.3	7947.7	9103.8	17051.5
28-269A-12R-4W 25-28cm	905.8	3728442.0	168857.0	33074.1	70626.6	29034.4	3919071.8	48228.7	144021.0	79521.6	223542.6
28-269A-12R-4W 125-128cm	906.8	3072708.0	130516.6	16421.6	59769.3	22098.5	3129816.3	44337.4	76395.4	44885.9	121281.3
28-269A-13R-1W 33-37cm	948.9	459448.0	21973.4	0.0	7378.4	3209.4	486734.0	6502.2	25618.2	14374.4	39992.6
28-269A-13R-2W 87-91cm	950.9	2347130.0	105004.3	0.0	51535.6	19066.5	2323012.3	33990.5	168605.3	101849.8	270455.1
28-269A-13R-4W 13-17cm	953.2	2251815.8	122400.4	21870.6	52940.5	18491.2	2273169.8	37531.8	98155.3	57310.7	155466.0

GDGT-IIa	GDGT-IIa'	SUM GDGT-IIa	GDGT-IIb	GDGT-IIb'	SUM GDGT-IIb		GDGT-IIc	GDGT-IIc'	SUM GDGT-IIc
1036-1	1036-2	1036-tot	1034-1	1034-2	1034-tot	OH-1034	1032-1	1032-2	1032-tot
18699.4	13806.1	32505.5	6965.0	14544.7	21509.7	0.0	3749.1	9198.9	12948.0
67665.6	73249.0	140914.6	52635.8	80306.2	132942.0	104047.4	13712.3	24680.3	38392.6
51122.1	38731.7	89853.8	32993.8	35129.8	68123.6	37714.4	9001.3	13210.8	22212.1
90077.1	50242.6	140319.7	54628.9	37768.2	92397.1	48924.1	13229.0	14742.5	27971.5
70443.5	65665.1	136108.6	69136.6	69015.9	138152.5	55351.3	22621.5	25153.8	47775.3
3065.6	5508.6	8574.2	0.0	0.0	0.0	0.0	0.0	0.0	0.0
52180.1	44458.8	96638.9	42485.1	34092.4	76577.5	47095.5	10714.1	14235.1	24949.2
8328.0	4752.0	13079.9	5463.0	4166.0	9629.0	0.0	1101.0	1475.0	2576.0
3557.1	4061.8	7618.9	0.0	0.0	0.0	0.0	0.0	0.0	0.0
5069.7	6338.1	11407.8	2383.1	4796.7	7179.8	0.0	2537.9	0.0	2537.9
68037.8	46249.2	114287.0	31120.5	25491.3	56611.8	58382.1	7456.9	9845.0	17301.9
39721.6	24584.5	64306.1	21236.2	17262.9	38499.1	21836.9	7235.3	6543.2	13778.5
14912.4	9208.5	24120.9	6242.0	5069.5	11311.4	0.0	1511.2	1574.5	3085.7
92141.9	50565.0	142706.9	41430.6	27951.3	69381.9	0.0	10227.7	11422.2	21649.9
54374.1	31827.6	86201.7	28874.5	21519.9	50394.4	0.0	5752.5	7663.4	13415.9

GDGT-Ia	GDGT-Ib					GDGT-Ic	TEX86	SST	BIT	SUM.ISO
1022	1020	OH-1020a	OH-1020b	OH-1020c	OH-1020d	1018				
40162.4	14362.6	0.0	0.0	0.0	0.0	12066.1	0.44	9.60	0.05	5935974.60
259286.0	48214.7	9688.9	309723.9	389706.7	31440.2	44094.6	0.48	12.52	0.06	26545953.10
115207.8	21693.6	12370.7	161634.8	228429.3	19674.6	17263.1	0.47	12.10	0.05	38526062.90
195084.8	29822.2	6062.6	214955.1	307641.0	14341.2	26600.7	0.47	11.49	0.13	9283385.70
379003.8	51333.5	18512.8	350091.6	461749.2	22602.7	47889.6	0.48	12.90	0.05	35191895.00
5851.6	2279.7	2355.4	31366.7	41509.1	9545.0	2403.8	0.72	32.04	0.83	42453.80
167211.4	23949.2	3173.1	198778.5	257938.0	11349.6	19038.2	0.46	10.76	0.08	12616572.90
15798.4	2882.8	0.0	0.0	0.0	0.0	1790.2	0.45	9.83	0.06	1733210.38
3545.1	0.0	2460.4	41030.8	52970.5	19288.3	0.0	0.70	30.15	0.56	63917.50
0.0	3250.4	2962.9	48828.5	58378.8	5677.2	3067.2	0.49	13.49	NA	399262.60
160392.1	17823.1	4769.6	113524.4	137038.3	8631.3	11332.4	0.47	11.45	0.11	7964260.50
102277.7	15114.2	3591.8	77430.9	100388.7	8322.0	10313.6	0.49	13.47	0.08	6459246.10
25200.1	3997.7	0.0	0.0	0.0	0.0	1824.3	0.44	9.06	0.16	985245.36
151594.1	26127.8	3518.7	56499.7	79548.7	7004.6	11069.5	0.50	14.07	0.20	4879739.20
111762.2	16782.5	4996.4	84776.7	101662.3	12490.3	8417.6	0.47	11.78	0.13	4756349.50

FA1302.ISO	FA1300.ISO	FA1298.ISO	FA1296.ISO	FA1292.ISO	A1292'.IS	GDGT2/GDGT3	GDGT2/cren	GDGT0/cren	Methzhang	RING	SUM.ALL
0.496	0.027	0.011	0.003	0.456	0.008	3.316	0.023	1.087	0.081	1.912	5902393.59
0.475	0.027	0.015	0.003	0.473	0.007	4.974	0.031	1.005	0.085	1.986	26500379.30
0.745	0.022	0.012	0.001	0.214	0.006	8.071	0.056	3.478	0.137	0.931	37746527.30
0.513	0.022	0.010	0.003	0.446	0.006	3.110	0.022	1.150	0.072	1.859	9741617.30
0.487	0.016	0.007	0.003	0.481	0.005	2.146	0.015	1.012	0.052	1.985	35424911.10
0.681	0.059	0.052	0.050	0.110	0.049	1.057	0.476	6.188	0.503	0.947	62973.30
0.476	0.020	0.007	0.004	0.487	0.007	1.874	0.014	0.977	0.058	2.019	12876337.30
0.459	0.024	0.009	0.003	0.497	0.007	2.785	0.018	0.924	0.068	2.070	1745906.93
0.517	0.041	0.031	0.032	0.346	0.032	0.993	0.091	1.493	0.216	1.713	NA
0.487	0.027	0.010	0.006	0.459	0.011	1.746	0.022	1.060	0.084	1.945	NA
0.468	0.021	0.009	0.004	0.492	0.006	2.433	0.018	0.951	0.063	2.042	8297033.40
0.476	0.020	0.009	0.003	0.485	0.007	2.705	0.019	0.982	0.063	2.015	6612432.20
0.466	0.022	0.007	0.003	0.494	0.007	2.299	0.015	0.944	0.062	2.050	1062216.84
0.481	0.022	0.011	0.004	0.476	0.007	2.703	0.022	1.010	0.069	1.986	5397118.00
0.473	0.026	0.011	0.004	0.478	0.008	2.863	0.023	0.991	0.077	2.003	5004957.70

SUM.BR	CBT	pH	MBT	MAT	outlierBIT	outlierGDGT2/3	outlierGDGT0/cren	outlierMethzhang	outlierRING	OUTLIER
207429.19	0.116	8.350	0.321	10.104	FALSE	FALSE	FALSE	FALSE	FALSE	FALSE
1134655.80	0.019	8.603	0.310	10.310	FALSE	FALSE	FALSE	FALSE	FALSE	FALSE
568285.90	0.094	8.407	0.271	8.686	FALSE	TRUE	TRUE	FALSE	TRUE	TRUE
785132.60	0.144	8.278	0.320	9.926	FALSE	FALSE	FALSE	FALSE	FALSE	FALSE
1178228.90	-0.005	8.664	0.406	13.419	FALSE	FALSE	FALSE	FALSE	FALSE	FALSE
27342.30	0.678	6.890	0.385	8.912	TRUE	FALSE	TRUE	TRUE	TRUE	TRUE
646164.60	0.079	8.446	0.325	10.446	FALSE	FALSE	FALSE	FALSE	FALSE	FALSE
76259.23	0.106	8.377	0.268	8.532	FALSE	FALSE	FALSE	FALSE	FALSE	FALSE
NA	NA	NA	NA	NA	TRUE	FALSE	FALSE	FALSE	TRUE	TRUE
NA	0.148	8.268	NA	NA	NA	FALSE	FALSE	FALSE	FALSE	TRUE
601290.90	0.249	8.004	0.315	9.170	FALSE	FALSE	FALSE	FALSE	FALSE	FALSE
365570.50	0.171	8.208	0.349	10.672	FALSE	FALSE	FALSE	FALSE	FALSE	FALSE
109532.69	0.264	7.965	0.283	8.093	FALSE	FALSE	FALSE	FALSE	FALSE	FALSE
692985.20	0.247	8.009	0.272	7.853	FALSE	FALSE	FALSE	FALSE	FALSE	FALSE
442440.30	0.186	8.169	0.310	9.354	FALSE	FALSE	FALSE	FALSE	FALSE	FALSE

R-script: GDGT Peak area calculation

required packages

```
library(caTools)
library(ggplot2)
library(dplyr)
##
## Attaching package: 'dplyr'
## The following objects are masked from 'package:stats':
##
## filter, lag
## The following objects are masked from 'package:base':
##
## intersect, setdiff, setequal, union
library(readr)
library(readxl)
library(tidyverse)
## ── Attaching packages ─────────────────────────────────────── ── tidyverse 1.
2.1 ──
## ✔ tibble 2.1.3 ✔ purrr 0.3.2
## ✔ tidyr 0.8.3 ✔ stringr 1.3.1
## ✔ tibble 2.1.3 ✔ forcats 0.3.0
## ── Conflicts ──────────────────────────────────────────── tidyverse_conflict
s() ──
## ✖ dplyr::filter() masks stats::filter()
## ✖ dplyr::lag() masks stats::lag()
library(plotly)
##
## Attaching package: 'plotly'
## The following object is masked from 'package:ggplot2':
## last_plot
## The following object is masked from 'package:stats':
## filter
## The following object is masked from 'package:graphics':
## layout
library(ggtern)
## --
## Remember to cite, run citation(package = 'ggtern') for further info.
## --
##
## Attaching package: 'ggtern'
## The following objects are masked from 'package:ggplot2':
##
## %+%, aes, annotate, calc_element, ggplot, ggplot_build,
## ggplot_gtable, ggplotGrob, ggsave, layer_data, theme,
## theme_bw, theme_classic, theme_dark, theme_gray, theme_light,
## theme_linedraw, theme_minimal, theme_void
theme = theme_set(theme_classic())
library(readxl)
setwd("~/Documents/Projects/Site 269")
OGdata <- read_excel("269 OG.xlsx")
#shows data tables below
OGdata
```

adds collumns with calculations from GDGT peak areas

```
#adds collumns with calculations from GDGT peak areas
OGdata <- OGdata %>%
mutate(
#TEX86 ratio from Schouten et al. 2002
TEX86 = (`1298` + `1296` + `1292'`)/(`1300` + `1298` + `1296` + `1292'`),
#SST calibrations from Kim et al., 2010; TEX86 linear calibration model (0 m)
```

```
SST = 81.5*TEX86 -26.6,
#Hopmans et al. 2004
BIT = (`1050-tot` + `1036-tot` + `1022`)/(`1292` + `1050-tot` + `1036
-tot` + `1022`),
#fractional abundances needed for the RING index
SUM.ISO = `1302` + `1300` + `1298` + `1296` + `1292` + `1292'`,
FA1302.ISO = `1302` / SUM.ISO,
FA1300.ISO = `1300` / SUM.ISO,
FA1298.ISO = `1298` / SUM.ISO,
FA1296.ISO = `1296` / SUM.ISO,
FA1292.ISO = `1292` / SUM.ISO,
`FA1292'.ISO` = `1292'` / SUM.ISO,
#depth contribution (Taylor et al., 2013) AOM (Weijers et al., 2011), lake in
situ production (Blaga et al., 2009), methanogenic (Zhang et al.) indices and
the RING index
`GDGT2/GDGT3` = `1298`/ `1296`,
`GDGT2/cren` = `1298` / `1292`,
`GDGT0/cren` = `1302` / `1292`,
`Methzhang` = (`1300` + `1298` + `1296`) / (`1300` + `1298` + `1296`
+ `1292` + `1292'`),
`RING` = FA1300.ISO + 2*FA1298.ISO + 3*FA1296.ISO + 4*FA1292.ISO + 4*
`FA1292'.ISO`,
#Summarizing
SUM.ALL = `1302` + `1292` + `1292'` + `1022` + `1020` + `1018` + `103
6-tot` + `1034-tot` + `1032-tot` + `1050-tot`,
SUM.BR = `1022` + `1020` + `1018` + `1036-tot` + `1034-tot` + `1032-t
ot` + `1050-tot`,
# weijers et al., 2007
CBT = -log10((`1020` + `1034-tot`) / (`1020` + `1036-tot`)),
pH = (3.3283-CBT)/ 0.3847,
MBT = (`1022` + `1020` + `1018`) / SUM.BR,
#Peterse et al., 2012 (MBT' = MBT, because 1048 and 1046 were not integrated)
`MAT` = 0.81 - 5.67*CBT + 31*MBT,)
CAPDELRI.L <- function(TEX86) -1.15*TEX86 + 2.98*TEX86^2 + 1.49
CAPDELRI.U <- function(TEX86) -0.39*TEX86 + 3.66*TEX86^2 + 1.69
Outlier ruleas for TEX86
#If:
#RING outside CAPDELRI curves,
#GDGT2/GDGT3 > 5 OR,
#GDGT2/cren > 0.1 OR,
#GDGT0/cren > 2 OR,
#BIT > 0.4 OR,
#Methzhang 1300+1298+1296/1300+1298+1296+1292+1292' > 0.3
#-->
#rejectTEX86
#this adds columns to your dataframe with a logical value (TRUE or FALSE) for
each outlier rule. The final OUTLIER column is added with a logical value for
whether any of the other oulier rule is true
OGdata <- OGdata %>%
mutate(
`outlierBIT` = BIT > 0.4,
`outlierGDGT2/3` = `GDGT2/GDGT3` > 5,
`outlierGDGT0/cren` = `GDGT0/cren` > 2,
`outlierMethzhang` = `Methzhang` > 0.3,
outlierRING = RING<CAPDELRI.L(TEX86) | RING>CAPDELRI.U(TEX86),
OUTLIER = `outlierBIT` | `outlierGDGT2/3` | `outlierGDGT0/cre
n` | `outlierMethzhang` | outlierRING
)
#shows new
```

Appendix 4

Supplementary figures for chapter 6

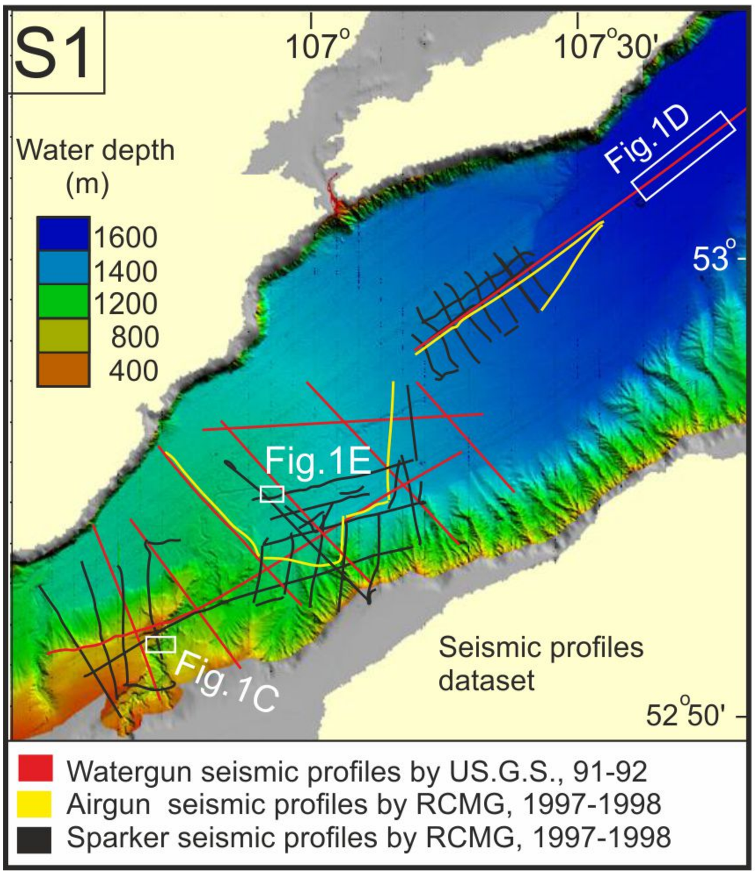

Fig. 10.4.1: Location of figures and selected seismic profiles.

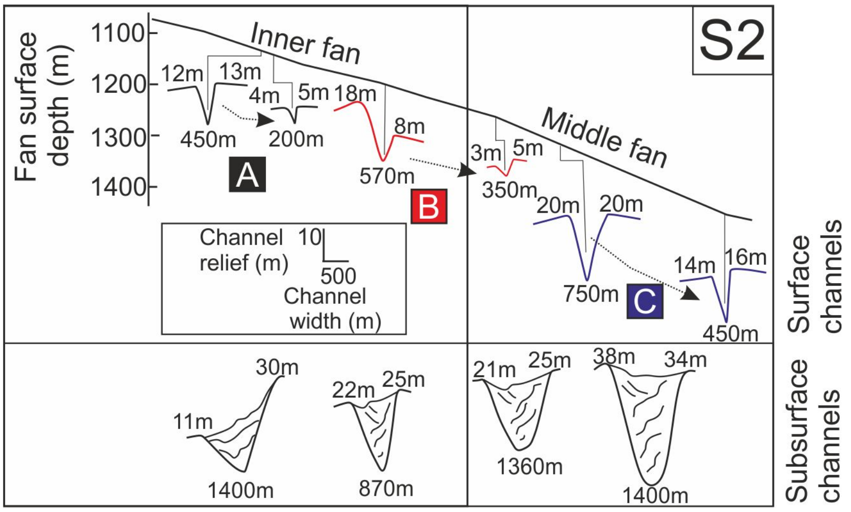

Fig. 10.4.2: Surface (upper panel) and subsurface (lower panel) inner and middle fan channel morphology. Note each channel proximal to distal characteristics. Channel outline colors keyed to Figure 1B. Note that values of subsurface channels are not corrected for compaction.

Appendix 5

Co-authored papers related to the topic of the Thesis:

Salabarnada, A.*, Escutia, C., Röhl, U., Nelson, C. H., McKay, R., Jiménez-Espejo, F. J., Bijl, P. K., Hartman, J. D., Strother, S. L., Salzmann, U.,* **Evangelinos, D***., López-Quirós, A., Flores, J. A., Sangiorgi, F., Ikehara, M. and Brinkhuis, H.: Paleoceanography and ice sheet variability offshore Wilkes Land, Antarctica – Part 1: Insights from late Oligocene astronomically paced contourite sedimentation, Climate of the Past, 14(7), 991–1014, doi:10.5194/cp-14-991-2018, 2018.*
Q1, Impact Factor: 3.47

López-Quirós, A., Escutia, C., Sánchez-Navas, A., Nieto, F., Garcia-Casco, A., Martín-Algarra, A., ***Evangelinos, D.****,* Salabarnada, A.*, 2019. Glaucony authigenesis, maturity and alteration in the Weddell Sea: An indicator of paleoenvironmental conditions before the onset of Antarctic glaciation. Scientific Reports. 9, 13580.*
Q1, Impact Factor: 4.525

López-Quirós, A., Lobo, F.J., Escutia, C., García, M., Hernández-Molina, F.J., Pérez, L.F., Bohoyo, F., ***Evangelinos, D.****,* Salabarnada, A.*, Maldonado, A., Naveira Garabato, A.C., 2020. Geomorphology of Ona Basin, southwestern Scotia Sea (Antarctica): Decoding the spatial variability of bottom-current pathways. Marine Geology 422, 106113.*
Q1, Impact Factor: 3.349

O'Brien, P.E., Post, A. L., Edwards, S., Martin, T., Caburlotto, A. Donda, F., Leitchenkov, G., Romeo, R. Duffy, M., ***Evangelinos, D.****, Holder, L., Leventer, A., López-Quirós, A., Opdyke, B. N., and Armand,L. K., 2020. Continental slope and rise geomorphology seaward of the Totten Glacier, East Antarctica (112ºE-122ºE). Marine Geology. (in press).*
Q1, Impact Factor: 3.349

List of Figures

List of Tables

Dimitris Evangelinos

Born: Heraklion, Crete, Greece January 13, 1989.
Address: c/ Beteta, nº19, 4-B
Granada, Spain
Mobile: (+34) 631877910
E-mail : dim.evage@gmail.com

HIGHER EDUCATION

2015-Present: PhD candidate in Earth Sciences. Andalusian Institute of Earth Sciences (CSIC-University of Granada), Spain.
PhD thesis project: "*Cenozoic ice sheets and ocean circulation variability controls on deep-water sediments in glaciated margins"*. Supervisor: Dr. Carlota Escutia Dotti.

September 2014: Master of sciences in Oceans & Lakes Sciences and Management. Interuniversity master programme: University of Brussels, University of Gent and University of Antwerp, Belgium.
Master thesis project: ***"****Dispersion and deposition of sediment plumes, resulting from intensive marine aggregate extraction"*. Supervisor: Dr. Vera van Lancker.

July 2012: Bachelor of sciences in Marine Sciences. University of the Aegean, Environmental school, department of Marine Sciences, Mytilene, Lesvos Island, Greece.
Bachelor thesis project: ***"****Recent sedimentary processes and marine geohazards across the continental shelf of Lesvos Island"*. Supervisor: Dr. Hasiotis Thomas

August 2010 - December 2010: Erasmus Studies in Environmental Sciences, University of Wageningen, department of Environmental Sciences, The Netherlands.

PROFESSIONAL EXPERIENCE

1/10/15-30/09/19 Andalusian Institute of Earth Sciences, Spain
PhD contract (Onassis Foundation-Scholarship ID: F ZL 026-1/2015-2016.
Marine Geosciences group - Antarctic Research.
Task: *Sedimentological, geochemical and isotopic analysis.*

01/06/15-31/08/15: Marine Geologist at Akti Engineering Marine and Land surveying services, Greece.
Project title: Power cable route survey.
Task: *Sub-bottom data acquisition, interpretation and mapping.*

14/10/14-31/05/15: Marine Geologist at Andalusian Institute of Earth Sciences, Granada, Spain.
Project title: Lake Baikal turbidite system evolution linked solely to Pleistocene glacial climate change, not water level change. Supervisor: Dr. C.H. Nelson.
Task: *Sub-bottom data interpretation and mapping.*

19/08/13-09/09/13: Marine Geologist at Renard Centre of Marine Geology, Ghent, Belgium.
Geophysical Research Project: Arch-Manche. Project title: Acoustic mapping of Langstone Bay. Supervisor: Dr. T. Missiaen.
Task: *Sub-bottom data interpretation and mapping.*

November 2011 - December 2011: Marine Geologist at Akti Engineering Marine and Land surveying services, Greece.
Project title: Power cable route survey.
Task: *Sub-bottom data acquisition, interpretation and mapping.*

01/02/12-31/05/12: Marine Geologist at Renard Centre of Marine Geology, Ghent, Belgium.
Project title: *Very high-resolution acoustic mapping of the intertidal area in Raversijde and comparison with electromagnetic data*. Supervisor: Dr. T. Missiaen.
Task*: Sub-bottom data interpretation, mapping and integration with electromagnetic data*.

June 2011- August 2011: Assistant student at CretAquarium Thalassocosmos- Aquarium, Heraklion, Crete, Greece.
Task: *Studying the life-cycle and behaviour of jelly-*fish (*Aurelia aurita)*

HONORS -AWARDS

July 2019: European Consortium for Ocean Research *Drilling* (ECORD) merit-based awards for outstanding young scientists for innovative research related to the International Ocean Discovery Program, *provided by the ECORD Science support and Advisory Committee (ESSAC) Committee.*

July 2018: PhD research grant for 12 additional months provided by the Onassis Public Benefit Foundation (FZL 026-1/2015-2016).

October 2015: PhD research grant for 36 months provided by the Onassis Public Benefit Foundation (FZL 026-1/2015-2016).

July 2012: EA- Merit scholarship for 2 years full time MSc studies in Belgium for the MSc programme "Ocean & Lakes Sciences and Management", provided by Vrije Universiteit Brussel, International Relations & Mobility Office

April 2011: Award for excellence in BSc studies for for the academic year 2008-09, provided by the State Scholarships Foundation (IKY).

ACCOMODATION, REGISTRATION FEE AND TRAVEL GRANTS

June 2019: Accommodation and registration fee grant for the International Symposium on Antarctic Earth Sciences (ISAES) 2019 in Incheon (Korea), provided by Organizing Committee of ISAES 2019.

June 2018: Travel grant for the Polar2018 conference in Davos, Switzerland, provided by International Arctic Science Committee (IASC) and Scientific Committee on Antarctic Research (SCAR).

September 2017: Travel grant for the Past Antarctic Ice Sheet Dynamics (PAIS) conference in Trieste, Italy, provided by the Organizing Committee of PAIS 2017.

PROJECTS

2017-2019: Project Title "*Tectonic and oceanographic events involved in the development of the Antarctic Circumpolar Current (ACC) and their links to paleoclimate and ice sheet evolution records"*.
Project reference: CTM2017-89711-C2-1-P.
Principal Investigators: Carlota Escutia y Francisco José Jiménez Espejo.

2015-2017: Project Title**:** "*The Tasman and Drake gateways and the Antarctic Circumpolar Current: origin, evolution and its effect on climate and Antarctic ice sheet evolution"*
Project reference: CTM2014-60451-C2-1-P.
Principal Investigators: Carlota Escutia y Francisco J. Lobo.

2014-2015: Project Title**:** "*Cenozoic East Antarctic Glacial Evolution from Sediments Collected by Ocean Drilling in the Wilkes Land Margin (CAGES)"*
Project reference: CTM2011-24079
Principal Investigator: Carlota Escutia

2014: Project title: "*Archaeology, Art & Coastal Heritage: Tools to Support Coastal Management" (Arch-Manche project)*
Led by the Maritime Archaeology Trust in the UK in partnership with the Centre National de la Recherche Scientifique in France, the University of Ghent in Belgium and the research institute Deltares in the Netherlands.

RESEARCH STAYS AND TRAINING ABROAD

8/03/19-29/03/19: Imperial College London, **United Kingdom**. South Kensington Campus, London SW7 2AZ. Task: *Neodymium isotopic analysis on fish teeth from selected Deep Sea Drilling Project (DSDP) sediment samples* Supervisor: Dr. Tina van de Flierdt

23/04/18-11/05/18: Imperial College London, United Kingdom. South Kensington Campus, London SW7 2AZ.
Task: *Neodymium isotopic analysis on fish teeth from selected Deep Sea Drilling Project (DSDP) sediment samples*. Supervisor: Dr. Tina van de Flierdt

21/08/17-01/09/17: MARUM, Center for Marine Environmental Sciences, University of Bremen, Germany. ECORD Summer School. Current-Controlled Sea Floor Archives: Coral Mounds and Contourites.

18/07/17-28/07/17: Paleomagnetic Laboratory CCiTUB and CSIC, Barcelona, Spain. Institut de Ciències de la Terra Jaume Almera, Universitat Autònoma de Barcelona, Facultat de Ciències, 08193 Bellaterra, Barcelona, Spain.
Task: *Measuring Paleomagnetism on selected Deep Sea Drilling Project (DSDP) sediment samples*.
Supervisor: Dr. Luis Valero

19/06/17-30/06/17: Imperial College London, **United Kingdom.** South Kensington Campus, London SW7 2AZ.
Task: *Neodymium isotopic analysis on fish teeth from selected Deep Sea Drilling Project (DSDP) sediment samples* Supervisor: Dr. Tina van de Flierdt

27/09/16-10/10/16: Core Repository- Texas A&M University in College Station, USA.
Task: *Conducting X-Ray Fluorescence (XRF)core scanning and Magnetic susceptibility measurements on selected Deep Sea Drilling Project (DSDP) and Ocean Drilling Project (ODP) sediment cores*

06/03/16-17/03/16: Core Repository- Texas A&M University in College Station, USA.
Task: *Core description, core sampling and obtaining high-resolution images from selected Deep Sea Drilling Project (DSDP) and Ocean Drilling Project (ODP) sediment cores.*

12/05/14-6/06/14: Andalusian Institute of Earth Sciences, Granada, Spain. Avda. de las Palmeras, 4 - 18100 Armilla, Granada, Spain. Project title: Lake Baikal turbidite system evolution linked solely to Pleistocene glacial climate change, not water level change. Task: *Seismic data interpretation and mapping.* Supervisor: Dr. C.H. Nelson

PARTICIPATION IN ANTARCTIC EXPEDITIONS

2/01/2020-4/02/20: Research scientist on the XXV Spanish Antarctic expedition (POWELL 2020) in the area of the Powell Basin, South Shetlands Islands, and Antarctic Peninsula.
Research vessel: ***RV Hespérides***.
Mission title: Onset and evolution of the Antarctic Circumpolar Current (ACC).
Task: *Water sampling for different proxies (e.g. phytoplankton, biomarkers, etc).*
Chief Scientists: Dr. Carlota Escutia and Dr. Fernando Bohoyo.
Duration: 36 days.

25/11/2119-24/12/19: Research scientist on the Korean Antarctic expedition (ANA Tra19) along the transect from Lyttleton (New Zealand) to Ross Sea (Antarctica).
Research vessel: ***RV Araon***
Task: *Water sampling for different proxies (e.g. phytoplankton, biomarkers, etc).*
Chief Scientists: Dr. Jung-Hyun Kim
Duration: 31 days.

10/01/2018-14/02/18: Research scientist on the XXXI Spanish Antarctic expedition (Drake 2018) in the area of the South Orkney Microcontinent, Ona Basin, South Shetlands Islands, and Antarctic Peninsula.
Research vessel: ***RV Hespérides***.
Mission title: Onset and evolution of the Antarctic Circumpolar Current (ACC).

Task: *Water sampling for different proxies (e.g. phytoplankton, biomarkers, etc).*
Chief Scientists: Dr. Carlota Escutia and Dr. Fernando Bohoyo.
Duration: 36 days.

14/01/2017-05/03/17: Research scientist on the Australian Antarctic Expedition (IN2017-V01) in the Sabrina Coast (East Antarctica).
Research vessel: ***RV Investigator***.
Mission title: Interactions of the Totten Glacier with the Southern Ocean through multiple glacial cycles.
Task: S*edimentological analysis and in charge of the Multi-sensor GEOTEK Core Logger.*
Chief Scientists: Dr. Leanne. Armand and Dr. Phil O´Brien.
Duration: 51 days.

PUBLICATIONS:

A1 publications

Evangelinos, D., Escutia, C., Etourneau, J., Hoem, F., Bijl, P., Boterblom, W., van de Flierdt, T., Valero, L., Flores, J. A., Rodriguez-Tovar, F. J., Jimenez-Espejo, F., Salabarnada, A., and López-Quirós. Late Oligocene-Miocene proto-Antarctic Circumpolar Current dynamics off the Wilkes Land margin, East Antarctica. Global and Planetary Change (in press).

López-Quirós, A., Lobo, F. J., Escutia, C., García, M., Hernández-Molina, F. J., Pérez, L. F., Bohoyo, F., **Evangelinos, D.,** Salabarnada, A., Maldonado, A., Naveira Garabato, A. C., 2020. Geomorphology of Ona Basin, southwestern Scotia Sea (Antarctica): Decoding the spatial variability of bottom-current pathways. Marine Geology, *422, 106113.*

López-Quirós, A., Escutia, C., Sánchez-Navas, A., Nieto, F., Garcia-Casco, A., Martín-Algarra, A., **Evangelinos, D.,** Salabarnada, A., 2019. *Glaucony authigenesis, maturity and alternation in the Weddell Sea: An indicator of paleoenvironmental conditions before the onset of Antarctic glaciation.* Scientific Reports *9, 13580.* doi:10.1038/s41598-019-50107-1.

Salabarnada, A., Escutia, C., Röhl, U., Nelson, C. H., McKay, R., Jiménez-Espejo, F. J., Bijl, P. K., Hartman, J. D., Strother, S. L., Salzmann, U., **Evangelinos, D.,** López-Quirós, A., Flores, J. A., Sangiorgi, F., Ikehara, M. and Brinkhuis, H., 2018. *Paleoceanography and ice sheet variability offshore Wilkes Land, Antarctica – Part 1: Insights from late Oligocene astronomically paced contourite sedimentation*, Climate of the Past, 14 (7), 991–1014, doi:10.5194/cp-14-991-2018.

Missiaen, T., **Evangelinos, D.,** Claerhout, C., De Clercq, M., Pieters M., Demerre, I., 2017. *Archaeological prospection of the nearshore and intertidal area using ultra-high resolution marine acoustic techniques: results from a test study on the Belgian coast (Ostend-Raversijde)* Geoarchaeology p.1-15. doi:10.1002/gea.21656.

Evangelinos D., Nelson C. H., Escutia C., De Batist M., Khlystov O., 2016. *Late Quaternary climatic control of Lake Baikal (Russia) turbidite systems: Implications for turbidite systems worldwide.* Geology. 45 (2), p.179-182. doi: 10.1130/G38163.1.

Technical and Expedition Reports

L.K. Armand, P.E. O'Brien and On-board Scientific Party*. 2018. (* L. Armbrecht, H. Baker, A. Caburlotto, T. Connell, D. Cotterle, M. Duffy, S. Edwards, **D. Evangelinos,** J. Fazey, A. Flint, A. Forcardi, S. Gifford, L. Holder, P. Hughes, K-A. Lawler, J. Lieser, A. Leventer, M. Lewis, T. Martin, N. Morgan, A. Lopez Quiros, K. Malakoff, T. Noble, B. Opdyke, R. Palmer, R. Perera, V. Pirotta, A. Post, R. Romeo, J. Simmons, D. Thost, S. Tynan and A. Young) *Interactions of the Totten Glacier with the Southern Ocean through multiple glacial cycles (IN2017-V01)*: Post-survey report, Research School of Earth Sciences, Australian National University: Canberra, http://dx.doi.org/10.4225/13/5acea64c48693.

Van Lancker, V., Baeye, M., **Evangelinos, D.,** Van den Eynde, D., 2015. *Monitoring of the impact of the extraction of marine aggregates*, *in casu sand, in the zone of the Hinder Banks. Period 1/1 – 31/12 2014*. Royal Belgian Institute of Natural Sciences, Operational Directorate Natural Environment: Brussel. 74 + annexes pp.,

Evangelinos, D., Missiaen, T., and Tidbury, L., 2013. *Acoustic mapping of Langstone Bay, Arch-Manche Archaeology, Art and Coastal Heritage.*

Book Chapters

Van Lancker, V., Baeye, M., **Evangelinos, D.,** Francken, F., Van den Eynde, D., De Mesel, I., Kerckhof, F., Norro, A., Van den Branden, R., 2014. *Integrated monitoring of sediment processes in an area of intensive aggregate extraction, Hinder Banks, Belgian part of the North Sea*, *in*: De Mol, L. *et al.* (Ed.) *'Which future for the sand extraction in the Belgian part of the North Sea?'. Study day, 20 October 2014, Belgium Pier - Blankenberge.* pp. 59-71

Missiaen, T., **Evangelinos, D.,** and Jongepier, J., 2014. Case Study 3L – Ostend-Raversijde, Belgium. In Satchell, J &
Tidbury, L (eds) *Arch-Manche: Archaeology, Art & Coastal Heritage: Tools to Support Coastal Management and climate change planning across the Channel RegionalSea:* Technical Report.

Theses

Evangelinos, D., 2012. "*Recent sedimentary processes and marine geohazards across the continental shelf of Lesvos Island"* BSc Thesis. Environmental school, department of Marine Sciences, Mytilene, Lesvos Island, Greece

Evangelinos, D., 2014. "*Dispersion and deposition of sediment plumes, resulting from intensive marine aggregate extraction*" MSc Thesis. VUB/Universiteit Gent/Universiteit Antwerpen: Brussel, Gent, Antwerpen. 15, 42 pp.

Publications at scientific meetings

(1) Hoem, F., **Evangelinos, D.,** Sangiorgi, F., Brinkhuis, H., and Bijl, P.K., 2019. Early Oligocene to middle Miocene surface ocean conditions offshore Cape Adare (Ross Sea, Antarctica); palynological and temperature records of DSDP Site 274. 13th International Conference on Paleoceanography (ICP13), Sydney, Australia.

(2) **Evangelinos, D.,** Escutia, C., Salabarnada, A., Etourneau, J., Jiménez-Espejo, F.J., López-Quirós, A., Bijl, P.K., Sangiorgi, F., Flores, J-A., 2019. Insights into the Oligocene-Miocene transition at the Wilkes-Adelie Land margin. XIII International Symposium on Antarctic Earth Sciences. ISAES 2019, Incheon, Republic of Korea.

(3) **Evangelinos, D.,** Escutia, C., van de Flierdt, T., Etourneau, J., Flores, J-A., Ducassou, E., Valero, L., Harwood, D., Kreissig, K., Perello, M-C., Holder, L., López-Quirós, A., Salabarnada, A., 2019. The evolution of the Antarctic Circumpolar Current across the Tasman Gateway during the last 30 million years. XIII International Symposium on Antarctic Earth Sciences. ISAES 2019, Incheon, Republic of Korea.

(4) López-Quirós, A., Escutia, C., Etourneau, J., Roignant, S., Bohoyo, F., Lobo, F.J., **Evangelinos, D.,** Salabarnada, A., Hoem, F., Bijl, P.K., Sicre, M-A., Klein, V., 2019.The South Orkney Microcontinent: an open door in the Weddell Sea mirroring the Cenozoic climate and tectonic impact of the opening of Drake Passage. XIII International Symposium on Antarctic Earth Sciences. ISAES 2019, Incheon, Republic of Korea.

(5) López-Quirós, A., Escutia, C., Sánchez-Navas, A., Nieto, F., García-Cascos, A., Martín-Algarra, A. **Evangelinos, D.,** Salabarnada, A., 2019. The nature, timing and implication of green-clay authigenesis: A reliable paleoenvironmental indicator for the Antarctic Cenozoic climate history. XIII International Symposium on Antarctic Earth Sciences. ISAES 2019, Incheon, Republic of Korea.

(6) **Evangelinos, D.,** Escutia, C., Etourneau, J., Flores, J-A., Ducassou, E., Harwood, D., Valero, L., Huck, D., Kreissig, K., Perello, M-C., López-Quirós, A., Salabarnada, A., van de Flierdt, T., 2019. The evolution of the Antarctic Circumpolar Current in the Southwest Pacific sector of the Southern Ocean throughout the Cenozoic era. Geophys. Res. Abstr., EGU General Assembly 2019, vol. 21, 14154.

(7) López-Quirós, A., Escutia, C., Etourneau, J., Hoem, F.S., Bijl, P.K., Harwood, D., Rodríguez-Tovar, F.J., Bohoyo, F., Lobo, F.J., **Evangelinos, D.,** Salabarnada, A., Expósito-Ceballos, C., 2019. Effects of Drake Passage

opening at the northwestern Weddell Sea (Antarctica): Climatic inferences from sediment accumulation and stable isotope data. Geophys. Res. Abstr., EGU General Assembly 2019, vol. 21, 14465.

(8) **Evangelinos, D.,** Escutia, C., Salabarnada, A., López-Quirós, A., Valero, L., Flores, JA., Etourneau, J., Rodríguez-Tovar,
F.J., Nelson, C.H., Bijl, P., Lobo, F.J., García, M., 2018. Paleoceanographic and paleoclimatic conditions during the late Oligocene to early middle Miocene, off the Wilkes Land margin (Antarctica). IX Simposio de Estudios Polares. CN-SCAR, CSIC, IGME, Madrid. ISBN 978-84-8344-670-6.

(9) López-Quirós, A., Escutia, C., Sánchez-Navas, A., Nieto, F., García-Casco, A., **Evangelinos, D.,** Salabarnada, A., Martín-Algarra, A. 2018. Green-clay authigenesis and diagenetic reactions in the South Orkney Microcontinent: Paleoenvironmental implications for the opening of Drake Passage (Antarctica). IX Simposio de Estudios Polares. CNSCAR, CSIC, IGME, Madrid. ISBN 978-84-8344-670-6.

(10) Etourneau, J., López-Quirós, A., Sicre, M-A., Bijl, P.K., Martinez, P., Klein, V., Boterblom, W., Charlier, K., **Evangelinos, D.,** Salabarnada, A., Escutia, C., 2018. Environmental impact of the Drake Passage opening during the
Eocene-Oligocene and Oligocene-Miocene transitions. IX Simposio de Estudios Polares. CN-SCAR, CSIC, IGME,
Madrid. ISBN 978-84-8344-670-6.

(11) Lobo, F.J., López-Quirós, A., García, M., Pérez, L.F., Hernández-Molina, J., Escutia, C., Bohoyo, F., **Evangelinos, D.,** Salabarnada, A., Rodríguez-Fernández, J., Maldonado, A. 2018. Mixed contourite and gravitational processes sculpting the morphology and the recent sedimentary record of Dove Basin, southern Scotia Sea. IX Simposio de Estudios Polares. CN-SCAR, CSIC, IGME, Madrid. ISBN 978-84-8344-670-6.

(12) Salabarnada, A., Escutia, C., Nelson, H.C., Evangelinos, D., López-Quirós, A., García, M., 2018. Origin and evolution of bottom current deposition in the Antarctic Wilkes Land Margin during the Oligocene and Miocene. IX Simposio de Estudios Polares. CN-SCAR, CSIC, IGME, Madrid. ISBN 978-84-8344-670-6.

(13) Escutia, C., Bohoyo, F., Lobo, F.J., Maestro, A., **Grupo de Investigación TASMANDRAKE. 2018**. Desarrollo y evolución de los pasos oceánicos de Drake-Scotia y Tasmania y de la corriente circumpolar antártica: relación con el paleoclima y el desarrollo del casquete de hielo. IX Simposio de Estudios Polares. CN-SCAR, CSIC, IGME, Madrid. ISBN 978-84-8344-670-6.

(14) **Evangelinos, D.,** Escutia, C., Van de Flierdt, T., Kreissig, K., Valero, L., Flores, J.A., Etourneau, J., López-Quirós, A.,
Salabarnada, A., Nelson, C.H., Lobo, F.J., García, M., 2018. Ocean circulation across the Tasman Gateway during mid-Oligocene to mid- Miocene. IASC & SCAR Conference - POLAR 2018, Davos, Switzerland, ISBN 978-0-948277-54-2.

(15) **Evangelinos, D.,** Escutia, C., Valero, L., Etourneau, J., López-Quirós, A., Salabarnada, A., Nelson, C. H., Lobo, F.J.,
García, M., 2018. Eocene-Oligocene tectonic-driven paleoceanographic changes, off the Cape Adare. IASC & SCAR Conference - POLAR 2018, Davos, Switzerland, ISBN 978-0-948277-54-2.

(16) López-Quirós, A., Escutia, C., Etourneau, J., Rodríguez-Tovar, F.J., Bijl, P.K., Lobo, F.J., Bohoyo, F., **Evangelinos, D.,** Salabarnada, A., 2018. Eocene-Miocene paleoceanographic changes in Drake Passage (Antarctica). IASC & SCAR Conference - POLAR 2018, Davos, Switzerland, ISBN 978-0-948277-54-2.

(17) López-Quirós, A., Lobo, F.J., Escutia, C., Bohoyo, F., Hernández-Molina, F.J., Pérez, L.F., García, M., **Evangelinos, D.,** Salabarnada, A., 2018. The ‘Ona Paleovalley’ (Drake Passage): A submarine slope failure system. IASC & SCAR Conference - POLAR 2018, Davos, Switzerland, ISBN 978-0-948277-54-2.

(18) López-Quirós, A., Escutia, C., Sánchez-Navas, A., Nieto, F., Martín-Algarra, A. **Evangelinos, D.,** Salabarnada, A., 2018. Late Eocene marine transgression indicated by glaucony facies (Drake Passage). IASC & SCAR Conference - POLAR 2018, Davos, Switzerland, ISBN 978-0-948277-54-2.

(19) Etourneau, J., Salabarnada, A., **Evangelinos, D.,** López-Quirós, A., Sicre, M-A., Bijl, P.K., Martinez, P., Klein, V., Boterblom, W., Charlier, K., Escutia, C. 2018. Major Climatic Transitions Linked to the Tasman-Drake Tectonic Evolution. IASC & SCAR Conference - POLAR 2018, Davos, Switzerland, ISBN 978-0-948277-54-2.

(20) López-Quirós, A., Lobo, F.J., Escutia, C., Bohoyo, F., Hernández-Molina, F.J., **Evangelinos, D.,** Salabarnada, A., García, M., Pérez, L.F., Rodríguez- Fernández, J., Maldonado, A. 2017. Recent sedimentation patterns in deep basins of the Scotia Sea: Interaction between gravitational and contour-current processes. 3rd Deep-Water Circulation Conference 2017. University of Geoscience (Wuhan), China.

(21) **Evangelinos, D.,** Escutia, C., Salabarnada, A., López-Quirós, A., Nelson, C.H., Valero, L., Etourneau, J., Rodríguez-Tovar, F.J., Bijl, P., Lobo F.J., García, M., 2017. Late Oligocene-Early Miocene transition: Paleoclimate and paleoceanogaphy changes linked to a dynamic East Antarctic Ice sheet, off the Wilkes Land margin. Past Antarctic Ice Sheet Dynamics (PAIS) Conference, September 10-15th 2017, Trieste, Italy.

(22) López-Quirós, A., Escutia, C., Valero, L., Rodríguez-Tovar, F.J., Flores, J.-A., **Evangelinos, D.,** Lobo, F.J., Martín Algarra, A., Salabarnada, A., 2017. Late Eocene-Miocene sedimentation in the southeastern margin of the South Orkney Microcontinent, Drake Passage, Antarctica : Evidence for a major marine transgression. Past Antarctic Ice Sheet Dynamics (PAIS) Conference, September 10-15th 2017, Trieste, Italy.

(23) López-Quirós, A., Lobo, F.J., Escutia, C., Bohoyo, F., Hernández-Molina, F.J., Pérez, L.F., García, M., **Evangelinos, D.,** Salabarnada, A., 2017. Recent morpho-sedimentary processes in the southern part of Ona Basin, Antarctica : Styles of contourite deposition. Past Antarctic Ice Sheet Dynamics (PAIS) Conference, September 10-15th 2017, Trieste, Italy.

(24) Salabarnada, A., Escutia, C., Nelson, H.C., **Evangelinos, D.,** López-Quirós, A., Castro, S. de, 2017. Bottom current deposition in the Antarctic Wilkes Land margin during the Oligocene. Past Antarctic Ice Sheet Dynamics (PAIS) Conference, September 10-15th 2017, Trieste, Italy.

(25) Salabarnada, A., Escutia, C., Nelson, C.H., Roehl, U., Jiménez-Espejo, F.J., **Evangelinos, D**., McKay, R., Ikehara, M., López-Quirós, A., 2017. Late Oligocene contourite sedimentation in the Antarctic Wilkes Land margin: IODP Site U1356. . Past Antarctic Ice Sheet Dynamics (PAIS) Conference, September 10-15th 2017, Trieste, Italy.

(26) Leanne, A., O'Brien, P., Leventer, A., Post, A., Opdyke, B., Caburlotto, A., **IN2017-V01 Science Team.** 2017. Searching for paleoclimate archives on the East Antarctic margin: Sabrina Seafloor Survey 2017. Past Antarctic Ice Sheet Dynamics (PAIS) Conference, September 10-15th 2017, Trieste, Italy.

(27) Noble, T., Chase, Z., Gadd, P., Armand, L., O'Brien, P., **IN2017-V01 Scientific Team.,** 2017. Geochemical reconstruction of paleoenvironmental conditions using sediment cores from the continental slope of Sabrina Coast, East Antarctica. Past Antarctic Ice Sheet Dynamics (PAIS) Conference, September 10-15th 2017, Trieste, Italy.

(28) Escutia, C., Gonzalez, J., de Castro, S., Salabarnada, A., **Evangelinos, D.,** López-Quirós, A., Insights into Cenozoic glacial evolution of the east Antarctic Wilkes Land sector based on seismic stratigraphic correlations with IODP 318 sites. Conference: EGU 2017, Volume: 19.

(29) Salabarnada, A., Escutia, C., Nelson, H.C., **Evangelinos, D.,** López-, A., Castro, S., 2017. Bottom current deposition in the Antarctic Wilkes Land margin during the Oligocene, in: EGU General Assembly 2017 Geophysical Research Abstracts. EGU General Assembly 2017, p. Vol. 19, EGU2017-12464-1.

(30) Salabarnada, A., Escutia, C., Nelson, C.H., Roehl, U., Jiménez-Espejo, F., **Evangelinos, D.,** Ikehara, M., McKay, R., López-Quirós, A., 2016. Late Oligocene contourite sedimentation in the Antarctic Wilkes Land margin: IODP Site U1356. IX Congreso Geologico de España.

(31) **Evangelinos, D.,** Escutia, C., López-Quirós, A., A., Salabardana, A., Nelson, C.H., 2016. Sedimentological evidences of enhanced bottom-currents developed across the Tasman Gateway from the Late Eocene to

Oligocene-Miocene Transition. XXXIV SCAR Meetings and Open Science Conference 2016. Conference: SCAR Meetings and Open Science Conference 2016, Kuala Lumpur, Malaysia

(32) López-Quirós, A., Lobo, F.J., Escutia, C., **Evangelinos, D.,** Salabarnada, A., García, M., Rodríguez-Fernández, J., Maldonado, A., Bohoyo, F., Hernández-Molina, F.J., Pérez, L.F., 2016. Late Quaternary sedimentation patterns in Ona Basin, southern Scotia Sea, Antarctica: Preliminary results. XXXIV SCAR Meetings and Open Science Conference 2016. Conference: SCAR Meetings and Open Science Conference 2016, Kuala Lumpur, Malaysia

(33) Lobo, F.J., López-Quirós, A., García, M., Pérez, L.F., Hernández-Molina, F.J., Escutia, C., **Evangelinos, D.,** Salabarnada, A., Rodríguez-Fernández, J., Maldonado, A., Bohoyo, F., 2016. Morphology and recent sub- Surface stratigraphy of Dove Basin, Scotia Sea: Physiographic constrains on bottom current deposition. 35th International Geological Congress 2016, Cape town, South Africa.

(34) López-Quirós, A., Lobo, J., Escutia, C., **Evangelinos, D.,** 2016 Antarctica's role in the Earth's climate system Conference: I Jornadas de Investigadores en Formación: Fomentando la interdisciplinariedad, University of Granada, Volume: Ciencias de la Tierra

(35) Salabarnada, A., Escutia, C., Nelson, C.H., Roehl, U., Jimenez-espejo, F., **Evangelinos, D.,** Ikehara, M., Mckay, R., Lopez, A., 2016. Obliquity paced contourite cyclicity in Antarctic sediments from the Wilkes Land (Site U1356) during Late Oligocene, in: Geophysical Research Abstracts Vol. 18, EGU2016-14854, 2016 EGU General Assembly 2016. p. 14854.

(36) Van Lancker, V.R.M, Baeye, M., **Evangelinos, D.,** Montereale-Gavazzi, G., Terseleer, N., Van den Eynde, D., 2016. MSFD-compliant investigative monitoring of the effects of intensive aggregate extraction on a far offshore sandbank, Belgian part of the North Sea, ***in***: Degraer, S. *et al.* (Ed.) *North Sea Open Science Conference 7-10/11/2016. Abstract Booklet.* pp. 111

(37) **Evangelinos, D.,** Baeye, M., Bertrand, S., Van den Eynde, D., Van Lancker, V., 2015. Dispersion and Deposition of sediment plumes resulting from intensive marine aggregate extraction. 11th Panhellenic symposium of oceanography and fisheries. Aquatic Horizons and Perspectives, Mytilene, Lesvos Island, Greece, May 2015, pp.12.

(38) Van Lancker, V., Baeye, M., **Evangelinos, D.,** Van den Eynde, D., De Mesel, I., Kerckhof, F., 2014. Use of Wave Glider monitoring for assessing changes in habitat integrity. Book of abstracts- Geohab-Marine Geological and Biological Habitat Mapping, Lorne Australia, 5-9 May 2014, pp. 101.

(39) Van Lancker, V., Baeye, M., Francken, F., Van den Eynde, D., **Evangelinos, D.,** De Mesel, I., Kerckhof, F., Van den Branden, R., Naudts, L., 2014. Working together on innovative monitoring strategies: adapting to nature, huge demands and grand challenges'in: Mees, J. et al. (Ed.) (2014). Book of abstracts – VLIZ Young Scientists' Day. Brugge, Belgium, 7 March 2014. VLIZ Special Publication, 67: pp. 110.

(40) **Evangelinos, D.,** Missiaen, T., Demerre, I.; Van Meirvenne, M., 2013. Buried under the sand: 'Integrated geophysical mapping of ancient peat exploitation at Raversijde beach. in: Mees, J. et al. (Ed.) (2013). Book of abstracts – VLIZ Young Marine Scientists' Day. Brugge, Belgium, 15 February 2013. VLIZ Special Publication, 63: pp. 44.

OUTREACH

May 2019: *Geolodía 2019*- Sociedad Geológica de España, participate as a guide in one-day field trip to the Sierra Nevada complex.
November 2018: Science week in Andalusia (Spain): (3 days)
April 2018: Imperial College Festival "*Was there always ice on Antarctica*?" at the Imperial College London, United Kingdom
April 2017: "*From Granada to the Southern Ocean (East Antarctica): Interactions of the Totten Glacier with the Southern Ocean through multiple glacial cycles"* at Andalusian Institute of Earth Sciences (CSIC-University of Granada), Spain
November 2016: PIISA "*Introduction of science and research to High-School students in Andalusia"*at Andalusian Institute of Earth Sciences (CSIC-University of Granada), Spain

November 2015: Science week in Andalusia (Spain): "*Antarctica and the oceanic basins around it*", at Andalusian Institute of Earth Sciences (CSIC-University of Granada), Spain
October 2015: PIISA "*Introduction of science and research to High-School students in Andalusia"*, at Andalusian Institute of Earth Sciences (CSIC-University of Granada), Spain

TECHNICAL & RESEARCH SKILLS

Opening cores, lithologic description, sediment sampling, physical properties logging, x-ray fluorescence logging, water sampling, seismic profile bathymetry mapping and stratigraphic correlation. chemical radiogenic isotopes analysis (Neodymium).
Equipments: Coulter Counter, Sedigraph, Geoteck Multisensor Core Logger, X-Ray fluorescence, paleomagnetitomerter, rock magnetometer.
Related softwares: Kingdom Suite 8.7 (seismic interpretation and geomodeling), Analyseries 2.0 (time-series analysis), Profex (X-Ray Diffraction processing software), SonarWiz (seismic interpretation), ISE software (seismic interpretation), Core Draw Graphics Suite x7, Adobe Pack (Illustrator, Photoshop) (graphic), Geographic Information System (GIS) (mapping), Surfer11 (mapping), Strater v.3, Grapher v.8, TASS v4.0 (Turbidity assessment software), Microsoft Office.

LANGUAGES

Greek: Native Language **English:** Proficiency: speaking, reading and writing. **Spanish:** Basic: speaking, reading and writing

MEMBERSHIPS

- SCAR: Scientific Committee on Antarctic Research
- APECS: Association of Polar Early Career Scientists
- EGU: European Geosciences Union